NEW MICROFLUIDIC SYSTEMS FOR SINGLE-CELL SIGNALING STUDIES IN IMMUNE CELLS

A Thesis
Presented to
The Academic Faculty

By

Loice Chingozha

In Partial Fulfillment
Of the Requirements for the Degree
Doctor of Philosophy in Chemical Engineering
School of Chemical and Biomolecular Engineering

Georgia Institute of Technology
August, 2015

NEW MICROFLUIDIC SYSTEMS FOR SINGLE-CELL SIGNALING STUDIES IN IMMUNE CELLS

Approved by:

Dr. Hang Lu, Advisor
School of Chemical and Biomolecular Engineering
Georgia Institute of Technology

Dr. Michelle Dawson
School of Chemical and Biomolecular Engineering
Georgia Institute of Technology

Dr. Cheng Zhu, Advisor
School of Mechanical Engineering
Georgia Institute of Technology

Dr. Wilbur Lam
Wallace H. Coulter Department of Biomedical Engineering
Georgia Institute of Technology

Dr. Victor Breedveld
School of Chemical and Biomolecular Engineering
Georgia Institute of Technology

Date Approved: July 16, 2015

This work is dedicated to the memory of my niece Munashe Destiny (2005 – 2011) and to my parents.

ACKNOWLEDGEMENTS

I owe great gratitude to my thesis advisors Dr. Hang Lu and Dr. Cheng Zhu for their support throughout my PhD. They help me learn a lot and to become a better researcher. I am grateful for my friends and work colleagues who supported and encouraged me throughout my PhD. In particular, I would like to thank Mei Zhan, Tom Levario, Lina Herrera Estrada, Sweta Ramathan, Jose Baltazar, Portia Chipendo, Chipo Dendere, Linah Rusere, and Michael Casciato for their support especially during times of frustration. Thank you for making the time here at Tech more enjoyable.

I would like to acknowledge the great support from Rochelle Moses who provided very important administrative support. I thank Larissa Doudy for keeping the Zhu lab running smoothly and for technical support in cell purification that was a critical component in some of my projects. In addition, Larissa was always there to provide as much help as needed and keeping a good moral in the lab.

I am thankful for my parents and siblings (Irene, Tendai, Tafadzwa, Nyasha and Ruvimbo for their support and cheering me on throughout my graduate school career.

TABLE OF CONTENTS

ACKNOWLEDGEMENTS IV
LIST OF TABLES X
LIST OF FIGURES XI
LIST OF SYMBOLS AND ABBREVIATIONS XXXV
SUMMARY XXXVI
1 INTRODUCTION 1
1.1 T cell immune function 1
1.2 Ca^{2+} signaling in T cell lymphocytes 3
1.3 Single-cell measurements enable cell heterogeneity to be analyzed 5
1.4 Analytical tools for immune cell signaling evaluation 6
1.5 Microfluidic systems for cell analysis 8
1.5.1 Microfluidics general 8
1.5.2 Microfluidic device fabrication 9
1.5.3 Microfluidic platforms for single-cell analysis 10
1.6 Thesis Outline 12
2 HIGH-THROUGHPUT, CELL TRAP ARRAY FOR CALCIUM PROFILING IN T CELLS 16
2.1 Introduction 16
2.2 Materials and methods 20
2.2.1 Cell culture 20
2.2.2 Device fabrication 21
2.2.3 Device functionalization with stimulating proteins 22
2.2.4 Calcium imaging 22
2.3 Microfluidic device design 23
2.3.1 Device surface functionalization 24
2.4 Cell loading and fluorescent-based calcium imaging 28
2.4.1 Calcium data analysis 30
2.5 Dynamic Ca^{2+} flux in Jurkat hybridoma cell line 31
2.6 Calcium signaling dynamics in primary OT-1 T cells 33
2.7 Evaluating Calcium signaling alterations in a tumor microenvironment 34
2.7.1 Simultaneous Ca^{2+} imaging and force mapping 39

2.8 Conclusions and Future directions 40

3 A GENERALIZABLE, TUNABLE MICROFLUIDIC PLATFORM FOR DELIVERING FAST TEMPORALLY VARYING CHEMICAL SIGNALS TO PROBE SINGLE-CELL RESPONSE DYNAMICS 43

3.1 Introduction 44

3.2 Materials and Methods 47

3.2.1 Device fabrication 47

3.2.2 Cell culture and cell preparation for calcium imaging 48

3.2.3 Device setup 49

3.2.4 Signal delivery characterization 49

3.2.5 Imaging and data analysis 50

3.3 Device design and operation 51

3.3.1 General design concept 51

3.3.2 Single-cell loading in device 57

3.3.3 Fluid flow design 58

3.4 Cell response to dynamic extracellular Ca^{2+} changes 64

3.4.1 Ca^{2+} response to oscillating extracellular Ca^{2+} concentration 65

3.5 Conclusions and future directions 72

4 PLATFORM FOR MULTIPLEXED FUNCTIONAL ASSAYS 74

4.1 Introduction 74

4.2 Materials and Methods 77

4.2.1 Cell Culture 77

4.2.2 Device fabrication 78

4.2.3 Stimulating ligands and antibodies 79

4.2.4 Device preparation 79

4.2.5 Calcium imaging and analysis 79

4.2.6 Immunofluorescence staining on chip 80

4.2.7 smFISH probe design and hybridization 80

4.2.8 smFISH imaging and analysis 81

4.2.9 Statistical analysis 81

4.3 Device system overview 82

4.3.1 Device functionality overview 82

4.3.2 Device modifications and setup 82
4.3.3 Device surface functionalization 86
4.3.4 Cell viability on chip 88
4.4 Performing single-molecule fluorescence hybridization on chip 88
4.4.1 mRNA quantification using smFISH 88
4.4.2 mRNA spot quantification 91
4.4.3 Application of smFISH on Jurkat cell line 93
4.5 OT-1 T cell activation to demonstrate longitudinal cell analysis with multiple assays 98
4.5.1 Protein phosphorylation events propagate TCR signaling 98
4.5.2 Coagonism in T cell activation 99
4.6 Combined Ca^{2+} analysis and ZAP-70 and Erk phosphorylation 100
4.7 Ca^{2+} and cytokine IL-2 and IFNG mRNA expression levels determination .. 105
4.8 Effect of coagonist peptide on Ca^{2+} and cytokine mRNA expression 107
4.8.1 Multiplexed data correlations using clustering algorithms 113
4.9 Conclusions 119
5 LEUKOCYTE SEPARATION, STIMULATION AND IMMUNOPHENOTYPING FROM LESS THAN A DROP OF WHOLE BLOOD 121
5.1 Introduction 121
5.1.1 Blood for immune analysis 121
5.1.2 Microfluidic-based platforms for cell separation 124
5.2 Materials and Methods 127
5.2.1 Device fabrication 127
5.2.2 Device preparation 127
5.2.3 Blood preparation 127
5.3 Device design and operation principle 128
5.4 Demonstrating the ability to separate out RBCs 131
5.5 Whole blood separation, stimulation and immunophenotyping 133
5.5.1 Leukocyte separation from whole blood 133
5.5.2 Stimulation and surface marker based immunophenotyping 135
5.6 Conclusions 138

6 TOWARDS A HIGH-THROUGHPUT PLATFORM FOR MEASURING ADHESION KINETICS OF MEMBRANE-ANCHORED RECEPTORS AND LIGANDS 140

6.1 Introduction 140

6.1.1 Receptor-ligand interaction kinetics 140

6.1.2 Conventional techniques for 2D receptor-ligand kinetics measurements 142

6.1.3 Microfluidic platforms 146

6.2 Design concept 1: Membrane-based platform for repeated cell contact 149

6.2.1 Selective surface functionalization using laminar coflow 152

6.2.2 Bead and cell loading 156

6.2.3 Membrane deformation characterization 158

6.2.4 Adhesion events detection 161

6.2.5 Measuring streptavidin/biotin interactions 162

6.2.6 Challenges with the setup 163

6.2.7 Using a bead attached to the membrane to make the contact 164

6.3 Design concept 2a: Flow-based adhesion frequency platform 169

6.3.1 Device design and setup 169

6.3.2 Working principle of the flow-based device 170

6.4 Design Concept 2b: Combined microfluidics and magnetic tweezers 171

6.5 Conclusions 173

7 CONCLUSIONS AND FUTURE DIRECTIONS 176

8 APPENDIX 181

A.1. Device Fabrication 181

A.1.1. Device design and fabrication process 181

A.1.2. PDMS replica molding 183

A.2. Calcium Response Analysis 184

A.2.1. Calcium assay protocol 184

A.2.1.1. Materials 184

A.2.1.2. Device preparation 184

A.2.1.3. Cell preparation 186

A.2.1.4. Calcium assay 187

A.2.1.5. Automated image analysis code 187

A.2.2. Calcium Assay Supplemental results 192
A.3. Multilayer design fabrication and characterization 193
A.3.1. Device 2-layer PDMS mold fabrication 193
A.3.2. Flow characterization 194
A.3.3. Additional Calcium Oscillation data 195
A.4. Muitiplexed single-cell analysis on chip 196
A.4.1. Statistical analysis algorithms for correlating different readouts 196
A.4.2. mRNA probe sequence design 200
A.4.3. Additional smFISH data 205
A.5. Single-layer valve device fabrication in PDMS 207

LIST OF TABLES

Table 1. Blood Composition 122

Table 2. Differential Leukocytes count in whole blood (192, 193) 124

Table 3. IFNγ mRNA probe sequences labeled with TAMRA. 202

Table 4. IL2 mRNA probe sequences labeled with Quasar 670 fluorophore 203

Table 5. IκBα mRNA probe sequences with TAMRA fluorophore 204

LIST OF FIGURES

Figure 1-1 T cell and antigen presenting cell (APC)initial interaction via the TCR and pMHC molecules. The initial interaction between a T cell and an APC occurs through the TCR and the pMHC on the APC. The coreceptor, CD8 or CD4 binds to the nonvariant portion of the MHC molecule. 2

Figure 1-2 Process outline for the rapid prototype development in PDMS-based microfluidics development. The design, fabrication and testing of a PDMS-based system can take ~2 days from the 2-dimensional design created with a computer aided design software, AutoCAD, pattern transfer into a 3D SU8 master mold, PDMS molding and device assembly, and finally testing. From this iterations can be made to the fabrication process or the design. 9

Figure 2-1 Simplified calcium signaling pathway in T cells. The TCR/pMHC interaction initiates the signaling cascade leading calcium release from the intracellular stores in the endoplasmic reticulum (ER). The depletion of the intracellular stores leads to the activation of the calcium release-activated channels (CRAC) that allow calcium influx from the extracellular space. The calcium influx through the CRAC channels allow prolonged calcium elevation that drives the nuclear translocation of a number of transcription factors including NFAT that drives IL-2 gene transcription. 18

Figure 2-2 Device design overview. The device is a simple, single inlet, single outlet platform with microstructures for confining cells in defined positions. (a) device overview with 4 chambers, the device has a serpentine channel along which the cell traps are arrayed as shown in (b), (c) shows a cross-sectional view indicated in (b), (d) shows a top view micrograph of the device made in PDMS, showing the cell traps, and (e) is a micrograph showing the cells trapped in the device. 23

Figure 2-3 Interacting molecules in the experimental setup. The device channels is coated with the stimulating ligands using biotin-streptavidin coupling. The device is first

coated with biotin-tagged BSA, followed by the streptavidin and finally biotin-tagged ligands; pMHC that interacts with the TCR and coreceptor CD8, anti-CD28 and anti-LFA1 that interact with costimulatory molecules CD28 and LFA-1 on the T cell surface. 26

Figure 2-4 Uniform coating of stimulating ligands on the device surface. The device was decorated with the stimulating and costimulatory ligands using protein physisorption and biotin/streptavidin interaction. (a) Overview of the device coating sequence, (b) device setup and fluorescent micrograph after coating of FITC-labeled BSA, and (c) average intensity measurements of the different rows on the device, show a uniform intensity indicating uniform distribution of the protein on the device surface. For each row, intensity is measured at 10 different positions, and the average and standard deviation are plotted, (d) along each row shown in b, the fluorescence intensity is uniform. 28

Figure 2-5 Imaging setup. (a) depiction of the device setting, the cell loading is achieved by placing a pipette tip containing the cell suspension at the inlet, and a tubing at the outlet that drives the flow in the device using gravity, and a representative micrograph of the fluorescence image obtained during the time-lapse image in monitoring calcium dynamics using a fluorescent, calcium indicator dye, (b) some time lapse images showing changes in cell intensity over time upon stimulation, and (c) individual cell trace for the calcium measurements over a span of 20 minutes of the cell marked with a dotted box in (b). 29

Figure 2-6 Automated image processing outline. To facilitate the analysis of the fluorescence changes in the individual cell, a custom-made automated image processing and analysis software was written in MATLAB. The software allows the identification of individual cell positions on the images and mean intensities of each cells is measured on each image slice of the image stack. This would allow the time series intensity changes for each cell to be determined. 30

Figure 2-7 Calcium intensity analysis. (a) Intensity trace for an individual cell (red), and background. For the cell trace, a jump in intensity from the background intensity indicates the time at which the cell was trapped in the device and therefore represents time zero for the individual cell, (b) cell trace shifted to the true time zero, (c) cell's intensity normalized with the initial intensity to account for differences in dye loading among cells, and representative (d) heatmap and (e) individual calcium curves (grey) and the population mean with SEM for calcium analysis in a single device, in a single field of view. 31

Figure 2-8 Calcium parameters derived from the calcium curve. From the Ca^{2+} time series data, multiple descriptive parameters can be derived to describe the extent of Ca^{2+} activation including, the time is takes for the cell to respond (resting time), the maximum Ca^{2+} peak, the peak rise time and area under the curve. 32

Figure 2-9 Jurkat T cell rapid Ca^{2+} flux upon stimulation. (a) cross-linking of the TCR with anti-CD3 and costimulatory molecule with anti-CD28 elicits Ca^{2+} signaling, (b) stimulation of Jurkat T cells with calcium ionophore, ionomycin and PMA. The results show that both surface-anchored molecules and soluble chemicals can be used on the platform for cell perturbation..... 33

Figure 2-10 OT-1 T cells show a specific, rapid calcium increase upon interaction with antigenic OVA peptide. Fluo3-loaded OT-1 T cells were stimulated with OVA peptide and costimulatory molecules anti-CD28 and anti-LFA1. The heatmaps show the individual ca^{2+} responses to stimulation with (a) OVA, and (b) VSV..... 34

Figure 2-11. The tumor microenvironment has a negative impact on calcium signaling in T cells. Fluo3-loaded T cells were stimulated with OVA:H2-K^b and anti-CD28 and anti-LFA1 costimulatory molecules. The T cells were harvested from either a healthy mouse or mouse implanted with a tumor. Calcium traces for T cells from (a) a healthy mouse spleen, (b) a healthy mouse lymph node, (c) spleen of a B16 mouse on day 7, and (d) cells from the tumor draining lymph nodes (TDLN) on day 7 post

tumor implantation. Overall, T cells in the tumor draining lymph nodes show an attenuated Ca^{2+} response compared to the cells from the spleen of the tumor-implanted mouse. In addition, T cells from the spleen of the tumor model animal show comparable response to the cells from a healthy mouse. 36

Figure 2-12. Population and single-cell analysis show distinct attenuation of calcium signal in T cells from TDLN. (a) Population average calcium show an overall lower calcium level in the T cells from the TDLN, (b) area under the Ca^{2+} curve distribution, and (c) maximum Ca^{2+} level. For both the area under the curve and calcium peak intensity distributions, the cells from TDLN were significantly different ($p < 0.0001$) from the other three conditions shown. On the other hand, there was no statistical significance among T cells from LN, spleen control and spleen B16..... 37

Figure 2-13 Stimulation with TCR antibody did not elicit a large Ca^{2+} flux in T cells from the TDLN. An antibody against TCR was used to provide a strong stimulation to thes T cells. (a) Calcium response traces for the TDLN T cells showing that the majority of the cells did not show an appreciable increase in Ca^{2+}, (b) Calcium response traces for splenic T cells, the cells showed a rapid increase and sustained Ca^{2+} level, (c) population average response, (c) distribution of the area under the curve, and (c) maximum Ca^{2+} level. Overall, the T cells for the TDLN show disrupted Ca^{2+} signaling even when stimulated with an antibody against the TCR. 38

Figure 2-14 Combined Ca^{2+} and force measurements using a DNA-based tension force probe. Using covalent modification a DNA-force probe is anchored to the surface, and pMHC is coupled to the DNA force probe using biotin-streptavidin coupling. When the cells are loaded in the device interact with the pMHC anchored on the DNA-force probe. (a) Fluo3-loaded cells in the device for Ca^{2+} changes visualization, (b) Fluo3-intensity changes, and (c) combined Ca^{2+} changes and probe fluorophore intensity changes of an individual cell. 39

Figure 3-1. Cellular perturbation by dynamic stimulation. A multilayer microfluidic platform is developed to deliver temporal chemical cues to spatially-confined suspension cells while measuring changes in Ca^{2+} level using a calcium-sensitive dye as an output readout. This platforms handles hundreds of cells in individual positions, thus allowing both population statistics and individual cell analysis to be performed. 44

Figure 3-2. Microfluidic platform design overview. (a) The devices has two layers, the fluid layer (red) where the stimulus and the buffer are introduced, and the cell trap layer (blue) where the cells reside, (b) top view micrograph showing the cell trap layer. The cell trap layer has a serpentine main channel, with cell trapping microstructures along the channel. Overall, the layer has 20 rows with 50 cell traps on each row. The traps are 10 μm wide and accommodate an individual cell as shown. The pores on the cell trap layer connect the layer to the top fluid layer allowing fluid exchange from the top layer to the cells, (c) 3D rendering showing the cell trap positions and the direction of the flow from the fluid layer, and (d) a cross-sectional perspective showing the fluid flow and distribution. The fluid (buffer or stimulus) is introduced from the stimulus channel at a flowrate Q, and a component of this flow (q) goes through the pores to the cell trap layer. 51

Figure 3-3 Device design view. (a) cross-sectional view showing the cell layer (blue) and the stimulus layer (red), (b) 3D rendering showing the PDMS layers and the cell position, and cross-sectional views depicting, (c) the pores on the PDMS membrane and (d) the cell position on the platform. 53

Figure 3-4. Schematic of the device setup. (a) device showing access holes for the inlets and outlets, (b) pipette tip containing the cell suspension is placed at the cell inlet, and cells are loaded in the device using gravity-driven flow with the inlets and outlet of the stimulus layer closed, (c) overall setup during the cell stimulation experiment, the buffer and stimulus reservoirs are at 0.5 psi. The flow into the stimulus layer is

controlled by alternating the opening and closing of valve A and B, and (d) waveforms are created by alternating the opening and closing of the valves, and (e) example of a waveform that can be generated in the device. 56

Figure 3-5. High-density single cell trapping. Cells are loaded in the device using gravity-driven flow, and each trap holds a single cell. The single-cell loading efficiency is > 95 - 98 % with some traps having double loading or no cells loaded. At 10x magnification shown in the figure, ~ 360 cells can be viewed enabling hundreds of cells to be analyzed simultaneously. 57

Figure 3-6 Analytical modeling of flow resistances in the device. (a) depiction of the fluid flow in the device, the fluid is introduced into the stimulus layer at a flow rate, Q, and based on the relative resistances, a flow rate of q goes through the cell trap layer, and (b) the resistance model 59

Figure 3-7 Fluid and mass transfer simulation in Comsol Multiphysics module. A 3-dimensional comsol model for a truncated version of the device consisting of 3 rows of the arrays was created in comsol multiphysics. (a) velocity distribution, and (b) the dynamic changes in the soluble cue concentration, at time t = 0 the soluble cue is delivered to the top layer and a constant concentration is achieved in the bottom cell trap layer within 100 ms. 61

Figure 3-8 Waveforms generated over a large dynamic range with rapid rise. The signal delivery in the device was measured using a fluorescent dye in PBS as a proxy for the signal and PBS as the switching buffer. Alternating solutions of PBS with fluorescent dye and PBS were delivered to the device. (a) fluorescent micrograph of the field of view when the device was filled with fluorescent dye, (b) signal traces of multiple rows in the platform for a period of 20 s, (c) zoomed out traces of signal generation showing that the signal is delivered with very small rise and fall time, and that the overlapping traces from the different positions in the device, (d) signal traces at different positions on the device for the same row showing uniformity of

the signal within each row, (e) period (right-hand y axis) and the rise time (left-hand y axis) for the 10 rows of the traps in the device show that there are negligible differences between the top and bottom row. The average rise is ~ 0.15 s, and (f) 2 s period representing the lowest period achieved in the platform. 63

Figure 3-9. Calcium elevation upon treatment with thapsigargin. Once the cells are loaded in the device, 1 µM TP in PBS without calcium is added, leading to intracellular calcium depletion observed by the elevation in calcium level of the individual cells as shown in the heatmap. 66

Figure 3-10 Heterogeneous cell response to extracellular calcium stimulation. Cell were loaded with Ca^{2+} dye then pretreated with thapsigargin for 5 minutes before being loaded in the device. Once cells were loaded alternating solutions of Ca^{2+} and no Ca^{2+} HBSS buffer were introduced into the device at for a duration of 20 s and 100 s respectively. (a) fluorescence micrograph of the Fluo3-loadeds cells in the device, (b) heatmap showing the changes in fluorescence intensity corresponding to changes in Ca^{2+} level (blue is low Ca^{2+} and red is high Ca^{2+}) for each individual cell, (c) average population response to the stimulus show an oscillatory response that follows the input signal, and (d) the four distinct signal patterns observed within the population. Even though the average response show that the cells follow the input signal, a fraction of cells show no response to the stimulus, some cells only show a peak at the first stimulation before returning to baseline, while some cells show a peak at the first stimulation then plateau to a level higher than the baseline, and some cells exhibit an oscillatory signal entrained with the input signal. 67

Figure 3-11 Population average responses follow the input signal. Cells were exposed to alternating solutions of Ca^{2+} and no Ca^{2+}, while measuring the cell response for each individual cell, and an average for the population was computed. For each data set the number of cells analyzed, n = 100 -200 cells. (a-e) the figures show the average Ca^{2+} response and the grey bars indicate the time when the cells were exposed to

Ca^{2+}. The cells show an increase in intensity within 1 s of exposure to the Ca^{2+} stimulus. (f) Interestingly with the 10 s period, the cells output response show a lag compared to the input signal showing the limit to which a cell can process and responds to a signal. 69

Figure 3-12 individual cell response of hundreds of cells to varying stimulation periodicities. The cells were exposed to 0 and 2 mM Ca^{2+} for varying periods as indicated. The figure panels show the response of each individual cell (blue), and the population average (red). All the intensity values are normalized to the initial intensity for each cell to account for differences in dye loading. Even though the cells are exposed to the same Ca^{2+} level, they show differences in amplitude of the signal output. At the short periods (a,b), the cells lose their ability to return to baseline after the Ca^{2+} is removed because the input signal is faster than the ability of the cell to respond. 71

Figure 4-1 Device function overview. Cells are loaded and stimulated while monitoring changes in Ca^{2+} levels, then incubated for a defined duration of time, and can be fixed/permeabilized and stained for specific molecular signatures. 82

Figure 4-2 Simple microfluidic platform enables high-throughput, multidimensional data acquisition at a single-cell resolution. Schematic overview of the system operation. Microfluidic platform used for analysis of T cell signaling is a 2-layer PDMS device with a cell trapping module and a fluid exchange chamber that facilitated fluid input using conventional pipette. (a) device filled with dye, b) cross-sectional and 3-D view of the 2-layer device, (c) top-view micrograph with cells loaded, (d) illustration of the device simplicity, solutions and cells are introduced into the device using a pipette tip as a reservoir and gravity-driven flow, and (e) illustration of the assays conducted on the platform starting with tracking of calcium dynamics inside the cell using Ca^{2+}-sensitive dyes and time-lapse fluorescence imaging, with subsequent mRNA quantification with smFISH and high-resolution fluorescence imaging and/or

protein expression quantification using immunostaining and fluorescence microscopy. 83

Figure 4-3 Device operation is simple and requires minimum auxiliary equipment. (a) microfluidic chip and all the required materials for running the device, and (b-g) sequence of operation from cell loading to analysis on the same chip. (b) the device cross-section outline showing the inlets and outlets of the cell layer and the fluid layer, (c) a syringe filled with PBS is connected to the outlet of the fluid layer, and thumb pressure is applied to remove bubbles from device, (d) protein coating step where aa pipette tip containing the protein solutions is placed at the fluid layer inlet and the solutions perfuse into the device via gravity-driven flow, (e) once the device is mounted on the microscope stage, a pipette tip containing the cell suspension at the cell layer inlet. Cells are loaded into the device using gravity-driven flow with simultaneous fluorescence imaging to track the Ca^{2+} dynamics, (f) cells are incubated for a defined time by placing the devices in the cell incubator. For long-term incubation (> 4 hours), media is perfused through the fluid layer, and a resistance channel is connected to the outlet to control the flowrate of the media to ~ 10 µL ml^{-1}, (g) device setup for imaging. 85

Figure 4-4 Device surface modification using protein physisorption and biotin-streptavidin coupling. (a) illustration of device configuration during the functionalization process, a pipette tip filled with the protein solution is placed at the fluid chamber inlet and the flow is driven by gravity, (b) sequences of the protein functionalization process, and (c) brightfield and fluorescent micrographs showing the device and fluorescence of BSA-Texas Red and biotin-FITC used to verify the protein functionalization sequence. 87

Figure 4-5 Viability in microfluidic platform and multiwell plate. Cells can be incubated in the device with comparable viability to off-chip conventional cell culture methods. (a) micrograph of cells stained with the live (green)/dead (red) fluorescent

dye, and (b) cell viability before seeding and after 24 hour incubation on- and off-chip..... 88

Figure 4-6 smFISH enables the direct quantification of mRNA copy numbers with spatial information. (a) Short (20-base pair) complementary DNA oligonucleotides are hybridized to the target mRNA sequence, and (b) a maximum projection fluorescence image taken at 63x magnification showing the bright, diffraction-limited spots with each spot representing an individual mRNA molecule. 90

Figure 4-7. Automated spot quantification using FISH-Quant Software. smFISH quantification was performed using a Matlab-based algorithm. (a) example 3D stack, (b) user-defined cell outlines, (c) Gaussian filtering to enhance the signal-to-noise ratio. Background signal is subtracted from the image, and the image signal is smoothed with a small Gaussian kernel, (d) the number of spots in one selected cell is computed over a range of user-defined intensities. Plotting the number of detected spots against intensity, the number of detected spots goes from infinity then plateaus before declining to zero. The intensity threshold is picked to be an intensity when the number of detected spots is invariant with the intensity changes, (e) The threshold intensity is applied to all the cells in the image stack and the number of spots are computed. The spots detected are then visualized to verify accuracy and the detection setting can be altered to improve the accuracy of spot detection. After the detection settings have been optimized, the detection settings are applied to all the image stacks for the experiment (typically 50 – 100 stacks per experiment), and (f) the mRNA transcript distribution for a population of cells, and (g) observed intensity distribution showing that the intensity of the spots is relatively invariant, and therefore very little impact on the detection of the spots. 92

Figure 4-8 Simplified NFκB/IκBα pathway. In the resting state, IκBα keeps NFκB sequestered in the cytoplasm, and when the cell is activated, IκBα undergoes phosphorylation-initiated degradation allowing the NFκB to enter the nucleus where

it drives the transcription of many genes including IκBα thus resulting in an increase in IκBα mRNA expression within 30 minutes of activation..... 94

Figure 4-9 Heterogeneity in mRNA expression levels in Jurkat cells. Cells were stimulated on-chip with ionomycin/PMA or TNF-α for one hour, then fixed and permeabilized overnight followed by hybridization with IkBα mRNA probes. (a) micrographs of the cells showing the nuclear stain (green), and probe imaging (red) at 40x magnification and the insert image at 63x during smFISH imaging, (b) distribution of mRNA copy number in each cell for unstimulated cells (control) and cells under stimulation. Overall, there is an increase in IkBα expression after stimulation, and cells show a distribution in their expression levels..... 95

Figure 4-10 The assay is repeatable on chip. Jurkat cells were stimulated with in separate experiments conducted on different days. Quantification of the IκBα mRNA expression who is similar distribution of expression level in 3 trials (n = 400+ for each trial) 96

Figure 4-11 Combined Ca^{2+} and IkBα mRNA quantification on chip. Fluo3-loaded Jurkat cells were loaded on the device, and stimulated with ionomycin/PMA or no stimulation in the buffer while monitoring changes in Ca^{2+} by fluorescence imaging for 1 hour. (a) Ca^{2+} traces for the cell where only buffer was introduced, the cells show no appreciable increase in Ca^{2+} levels, (b) upon introduction of ionomycin/PMA the cells show a rapid increase in Ca^{2+} followed by a plateau (blue is low Ca^{2+} and red is high Ca^{2+}), (c) after Ca^{2+} imaging the cells were subsequently fixed, permeabilized and hybridized with IκBα mRNA. The transcript levels for the cells under different stimulations, the error bars show the standard deviation from the mean indicated by the horizontal line for each condition, and (d) with the spatial information of the positions of the cells in the device, number of transcripts can be directly compared to the Ca^{2+} dynamics..... 97

Figure 4-12 Coagonist, VSV amplifies Ca^{2+} signaling OT-1 T cells stimulated with agonist OVA. OT-1 spleenocytes are activated pMHC surfaces while simultaneously measuring Ca^{2+} flux. The cells were activated on surfaces coated with (a) OVA, (b) OVA/VSV, (c) VSV. The cells show no change in calcium on VSV peptide, and rapid Ca^{2+} flux with OVA antigenic peptide. However the presence of OVA/VSV peptides results in some cell that have a much higher Ca^{2+} level compared to the cells on OVA surface only. (d) average Ca^{2+} response show a higher Ca^{2+} level with the coagonist, and (e) and (f) show the area under the curve and the maximum Ca^{2+} peak for the individual cells showing that coagonism increases the number of cell with higher levels of Ca^{2+} responses. The mean for each condition is represented by the horizontal bar and the vertical bar represents the standard deviation. 101

Figure 4-13 Effect of coagonism on pZAP70 and pErk. After Ca^{2+} measurements the cells were fixed, permeabilized and stained against phosphorylated Erk and ZAP-70. (a) fluorescent image of anti-pZAP70, and (b) phosphorylation levels of ZAP-70 and Erk in cells stimulated with antigenic peptide, OVA, antigenic peptide OVA in the presence of coagonist peptide VSV, and only coagonist VSV. 102

Figure 4-14 Correlation of Ca^{2+} signaling parameters and Erk and ZAP-70 phosphorylation. The maximum peak for each Ca^{2+} trace was deduced from the Ca^{2+} data, and then matched to the corresponding pZAP70 and pErk intensity for the three stimulating conditions; agonist (OVA), agonist/coagonist (OVA/VSV), and coagonist (VSV). (a-c) Ca^{2+} correlations with ZAP70 phosphorylation, and (d-f) Ca^{2+} correlations with Erk phosphorylation. 104

Figure 4-15. IFNγ mRNA expression dynamics in OT1 CD8+ T cells after stimulation with OVA peptide. T cells were stimulated with OVA peptide for different durations before being analyzed for IFNγ mRNA expression. (a) micrograph of maximum projection for imaging IFNγ mRNA fluorescently-labeled probes, (b) number of mRNA transcripts per cell for 0, 1, 4 , 18 and 24 hours of stimulation, the horizontal

bar is the mean transcript count and the vertical bars show the standard deviation for the cell population and (c) the population average expression levels. * number of cells = > 600 per condition. 106

Figure 4-16. IFNγ expression in OT-1 T cells under different stimulating conditions. OT-1 CD8+ T cells were stimulated with OVA, anti-TCR and a negative stimulation control on BSA surface for 4 hours. (a) Representative micrograph of the maximum Z-projection for smFISH probe imaging. The probes are tagged with TAMRA fluorophore, (b) mRNA transcript count for the 4 conditions, each data point represents the total mRNA count for an individual cell, and the mean and standard deviation are shown for each condition, (n = 400 – 600 cells per condition), and (c) histograms showing the distribution of total mRNA count per cell for OT-1 T cells treated under different conditions. 107

Figure 4-17. OT-1 Ca^{2+} dynamics with and without coagonist VSV. OT-1 T cells were stimulated with the indicated peptide in the presence of anti-CD28 and anti-LFA1. Heatmaps were plotted for the temporal Ca^{2+} dynamics for the individual cells under stimulation with, (a) OVA agonist, (b) OVA agonist and VSV coagonist, (c) VSV coagonist only, and (d) taking the population average for the three conditions, overall T cells show a higher Ca^{2+} response in the presence of a coagonist compared to having only the agonist. 108

Figure 4-18. Analyzing Ca^{2+} dynamics parameters show an overall higher calcium response in the presence of a coagonist. (a) The maximum Ca^{2+} reached for each cell, the average and standard deviation within each population are shown, and (b) area under the Ca^{2+} curve showing the total calcium dose during the first 10 minutes of stimulation. 109

Figure 4-19. mRNA expression levels. After 6 hours of stimulation, cells were fixed, and subsequently hybridized with mRNA probes for IL2 and IFNγ. (a) T cells stimulated on OVA peptide surface show higher mRNA expression level, and a larger dynamic

range compared to cells on OVA/VSV and VSV surface, (b) OVA-stimulated surface show a slightly higher IL2 mRNA expression level, and no detectable spots were observed in cells that were on VSV surface. *number of cells = 600 – 800 for each condition. 111

Figure 4-20. Direct correlation of Ca^{2+} response and IL-2 and IFNγ mRNA expression levels. With the identity of each cell conserved throughout the assays, direct correlations between the Ca^{2+} dynamics and mRNA expression were drawn at a single cell level. Overall the data shows no correlation between the Ca^{2+} does and IL2 or IFNγ mRNA, thus demonstrating that the observation of cells exhibiting high Ca^{2+} may not be enough in identifying functionally responsive T cells. Ca^{2+} dose vs IFNγ expression for (a) OVA, and OVA/VSV, and Ca^{2+} dose vs IL-2expression for (c) OVA, and (d) OVA/VSV. 112

Figure 4-21. Ca^{2+} dynamics clustering using k-means clustering algorithm. The individual calcium traces for OT-1 T cells on either OVA or OVA/VSV surface. For the OVA/VSV surface the OVA density was 0.2 compared to the condition with OVA only. Heatmaps showing individual calcium traces arranged by the clusters, (a) OVA, (b) OVA/VSV. The clusters are indicated on the heatmaps. Average calcium trace for each cluster for (c) OVA and (d) OVA/VSV. Distinct calcium traces are observed for each cluster. 114

Figure 4-22. Clustering of OT-1 T cells stimulated on OVA surface by PCA of the Ca^{2+} dynamics and mRNA expression. The color for each data point represents the clusters of the cell from the k-means clustering of the calcium dynamics above as indicated in the legend. (a,b) for the OVA-treated cells the 4 clusters from k-means clustering are separated, showing a positive correlation between the calcium dynamics and mRNA expression levels, and (c,d) for the OVA/VSV treated cells, the calcium clusters are diffuse in the PCA analysis showing no direct correlation with the mRNA expression levels..... 116

Figure 4-23. Clustering of OT-1 T cells stimulated on OVA surface by PCA of the Ca^{2+} dynamics and mRNA expression. The variance contribution is 83.4 % for PC1 and 14.7 % for PC2. (a) plot of the three principal components , the color of each point represents the IFNγ mRNA count (blue = low, and red = high), (b) PC1 and PC2 plot show that the IFNγ mRNA count is described by the first PC. (c,d) The color of each point represents the IFNγ mRNA count (blue = low, and red = high), (c) a plot for the 3 principal components, and (d) plot of first 2 PCs show no distinct subsets for IL-2 mRNA expression. 117

Figure 4-24. Clustering of OT-1 T cells stimulated on OVA/VSV surface by PCA of the Ca^{2+} dynamics and mRNA expression. The variance contribution is 98.6 % for PC1 and ~ 1 % for PC2. (a) plot of the three principal components , the color of each point represents the IFNγ mRNA count (blue = low, and red = high), (b) PC1 and PC2 plot show that the IFNγ mRNA count is described by the first PC. (c,d) The color of each point represents the IFNγ mRNA count (blue = low, and red = high), (c) a plot for the 3 principal components, and (d) plot of first 2 PCs show no distinct subsets for IL-2 mRNA expression..... 118

Figure 4-25. PCA clustering of the combined data for OVA, OVA/VSV and VSV conditions for calcium dynamics and IFNγ mRNA expression. The variance contribution is 85.6 % for PC1 and ~ 14.1 % for PC2. All the data for the T cell activation with OVA, OVA/VSV, and VSV was pooled together and PCA was performed. 3 distinct groups are observed that correspond to the cells under the different treatment conditions are observed. The color for each point represents the stimulating condition for that cell. 119

Figure 5-1 Device operation. (a) Single inlet/single outlet device for the separation of leukocytes from whole blood, (b) depiction of the separation of the removal of red blood cells. The red blood cells are very flexible and can pass through very small gaps, therefore in the device the red blood cells can pass through the 2 μm

constriction at the cell trap while the more rigid leukocytes are directed to the cell trap and remain in the cell traps, (c) micrograph of the device showing the array of cell traps in the device, and (d) jurkat cells after being separated from red blood cells and trapped in the device. 128

Figure 5-2. Microfluidic platform enables rapid analysis of minute quantities of blood. Multiple analysis can be performed on chip starting with the removal of reds blood cells and trapping of leukocytes for subsequent analysis including differential leukocyte counting, stimulation and time-lapse analysis and measurement of activation marker expression and gene expression of specific cells. The platform is very simple, and the flow is driven by gravity-driven flow implemented by suspending the outlet tubing to a height, h ≈ 15 cm. 130

Figure 5-3. Capture of Jurkat cells mixed with red blood cells. Jurkat Jurkat cells mixed with red blood cells (1,000 red blood cells per Jurkat cells), and then introduced into the device. (a) device micrograph, (b) Jurkat cells capture in the device, (c) cell tracker red imaging of Jurkat cells. After trapping the cell were loaded with Fluo3 calcium-sensitive dye and stimulated with ionomycin (1 μg/ml) with simultaneous calcium imaging. (d) heatmap showing the individual cell response upon stimulation with ionomycin, and (e) individual curves and the average (red) calcium response. 132

Figure 5-4 Whole blood in the device. (a) Whole blood in device at 10-fold dilution, (b) demonstration of the escape of red blood cells through the cell traps allowing the red blood cells to exit the device channel, and (c) the first 2 rows on the platform showing trapping of leukocytes. 135

Figure 5-5. Fluorescence imaging to characterize surface marker expression levels. Stimulated cells were stained for CD66b (a), and CD11b (b) expression levels. (c) Merged micrograph image. 136

Figure 5-6 Surface marker expression of neutrophils after stimulation with LPS. Leukocytes separated from whole blood and stimulated with LPS were stained for CD66b and CD11b surface marker expression. (a) micrograph for fluorescence imaging in green and red channel (merged) for imaging of expression of CD66b and CD11b showing cells that express both CD11b and CD66b and a cell expressing CD11b only, and (b) Expression levels of CD66b (x-axis) and CD11b (y-axis). The cells were divided into a quadrant representing $CD66b^{low}$ and $CD11b^{low}$, $CD66b^{low}$ and $CD11b^{high}$, $CD66b^{high}$ and $CD11b^{high}$, and $CD66b^{high}$ and $CD11b^{low}$. Neutrophils constitutively express CD66b and CD11b, and higher levels of CD11b when stimulated. (n = 401) 137

Figure 6-1. Micropipette assay setup. A red blood cell (RBC) bearing the ligand (pMHC) is aspirated on a micropipette and the cell bearing the interacting receptor (TCR) is aspirated on another micropipette. The cells are brought into contact for a defined duration using a piezo-driven micromanipulator. If there is bond formation, the RBC shows detectable elongation upon retraction of the RBC which indicates an adhesion event. 143

Figure 6-2. Design concept overview. The figure depicts the design concept for developing a platform. A ligand-coated surface or cell and receptor bearing cell needs to come into contact for a defined period of time and then adhesion events are detected and the process is repeated > 50 times to get adhesion probability. From the adhesion probability data kinetic parameters can be computed..... 145

Figure 6-3. PDMS valves. The deformability of the PDMS polymer can be modulated by varying the crosslinking ratio used in the polymer curing. Two main types of valves are used (a) top-down valves that require a 2-layer PDMS device, the top channel is a control layer that is pressurized to deflect the bottom flow channel, and a single-layer (in-plane) valve where both the control and flow layer are on the same plane, and the control channel is deflected into the flow layer. With both valves the control

and flow layer are separated by a thin PDMS membrane, and the aspect ratio of this membrane determines that maximum deflection that can be achieved. 147

Figure 6-4. Combined single-layer valve control and cell trapping platform. (a) device outline showing the cell trapping module (blue) and the control layer (red), the cell trapping module has 2 or 3 inlets (1-3) and two outlets (4,5). The control layer has a single inlet (6) and no outlet, (b) micrograph of device showing the cell trapping area and the membrane channel. Each cell trap has a corresponding membrane channel on the opposing side, and (c) illustration of how the device works showing beads loaded in the device, membrane actuation to allow the beads to contact the membrane wall bearing the ligand, and after membrane retraction where some beads bind and remain stuck to the wall of the membrane. 150

Figure 6-5. Device design layout. (a) top view of device design showing the cell trapping module (blue), and the single-layer membrane valve (red), (b) cross-sectional view (Z → Z') , (c) cross-sectional view showing the position of the cell in the device, and (membrane actuation that deflects into the cell trapping module channel to contact the loaded cell/bead. 151

Figure 6-6. Interacting molecules on the device platform. On the platform the receptor is on the cells/beads loaded in the trapping microstructures and the ligands are coated on the side of the membrane using biotin-BSA physisorption and biotin-streptavidin coupling, and laminar coflow for restricted coating of the ligands to the membrane wall only..... 153

Figure 6-7. Laminar flow in microfluidic channels enable coflow of multiple streams and mixing between adjacent streams is by diffusion. The flow in microfluidic channels is laminar, and convective transport between adjacent streams is minimized. In a 3 inlet channel device, the relative flow rates introduced will determine the width of the individual streams. (a) the streams will have equal widths if the flow rates are the same for all inlets, and (b) changing the relative flow rates will alter the widths of

the streams, thus allowing for patterns of different widths to be made in the device, and these can also evolve over time..... 154

Figure 6-8. Laminar flow-enabled selective device functionalization with stimulating molecules. (a) coflowing of solutions of biotin-BSA and BSA (or BAS-FITC for visualization) with the biotin-BSA stream flowing over the membrane wall enables the membrane well to be biotinylated to coupling of biotinylated ligands using biotin-streptavidin coupling. Micrographs for visualizing the fluorescently tagged stream (BSA-FITC) to verify the fidelity of the maintenance of the laminar flow stream in the device, (b) upstream, and (c) in the center of the device. 155

Figure 6-9. Cell and bead loading in the device. (a) Device setup during loading, (b) cells loaded in the device, and (c) beads loaded in the device. Cell and bead loading has an efficiency > 90 % for single cell/bead loading..... 157

Figure 6-10. Membrane deflection characterization. The membrane channels were filled with 50 % glycol w/w and the inlet of the control module was connected to a pressure source with a electronically-controlled solenoid valve controlling the opening and closing of the valve. (a) micrographs of the device before pressure is applied and at 10, 30, and 40 psi showing the deflection of the membrane into the cell trapping channel, (b) deflection of the membrane as a function of pressure for different devices, (c) deflection at the indicated pressures on different channels along the device, and (d) membrane deflection with beads loaded in the device at 25 psi and 35 psi. 159

Figure 6-11. Visualizing the contact between membrane wall and beads by confocal microscopy. To get a clear view of the contact point between the membrane and the bead, confocal imaging was performed, the device membrane channels were filled with FITC dye, and red fluorescent beads were loaded in the device. (a) Beads loaded, membrane valve closed, and (b) membrane valve open, the beads are in contact with the membrane. 161

Figure 6-12. Observing adhesion to the ligand-coated membrane wall. Upon contact with the membrane, the receptor-bearing beads can form a bond with the ligand on the membrane, when the membrane is retracted if the bead forms an attachment with the membrane it will be dragged out of the trap for a distance and may detach if the drag force becomes larger than the bond force. When the bead detaches it may return to the trap or flow along the channel. In the figure the third bead from the left disappeared during membrane retraction as a result of being washed away with the flow induced during membrane movement. 161

Figure 6-13. Adhesion events between biotin and streptavidin interactions. Repeated contacts between the biotinylated membrane and streptavidin-coated beads loaded in the device, and adhesion events were counted. (a) Contact time dependent adhesion events at 2s and 5 s contact time, and (b) density dependent adhesion frequency showing no change in adhesion frequency at the two concentrations used in the experiments. 163

Figure 6-14. Setup using membrane-bead actuation. (a) Streptavidin beads are loaded in the device after the device membrane wall is coated with biotin-BSA. The membrane is then actuation for 10 s to ensure all the beads attach to the membrane via the biotin-streptavidin interaction, and then the membrane is retracted, and we can see that the beads are attached to the membrane. (b) Molecule configuration on the membrane side. The streptavidin beads also have streptavidin molecules coupled to biotinylated beads, and (c) second set of beads bearing the receptor are loaded into the traps..... 165

Figure 6-15. Bead-bead contact enables better visualization of contact area. (a) Pairing of streptavidin beads (on the membrane), and biotinylated beads (in the trap), (b – d) membrane actuation at increasing pressures shows that the bead pairs come into contact at 5 psi. 167

Figure 6-16. Flow-based adhesion frequency platform. The device consists of 2 inlets for use in laminar coflow. The device is a single layer PDMS mold, and is molded from a 2-layer SU8 mold. The main channel is 20 μm and cell traps are 10 μm wide with 2 μm restriction channels. The first configuration had cell traps on one side of a channel and restriction channels 2 μm tall, and the second configuration has cell traps on both sides of the main channel. 169

Figure 6-17. Fluid flow setup for device operation. (a) device inlets/outlets, (b) beads are loaded through inlet 1, while P_1 = 1 atm, P_2 & P_3 are off, and the outlet is at atmospheric pressure, and (c) the beads are moved to the ligand-coated surface by pressure-driven flow, P_1 = 0.5 psi, P_2 and P_3 are off. 170

Figure 6-18. Using magnetic force to drive movement of ligand-coated beads. In the proposed setup two electromagnets are setup. Cells or beads are loaded in the device, and then magnetic, ligand-coated beads are loaded on the adjacent traps. Ligand-coated beads come into contact with the receptor-bearing beads/cells by turning on electromagnetic 1 for a defined time and then electromagnet 1 is turned off and electromagnetic 2 is turned on to break the contact. Adhesion is observed by the ability to observe movement of the receptor-bearing bead/cell. 172

Figure 8-1. SU-8 master mold fabrication. 182

Figure 8-2 Device PDMS molding for a single-layer PDMS device. PDMS prepolymer is mixed with the curing agent at a ratio of 10:1 w/w prepolymer to crosslinker. The PDMS is degassed is a vacuum desiccator, then poured on the silicon master mold. The PDMS is baked at 70 degrees Celsius for at least 2 hours. The cured PDMS mold is then peeled off the mold, individual devices are cut out, and access holes are punched at the device inlets and outlets with a blunt 19-gauge needle. The devices are treated with oxygen plasma and bonded to a coverslip. 183

Figure 8-3 Device preparation for the Calcium assay. (a) This a simple assay that requires the microfluidic chip, tubing with a 19-gauge pin, syringe filter and a syringe, (b &

c) the syringe is filled with PBS used to prime the device to remove bubbles, (d) can see a puddle of fluid at the inlet of the device, (e) insert a pipette tip filled with solutions for coating the device at the inlet, and (f) allow the solution to perfuse for a defined time with flow driven by gravity. 186

Figure 8-4. Heterogeneous calcium response of Jurkat E6.1 on anti-CD3-coated surfaces 192

Figure 8-5. Fabrication of the 2-layer PDMS device**.** The device mold fabrication utilizes multilayer lithography and thermal bonding between the PDMS layers. (a) The cell trap layer is molded by spinning PDMS prepolymer:crosslinker (10:1) at 1500rpm for 5 minutes to make a ~10-15 um layer of PDMS such that the features of the posts used to make pores in the PDMS are protruding and then partially baked for 15 minutes. This layer is then partially baked and then aligned to the partially baked top layer, and then fully baked, (b) for the top layer, PDMS (10:1) is poured on the wafer and partially baked for 20 -25 minutes, and (c) individual devices from the top layer mold are cut out and aligned to the cell trap layer mold. PDMS is poured on the master mold and then baked at 70 degrees for at least 2 hours, the PDMS is peeled off, access holes are punched and devices are bonded to a coverslip. 193

Figure 8-6 Microfluidic device components. (a) overall depiction of the device showing the top view of the stimulus and device layer which consists of the cell trapping module, and (b) an illustration of the different layers of the device module, the cell trap and perforated membrane make up one module and the access holes on the membrane connect fluid exchange between the stimulus layer and the cell trap layer. 194

Figure 8-7 Characterization of the pulse signal showing the periodicity in each row (5 s) and the risetime. The period is approximately the same regardless of the position in the device and the rise time is on average 150 ms. 194

Figure 8-8 Calcium response of cells exposed to 20 s pulses of calcium and 100 s of buffer, and (b) the average cell response. 195
Figure 8-9 Overview of mRNA quantification using smFISH. T 199
Figure 8-10. Device setup and operation setup demonstrate ease of use. The platforms requires very few simple peripheral supporting systems for operation. (a) The autoclaved device is primed with sterile PBS through the fluid layer outlet/inlet using the thumb finger pressure to remove bubbles and fill the device with PBS, (b) the device setup during protein coating. Protein solutions are introduced through the fluid inlet by gravity-driven flow, (c) cell loading by gravity-driven flow and simultaneous image acquisitions, (d) device configuration during incubation, fixation, hybridization and immunostaining steps, and (e) imaging..... 200
Figure 8-11 Ca^{2+} dynamics and subsequent mRNA quantification. Jurkat cells were stimulated while simultaneously measuring the calcium dynamics and subsequently mRNA transcripts were hybridized. On a population average, the higher average calcium level measured by the area under the calcium curve corresponded with higher average mRNA level expression. 205
Figure 8-12 IFNγ and IL-2 mRNA expression of OT-1 T cells. OT-1 CD8+ spleenocytes were stimulated with either OVA or VSV peptides in the presence of anti-CD28 and anti-LFA1 for 6 hours. As expected T cells stimulated on OVA surface showed significantly higher IFNγ mRNA expression levels compared to those on VSV, nonstimulatory surface but the IL-2 mRNA expression was comparable. 206
Figure 8-13 Membrane-based adhesion device replica molding. (a) Device 2-layer master mold, (b) 22:1 PDMS prepolymer-to-crosslinker ratio was poured and partially baked for 30 minutes then a 10:1 PDMS PDMS prepolymer-to-crosslinker ratio was poured on top then the mold was fully baked, and (c) the mold was peeled off and bonded to a coverslip. 207

LIST OF SYMBOLS AND ABBREVIATIONS

TCR	T cell receptor
BSA	Bovine serum albumin
APC	Antigen Presenting Cell
pMHC	Peptide Major Histocompatability Complex
smFISH	single molecule Fluorescene In Situ Hybridization
CRAC	Calcium Release-Activated Channels
ER	Endoplasmic Reticulum
OVA	Ovalbumin peptide
VSV	Vesicular stomatitic virus
EDTA	Ethylenediaminetetraacetic acid
RPMI	Roswell Park Memorial Institute medium
PBS	Phosphate Buffered Saline
SA	streptavidin
LPS	Lipopolysaccharide
PDMS	Polydimethylsiloxane
IFNγ	Interferon gamma
IL-2	Interleukin 2
PCA	Principal component analysis

SUMMARY

Profiling immune cell signaling pathways requires techniques that allow for precise spatial cell positioning, control of the cellular microenvironment, and the ability to perform high-throughput multiplexed measurements at a single-cell resolution. Traditional tools often focus on bulk measurements that can mask the inherent cell heterogeneity or assays that enable a single snapshot of individual cells, therefore missing information on the temporal dynamics. Emerging microscale tools have been applied to improve on traditional approaches and also to introduce new ways of analyzing immune cell signaling events.

Immune cell signaling specifically in T cells involves cell-cell interactions via surface-anchored molecules, and receptor interactions with soluble cues that induce intracellular signaling cascades. These signaling events involve morphological changes in cell shape, and molecular changes such as calcium dynamics, mRNA and protein expression, and proliferation. The signaling cascades span a large dynamic range from seconds to days. Therefore assays that enable long-term monitoring of the signaling dynamics and multiplexed measurements of different molecules are necessary in obtaining a comprehensive understanding of the immune signaling pathways. Moreover, the cell heterogeneity within seemingly homogenous cell populations necessitates the need for platforms that allow for high-throughout, single-cell analysis. Most of the conventional assays allow for the evaluation of cell behavior in the context of a population of cells. However, this will mask some of the heterogeneity within a cell population that may have functional consequences. Experimental assays that enable a diverse range of

perturbations and multiple measurements to be conducted will be critical in enabling a more comprehensive understanding of cell signaling dynamics. On the other hand, the development of microfluidic systems has enabled the emergence of new assays that facilitate cell handling allow for high-throughput, single-cell analysis. In addition, T cells are non-adherent and highly mobile once activated. Therefore, cell handling and spatial confinement is important in image-based approaches used in monitoring the dynamic changes in signaling.

This thesis presents microscale tools and image-based approaches for analyzing immune cell responses. The first application is designed for short-term (~ 1 hour) monitoring of calcium signaling in T cells upon stimulation with surface ligands. The platform enables high-density trapping of individual cells and monitoring of calcium dynamics with ~ 300 cells in a single field of view. I further developed a high-density cell trap array coupled with a dynamic soluble signal generator that enables temporal changes in the cellular microenvironment to be performed while simultaneously monitoring calcium changes in the cells. Building on these above mentioned platforms an integrated platform was developed to enable defined cell spatial positioning, stimulation with both surface-anchored molecules and soluble cues, monitoring of dynamic changes with fluorescence live imaging, incubation times of up to 24 hours and multiple assays to quantify changes in mRNA using single molecule Fluorescene In Situ Hybridization (smFISH) and protein expression by immunofluorescence staining. We further sought to advance the throughput at which the receptor/ligand interaction kinetics are measured in a more physiological context. I developed a microfluidic-based tool combined with automated

operation and image processing that will allow for parallelization of the receptor/ligand interaction kinetics measurements. Finally, I utilize the microscale tools capabilities to develop an assay for separating leukocytes from less than 1 μL of whole blood. The platform enables leukocyte immunophenotyping from minute quantities of blood, and has potential applications when handling blood samples from small experimental animals like mouse, and for performing routine monitoring of a patient's immune response.

Overall, the systems developed in this study enable robust single-cell handling and easy fluid exchanges that facilitate the control of the cell microenvironment. In addition, the platforms developed are easy to use, and do not require sophisticated auxiliary equipment to function, making them easily transferrable to a typical biological laboratory.

1 INTRODUCTION

Fundamental to the maintenance of a healthy individual is the ability of the immune system to keep checks and balances in immune cells to protect the body from pathogenic insults and prevent overactive immune cells that may result in autoimmunity. Our understanding of the mechanism underlying the immune system response has been informative in the development of immunotherapies, vaccines, and in understanding some of the causes of autoimmunity and chronic illness. A number of technologies including the development of transgenic mouse models (*1, 2*), intravital microscopy (*3*), and *in vitro* models for immune cell analysis have facilitated the understanding of the immune system. In this thesis the focus is on the development of tools that will facilitate *in vitro* studies of immune cell response, with a particular focus on the T cells that are part of the adaptive immune system. However, the tools developed are applicable to other immune cells, as well as to other mammalian cells beyond those in the immune system. Our goal is to bridge some of the gaps in the existing assays and enhance the information that can be collected.

1.1 T cell immune function

T cells are a critical component of the adaptive immune system and are responsible for mounting an immune response during foreign insults. In addition, T cells have to tolerate self-antigens that are more abundant on cells to prevent aberrant T cell activation that can lead to autoimmune diseases. This intricate balance in T cell response is of great interest in immunology and understanding of the mechanism underlying T cell self-tolerance, and antigen recognition can be informative for disease diagnosis, therapeutics, and vaccine

development. T cells are able to recognize foreign antigen with high sensitivity, specificity, and speed, a phenomena that has been of great interest to study.

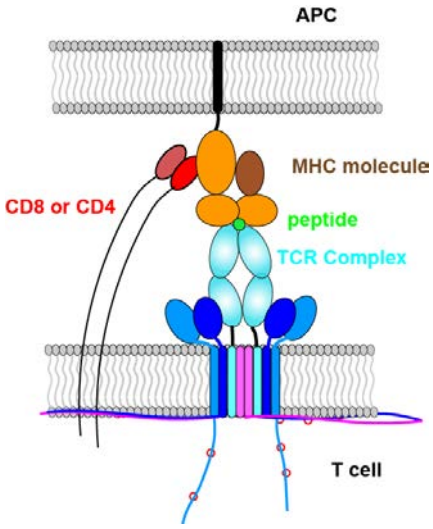

Figure 1-1 T cell and antigen presenting cell (APC)initial interaction via the TCR and pMHC molecules. The initial interaction between a T cell and an APC occurs through the TCR and the pMHC on the APC. The coreceptor, CD8 or CD4 binds to the nonvariant portion of the MHC molecule.

T cell activation is initiated by the interaction of the T cell receptor (TCR) complex with a cognate peptide on a major histocompatibility complex (pMHC) (Figure 1-1). The interaction between the TCR and pMHC triggers intracellular signaling cascades that lead to proliferation, cytokine production, apoptosis, and T cell-mediated killing of infected cells (*4-6*). The high abundance of self-antigens that do not elicit an immune response highlights the TCR's high sensitivity to a cognate antigen peptide that is in low abundance on the cell surface. Even early events in T cell signaling such as calcium flux show high sensitivity to antigenic peptides in a pool of endogenous self-peptides (*7*). Furthermore, the peptide sequences of self and antigenic peptides may differ by a single amino acids; thus the T cell interaction that elicits a response is highly specific (*7*).

Studies demonstrated that as few as a single specific pMHC can trigger calcium signaling (*8*), and that even a single TCR-pMHC interaction can trigger cytokine production (*9*). Finally, the events in T cell signaling are very rapid, occurring within seconds of T cell engagement with a cognate pMHC, and the signal propagation span a large dynamic range (*10*). These signaling events include the rapid intracellular protein phosphorylation, immediate burst in calcium, the upregulation of activation surface markers, secretion of cytokines and proliferation (*4-8, 11, 12*). The dynamic nature of these signaling events necessitates the need for experimental tools that allow multiparameter data to be collected at different timescales to obtain a comprehensive understanding of signal transduction pathways.

1.2 Ca^{2+} signaling in T cell lymphocytes

Ca^{2+} is a second messenger in T cell signaling. In the resting state, T cells maintain a low Ca^{2+} concentration in the cytosol (~ 100 nM), and a higher concentration in the endoplasmic reticulum (~ 100 µM), while the extracellular calcium level is ~ 1 mM. Once activated, the cytosolic calcium increases by a 10-fold through the release of calcium from the intracellular calcium stores in the ER, and the calcium levels are sustained for a duration of time by calcium influx from the extracellular space through the Calcium Release-Activated Channels (CRAC). At the early time points, Ca^{2+} drives cytoskeleton rearrangements and cell motility that helps stabilize the contact between the T cell and the APC. A sustained Ca^{2+} elevation over a duration of minutes to hours regulates specificity in gene activation. The gene activation is dependent on the nature of the calcium dynamics, and may depend on the amplitude, duration and dynamics of the Ca^{2+} signal. For example, activation and nuclear translocation of NFAT transcription

factor is driven by a sustained high Ca^{2+} level. NFAT drives the transcription of IL-2 cytokine genes. In addition to the CRAC channels and the ER intracellular stores that are key to the cytosolic Ca^{2+} concentration, there are channels that also regulate the calcium dynamics in the T cell by pumping Ca^{2+} from the cytosol. The Sarco-endoplasmic reticulum Ca^{2+}-ATPases removes Ca^{2+} from the cytosol to the ER. Plasma membrane Ca^{2+}-ATPases (PMCA) pump Ca^{2+} from the cytosol into the extracellular space. These Ca^{2+} pumps modulate the Ca^{2+} dynamics and stability of the Ca^{2+} signal (*4, 5, 13-20*). The development of calcium-sensitive dyes in combination with use of fluorescence microscopy enables the direct visualization of calcium dynamics in the cells (*21, 22*). Cells can be easily loaded with the Ca^{2+} - sensitive dye and changes in cytosolic Ca^{2+} inside the cell can be monitored using fluorescence microscopy or flow cytometry (*5, 14, 18-20, 23, 24*). However, *in vitro* the challenge in measuring Ca^{2+} dynamics lies in sample handling and the application of the appropriate perturbations to elucidate function. T cells are nonadherent and are highly mobile when activated, making it difficult to capture the Ca^{2+} dynamics *in vitro* using fluorescence microscopy imaging. While flow cytometry can be used in analyzing the Ca^{2+} response, only a snapshot for each cell can be obtained and the Ca^{2+} dynamics are captured on a population level. Therefore, it is difficult to identify small subsets of cells within the population with interesting behaviors that may have functional consequences. As a result, evaluating the Ca^{2+} response dynamics at a single cell level may be important in analyzing T cell behavior especially in polyclonal T cell populations.

1.3 Single-cell measurements enable cell heterogeneity to be analyzed

The inherent heterogeneity in cellular response to perturbations arising from stochasticity in gene (*25-28*) and protein expression (*29*), and differences in cell state have inspired the need to perform assays at single-cell resolution (*27, 30-35*). This heterogeneity can give rise to emergent behavior and have interesting implications on function (*36-45*) . Cohen *et al* showed cancer drug resistance in a subpopulation of seemingly identical human lung carcinoma cells evidenced by heterogeneity in protein dynamics that then influenced cell fate. Other studies have also demonstrated drug resistance on an individual cell level that would otherwise not be apparent in ensemble measurements (*37, 40, 41, 43*). As a result, population averages may mask these interesting behaviors that are contributed by a small subset of the cell population (*25, 27, 35*). In the context of immune cells, differential responses to stimulation has been observed even in a seemingly homogenous T cell population with subsets of T cells emerging that are either responsive, anergic, inhibitory or autoreactive (*46, 47*). Ma *et al* demonstrated heterogeneity in cytokine and chemokine secretion in tumor-specific T cells upon stimulation with distinct cell subtypes (*48*). These differences may have implications on the responsiveness of the cells to drug treatment.

Therefore, efforts have been focused on developing assays that enable single-cell analysis while evaluating hundreds to thousands of cells to enable population statistics to be obtained. Flow cytometry enables high-throughput analysis of tens of thousands of cells for protein expression. However, for dynamic measurements, flow cytometry can only provide population level dynamics and only a snapshot of each individual cell. Being able

to monitor changes on an individual cell through time can be insightful in linking early and late time signaling events, therefore allowing a comprehensive understanding of signaling transduction pathways (*30, 33, 49*).

1.4 Analytical tools for immune cell signaling evaluation

Many analytical tools for measuring immune cell response rely on bulk measurements that give a population average, and with cell heterogeneity interesting behaviors may not be elucidated. Experimental approaches for characterizing single-cell immune response have been focused on measuring signatures of the central dogma (DNA, RNA and protein content), with each strategy enabling one or more of these signatures to be evaluated. Ideally, a technique allowing DNA, RNA, and protein expression would be insightful in understanding transcription and translation relationships.

Flow cytometry has been extensively used to monitor immune cell signaling including calcium flux, and expression of surface markers, and intracellular proteins (*31*). The robustness of the assay, ease of use, and the ability to assay a large number of cells makes it an attractive standard assay to perform. The development of polychromatic dyes and barcoding has enabled a large number of proteins to be assayed at the same time (*50, 51*). However, flow cytometry often requires a large number of cells that may become a challenge when only a small number of cells (~ 1000 cells) are available, especially when studying very rare cells such as antigen-specific cells. In addition, flow cytometry relies on the availability of specific antibodies for the identification for cellular markers, and this can limit the scope of analysis to antibody availability. Although still in its infancy,

mass cytometry has the potential to revolutionize cytometry analysis by increasing the number of different molecules that can be analyzed simultaneously (*52-57*). In addition to flow cytometry, fluorescent-based microscopy techniques have been implemented to enable spatial and temporal visualization of signaling events. Surface markers and intracellular protein expression can be visualized using target antibodies. Time-lapse fluorescence microscopy together with calcium-sensitive dyes can enable the calcium dynamics of individual cells to be monitored (*12, 14, 17-22, 58-61*).

However, while there have been great advances in the imaging techniques, development in robust cell handling and techniques that allow manipulation of the cell microenvironment has been lagging. T cells are suspension cells and are not easily anchored on the surface without perturbing their function, and become highly mobile when activated. In microscopy imaging, it will be challenging to image T cells continuously as they may drift out of focus or move out of the field of view. In addition, it will be difficult to introduce soluble stimulation while simultaneously imaging. Therefore, an ideal platform for immune cell studies would enable ease of cell handling, the ability to alter the microenviroment for cell perturbation studies, and the ability to acquire data for different molecular signatures. A number of cellular traits can be assayed including surface marker expression, protein secretion, receptor/ligand interaction kinetics (*58, 62-64*), cell motility, proliferation, and intracellular protein or transcript expression (*46, 59, 65-67*). The emergent of microfluidic technology has helped bridge the gaps in sample handling and controlling of cellular microenvironment and also in

improving the repeatability and throughput of the assay. More details on microfluidics are discussed below.

1.5 Microfluidic systems for cell analysis

1.5.1 Microfluidics general

The ability to obtain high-content, high-throughput data from single cells to better understand cell heterogeneity has often been limited by the lack of tools that provide a robust way to control handling and manipulation of individual cells in a high-throughput manner. Miniaturization allows for the fabrication of feature sizes that match cell dimensions, which facilitates the integration of cell handling and fluid manipulation. Microfluidics involves the manipulation of fluids and particles in micron-sized channels (*68-71*). At this scale, the microstructures match the size of individual cells and small organisms enabling manipulation and ease of handling of biological specimen (*70-74*). In addition, at this scale the fluid flow is laminar, thus facilitating deterministic design of robust experimental tools. Microfluidic systems offer reduced sample size, which facilitates efficient use of precious reagents. Thus microfluidic platforms have been poised to address some of the limitations in conventional, macroscale experimental approaches such as throughput, reagent consumption, and precision in environmental control. Through automation and parallelization, microfluidic systems have been demonstrated to result in orders of magnitude increase in experimental throughput, and also enabling the study of multiple experimental conditions on the same chip. The development of on-chip valves allows for the integration of multiple, individually-addressable chambers on the same chip, which facilitates experimental parallelization and

integration of different functional modules (*75-80*). Many researchers have leveraged the intricacies of microfluidics in developing tools for cell handling (*29, 81-85*) and microenvironment manipulation (*86-99*). In addition integration of multiple processes enables high-throughput analysis and ease of sample handling while performing multiple steps on the same chip (*78-80, 100-102*).

1.5.2 Microfluidic device fabrication

Microfluidic devices have been fabricated in silicon, glass, metals, ceramic, plastics and elastomers (*70, 72, 103-109*). The introduction of soft lithography has enabled rapid prototyping and batch processing (*73, 108-110*) allowing one to go from a design to testing of a device within 2 days (***Figure 1-2***). Soft lithography utilizes elastomeric polymers, such as poly (dimethylsioloxane) (PDMS) that are biocompatible, optically transparent down to 230nm, gas permeable, water impermeable, and relatively cheap (*103, 109, 111, 112*). PDMS-based devices are easier to fabricate compared to devices fabricated in glass or silicon, and allow laboratories without prior experience with microfabrication techniques to explore microfluidic technology.

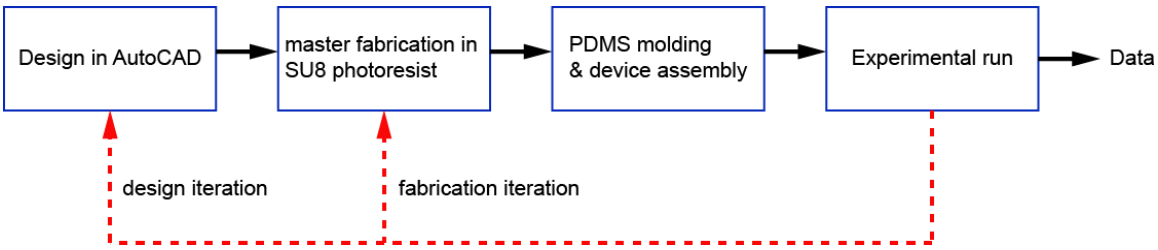

Figure 1-2 Process outline for the rapid prototype development in PDMS-based microfluidics development. The design, fabrication and testing of a PDMS-based system can take ~2 days from the 2-dimensional design created with a computer aided design software, AutoCAD, pattern transfer into a 3D SU8 master mold, PDMS molding and

device assembly, and finally testing. From this iterations can be made to the fabrication process or the design.

1.5.3 Microfluidic platforms for single-cell analysis

Performing single cell analysis of nonadherent cells would require robust cell handling to minimize cell loss and allow tracking of individual cells over periods of time. Microfluidic systems have features that match the dimensions of single cells, thus facilitating the development of tools that can handle hundreds to thousands of individual cells. Several techniques have been developed that enable trapping of particles such as beads and cells inside microfluidic channels. Particle trapping has been achieved by hydrodynamic trapping (*30, 81, 83, 113-116*), dielectrophoresis (*117, 118*), optical tweezers and magnetic force to confine particles within a particular region, using surface patterned surfaces to immobilize cells (*84, 113, 114, 116, 119-127*), microwell platforms (*84, 128*), and droplet encapsulation (*129-132*). Hydrodynamic trapping is cheaper to implement and does not require sophisticated peripheral equipment, in contrast to optical and magnetic trapping, and is simpler and cheaper than chemical trapping, and cells are less susceptible to unintended perturbations. Single-cell trapping allow for single-cell data to be obtained that can be used to analyze population heterogeneity, and has found use in microarray applications.

A number of microfluidic platforms have been developed with specific applications in immunology (*48, 133*). One of the prominent microscale tools developed is the microengraving-based platforms (*133-135*), designed to facilitate the acquisition of large data sets of individual cells secreting different cytokines in a dynamic manner, thus

allowing the polyfunctionality nature of immune cells to be elucidated. Microengraving technique relies on gravity for cells to settle in microwells in a stochastic manner, and protein secretion can be measurement at a single-cell level. On the other hand, hydrodynamic flow and restrictive microstructures have been used to confine cells in defined spatial positions, allowing time-lapse microscopy to be performed with ease (*59, 81, 136*). Confinement of individual cells is particularly important for long-term imaging of suspension cells such as T cells that will tend to float out of focus or out of the field of view during imaging if they are not anchored. Overall, the key advantage of these microfluidic tools is being able to pack a large number of cells on a very small footprint that increases the throughput of each experiment.

Previously, our lab developed a high-density cell trap array that allows for deterministic positioning of individual cells in a densely-packed array (*81*). This platform was developed to enable time-series measurements on suspension cells that tend to float out of focus or field of view during imaging if they are not anchored to the surface. In addition to the precise placement of individual cells in defined positions, the device was also used to apply soluble chemical stimulation while simultaneously observing the cellular response using fluorescence microscopy. In this thesis, I build upon this platform to demonstrate the versatility in applications to different biological systems to advance multiplexed, high-throughput analysis of single cells under diverse range of input signals. In addition, we further develop the platform to add more functionality and enable rapid fluid exchanges that create a dynamic microenvironment for the cells.

1.6 Thesis Outline

This thesis presents new and improved approaches and toolsets for analyzing individual immune cell responses to a diverse range of external stimuli including surface-anchored molecules and soluble cues. In this study, we exploit the power of microfluidics in handling small amounts of fluids, developing microstructures that match the size of a cell for robust cell handling, and the emergent physics at the micron scale to develop platforms for single-cell analysis under a diverse range of stimulations.

Chapter 2 (High-throughput, cell-trap array for calcium profiling in T cells), Presents a platform for rapid analysis of calcium measurements in T cells upon stimulation with surface-anchored molecules or soluble cues. This work builds on the cell trap array developed in our lab (*81*) to provide an easy-to-use platform for calcium assay measurements upon T cell activation on surfaces decorated with stimulating molecules. The tool provides a well-controlled system, allows hundreds of cells to be assayed simultaneously, and the cells are kept in defined positions throughout the experiment, thus enabling multiple assays to be correlated at a single-cell level. With the surface modification, surface ligands are incorporated allowing cellular response to surface-anchored molecules to be elucidated, thus providing a more physiological molecule configuration in the *in vitro* calcium assay. As a result, calcium dynamic data on a single-cell level can be captured; this would not be achievable using the gold standard assay, flow cytometry.

Chapter 3 (A generalizable, tunable microfluidic platform for delivering fast temporally varying chemical signals to probe single-cell response dynamics), presents the design and fabrication of a microfluidic-based platform for precise application of temporally-varying soluble stimulation. This work presents a new, and generalizable approach in designing stimulus generating modules, and this method can be implemented in other existing chip designs. Moreover, by incorporating the stimulus generating module with the high-density cell trap array that ensures spatial confinement of cells, dynamic stimulus can now be applied to nonadherent cells that would otherwise be washed away by chemical solutions in the current setups used in dynamic soluble stimulation setups.

Chapter 4 (**Platform for multiplexed functional assays)** demonstrates the versatile utility of the microfluidic platform developed in Chapter 3 as a tool for the analysis of important biological questions in immune cells. In this chapter, I present the analysis of the dynamic nature of T cell response by characterizing calcium response upon stimulation and then correlating the calcium response to the expression of cytokine mRNA and protein expression using single- molecule Fluorescence In Situ Hybridization (smFISH) and immunofluorescence staining, respectively. The platform enables high-density trapping of individual cells in spatially defined positions and robust fluid exchanges; thus allowing for longitudinal analysis of nonadherent cells like T cells, and incorporation of multiple image based assays at different time points to characterize mRNA and protein expression. In addition, the platform's simplicity will make it easily

transferable to other laboratories for multiplexed assays at different time points at a single-cell level.

Chapter 5 (Leukocyte separation, stimulation and immunophenotyping from whole blood), demonstrates a way to achieve separation of white blood cells from whole blood on chip. This will allow for the use of whole blood or minimally processed blood on chip and significantly reduce the volume of blood required for analysis by > 3 orders of magnitude. Ultimately, we would like to take advantage of the small scale offered by microfluidics to reduce the volume of samples required for an assay. This can be important when using patient samples such as blood, where it is necessary to reduce the burden on the patient. Previous platforms that use filtration often suffer from clogging by red blood cells, and other platforms use antibody capture, which can be costly. In this work, we explored the use of our modified cell trap for the separation of white blood cells from whole blood, thus requiring only 1-5 μL of whole blood for an assay.

Chapter 6 (Towards a high-throughput platform for measurement of receptor-ligand interaction kinetics at single-cell resolution), presents a microfluidic platform for measuring the kinetics of cell-cell interactions via receptor-ligand interactions that are fundamental in T cell immunology. Presented earlier in the thesis are assays for evaluating the intracellular signaling signatures after stimulation via receptor-ligand interactions. Here, I focus on the initial molecular engagement between receptors and ligands on cell surfaces. These juxtacrine interactions may be the first step in initiating a signaling cascade. For example, in T cell antigen activation signaling is initiated by

interaction of the T cell receptor with a peptide-MHC molecule on an antigen presenting cell surface. Current platforms such as biomembrane force probe (*58*), micropipette adhesion frequency (*62, 137, 138*) assay and atomic force microscopy developed to measure receptor/ligand interaction kinetics are laborious, and low-throughput as they only allow a single cell to be analyzed at a time. Here we combine some of the intricate features developed in microfluidic systems to design a platform that could be used to measure interaction kinetics of cell membrane bound receptors and ligands. This is a first step towards parallelization of the micropipette adhesion frequency assay to enable multiple cell pairs to be interrogated simultaneously. In the future, this assay could also be combined with fluorescence-based calcium imaging demonstrated in the previous chapters to allow for direct observation of both adhesion events and subsequent calcium signaling.

In summary, this thesis seeks to advance the field of immunology through the development of microscale tools that allow for robust cell handling, precise control of the cellular microenvironment and multiplexed measurements of different types of molecular signatures using image-based approaches.

2 HIGH-THROUGHPUT, CELL TRAP ARRAY FOR CALCIUM PROFILING IN T CELLS

Ca^{2+} is an important second messenger in a number of biological processes, and the availability of fluorescent calcium-indicator dyes makes it easier to visualize calcium dynamics in cells (*21, 22, 139*). Immune cells show variation in calcium levels when activated, and calcium is used to assess the activation state of cells. To efficiently handle immune cells *in vitro* and be able to continuously monitor calcium changes would require a reliable way to handle the suspensions cells under investigation. This work builds on the cell trap array platform developed in our lab to provide an easy-to-use platform for calcium assay measurements upon T cell activation on surfaces decorated with stimulating molecules. The tool provides a well-controlled system, and allows hundreds of cells to be assayed simultaneously; the cells are kept in defined positions throughout the experiment, thus enabling multiple assays to be correlated at a single-cell level. As a result, calcium dynamic data on a single-cell level can be captured; this would not be achievable using the gold standard assay, flow cytometry.

2.1 Introduction

Ca^{2+} is a known second messenger in T cell activation and sustained calcium signaling is essential for NFAT activation, which initiates IL-2 gene transcription. Seminal papers have demonstrated the role of Ca^{2+} oscillations in modulating gene transcription(*16, 140*). Therefore, the ability to track the calcium signaling dynamics can be insightful in predicting the immune cell functional outcome. At the resting state the calcium level in the cytosol is ~ 100nM, and the endoplasmic reticulum (ER) is 100-800 μM, while the

extracellular calcium level is 1mM once activated, the cytosolic calcium increases to 1 μM (*14*). Upon TCR engagement with a cognate pMHC, a signaling cascade ensues that includes the phosphorylation of Src family protein tyrosine kinases, Lck and Fyn (**Figure *2-1***). These kinases phosphorylate ITAMs bound to the TCR subunits, followed by the recruitment and subsequent phosphorylation of ZAP70 at the ITAMS. The phosphorylated ZAP70, Lck and Fyn then facilitate the phosphorylation of other protein kinases including the adaptor protein LAT, which in turn activates PCLγ via phosphorylation. PLCγ modulates the PIP2 hydrolysis to IP3 which then binds to the IP3 receptor on the ER membrane thus activating calcium release from the intracellular stores into the cytosol. The calcium depletion in the intracellular stores is sensed by STIM1 proteins that translocates to the plasma membrane to activate the CRAC channels through the interaction with the ORA1 proteins. The opening of the CRAC channels then allows calcium influx from the extracellular space, thus enabling a sustained calcium inside the cell necessary for signal propagation involving translocation of transcription factors into the nucleus. These transcription factors drive gene transcription for cytokine production, differentiation and proliferation. Therefore, Ca^{2+} can be used as an indicator for T cell activation.

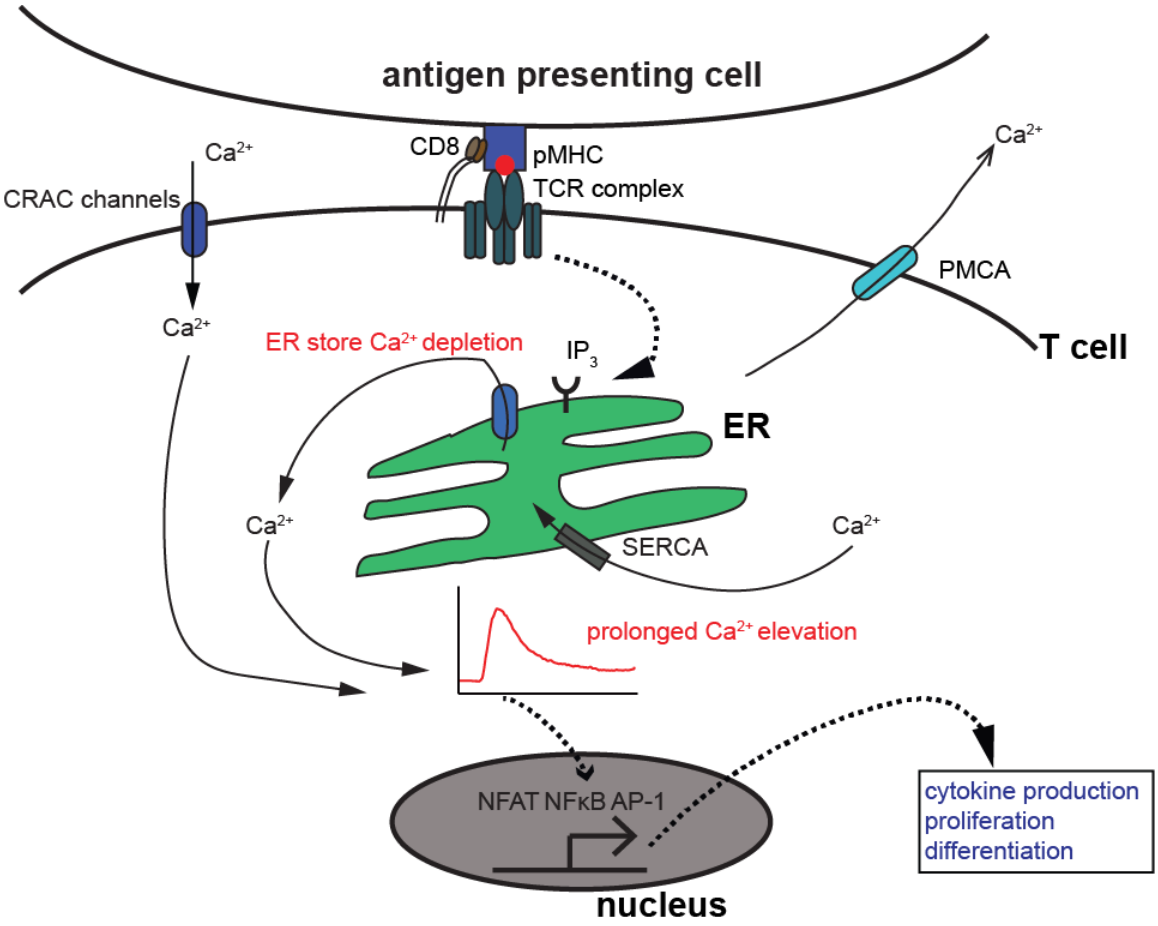

Figure 2-1 Simplified calcium signaling pathway in T cells. The TCR/pMHC interaction initiates the signaling cascade leading calcium release from the intracellular stores in the endoplasmic reticulum (ER). The depletion of the intracellular stores leads to the activation of the calcium release-activated channels (CRAC) that allow calcium influx from the extracellular space. The calcium influx through the CRAC channels allow prolonged calcium elevation that drives the nuclear translocation of a number of transcription factors including NFAT that drives IL-2 gene transcription.

The development of calcium-sensitive dyes and intravital microscopy has enabled the direct visualization of calcium dynamics exhibited by T cells while interaction with APCs *in vivo* (*23, 61, 139, 141*). However, *in vitro* models are useful in enabling individual effects and pathways to be teased out, and also in performing rapid screening of T cell responsiveness that can be useful in determining an individual's immune status. Conventional assays for visualizing calcium dynamics *in vitro* include flow cytometry

where the cells are briefly exposed to the antigen then run through the flow cytometer or an antigen in solution in a tetramer form. The dynamic data is then captured at a population level, but only a snapshot of the calcium level of each individual cell is obtained. Other assays include stimulating ligands anchored on supported lipid bilayers or solid surfaces (*20*), and monolayer of APCs pulsed with the antigen.

While these provides a more physiological condition, it is challenging to determine when the cells are in contact with the surface, and the T cells being suspension cells can easily float out of focus or move out of the field of view, making it challenging to keep track of the individual cells. In addition, it is challenging to control the distribution of the cells on the surface and often only a few cells can be analyzed. In addition, analysis on functionalized lipid bilayers or solid surfaces or APC monolayers does not offer control of the microenvironment to enable soluble stimulation or further downstream analysis. On the other hand, the advent of microfluidic platforms for biological studies has seen the development of platforms that enable precise cell handling (*81, 136*), and better control of the cell microenvironment that could facilitate the direct measurement of calcium signaling in immune cells. Recently, Dura *et al* developed a microfluidic platform to enable a deterministic and timed pairing of T cells and APCs coupled with live imaging to enabling real-time analysis of calcium flux in T cells upon engagement with an antigen presenting cell(*59*). With this platform the authors were able to demonstrate how microfluidics can bridge the technical challenges in cell handling faced with suspension cells, and capture the dynamics of calcium response that occurs within seconds of activation. However, there is still room for improvement in increasing the number of cells

assayed in the field of view and simplicity in the device operation to allow for use by non-experts.

Inspired by the high-density cell trap array developed in our lab (*81*), I developed a simple calcium assay that incorporates the ability to stimulate immune cells with surface anchored molecules in addition to the soluble stimulation previously demonstrated. This platform offers a higher throughput, and fast assay that enables the immune response of different immune cells to be elucidated. The high-density trap array enables a large number of cells to be assayed in the same experiment, thus eliminating the need to pool data from different experiments.

2.2 Materials and methods

2.2.1 Cell culture

OT-1 CD8+ T cells were harvested from the spleen of an OT-1 transgenic mouse on the same day of the calcium experiment. Briefly, the mouse spleen was grinded in HBSS buffer with calcium and magnesium in a cell strainer, followed by lysis of erythrocytes using a mouse erythrocyte lysis kit (R&D Systems, Cat: WL2000), and CD8+ T cells were by negative selection using Mouse CD8+ T cell Enrichment kit (StemCell Technologies, Cat:19853). Cells were suspended in R10 medium (RPMI 1640 with 2 mM L-glutamine, 10% fetal bovine serum, 0.01M HEPES buffer, 100ug/ml gentamicin, and 0.2mM 2-beta mercaptoethanol).

For Jurkat E6-1 human acute T lymphoma cells (ATCC), the cells were cultured in RPMI 1640 medium with 2 mM L-Glutamine and HEPES (ATCC) supplemented with 10 % fetal bovine serum (Sigma-Aldrich) and 100 units mL^{-1} penicillin-streptomycin (Life Technologies), in a 37 °C, 5 % CO_2 humidified incubator.

2.2.2 Device fabrication

Devices were fabricated using standard soft lithography techniques (*109, 110*), and the fabrication protocol is shown in Appendix A.1 and Figure 8.1. For the master mold fabrication, a 15 μm adhesion layer using SU 2015 (Microchem) was spun on a silicon wafer and fully cross-linked under UV. Then 2-3 μm layer was spun and cross-linked with the photomask to pattern the features of the restriction channels using a mix of SU8 2002 and SU8 2005 at a ratio of 3:2 (SU8 2002:SU8 2005) to address the challenges faced in the weak adhesion of SU8 2002. Finally, the microstructures for the main serpentine channel and the cell traps was fabricated using SU8 2015. After the master fabrication, the master molds were treated with trodecafluoro-1,1,2,2-tetrahydrooctyl-1-trichlorosilane (United Chemicals Technology) vaporized in a desiccator under vacuum to allow ease of release of PDMS from the mold. PDMS mixture of prepolymer:curing agent (10:1) was degassed to remove bubbles and poured over the master mold in a petri dish. The PDMS was cured in an oven at 70 degrees for 2 hours. The PDMS was peeled off the mold, the individual devices were cut out, and access holes were punched at the inlet and outlet of the device using a 19-gauge blunt needle (Figure 8.2). Tygon tubing with internal diameter 1/32” (McMasterr Carr # 5155T11), and 19-gauge stainless steel

tubing (McMasterr Carr # 8987K51) to make pins were used as connections at the outlet of the device.

2.2.3 Device functionalization with stimulating proteins

Devices were primed with PBS 1X to remove bubbles by pressurizing the device using a PBS-filled syringe through the device outlet. After priming, 10 μL of biotin-BSA (0.5 mg/ml) was perfused through the device at ~ 10 μ h^{-1} for 1 hour, then PBS was perfused through the device to remove excess biotin-BSA. Streptavidin (10 μL, 0.2 mg ml^{-1}) was then coupled to the biotin molecules, and finally a mixture of the biotinylated stimulating ligands (5 μL); pMHC (10 μg ml^{-1}), anti-CD28 (2 μg ml^{-1}), and anti-LFA1 (2 μg ml^{-1}), was perfused at ~ 10 μ h^{-1}.

2.2.4 Calcium imaging

A protocol for the assay is included in Appendix A.2. Cells were loaded with Fluo3-AM dye (Life Technologies # F14242) in R10 medium at a final dye concentration of 5μg/ml for 45 minutes in the cell incubator. Cells were then washed twice in PBS, and then resuspended in the calcium imaging buffer (phenol red-free RPMI 1640 with 10% FBS). Surface modified device was mounted on the microscope with the outlet tubing attached. The device was primed with the imaging buffer using a syringe filled with the imaging buffer and pushing the fluid through the outlet until there was a puddle of buffer at the inlet. 5μL of cell suspension at 5 x 10^6 cells/ml was aspirated into a pipette tip, and the pipette tip placed in the device inlet. Imaging in the fluorescent mode was initiated once cells started loading. Images were acquired every 3-5 s for 20-30 minutes at 37 degrees.

2.3 Microfluidic device design

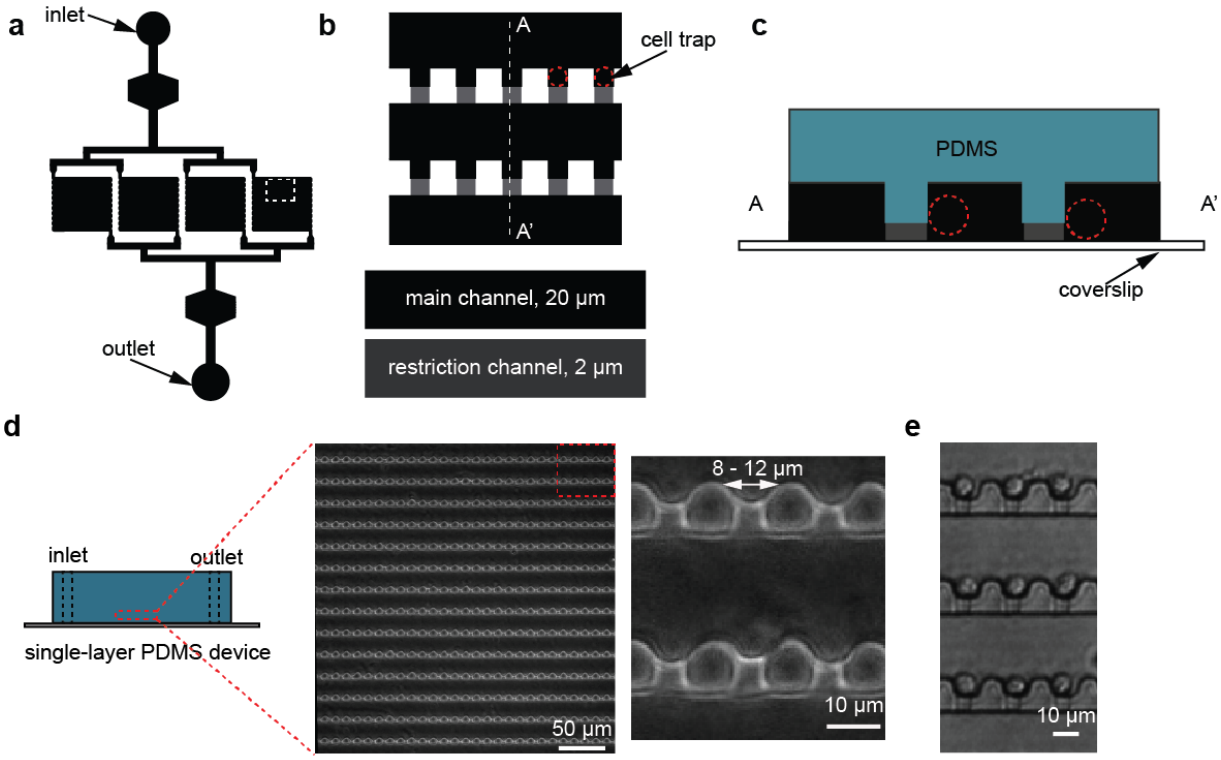

Figure 2-2 Device design overview. The device is a simple, single inlet, single outlet platform with microstructures for confining cells in defined positions. (a) device overview with 4 chambers, the device has a serpentine channel along which the cell traps are arrayed as shown in (b), (c) shows a cross-sectional view indicated in (b), (d) shows a top view micrograph of the device made in PDMS, showing the cell traps, and (e) is a micrograph showing the cells trapped in the device.

The device is a single-layer PDMS device fabricated using standard lithography techniques as detailed in Appendix A. The devices were designed with 1-8 chambers (Figure 2-2), and each chamber has 1,000 cell traps on a 1 mm^2 footprint. The device has a serpentine main channel (30 µm width and 20 µm height), single inlet and a single outlet. Along the serpentine channel are cell trap microstructures that have dimensions of 8 – 12 µm depending on the size of the cells to be used in the experiments. The devices with 8 µm traps are for primary murine cells that have sizes ranging 6 -8 µm in diameter,

and the 10 μm traps for the larger human cells. Each cell trap has a shallow restriction channel (10 μm wide and 2 μm height) that allows the cell to sit inside the cell trap but not go through the trap. The cell trapping mechanism is passive hydrodynamics. In the device, there is flow through the main serpentine channel, and cross-flow through each trap. This cross-flow directs the cells towards the trap, and once a trap is occupied by a cell, the cell block flow through the trap allowing cells to pass through and achieve single cell loading. The device represents a high-density cell trap that enables hundreds of cells to be analyzed simultaneously, and with a motorized stage, all the chambers can be assayed increasing the throughput per experiment to ~ 10, 000 cells. In the previous studies in our lab, the cell trap array for deterministic cell trapping and subsequent soluble stimulation with live imaging was developed enabling the cell response to a range of concentrations could be assayed on a single chip (*81*). We sought to expand this line of work, by exploring other modalities of cell stimulation, and incorporating surface-anchored molecules to immune cells. Surface-anchored molecules are a critical component T cell signaling, and the interaction between the TCR and pMHC initiate signaling events including calcium. To develop an assay for Ca^{2+} measurements upon stimulation through the TCR, we optimized an approach to functionalize the device with stimulating ligands for T cells (pMHCs), and costimulatory ligands such as anti-CD28 using biotin/avidin coupling (***Figure 2-3).***

2.3.1 Device surface functionalization

Surface protein modification in microfluidic channels has been done using covalent modification, bioaffinity interactions and protein physisorption (*142, 143*). Protein

physisorption involves the adsorption of a protein from solution onto the surface of glass and/or PDMS via van der Waals, hydrogen bonds interactions, hydrophobic interactions or electrostatic interactions. The process is relatively fast, does not have complex protocols, and free of toxic chemicals. However, protein adsorption will depend on the specific protein, the protein configuration on the surface will be random thus not all the molecules on the surface will be functional, the interaction is generally weak, and the protein adsorption may alter protein properties or function. On the other hand, covalent modification may be more reliable and enables a better control of the protein orientation through site-specific reactions. However, the processes can be very long, involve toxic reagents, and solvents that are not compatible with PDMS used in microfluidic platforms for biological applications. Finally, bioaffinity interactions between naturally occurring molecules such as biotin/streptavidin and antibody/ligand interactions can also be used to in surface modification. These are noncovelent, but stronger interactions compared to those in protein physisorption.

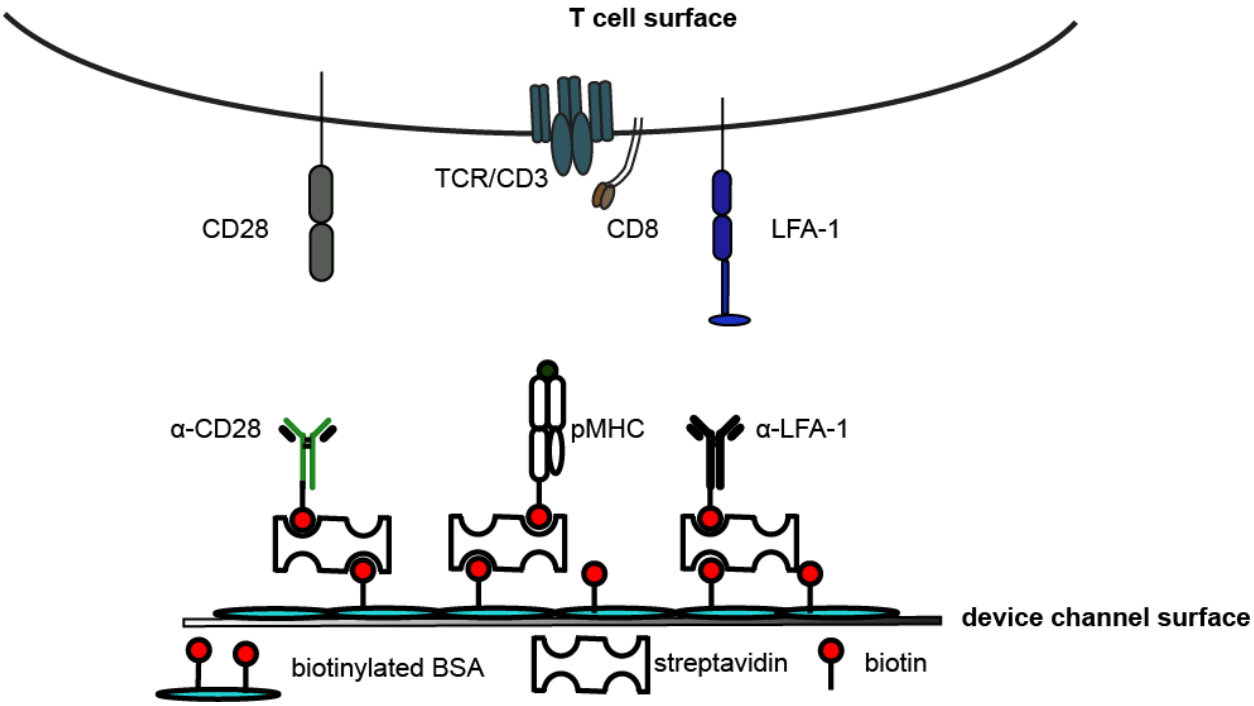

Figure 2-3 Interacting molecules in the experimental setup. The device channels is coated with the stimulating ligands using biotin-streptavidin coupling. The device is first coated with biotin-tagged BSA, followed by the streptavidin and finally biotin-tagged ligands; pMHC that interacts with the TCR and coreceptor CD8, anti-CD28 and anti-LFA1 that interact with costimulatory molecules CD28 and LFA-1 on the T cell surface.

In our case, we employed protein physisorption and biotin-streptavidin coupling to decorate the device surfaces with the stimulating ligands. The approach allows for biotinylated ligands to be decorated on the device surface. In our case, we focused on the molecules involved in the initial interaction TCR/pMHC and coreceptor CD8, and costimulatory molecules LFA-1 and CD28 (Figure 2-3). However, the approach is broadly applicable to biotinylateds ligands. This approach relies on prior biotinylation of the stimulatory ligands, and usually the ligands have a single biotin tag. Site-specific biotin tag on the ligand ensures that all the ligands on the surface assume the same desired configuration. Biotin and avidin form a high affinity (10^{-15}M), noncovalent link

(*144*) ideal for incorporating other interacting molecules as it is unlikely to rupture. Avidin is a 66-69 kDa tetrameric glycoprotein, and biotin (Vitamin H) is a small molecule that can be conjugated to proteins using amine modification, thus allowing ligand proteins to be coupled to avidin. Protein biotin modification is readily employed using well-established N-Hydroxysuccinimide (NHS ester) chemistry, and there are available biotinylation kits that makes it convenient to biotin tag proteins in the laboratory. The approach starts with the physisorption of biotin-tagged BSA. BSA readily adsorbs to glass and PDMS, and therefore guarantees full coverage on the surface. Once the BSA is physisorbed, streptavidin is introduced to couple to the biotin, and finally biotin ligands can be introduced to link to the streptavidin (Figure 2-3). To ensure that there was full coverage on the surface and that the amount of protein was not limiting in the process, the protein solutions were perfused in the device at a flowrate of ~ $10\mu Lhr^{-1}$ using gravity driven flow (Appendix B).

Fluorescently labeled proteins were used to verify protein coating on the device surface. We first optimized the adsorption of the BSA to the device surface. In this case, we aimed to ensure uniformity in the device coating. After coating with a FITC-labeled BSA, fluorescent images were acquired at 20x magnification, and by measuring the average intensity at different positions on the device micrograph, the uniformity of the protein loading was confirmed.

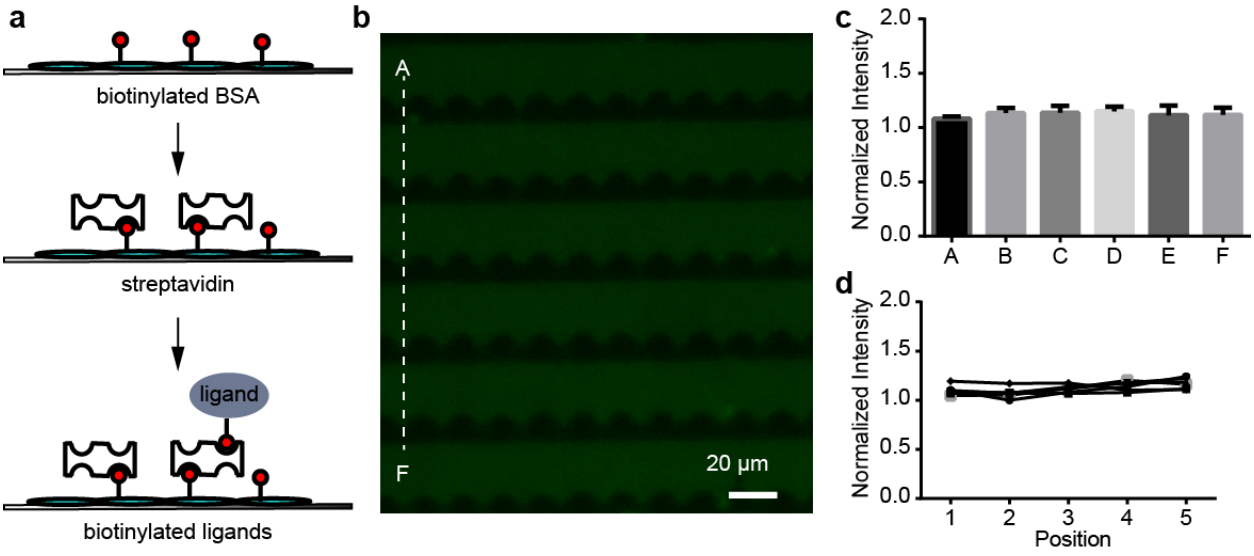

Figure 2-4 Uniform coating of stimulating ligands on the device surface. The device was decorated with the stimulating and costimulatory ligands using protein physisorption and biotin/streptavidin interaction. (a) Overview of the device coating sequence, (b) device setup and fluorescent micrograph after coating of FITC-labeled BSA, and (c) average intensity measurements of the different rows on the device, show a uniform intensity indicating uniform distribution of the protein on the device surface. For each row, intensity is measured at 10 different positions, and the average and standard deviation are plotted, (d) along each row shown in b, the fluorescence intensity is uniform.

2.4 Cell loading and fluorescent-based calcium imaging

Once the devices are decorated with the stimulating ligands, cell loaded with a calcium indicator dye, Fluo3-AM are introduced in the device using gravity-driven flow. The device is mounted on a microscope stage during the loading, and imaging starts when the cells start loading in the device. At 10x magnification, there are about 300 cells in the field of view (Figure 2-5a), and the throughput can be further increase with an automated XY stage to image at different positions on the device. The cells are docked in spatially-defined positions and time-lapse fluorescence imaging is performed to track the calcium dynamics over a defined time (Figure *2-5*b). Figure *2-5*c shows a calcium trace for an individual cell demonstrating the power of this platform to provide single-cell data and

capture the dynamics of each cell while also analyzing a large number of cells to allow population statistics to be deduced. Importantly, the setup is relatively simple, with no need for any specialized equipment required to run the device.

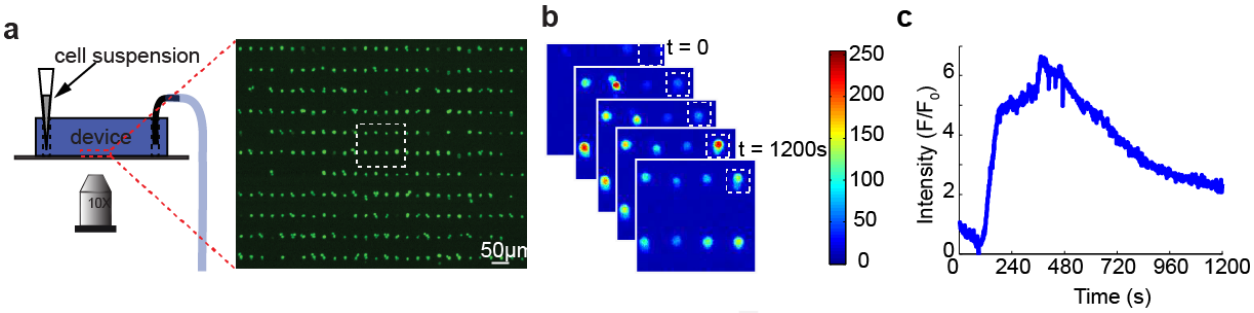

Figure 2-5 Imaging setup. (a) depiction of the device setting, the cell loading is achieved by placing a pipette tip containing the cell suspension at the inlet, and a tubing at the outlet that drives the flow in the device using gravity, and a representative micrograph of the fluorescence image obtained during the time-lapse image in monitoring calcium dynamics using a fluorescent, calcium indicator dye, (b) some time lapse images showing changes in cell intensity over time upon stimulation, and (c) individual cell trace for the calcium measurements over a span of 20 minutes of the cell marked with a dotted box in (b).

2.4.1 Calcium data analysis

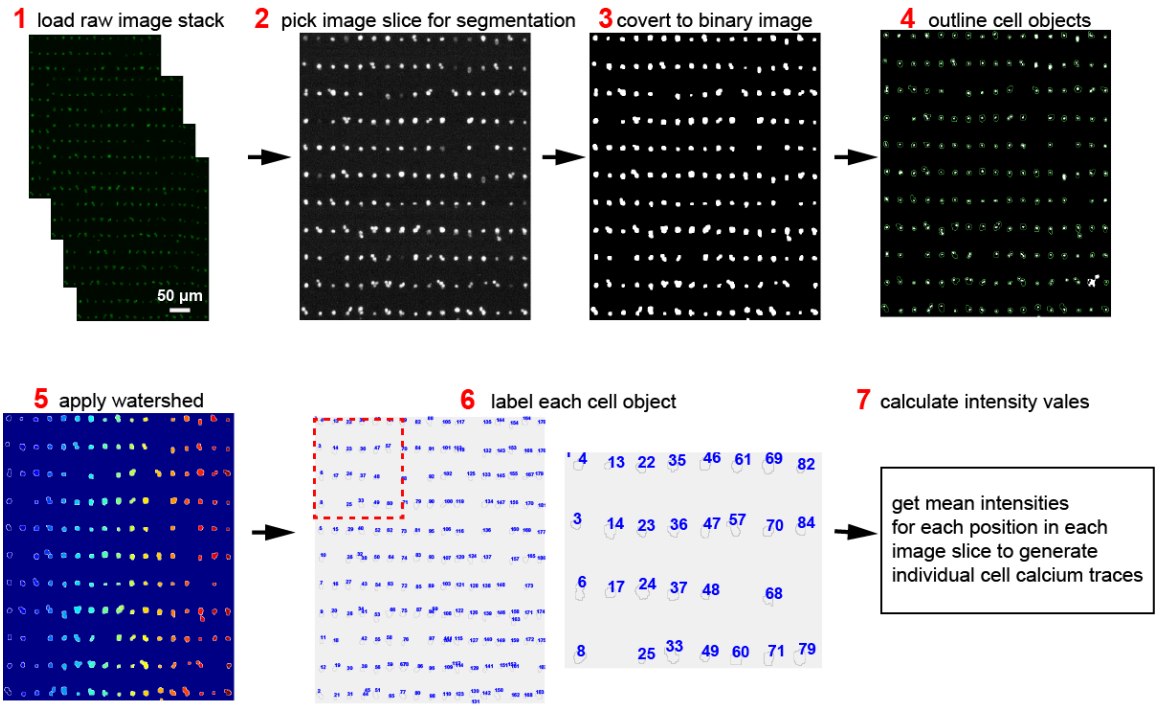

Figure 2-6 Automated image processing outline. To facilitate the analysis of the fluorescence changes in the individual cell, a custom-made automated image processing and analysis software was written in MATLAB. The software allows the identification of individual cell positions on the images and mean intensities of each cells is measured on each image slice of the image stack. This would allow the time series intensity changes for each cell to be determined.

The intensity of each cells was determined throughout the time series stack using a custom-made MATLAB-based software (Appendix A.2.1.5), and the main steps in the analysis are show in Figure 2-6**.** Background intensities were subtracted from all the intensity values. Because the cells do not load at the same time, the time zero for each individual cell was determined by setting a threshold intensity below which the position will be considered unoccupied. A jump in intensity above the set threshold would indicated that a cell was now occupying the region and that point would be considered the time zero for that specific cell (Figure 2-7 a, b). The intensity is then normalized to

the initial cell intensity for each cell to account for the unequal dye loading within the cell population (Figure 2-7c). This analysis is applied to all the cells to generate individual cell traces (Figure 2-7d & e).

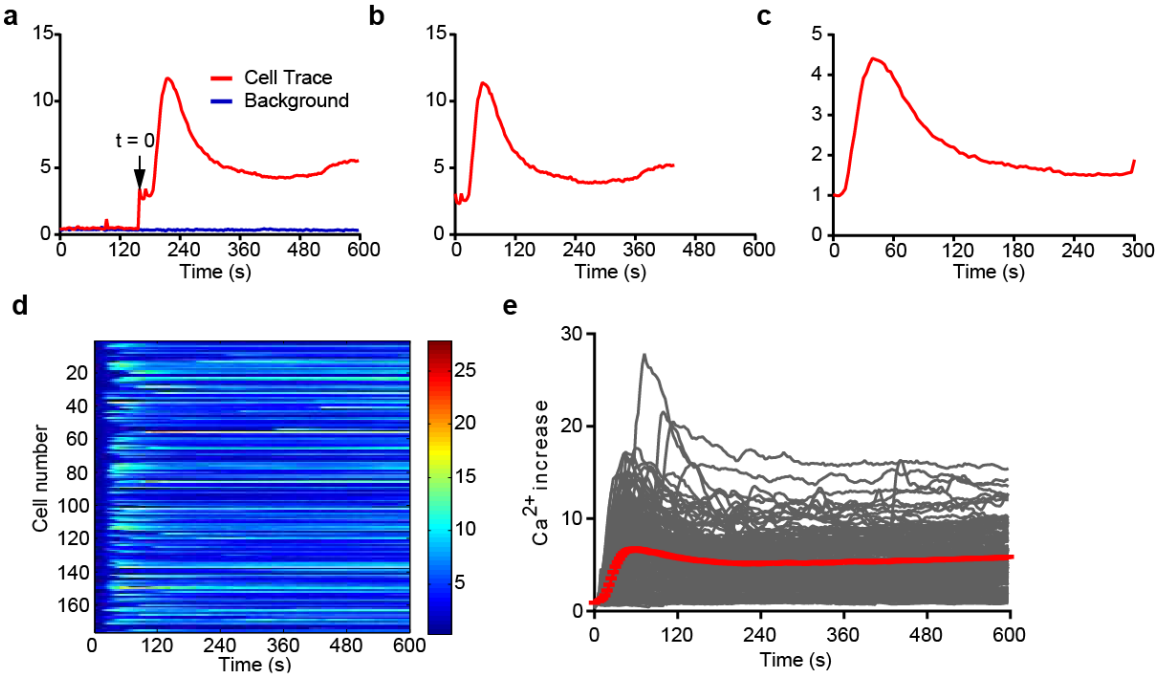

Figure 2-7 Calcium intensity analysis. (a) Intensity trace for an individual cell (red), and background. For the cell trace, a jump in intensity from the background intensity indicates the time at which the cell was trapped in the device and therefore represents time zero for the individual cell, (b) cell trace shifted to the true time zero, (c) cell's intensity normalized with the initial intensity to account for differences in dye loading among cells, and representative (d) heatmap and (e) individual calcium curves (grey) and the population mean with SEM for calcium analysis in a single device, in a single field of view.

2.5 Dynamic Ca^{2+} flux in Jurkat hybridoma cell line

As a proof of concept, we measured the Ca^{2+} response of Jurkat T cell line under stimulation with anti-CD3/anti-CD28 that elicits a strong stimulation, and also with a nonspecific soluble stimulation, ionomycin/PMA (Figure 2-9). Here we sought to

demonstrate the multifaceted application of our platform to perform both soluble stimulation, and stimulation with surface-anchored molecules. Calcium dynamics were captured in each individual cell, while analyzing hundreds of cells to ensure population statistics can also be obtained from the data.

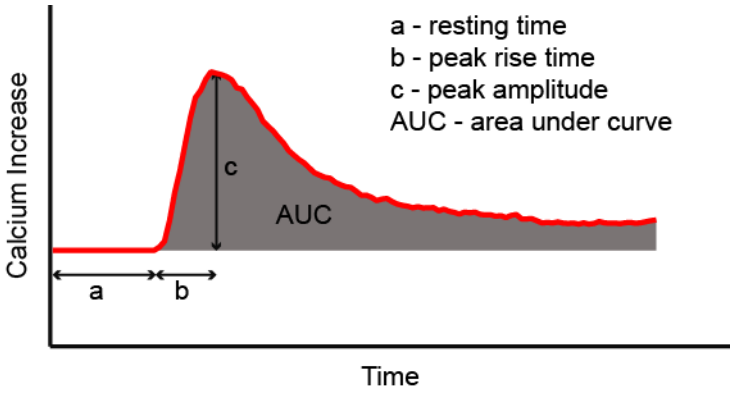

Figure 2-8 Calcium parameters derived from the calcium curve. From the Ca^{2+} time series data, multiple descriptive parameters can be derived to describe the extent of Ca^{2+} activation including, the time is takes for the cell to respond (resting time), the maximum Ca^{2+} peak, the peak rise time and area under the curve.

From this dynamic data, we can obtain population statistics such as the average response. In addition, from the individual Ca^{2+} traces, useful parameters such as maximum peak, area under the Ca^{2+} curve, time the cell takes to respond, and the decay rate constant as illustrated in Figure 2-8. These parameters help us to understand the different behaviors that the cell exhibit that may be informative on the functional potential of the cell.

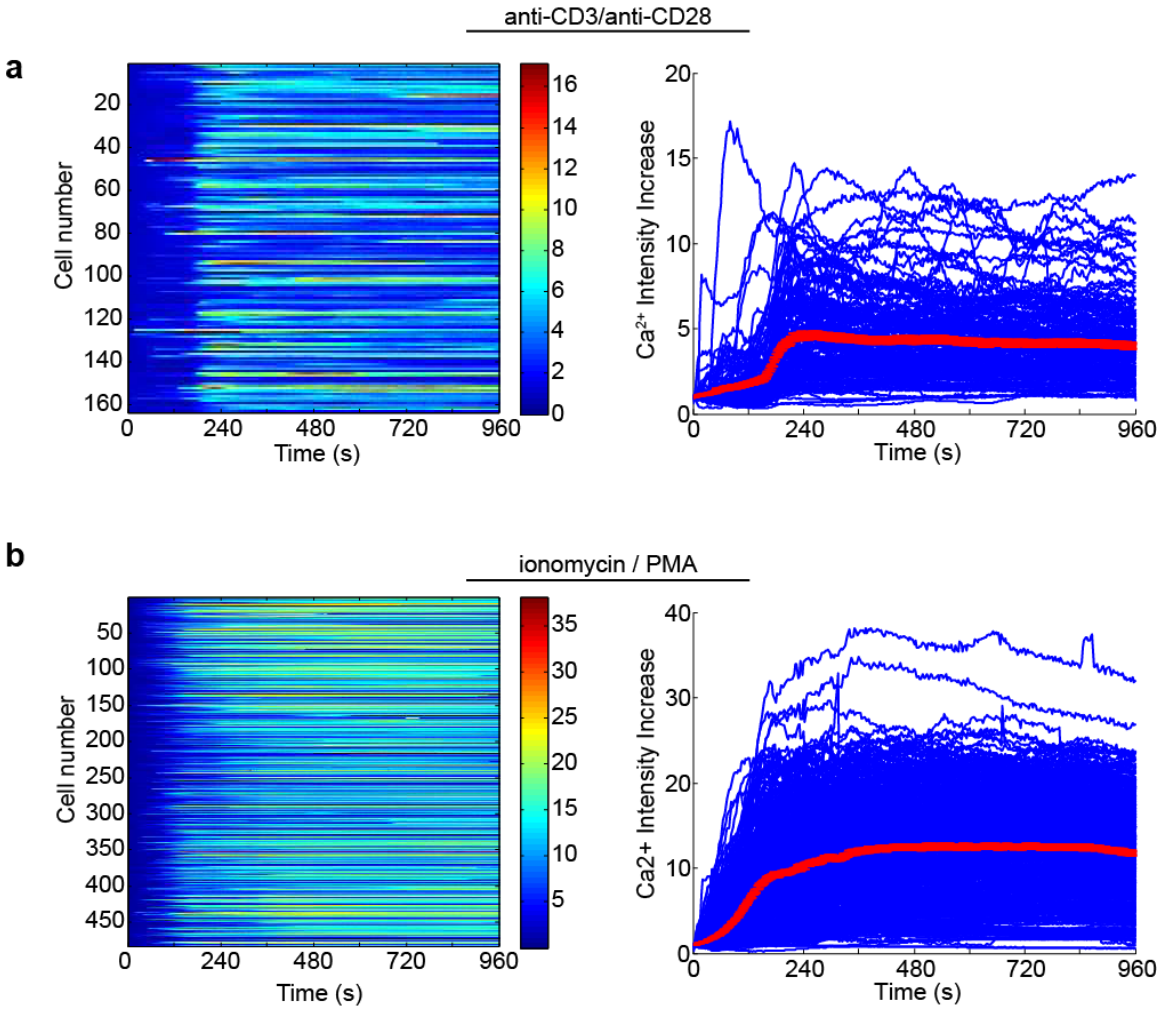

Figure 2-9 Jurkat T cell rapid Ca^{2+} flux upon stimulation. (a) cross-linking of the TCR with anti-CD3 and costimulatory molecule with anti-CD28 elicits Ca^{2+} signaling, (b) stimulation of Jurkat T cells with calcium ionophore, ionomycin and PMA. The results show that both surface-anchored molecules and soluble chemicals can be used on the platform for cell perturbation.

2.6 Calcium signaling dynamics in primary OT-1 T cells

To demonstrate the utility of our platform, we analyzed the calcium dynamics in naïve OT-1 T cells obtained from a transgenic mouse whose T cells are reactive to ovalbumin peptide (SIINFEKL), commonly referred to as OVA. We show in Figure 2-10a the cells exhibit an increase in cytosolic Ca^{2+} upon encounter with the antigen-coated surface.

Cells loaded in a device coated with a nonstimulatory peptide, VSV show no appreciable increase in Ca^{2+} (***Figure 2-10*** **b**), and thus the response to OVA-coated surface is specific.

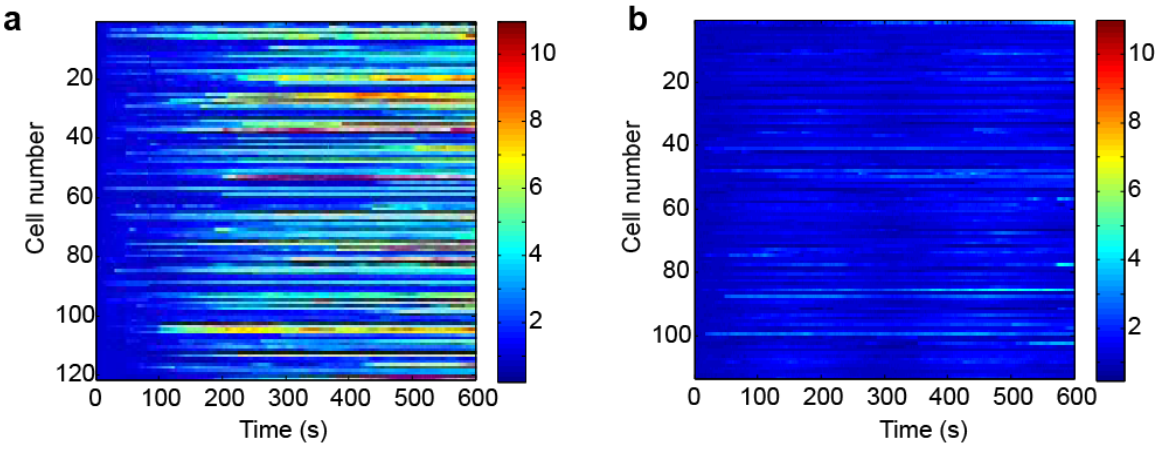

Figure 2-10 OT-1 T cells show a specific, rapid calcium increase upon interaction with antigenic OVA peptide. Fluo3-loaded OT-1 T cells were stimulated with OVA peptide and costimulatory molecules anti-CD28 and anti-LFA1. The heatmaps show the individual ca^{2+} responses to stimulation with (a) OVA, and (b) VSV

2.7 Evaluating Calcium signaling alterations in a tumor microenvironment

Cancer immunotherapy is of great interest, and it has been demonstrated that CD8+ T cells against tumor antigens have been found in cancer patients. As a result, immunotherapy has been seen as a promising therapeutic intervention in cancer patients. However, the presence of the T cells against tumor antigens have yielded poor results in getting rid of tumors. The tumor microenvironment is unique, and has been shown to have an impact on T cell activity. T cells residing in the tumor draining lymph nodes have been shown to exhibit attenuated functional activity compared to T cells in peripheral blood and residing in non-tumor tissues, and non-tumor draining lymph nodes (*145-147*).

Using a tumor mouse model B16, we tested Ca^{2+} activation of the T cells harvested from different compartments to elucidate the impact of the tumor microenvironment on T cell Ca^{2+} signaling. The T cells were harvested from the lymph nodes and spleen of a healthy mouse for the control and from the tumor draining lymph node (TDLN) and spleen of a tumor-bearing mouse 7 days after tumor implantation. T cells harvested from the TDLN exhibited lower Ca^{2+} response to antigenic stimulation compared to splenic T cells in a mouse 7 days after tumor implantation. Interestingly, the splenic T cells from the tumor mouse showed comparable Ca^{2+} behavior to splenic T cells from a healthy mouse (Figure 2-11). These results demonstrate that the tumor microenvironment may have an impact on T cell signaling. This behavior was also prominent at a population level; the average response, maximum Ca^{2+} amplitude, and total Ca^{2+} response of TDLN T cells was lower compared to the splenic T cells and T cells from a healthy mouse (Figure 2-12). This preliminary finding is in agreement with observations that have been made on the lack of functional responsiveness in tumor-antigen specific T cells in cancer patients (*145*). Therefore, our platform can be used to screen T cells from individual on their capacity to mount an immune response if the tumor antigens are known.

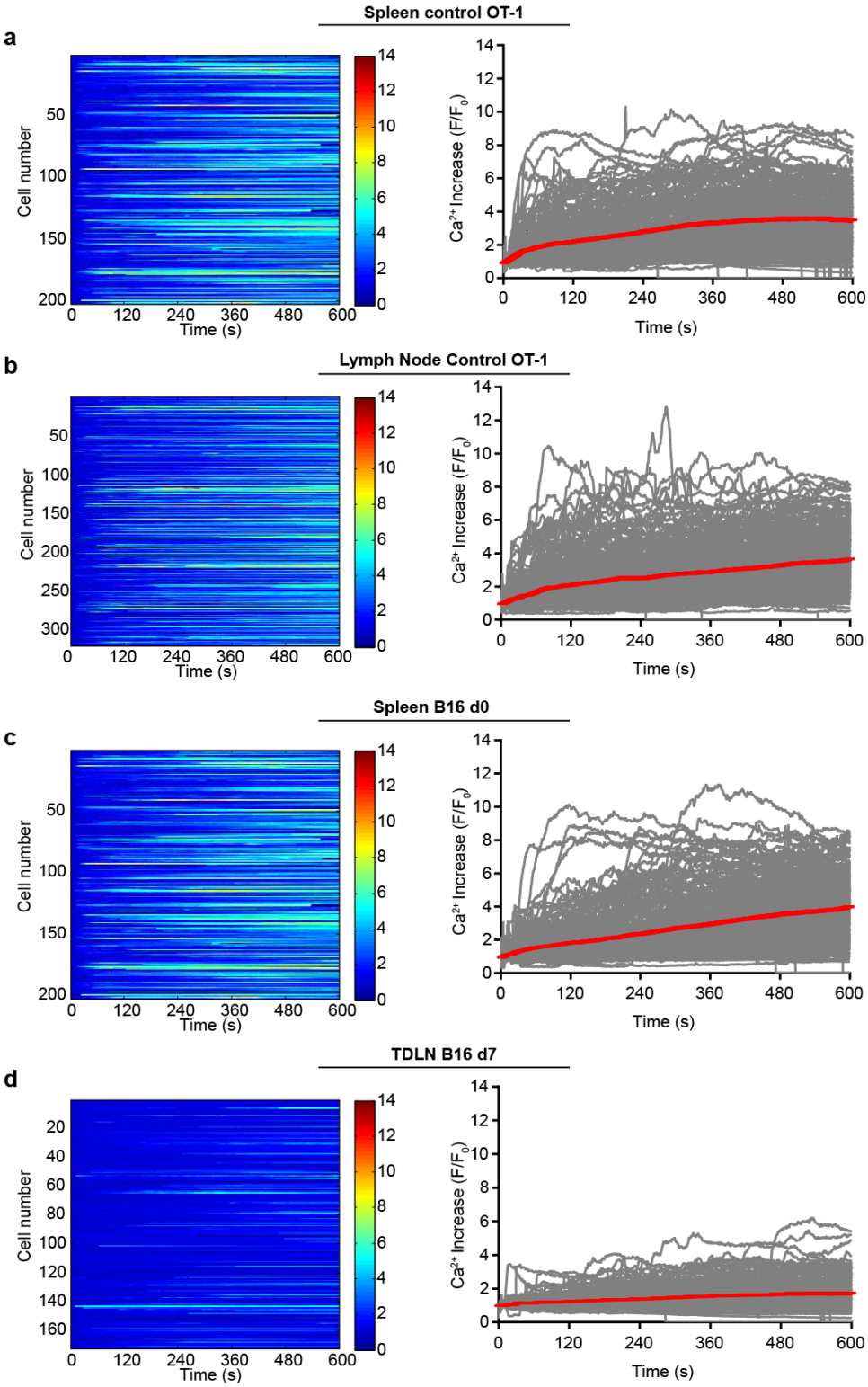

Figure 2-11. The tumor microenvironment has a negative impact on calcium signaling in T cells. Fluo3-loaded T cells were stimulated with OVA:H2-K^{b} and anti-CD28 and anti-LFA1 costimulatory molecules. The T cells were harvested from either a healthy mouse or mouse implanted with a tumor. Calcium traces for T cells from (a) a healthy mouse

spleen, (b) a healthy mouse lymph node, (c) spleen of a B16 mouse on day 7, and (d) cells from the tumor draining lymph nodes (TDLN) on day 7 post tumor implantation. Overall, T cells in the tumor draining lymph nodes show an attenuated Ca^{2+} response compared to the cells from the spleen of the tumor-implanted mouse. In addition, T cells from the spleen of the tumor model animal show comparable response to the cells from a healthy mouse.

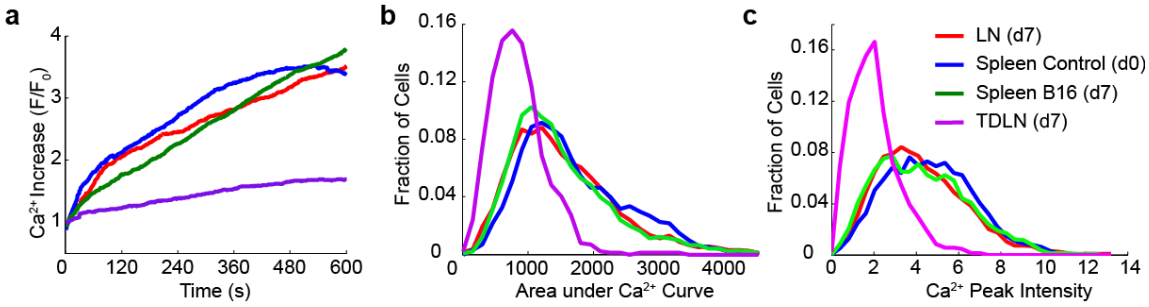

Figure 2-12. Population and single-cell analysis show distinct attenuation of calcium signal in T cells from TDLN. (a) Population average calcium show an overall lower calcium level in the T cells from the TDLN, (b) area under the Ca^{2+} curve distribution, and (c) maximum Ca^{2+} level. For both the area under the curve and calcium peak intensity distributions, the cells from TDLN were significantly different ($p < 0.0001$) from the other three conditions shown. On the other hand, there was no statistical significance among T cells from LN, spleen control and spleen B16.

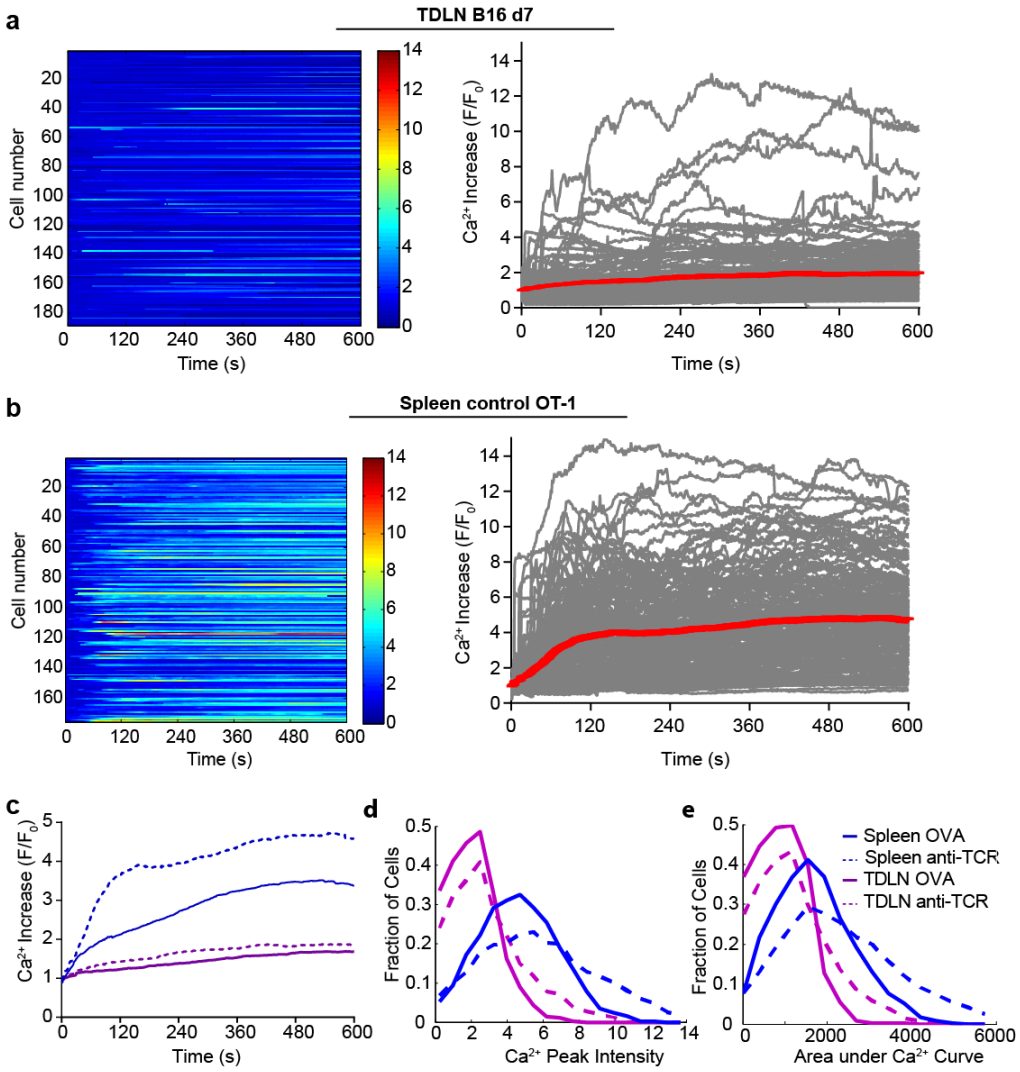

Figure 2-13 Stimulation with TCR antibody did not elicit a large Ca^{2+} flux in T cells from the TDLN. An antibody against TCR was used to provide a strong stimulation to thes T cells. (a) Calcium response traces for the TDLN T cells showing that the majority of the cells did not show an appreciable increase in Ca^{2+}, (b) Calcium response traces for splenic T cells, the cells showed a rapid increase and sustained Ca^{2+} level, (c) population average response, (c) distribution of the area under the curve, and (c) maximum Ca^{2+} level. Overall, the T cells for the TDLN show disrupted Ca^{2+} signaling even when stimulated with an antibody against the TCR.

2.7.1 Simultaneous Ca^{2+} imaging and force mapping

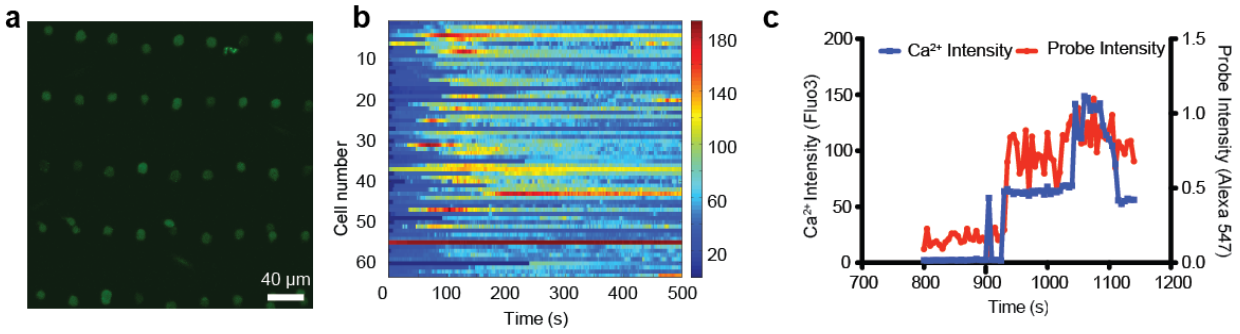

Figure 2-14 Combined Ca^{2+} and force measurements using a DNA-based tension force probe. Using covalent modification a DNA-force probe is anchored to the surface, and pMHC is coupled to the DNA force probe using biotin-streptavidin coupling. When the cells are loaded in the device interact with the pMHC anchored on the DNA-force probe. (a) Fluo3-loaded cells in the device for Ca^{2+} changes visualization, (b) Fluo3-intensity changes, and (c) combined Ca^{2+} changes and probe fluorophore intensity changes of an individual cell.

With the adaptation of covalent modification using silane chemistry, other molecules such as a DNA-based tension force probe can be coated on the device, enabling the threshold force exerted by the cells to be directly measured (*148*). Force has been shown to be important in T cell activation, and recent studies have demonstrated the importance of force through the TCR-pMHC bond in T cell Ca^{2+} signaling (*58*). In this study, external force was applied to TCR-pMHC bond to elucidate the impact of force on the bond and T cell activation. However, under physiological conditions the force is likely generated by the cell, and the development of DNA-based tension probes has enabled the visualization of force exerted by cells through receptor-ligand bonds (*148*). The pMHC is attached to a tension force probe, and when the T cell exerted a force on the TCR-pMHC bond, the DNA opens up resulting in the increase in fluorescence intensity of the probe as the fluorophore moves away from the fluorescence quencher. In Figure 2-14 we show that combining this force measurement with our calcium assay, we can visualize both the Ca^{2+} and force dynamics at a single cell resolution. In addition, the utility of the platform can be expanded to include capture antibodies on the device surface that capture secreted

proteins. This approach would then allow both Ca^{2+} and force measurements, and downstream signaling such as cytokine secretion to be measured in the same sample, and thus direct correlations can be drawn. However, it is noteworthy to mention that because the measurements described above are fluorescence based, the number of different measurements that can be obtained is ultimately limited by the spectral resolution. Therefore, on most microscopy setups up to 4 different measurements can be done while keeping the identity of each cell.

2.8 Conclusions and Future directions

Ca^{2+} is a critical component in the signaling transduction pathways in T cells. The Ca^{2+} behavior is rapid and show interesting dynamics that can have functional implications. We developed a simple platform for measuring Ca^{2+} levels of hundreds of T cells upon stimulation with surface ligands or soluble cues at a single-cell resolution. The platform enables dynamic data for each individual cell to be captured, and enough cells to be analyzed is a single experiment to derive relevant population statistics. Often flow cytometry is used to evaluate calcium changes in stimulated cells, however only a snapshot of each cell can be obtained and the calcium dynamics are determined on a population level. Ligand-coated surfaces have been utilized for monitoring dynamics. However, the number of cells analyzed is low primarily due to the high mobility of activated T cells that makes it difficult to track the cells over time.

Therefore, the key challenges with existing techniques are ability to handle and spatially confine nonadherent T cells to enable time-lapse imaging, the ability to incorporate different stimulating ligands on the surface, and being able to analyze hundreds to

thousands of cells in a single experiment. The high-density trap array allows deterministic, spatial position of hundreds of cells that allows ~ 300 cells to be viewed in a field of view at 10x magnification. Coupled with surface modification, this platform offers a rapid assay for evaluating immune cell functional response. With this platform we demonstrated the attenuated Ca^{2+} response to OVA antigen stimulation of OT-1 T cells residing in the tumor microenvironment. Such a measurement can be informative in evaluating cancer patient's ability to mount an immune response against tumors, and also monitor the immune system competency against infections.

Furthermore, we demonstrated the ability to simultaneously measure both the Ca^{2+} response and the force that the cell exerts on the TCR-pMHC bond during interaction and activation. Mapping the threshold force exerted by the cell through the TCR-pMHC bond in enabled by DNA-based tension force probes. Knowing the force that the T cell exerts gives insights on the interaction between the TCR and pMHC that may have functional consequences. As previously demonstrated by Liu *et al,* force regulates TCR-pMHC interactions and have a direct impact on calcium signaling (*58*), however the biomembane force probe used in this study is low throughput and uses an external force to infer on the effect of force on bond kinetics and calcium signaling. With the tension-force probe, the cell provides the force applied on the bond, which is more physiological. Therefore, the platform will allow for the direct correlations of the force applied by the cell through the TCR-pMHC bond and calcium signaling dynamics at a single-cell resolution while analyzing hundreds of cells in a single experiment.

Overall, this work provides a new application of the high-density cell trap array in enabling rapid calcium functional response analysis in a large number of cells stimulated with selected ligands with great potential for multiplexed with other assays including force mapping and immunofluorescence staining for surface marker expression characterization.

3 A GENERALIZABLE, TUNABLE MICROFLUIDIC PLATFORM FOR DELIVERING FAST TEMPORALLY VARYING CHEMICAL SIGNALS TO PROBE SINGLE-CELL RESPONSE DYNAMICS

The work presented in this chapter has been published in Analytical Chemistry[1].

The cellular microenvironment is highly dynamic, and the cell has the ability to interpret and transforms these signals into a functional outcome. Understanding how biological systems transduce dynamic, soluble chemical cues into physiological processes requires robust experimental tools for generating diverse temporal chemical patterns. This chapter focuses on the development of an integrated platform for applying dynamic soluble chemical cues to a dense array of cells while using fluorescence microscopy to visualize cell behavioral response (***Figure 3-1***). This device achieves fast fluid exchanges that are useful in analyzing cell response to a dynamic environment and determining the response kinetics of specific signaling pathways.

---

[1] Chingozha, L., et al. (2014). "A Generalizable, Tunable Microfluidic Platform for Delivering Fast Temporally Varying Chemical Signals to Probe Single-Cell Response Dynamics." Analytical Chemistry **86**(20): 10138-10147

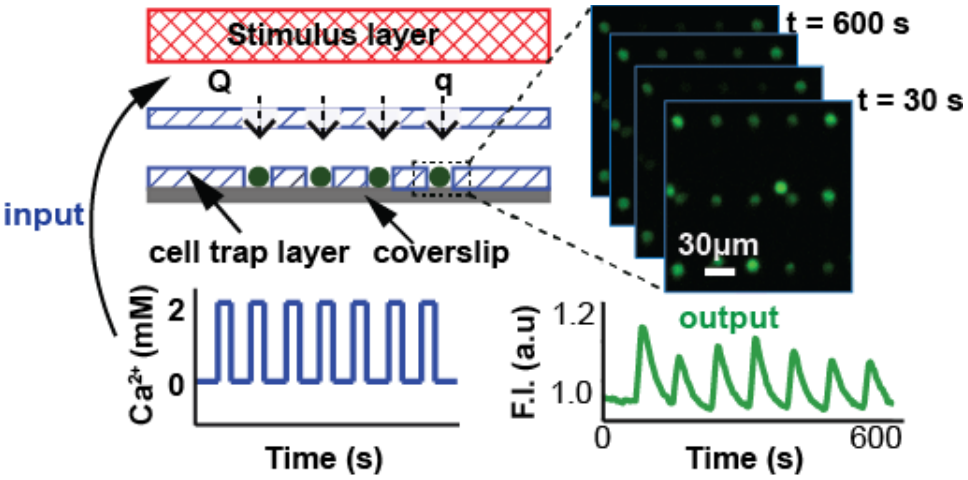

Figure 3-1. Cellular perturbation by dynamic stimulation. A multilayer microfluidic platform is developed to deliver temporal chemical cues to spatially-confined suspension cells while measuring changes in Ca^{2+} level using a calcium-sensitive dye as an output readout. This platforms handles hundreds of cells in individual positions, thus allowing both population statistics and individual cell analysis to be performed.

3.1 Introduction

Biological systems are exposed to a dynamic environment, and can processes complex signals while filtering out random noise. How cells respond to dynamic signals to give rise to productive output behavior is of interest to understand cell signaling transduction pathways. In dissecting, cellular response, the cell is usually treated as a black box, and an input signal is applied and an output behavior of the cell can be measured. From the input/output signals relationships, insights on cellular response can be drawn, and working models can be proposed. From the experimental perspective, a controlled application of the input signal and a defined approach in measuring the output behavior is critical, and the ability to vary the signal pattern may enable insightful observations to be made. The cellular microenvironment can vary spatially and temporally, and the ability to mimic the cell microenvironment enables the recapitulation of in vivo dynamic in vitro.

For example, chemical perturbations in the form of step inputs, oscillations, and constant stimulation have been demonstrated to have an impact on cell response (*149-151*). From these studies, it is clear that the temporal signals that span a large dynamic range drive cell behavior, and since it is difficult to ascertain the nature of the input signal in vivo, the development of tools that allow the generation of a variety of complex signals would enable multiple signals to be assayed in probing biological systems. Conventional approaches only allow constant concentrations or a step input to be applied with limited resolution.

Microfluidics approaches offer more robust way to introduce complex, spatio-temporal signal through the use of laminar coflow shifting (*150*), on- and off-chip valves, flow switching, acoustic waves (*99*) and diffusion through porous membranes (*88, 152*). In general, the generation of chemical gradients in microfluidic platforms can be categorized into two groups; using convection and diffusion-based approaches. Diffusion-based approaches incorporate sinks and sources where the chemical cue diffuses through a porous membrane (*88*), hydrogels (*87*), restricted channels or from pressure-balanced sources (*96*) to the sink where the biological specimen is located. Using diffusion to generate a chemical gradient ensures that the systems is shear free as shear stress can have an impact of cell behavior. However, the time required to establish a gradient may be on the order of minutes (*96*), thus limiting the dynamic range that can be applied to the system. With convection-based approaches fast dynamics can be generated, however there is need to ensure that the shear stress does not impact cell response since high shear stress can alter cell physiology (*153, 154*). The characteristic laminar flow in microfluidic

channels has been utilized for creating both temporal and spatial gradients. Laminar flow interface shifting enables rapid fluid switching to create oscillating chemical gradients. In addition, rapid fluid switching over cells has been impended in generating temporal chemical cues. These systems enabling the application of spatio-temporal signals have been developed for a range of biological specimens including small organisms such as the nematode (*1, 151*), unicellular organisms such as bacteria (*155*) and yeast (*156*), and for mammalian adherent cells (*89, 152, 157*). The platforms are unable to accommodate nonadherent cells like T cells that will drift or get washed away during application of a soluble stimulus. This is especially challenging in convection-based approaches, but even when using diffusion, nonadherent cells can drift out of focus or field of view during imaging. As a result, a way to ensure the cells are spatially confined during the chemical perturbation is needed.

The field of microfluidics has also advanced in developing platforms for single-cell handling and spatial confinement of suspension to enable time-lapse imaging (*59, 81-85, 136*). Combining these cell handling approaches with chemical gradient generators would enable the development of the next generation of devices for chemical gradient perturbation of suspension-based cells while simultaneously monitoring cell behavior using microscopy-based methods. The challenge lies in effectively coupling the cell trapping module with chemical gradient generation while maintaining robust cell trapping and efficiency in gradient generation. For instance, the flow profiles used in the gradient generation may not be compatible with the cell trapping criteria.

In this chapter, I introduce a multilayer microfluidic chip that enables the robust application of soluble cues to a dense array of cells with simultaneous fluorescence time-lapse imaging. The platform uses convective transfer for rapid switches combined with a perforated membrane that ensures controlled flow to ensure low shear stress on the cells, and incorporates the high-density cell trap array to allow the handling of a large number of nonadherent cells. The high-density cell trap array ensures hundreds of cells are analyzed in a single experiment to get population statistic with single-cell resolution.

3.2 Materials and Methods

3.2.1 Device fabrication

A more detailed explanation of the device fabrication is given in Appendix A.2 and Appendix A.3. The two-layer PDMS devices were fabricated in PDMS (Dow Corning Sylgard 184, Essex-Brownwell Inc) and negative master molds were fabricated in SU8 (Microchem) using the standard multi-layer soft lithography techniques (*110*)_ENREF_36. The master mold for the cell trap module was fabricated in a three-step photolithography process of heights 2 µm, 15 µm, and 15 µm respectively fabricated with SU8 2002, SU8 2005 and SU8 2010. The first two layers make the cell-trapping module, and the third layer is an array of micro posts for the making the pores in PDMS. The mold for the stimulus chamber was 50 µm, fabricated with SU8 2050. The negative molds were exposed to silane vapor, tridecafluoro-1,1,2,2-tetrahydrooctyl-1-trichlorosilane (UCT Special Ties, LLC) in a desiccator to allow release of the PDMS mold form the SU8 mold. For the PDMS devices, 10:1 PDMS prepolymer to cross-

linking ratio was spun on the cell trap master mold to make a thin layer (~10-12 μm) encompassing the cell-trapping module with the PDMS mold being thinner than the micro posts such that the posts were still protruding to make pores in the PDMS layer. The mold was partially cured at 70 °C for 15 minutes and then aligned and thermally bonded to a partially cured PDMS mold of the stimulus chamber, also made from 10:1 PDMS prepolymer to crosslinker ratio. The assembled mold was baked for complete curing of the PDMS overnight. Access holes were punched at the inlets and outlets with 19-gauge blunt needle and the two-layer device assembly was plasma-bonded to a coverslip.

3.2.2 Cell culture and cell preparation for calcium imaging

Jurkat E6-1 human acute T lymphoma cells (ATCC) were cultured in RPMI 1640 medium with 2 mM L-Glutamine and HEPES (ATCC) supplemented with 10 % fetal bovine serum (Sigma-Aldrich) and 100 units mL^{-1} penicillin-streptomycin (Life Technologies), in a 37 °C, 5 % CO_2 humidified incubator. For the cytosolic Ca^{2+} level measurements, cells were loaded with 5 μM Fluo3-AM (Life Technologies) calcium indicator dye in Hank's balanced salt solution (HBSS) without calcium and 0.02 % pluronic acid (Sigma Aldrich) to enhance calcium dye uptake by cells for 1 hour at room temperature, and washed with HBSS without calcium (Cellgro). Cells were then pre-treated with 1 μM thapsigargin (Sigma Aldrich) in HBSS without calcium for 5 minutes before being loaded in the device by gravity-driven flow. Thapsigargin depletes the intracellular calcium stores(*158*), which facilitates the opening of the calcium-activated release channels (CRAC) allowing entrance or exit of Ca^{2+} from the cytosol into the

extracellular space. Cells were exposed to oscillatory Ca^{2+} signals of varying frequencies while images were acquired every 2 seconds for 30 minutes on a fluorescent inverted microscope.

3.2.3 Device setup

The devices were primed with HBSS with 2 % bovine serum albumin (Sigma Aldrich) to prevent nonspecific cell adhesion to the device surface and remove bubbles from the device. The stimulus chamber inlets were connected to two pressurized reservoirs (at a pressure of 1 psi), one containing HBSS with 2 mM EGTA and the other HBSS with 1.5 mM Ca^{2+}. Cells were loaded into the cell trap module using gravity-driven flow (~ 4 kPa) corresponding to a flow rate of ~5 µL/hr. Once the cells were loaded, alternating solutions of the 1.5 mM Ca^{2+} and EGTA buffer were delivered to the cells using off-chip pinch valves at user-defined durations with simultaneous fluorescence imaging to track calcium dynamics, as indicated by the reporter Fluo-3 AM, in individual cells. Valve control and image acquisition were performed using custom MATLAB-based scripts (Mathworks Inc.).

3.2.4 Signal delivery characterization

The delivery of chemical cues into the cell trap chamber was characterized using fluorescein dye with cells loaded in the device. Briefly, alternating solutions of fluorescein (50 µg/ml) in PBS and PBS in pressurized reservoirs were delivered to the stimulus chamber at user-defined oscillating periods (2 s – 2 mins) using off-chip pinch valves, while simultaneously acquiring fluorescence images at 10 fps. Fluorescence

intensity of the images was measured at all the rows in the cell trap chamber to determine the delivery of signal from the stimulus chamber to the cell trap channel.

3.2.5 Imaging and data analysis

Images were acquired every 2 seconds for thirty minutes on a fluorescent microscope using MATLAB interfaced with Micromanager Software (*159*) for image acquisition and automated valve control. All the image processing and analysis were performed with custom-made scripts in MATLAB. Briefly, to analyze the calcium dynamics the average intensity for each cell was determined and in every frame, the background was subtracted from the mean intensity for the individual cell being analyzed. The mean intensity for each cell was then normalized to the initial intensity to account for the differences in the initial dye loading for each cell. The average response for the cell population was also computed at each time point.

3.3 Device design and operation

3.3.1 General design concept

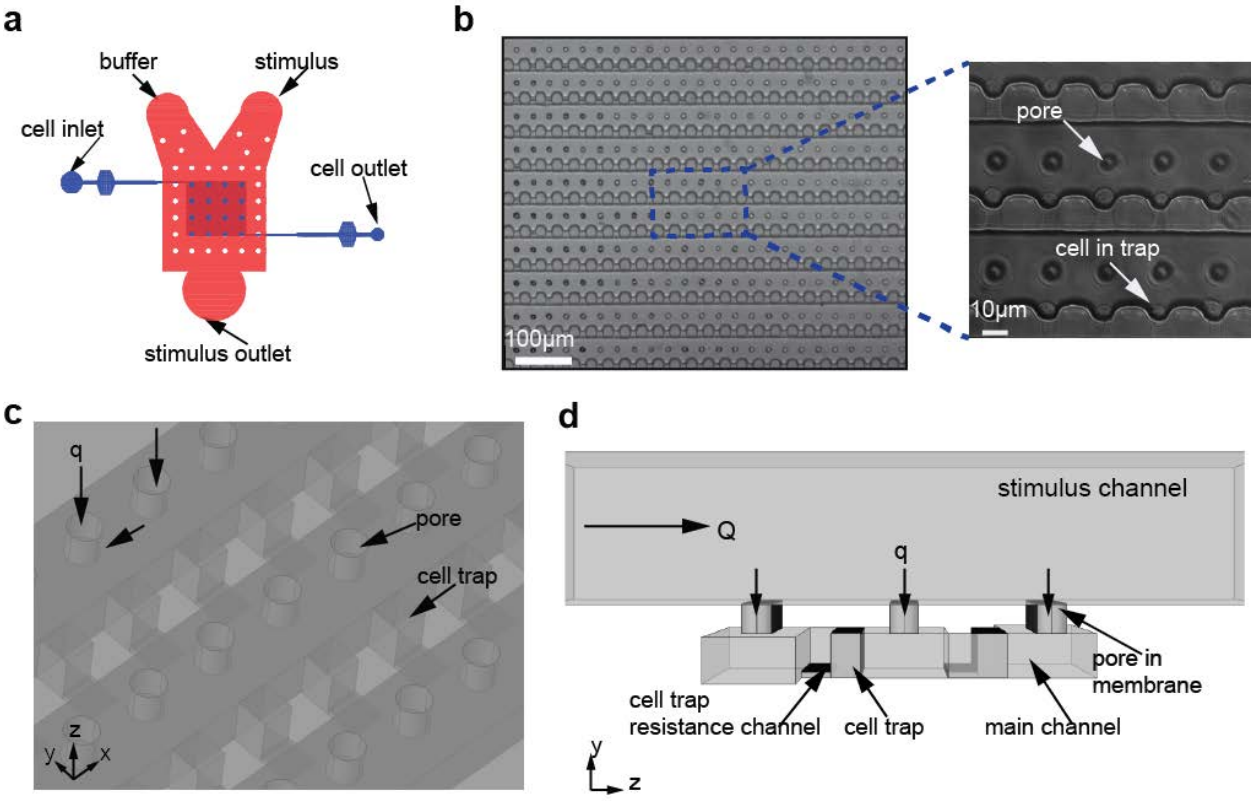

Figure 3-2. Microfluidic platform design overview. (a) The devices has two layers, the fluid layer (red) where the stimulus and the buffer are introduced, and the cell trap layer (blue) where the cells reside, (b) top view micrograph showing the cell trap layer. The cell trap layer has a serpentine main channel, with cell trapping microstructures along the channel. Overall, the layer has 20 rows with 50 cell traps on each row. The traps are 10 μm wide and accommodate an individual cell as shown. The pores on the cell trap layer connect the layer to the top fluid layer allowing fluid exchange from the top layer to the cells, (c) 3D rendering showing the cell trap positions and the direction of the flow from the fluid layer, and (d) a cross-sectional perspective showing the fluid flow and distribution. The fluid (buffer or stimulus) is introduced from the stimulus channel at a flowrate Q, and a component of this flow (q) goes through the pores to the cell trap layer.

The device was designed to accommodate hundreds of suspension cells, and deliver temporal chemical cues over a large dynamic range. The device is a two-layer PDMS platform that incorporates a cell trapping modules and a dynamic stimulus generating module as shown in Figure 3-2a. The cell trapping module consists of a dense array of 10 μm cell traps with each trap accommodating an individual cell (Figure 3-2b). This cell trap modules in molded on a thin PDMS membrane that also has 8-10 μm-sized pores. Overall each device has 1,000 cell traps on a 1 mm^2 footprint. The pores on the membrane make a fluidic connection between the cell trap module and the stimulus channel module (Figure 3-2 & Figure 3-3), allowing a fraction of flow, q to go through the cell trap layer. Introducing the stimulus into the cell trap layer using this approach ensures the stimulus reaches the cell trap layer at the position where the cells are thus avoiding dead volume effects that would otherwise smear the signal. In addition, the resistance of the cell trap layer and the pores ensures that the flow through the cells is very low, guaranteeing that the cells experience very low shear stresses.

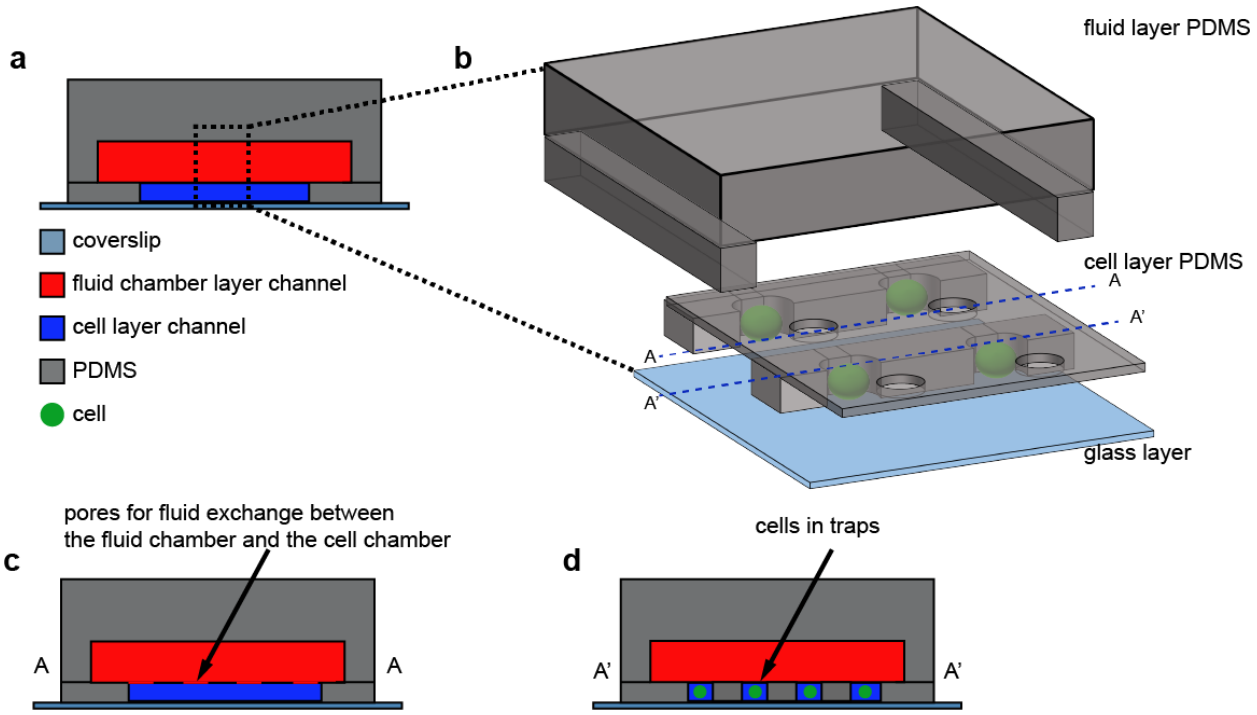

Figure 3-3 Device design view. (a) cross-sectional view showing the cell layer (blue) and the stimulus layer (red), (b) 3D rendering showing the PDMS layers and the cell position, and cross-sectional views depicting, (c) the pores on the PDMS membrane and (d) the cell position on the platform.

The key feature in our design is the monolithic integration of PDMS porous membrane with cell-trapping microstructures. The ability to make a porous PDMS membrane as previously described (*160, 161*) allows us to interface the cell-trapping microstructures with pores in the same module for stimulus delivery from the stimulus chamber using convective flow. The use of convective flow ensures fast transport to all cells simultaneously compared to relying on diffusion through the device and the cell trap prevents cell displacement during flow. The porous membrane is made using soft lithography and the pore size and pore length are user-defined allowing more flexibility in membrane properties compared to commercial polycarbonate membranes. During

fabrication, it is crucial that the desired PDMS membrane thickness is smaller than the height of the posts on the master mold so as to ensure that through holes are made in the PDMS. In our design, the membrane thickness was ~10 µm and our posts on the mold were 15 µm. The aspect ratio (height/diameter) of the posts is critical in making a robust mold. We aimed for an aspect ratio between 1.5 and 2, as higher aspect ratios would cause the posts to collapse. In addition, we observed that the density of the posts on the master mold was critical in ensuring the stability of the posts during development of the SU8 mold and replica mold. With a sparse post density, the posts would collapse. Therefore, our designs had 10 µm posts with a pitch of 35 µm.

The predefined perforations in the PDMS membrane enable stimulus and buffer delivery from the stimulus chamber bulk flow into the cell trap area using off-chip pinch valves. Using vertical flow to exchange fluids in the cell trap allows the entire cell trapping layer to be exposed to the same concentration of stimulus at the same time, and circumvents diffusion that would otherwise limit the temporal resolution of the signal delivery. Moreover, having a monolithically integrated membrane makes this approach generalizable to existing microfluidic platforms for delivering soluble cues. Furthermore, using PDMS to make the porous membrane rather than using commercial membranes not only enables the integration with cell-handling microstructures, but also enables ease of fabrication of the device using established soft lithography methods for thermal bonding PDMS to PDMS, and plasma-bonding the PDMS assembly to glass. Even though our device is a multi-layer PDMS device, which may add to the complexity of the fabrication,

the alignment of the two layers does not require a microscope, and the cells will be in contact with the coverslip, which also allows for high-resolution imaging.

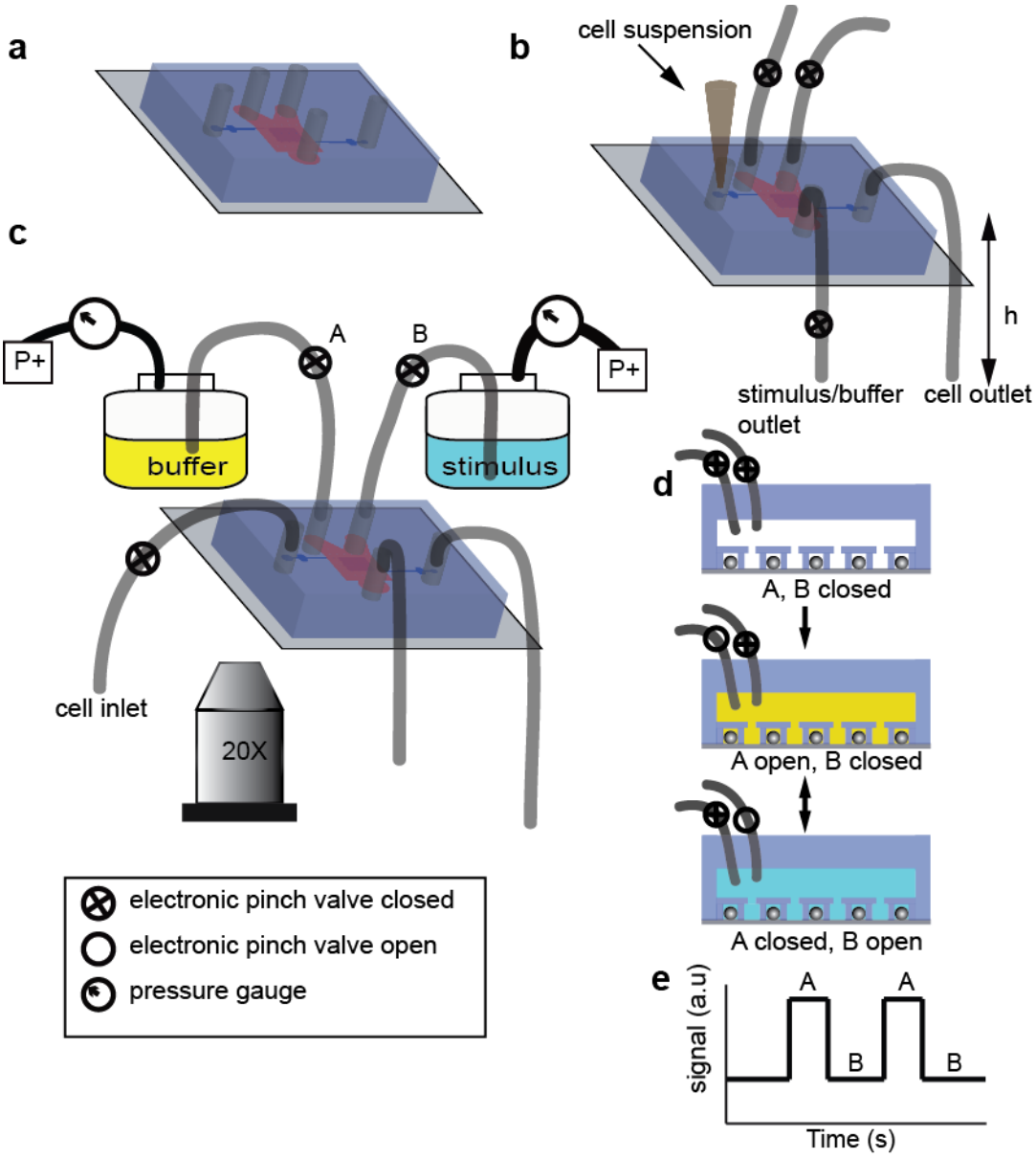

Figure 3-4. Schematic of the device setup. (a) device showing access holes for the inlets and outlets, (b) pipette tip containing the cell suspension is placed at the cell inlet, and cells are loaded in the device using gravity-driven flow with the inlets and outlet of the stimulus layer closed, (c) overall setup during the cell stimulation experiment, the buffer and stimulus reservoirs are at 0.5 psi. The flow into the stimulus layer is controlled by alternating the opening and closing of valve A and B, and (d) waveforms are created by alternating the opening and closing of the valves, and (e) example of a waveform that can be generated in the device.

To operate the platform, pressure sources are required for the buffer and stimulus reservoirs (***Figure 3-4***), and fluid flow is controlled by electronic pinch valves. Cell loading is achieved by gravity-driven flow, and the stimulus dynamics are achieved by alternating the opening and closing of the pinch valves attached to the inlet tubing. This is a relatively simple setup that can be easily adopted into other laboratories.

3.3.2 Single-cell loading in device

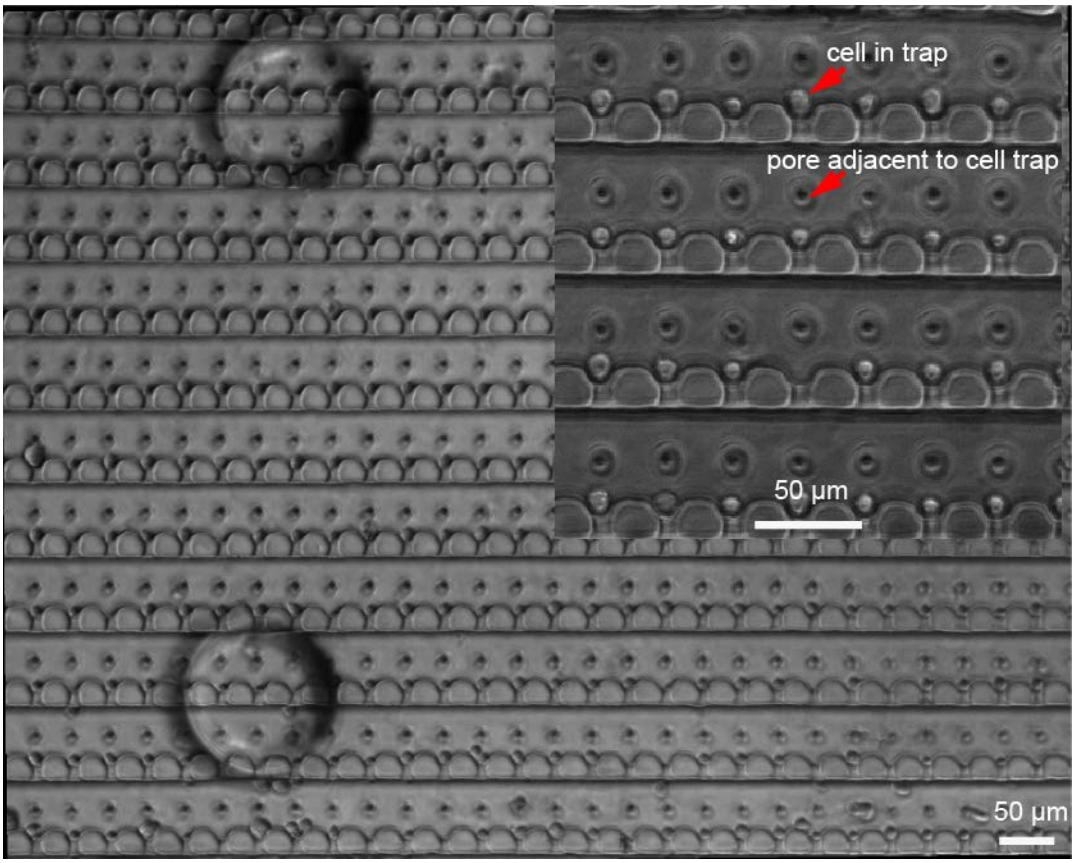

Figure 3-5. High-density single cell trapping. Cells are loaded in the device using gravity-driven flow, and each trap holds a single cell. The single-cell loading efficiency is > 95 - 98 % with some traps having double loading or no cells loaded. At 10x magnification shown in the figure, ~ 360 cells can be viewed enabling hundreds of cells to be analyzed simultaneously.

Cells are loaded in the device using gravity-driven flow and are directed into the traps by hydrodynamic flow (Figure 3-4b). With the addition of the stimulus generator we wanted to ensure that we would still retain the ability to efficiently load individual cells in our device. The pore size of the perforated membrane was designed as a 10 μm feature on the design and due to the shrinkage of the PDMS, the actual pore size on the device was measure to be ~ 8 μm. This pore size is optimal in ensuring that the cells being loaded in the device do not easily go through the pores into the stimulus layer. Figure 3-5 shows the cell trap array with cells loaded in the device. Each cell is adjacent to a pore that delivers the soluble signal to the cells. The device offers high-density cell trapping with ~ 360 cells in the field of view at 10x magnification.

3.3.3 Fluid flow design

Having optimized the cell loading, we then focused on having precise stimulus delivered to the cell while maintaining a low shear stress environment. The lateral dimensions of the stimulus chamber were determined by the overall size of the cell trap chamber. In our case the stimulus chamber had a lateral dimension of 2 mm by 2 mm and a height of 50 μm. Figure 3-6 shows a simplified analytical model for the flow resistances in the device, and the resistances can then be used to estimate the flow in the cell trap layer, q.

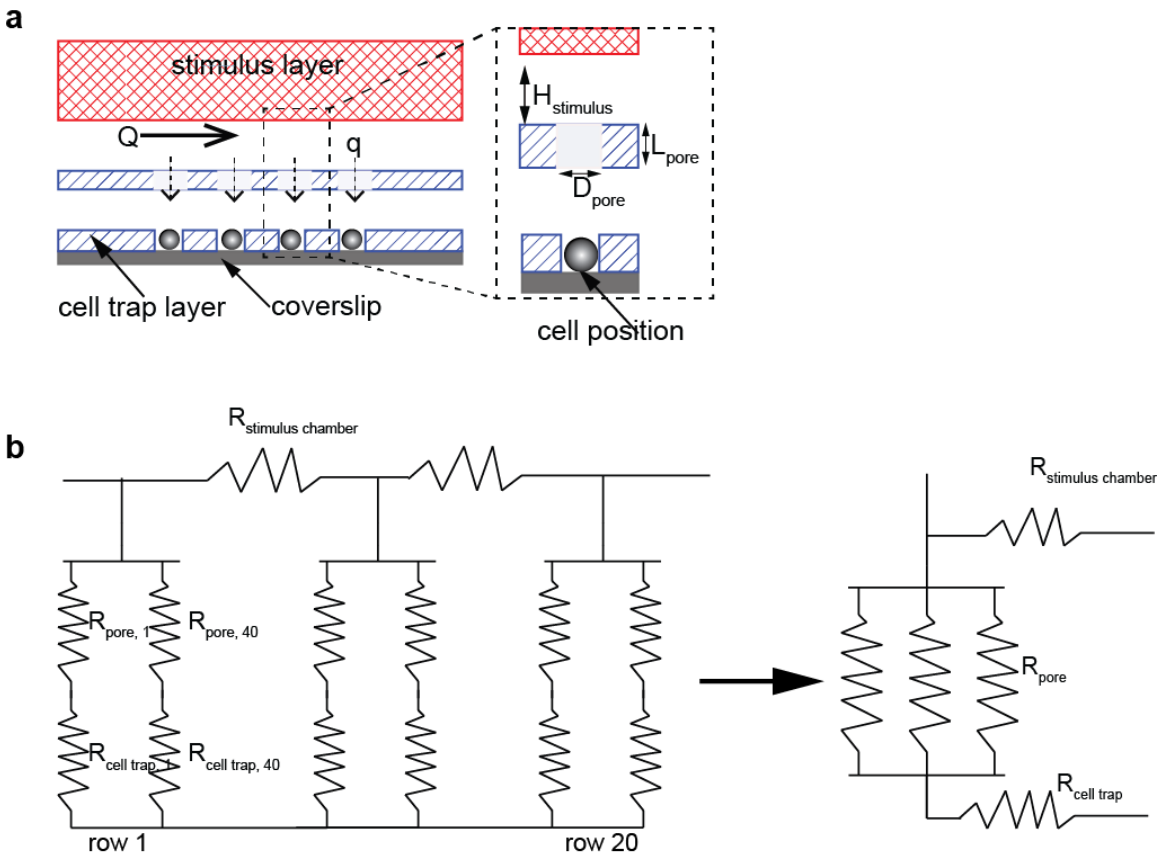

Figure 3-6 Analytical modeling of flow resistances in the device. (a) depiction of the fluid flow in the device, the fluid is introduced into the stimulus layer at a flow rate, Q, and based on the relative resistances, a flow rate of q goes through the cell trap layer, and (b) the resistance model

The resistance of the system is contributed by $R_{stimulus\ chamber}$ (low resistance), $R_{cell\ trap}$ (high resistance), and the resistance R_{pore} of the pores in the membrane (high resistance). The resistance of the bottom chamber is a combination of R_{pore} and $R_{cell\ trap}$.

$$R_{pore} = \frac{128\eta L_{pore}}{D_{pore}^4}$$

The membrane resistance depends on the underlying chip design of the cell trap and the dimensions of the pore; diameter, (D_{pore}), length (L_{pore}) and number of pores (N_{pore}). The pore dimensions are user-defined during mask design (D_{pore}, N_{pore}) and in the fabrication steps (L_{pore}), and are subject to printing and lithography resolution and aspect ratio

restrictions, which is easily variable. In our studies, we experimentally varied the pore dimensions (D_{pore} from ~ 7-10μm, L_{pore} from ~ 8-12 μm, and N_{pore} from 200-800 pores) and theoretically determined the flow resistance and average velocity in the cell trap chamber. With these designs we characterized the fidelity of the signal in the device over a large temporal range. The optimal designs allowed us to keep the flow rate in the cell chamber relatively small and therefore shear stress is under control, yet still be able to obtain high fidelity in the signal delivery. The input flow rates were measured to be ~0.5 ml/min resulting in an exchange time of 6 ms in the stimulus chamber, which translates to theoretical flow rates of 1-10 μL/hr in the cell trap chamber. At these flow rates the corresponding shear stress was 0.1 – 5 dynes/cm^2. The tunability of the device design will allow a user to vary the device dimensions to fit the need. However, there is a tradeoff between high temporal resolution and low shear stresses. In general, in order to achieve a high temporal resolution while maintaining low shear stress, we can vary the pore dimensions or the overall size of the device.

We further characterized fluid flow and exchange using a 3D simulation in COMSOL Multiphysics using the coupled fluid and mass transfer equations. To reduce the computational needs for the simulation, the model was based on a truncated version of the device with only 3 rows of the cell trap array as shown in Figure 3-7a. With a pressure difference between the inlet and outlet of the stimulus layer of 0.5 psi, an average velocity of 2 mm/s in the cell trap chamber was achieved (Figure 3-7b). This value is in close agreement with the average velocity determined in the lumped resistance analytical model (2.73 mm/s). Transient mass transfer was then simulated using the flow

profile with a switching periods of 10s. Figure 3-7c shows the changes in the concentration gradient in the stimulus and cell trap layer at time, t = 0, 100 ms, and 10 s. A steady concentration in the cell trap layer was reached within 0.2 s. Thus, signal patterns can be obtained with fast rise time.

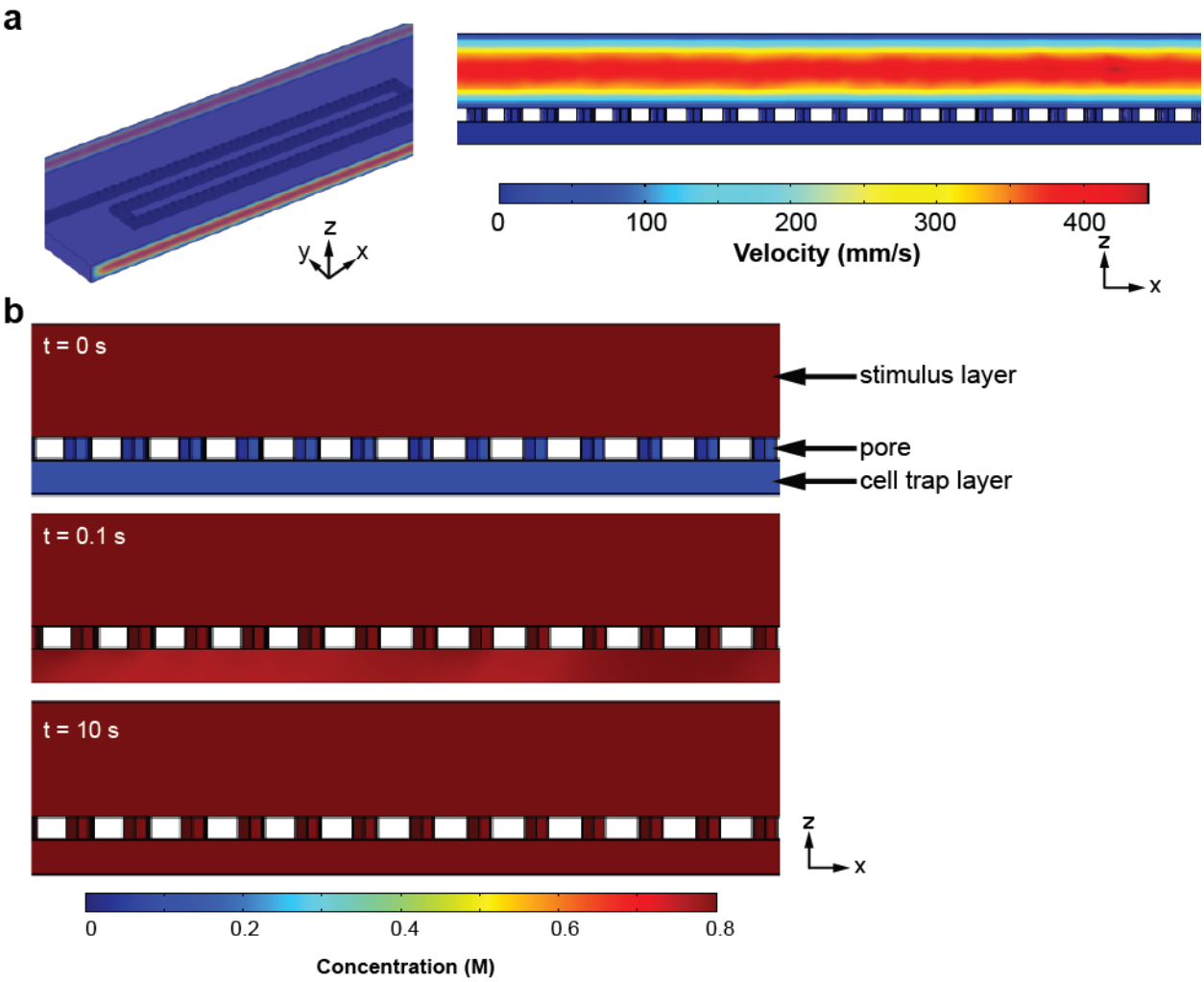

Figure 3-7 Fluid and mass transfer simulation in Comsol Multiphysics module. A 3-dimensional comsol model for a truncated version of the device consisting of 3 rows of the arrays was created in comsol multiphysics. (a) velocity distribution, and (b) the dynamic changes in the soluble cue concentration, at time t = 0 the soluble cue is delivered to the top layer and a constant concentration is achieved in the bottom cell trap layer within 100 ms.

To visualize the signal delivery, we used a fluorescent dye as a proxy for the stimulus, and alternated solutions of PBS buffer and fluorescent dye over a range of periodicities (2 s – 2 minutes). Figure 3-8a shows a fluorescent micrograph of a dye-filled device. By measuring the fluorescence intensity at different rows, we showed that the signal is uniformed throughout all the rows (Figure 3-8b, c), and repeatable for a defined duration of time. Within each row, the signal is also uniform (Figure 3-8d), demonstrating that the asymmetric position of the stimulus layer inlets do not have an effect on the signal delivery to the cell trap layer. Therefore, cells loaded in the platform will experience the same microenvironment changes at the same time. As a result, differences observed in cell behavior can be attributed to cell-to-cell variation and not experimental artifacts.

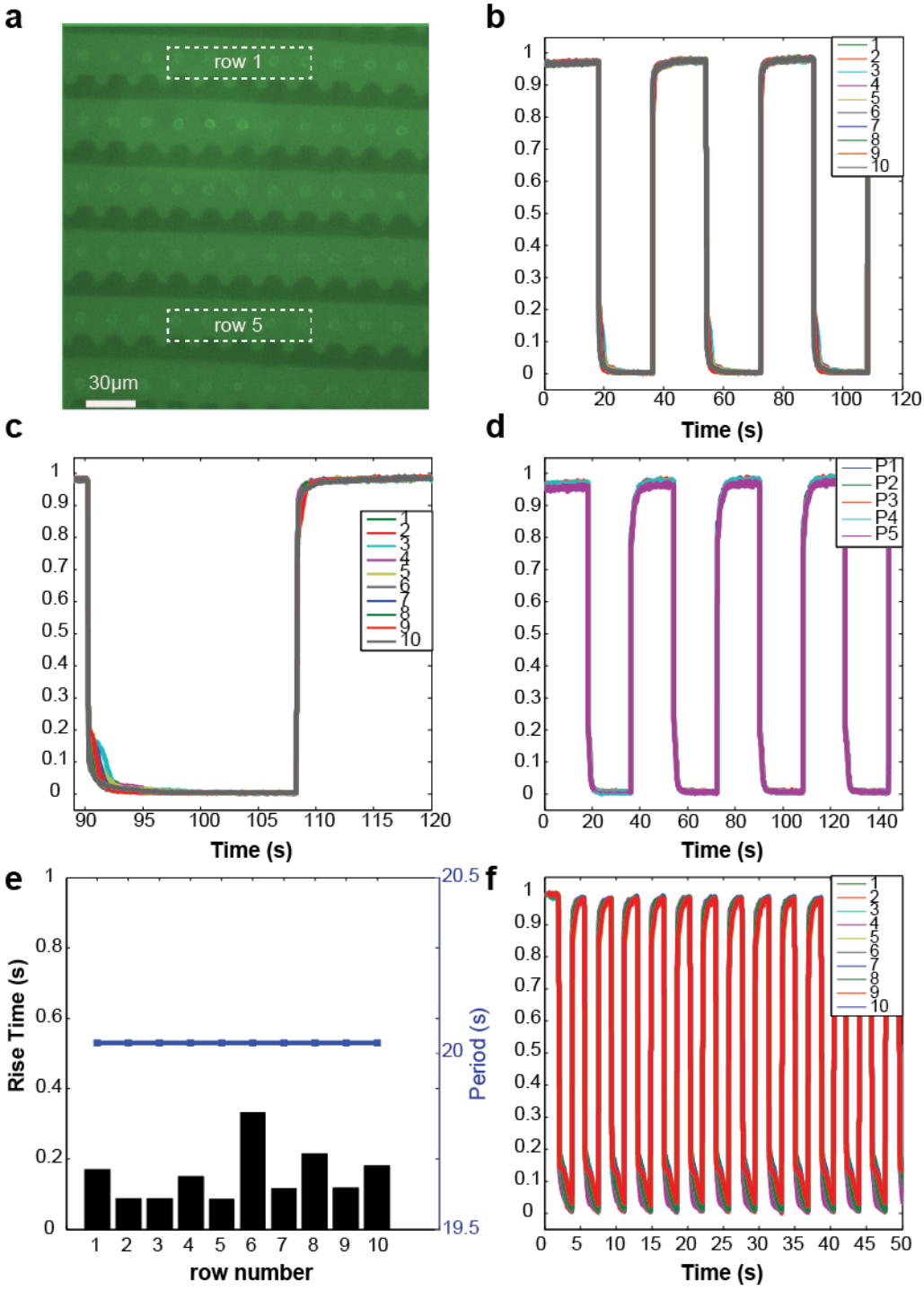

Figure 3-8 Waveforms generated over a large dynamic range with rapid rise. The signal delivery in the device was measured using a fluorescent dye in PBS as a proxy for the signal and PBS as the switching buffer. Alternating solutions of PBS with fluorescent dye and PBS were delivered to the device. (a) fluorescent micrograph of the field of view when the device was filled with fluorescent dye, (b) signal traces of multiple rows in the platform for a period of 20 s, (c) zoomed out traces of signal generation showing that the signal is delivered with very small rise and fall time, and that the overlapping traces from

the different positions in the device, (d) signal traces at different positions on the device for the same row showing uniformity of the signal within each row, (e) period (right-hand y axis) and the rise time (left-hand y axis) for the 10 rows of the traps in the device show that there are negligible differences between the top and bottom row. The average rise is ~ 0.15 s, and (f) 2 s period representing the lowest period achieved in the platform.

The perforated membrane design enables a fast delivery of the soluble cue, thus allowing rapid generation of a uniform signal throughout the entire device. The low resistance in the stimulus layer relative to the high flow resistance in the cell trap layer allows small amounts of the stimulus to bleed through the pores into the cell trap layer. Since the pores are evenly distributed through the entire device, the signal is established rapidly. Figure 3-8e shows further quantification of the signal at each row, and observed a negligible difference in periodicity (<0.01%) between the upstream and downstream rows. The average rise-time was ~ 154 ms which is consistent with our COMSOL simulation (< 200 ms). Therefore, our platform can achieve switching frequencies of up to 0.5 Hz, and will be a versatile tool in modulating the cell microenviroment and application of different types of signal patterns. The nature of the signal pattern generated is controlled by the off-chip valve components, thus other off-chip accessories can be coupled to generate complex patterns, and our perforated membrane design enables the temporal gradients to be established with a short rise time.

3.4 Cell response to dynamic extracellular Ca^{2+} changes

To demonstrate the utility of the platform we measured changes in intracellular Ca^{2+} response of Jurkat E6.1 cells upon exposure to stimulation. We used a Ca^{2+}-sensitive dye, Fluo3 to visualize Ca^{2+} changes in the cells.

3.4.1 Ca^{2+} response to oscillating extracellular Ca^{2+} concentration

We then further analyzed the effect of an oscillating extracellular Ca^{2+} concentration on the intracellular Ca^{2+} concentration. Ca^{2+} is a ubiquitous messenger in a number of signaling processes, and the Ca^{2+} patterns in the cell can influence signal transduction. We sought to demonstrate how our platform can be used to induce Ca^{2+} patterns that can be used to elucidate how the Ca^{2+} signals affect different cell signaling pathways. Dometsch et al. demonstrate that the amplitude and frequency of Ca^{2+} oscillations influenced the efficiency and the type of genes expressed by the cell (*140*). In general, calcium oscillations in both excitable (neurons), and nonexcitable cells such as immune cells has been shown to result in differential signaling and gene expression (*16, 17, 60, 140*) thus making Ca^{2+} an important molecule to study and manipulate. Intracellular and plasma membrane Ca^{2+} channels regulate the Ca^{2+} levels. In immune cells, at the resting state, the cytosolic Ca^{2+} level is 1 µM while in the ER the CA^{2+} level is 100 µM, while the extracellular Ca^{2+} level is ~ 1 mM. The Ca^{2+} channels and pumps are activated to enable Ca^{2+} entry and exit from the stores.

To activate the CRAC channels that enable Ca^{2+} entry from the extracellular space, cells were pretreated with thapsigargin to deplete intracellular Ca^{2+} stores. Thapsigargin inhibits sarco/endoplasmic reticulum Ca^{2+} ATPASE (SERCA) thus blocking the ability of the cell to pump calcium into the ER (*162*). The depletion of the ER Ca^{2+} intracellular stores, leads to the opening up of the CRAC channels to allow Ca^{2+} entry into the cytosol from the extracellular space. Upon treatment with treatment with TP, cell will show a rise in cytosolic Ca^{2+} due to the release of Ca^{2+} from the ER stores (Figure 3-9). Once treated

with TP, the calcium levels in the intracellular Ca^{2+} stores remain low since the SERCA pumps are inhibited from pumping Ca^{2+} into the ER, and therefore the CRAC channels remain open. As a result the cytosolic Ca^{2+} can be modulated by altering the extracellular Ca^{2+} concentration.

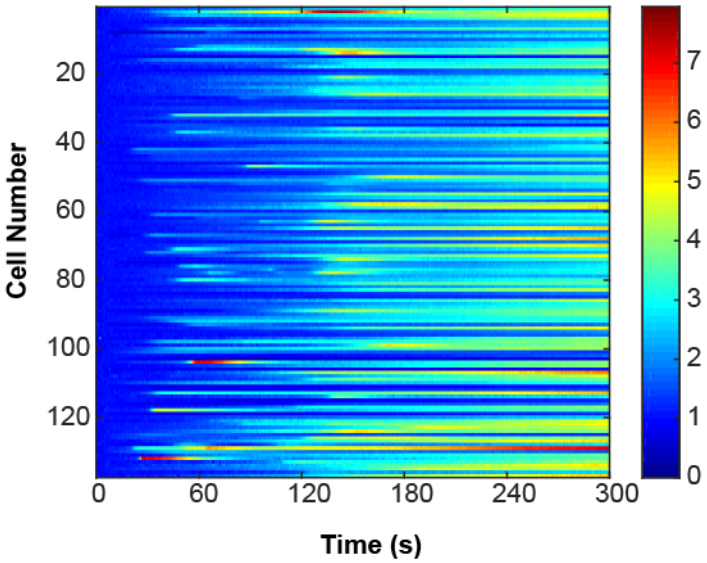

Figure 3-9. Calcium elevation upon treatment with thapsigargin. Once the cells are loaded in the device, 1 µM TP in PBS without calcium is added, leading to intracellular calcium depletion observed by the elevation in calcium level of the individual cells as shown in the heatmap.

After treatment with TP, the cells were exposed to alternation solutions of 0 mM and 2 mM Ca^{2+} concentration at user defined durations ranging from 10 s to 120s while simultaneously imaging to monitor changes in the Ca^{2+} level. In Figure 3-10a, we show a snapshot an array of cells loaded with Fluo3 dye in the device during the time-lapse stimulation. Alternating the extracellular Ca^{2+} level resulted in changes in the cytosolic calcium level in the individual cells as shown in Figure 3-10. These cells were exposed to a 20 s pulse of 2 mM Ca^{2+} followed by 100s of 0 mM Ca^{2+}. On average the population

response follows the input signal. However further analysis of the individual cell response revealed four distinct behaviors that the cells exhibited (Figure 3-10d). Cells were categorized as oscillatory (85%), peak then plateau (7%), peak then drop to basal level (4%), and cells that show no response (4%). These response demonstrate the inherent heterogeneity in cellular responses and would be masked in average population statistics. These differences may have functional implications as gene expression may be regulated by the amplitude, duration and frequency of the Ca^{2+} signals (*16*, *140*).

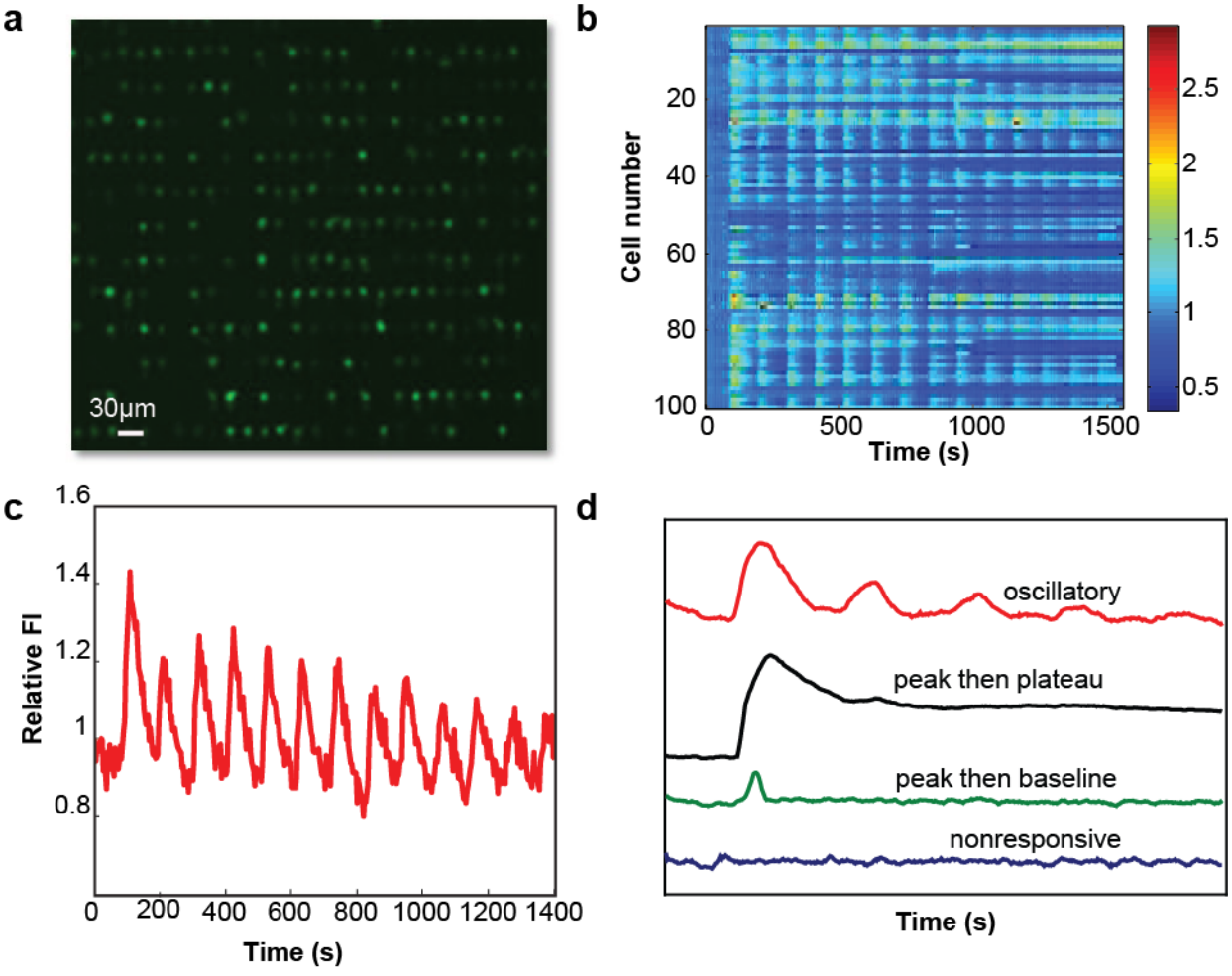

Figure 3-10 Heterogeneous cell response to extracellular calcium stimulation. Cell were loaded with Ca^{2+} dye then pretreated with thapsigargin for 5 minutes before being loaded in the device. Once cells were loaded alternating solutions of Ca^{2+} and no Ca^{2+} HBSS

buffer were introduced into the device at for a duration of 20 s and 100 s respectively. (a) fluorescence micrograph of the Fluo3-loadeds cells in the device, (b) heatmap showing the changes in fluorescence intensity corresponding to changes in Ca^{2+} level (blue is low Ca^{2+} and red is high Ca^{2+}) for each individual cell, (c) average population response to the stimulus show an oscillatory response that follows the input signal, and (d) the four distinct signal patterns observed within the population. Even though the average response show that the cells follow the input signal, a fraction of cells show no response to the stimulus, some cells only show a peak at the first stimulation before returning to baseline, while some cells show a peak at the first stimulation then plateau to a level higher than the baseline, and some cells exhibit an oscillatory signal entrained with the input signal.

We the evaluated the dynamic range over which these immune cell would show a response to changes in Ca^{2+} level. In Figure 3-11 we showed the response of the cells to a range of periodicities of the stimulus. Over the range assayed, the average response is synchronized with the input signal. However, for the 10 s period of stimulation, we start to observe a lag in the output signal, thus potentially showing that we have reached at the limitation of the response kinetics in the control of Ca^{2+} entry or exit from the cell.

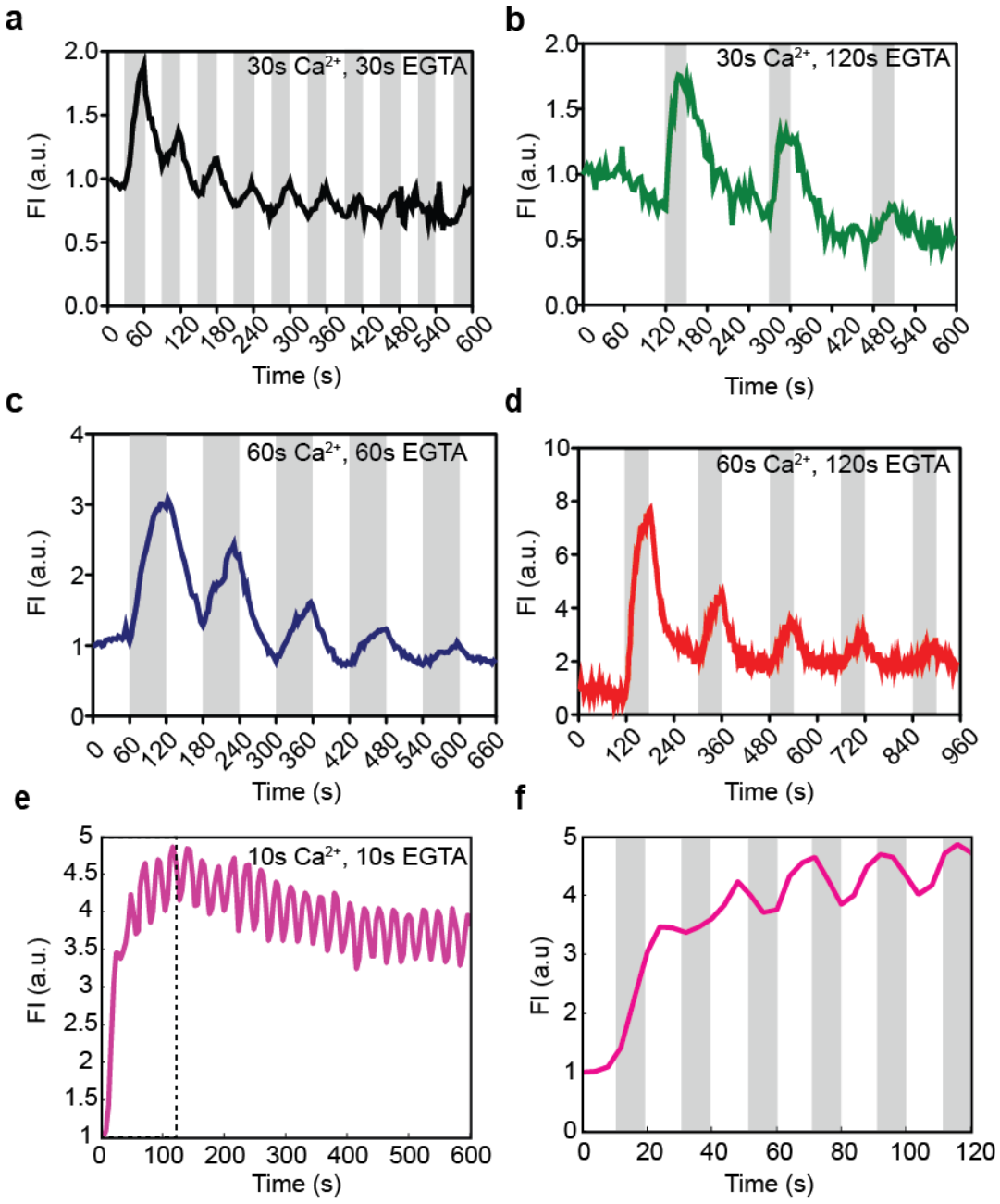

Figure 3-11 Population average responses follow the input signal. Cells were exposed to alternating solutions of Ca^{2+} and no Ca^{2+}, while measuring the cell response for each individual cell, and an average for the population was computed. For each data set the number of cells analyzed, n = 100 -200 cells. (a-e) the figures show the average Ca^{2+} response and the grey bars indicate the time when the cells were exposed to Ca^{2+}. The cells show an increase in intensity within 1 s of exposure to the Ca^{2+} stimulus. (f) Interestingly with the 10 s period, the cells output response show a lag compared to the input signal showing the limit to which a cell can process and responds to a signal.

We further demonstrate the ability of our platform to assay hundreds of cells in a single experiment and expose the cells to a stimulus over a range of periodicities. In Figure 3-12, the Ca^{2+} response of individual cells (blue) is shown, each panel represent a single experiment where 150 – 200 cells were analyzed, and the average of the population could be computed (red). Figure 3-12a,b show that at smaller periods of both the stimulus and buffer exposures, the cell fail to return to baseline after the stimulus is removed in contrast to Figure 3-12c-f, indicating a limit in how fast these cells are able to respond. In addition, even though the cells are exposed to the same Ca^{2+} level, they show varying Ca^{2+} level amplitudes indicative of the heterogeneity in the Ca^{2+} uptake within a cell population.

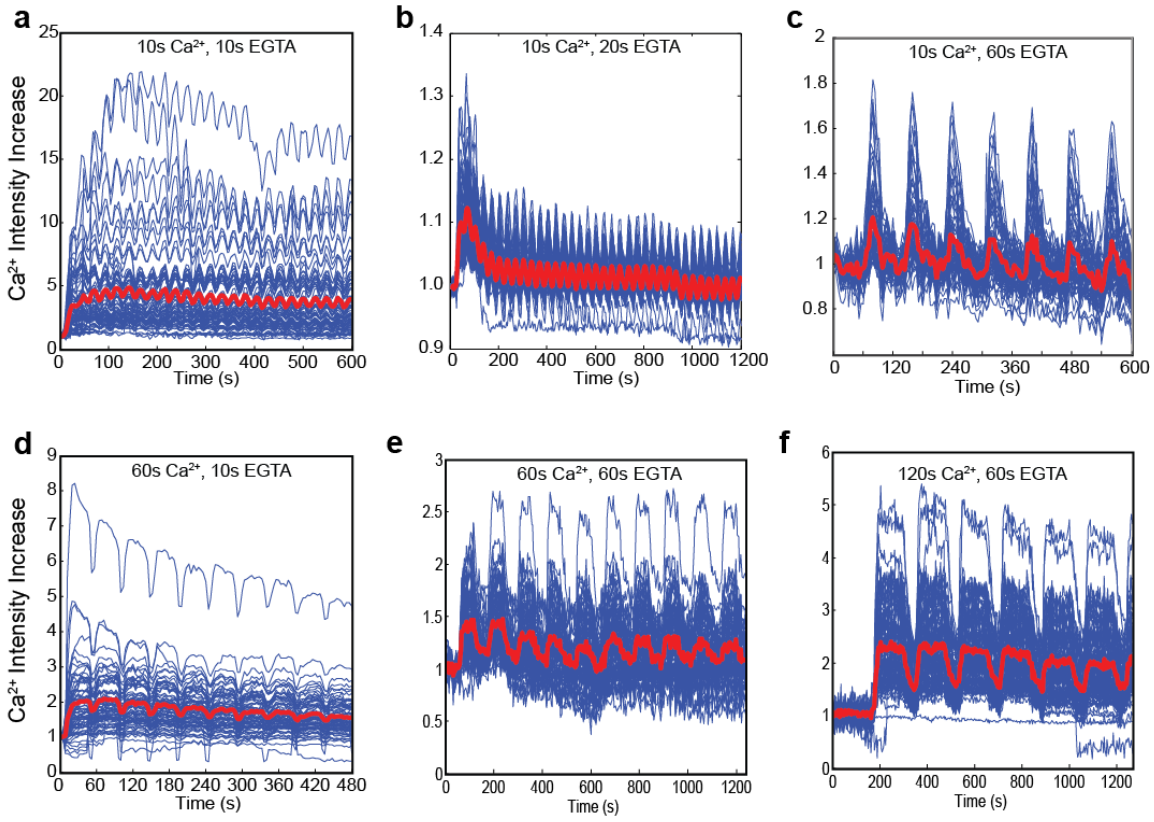

Figure 3-12 individual cell response of hundreds of cells to varying stimulation periodicities. The cells were exposed to 0 and 2 mM Ca^{2+} for varying periods as indicated. The figure panels show the response of each individual cell (blue), and the population average (red). All the intensity values are normalized to the initial intensity for each cell to account for differences in dye loading. Even though the cells are exposed to the same Ca^{2+} level, they show differences in amplitude of the signal output. At the short periods (a,b), the cells lose their ability to return to baseline after the Ca^{2+} is removed because the input signal is faster than the ability of the cell to respond.

One can envision that by having a platform that enables the modulation of the Ca^{2+} temporal signal by varying the amplitude, duration and concentration of the Ca^{2+} level, the specificity of the Ca^{2+} signal in modulating many biological functions can then be elucidated. Therefore, this platform setup in combination with computational modelling may be useful in studying signal transduction pathways under a dynamic environment to

identify the time scales involved in the response and determine the rate determining steps. Moreover, dynamic input signals are important in evaluating system dynamic both in vitro and in vivo where the system is largely unknown, and therefore treated like a black box. Evaluating systems under dynamic input signals like oscillatory pattern may provide more information as a number of parameters for both the input and output can be measured and relationships deduced.

3.5 Conclusions and future directions

Overall, we have developed a versatile platform for stimulating a dense array of cells with spatially independent, temporally diverse chemical signals while performing time-lapse imaging to monitor cell response. The coupling of a cell trapping array and a stimulus delivery module enable the application of temporal soluble cues to nonadherent cells. Previous designs have focused on applications with adherent cells that are easily adhered to the surface before flowing a soluble cue over them without displacing them (*86, 88, 89*). However, nonadherent cells will be washed off the surface if they are not anchored, and we resolve this by incorporating the cell trap array (*81*) in our design. In addition, the high density trap allow us to analyze a large number of cells in a field of view, thus enough cells can be analyzed in a single experiment to also provide population statistics. Beyond the application of a stimulus to elucidate cellular functions, this platform can offer a new approach in evaluating drug response by enabling timed exposures with simultaneous observation of response.

The facile integration of the monolithic perforated membrane is a new approach to applying stimulation using well controlled convective transport and also eliminates dead volume upstream of the cell trap array. Previous designs have used commercially available polycarbonate porous membranes to deliver temporal signals by diffusion (*88, 152*). However, commercial membranes do not offer the ability to easily alter the pore dimensions, and the assembly of the membranes on a microfluidic platform will require specialized bonding. Our perforated membrane is molded in PDMS, the same material used in most microfluidic platforms for biological applications. Therefore, we use the standard replica molding, and plasma and thermalbonding techniques. Moreover, the design concept is applicable to any chip design. Our approach is additive, involving the addition of functional modules to existing chip designs. As a result the idea of a perforated membrane can be translated to platforms developed for small organism and single cell handling to allow for dynamic soluble to be applied in a more controlled manner while minimizing dead volume effects and shear stress effects.

With a dense array of cells, the ability to deliver uniform, temporal signal enables cell heterogeneity within a cell population to be elucidated. Here we demonstrated how varying the extracellular Ca^{2+} level can be used to modulate the Ca^{2+} levels in Jurkat cells. These Ca^{2+} signals may have functional consequences. Further probing into the subsequent signaling molecules by measuring gene and protein expression could provide more insightful information on the functional relevance of the signal variations and also any functional implications of the cell heterogeneity.

4 PLATFORM FOR MULTIPLEXED FUNCTIONAL ASSAYS

A manuscript has been prepared for publication of this work.

Thus far, I have demonstrated the use of microfluidics in single-cell analysis and dynamic soluble stimulation. The platforms in Chapter 2 and 3 were developed for soluble and surface-anchored stimulation in T cells, and calcium was used as a readout. Here, we extend the application of the platform developed in chapter 3 to perform multiplexed assays, thus enabling multiple different readouts to be measured on the same cell population. We envision that this platform addresses some of the technological gaps in conventional and microfluidic-based assays and its simplicity will make it easily transferable to other labs.

4.1 Introduction

T cell signaling involves a cascade of dynamic events that span from seconds to days, and distinct changes in molecular expressions enable the measurement of features indicative of T cell activation. Most studies involve perturbation of the cells with a stimulus that can be either an antigenic peptide on the surface or lipid bilayer, or on an antigen presenting cell, or soluble chemical cues followed by measurement of changes in cytosolic Ca^{2+} level, surface marker expression, cytokine secretion, cytotoxicity or proliferation (*3, 163-165*). These cell signaling cascades involve different molecular species; small molecules, DNA, RNA, protein expression, and protein phosphorylation that require different techniques for the determination of their expression level and dynamics. For example, flow cytometry has been applied to the measurement of protein expression through the

use of specific antibodies and fluorescent labeling, and RT-PCR is used to determine mRNA expression levels. Generally these assays are applied separately on a different batch of cells, therefore how these different molecular signatures are related is often deduced by performing measurements in independent experiments with the assumption that the cells would behave the same. Moreover, these events occur at different timescales: Ca^{2+} signaling occurs within seconds of activation whereas cytokine secretion starts hours after activation. Therefore, to make direct correlations one would need to perform multiple assays on the same sample while keeping the identity of each cell for single-cell analysis. A comprehensive analysis of cell signaling requires multiplexed assays for applying a diverse range of perturbations, capturing dynamic information, and evaluating different molecular signatures at both single-cell and population level. Microfluidics is well poised to address some of the technical challenges in cell handling and fluid exchanges that facilitate the nature of input signals that can be introduced and the ability to perform multiple wash steps and staining for specific markers (*3, 69-71, 74, 77, 166, 167*). The ability to integrate multiple functional modules makes it easier to incorporate multiple assays on a single chip. So far, we have demonstrated the power of microfluidics in enabling the analysis of a large number of cells at a single-cell resolution, thus allowing cell heterogeneity to be observed. These developments have been focused on obtaining one type of readout, specifically the measurement of Ca^{2+} changes in the cell. Ideally we would want a platform that (1) allows robust single-cell handling of hundreds of cells on a small footprint to assay enough cells for population statistics to be computed, (2) enables precise perturbation of cell signaling by allowing the application of a range of stimulation modalities such as surface ligands and soluble

cues, and (3) enables the ability to perform multiple assays on the same sample of cells to allow direct correlations to be deduced. The challenges lies in having robust fluid exchanges as most assays involve multiple wash steps and buffer exchanges, and the ability to retain the biological specimen throughout the duration of the experiment.

Here, I realize the use of the integrated microfluidic platform that will enable different types of molecular signatures to be measured at different time points. This platform builds on the microfluidic system developed in Chapter 3 with addition of simplicity to device operation and the ability to perform multiple assays on the same device. The data collected includes dynamic data such as calcium signaling and static molecular signatures, thus enriching the quality of data obtained from a single experiment. The platform has the following characteristics that makes it an attractive platform for immune cell signaling studies where signaling involves a number of different molecular signatures, and dynamic signals.

1. Cell trapping capability that allows suspension cells to be kept in a defined spatial position necessary for performing live cell imaging. These cells could otherwise float out the focal plane or the field of view.
2. The defined spatial position of each individual cells then enables the live imaging data that captures the early signaling data to be correlated with smFISH mRNA and immunofluorescence staining data, thus allowing molecular signatures of cell response that occur at different time points to be measure in the same cell using multiple assays. This feature allows us to probe the signaling dynamics in T cells.

3. The high density trap enables a large number of cells to be studied simultaneously in a single experiment, thus eliminating the need to pull data from different experiments.
4. This platform is easy to use and can be placed in a cell incubator for defined periods of time depending on the duration of the stimulation. The cells remain viable in the device, with a viability comparable to the conventional well-plate format.
5. This platform enables different modes of stimulation to be applied to the cells; cells can be stimulated using soluble cues as we have previously demonstrated, and also through surface-anchored ligands. We previously demonstrated the ability to apply dynamic soluble stimulation that can enable cell response kinetics to be measured.

4.2 Materials and Methods

4.2.1 Cell Culture

Primary OT-1 spleenocytes were harvested from the spleen of an H-2K^{b} OT-1 TCR transgenic mouse that produces T cells whose TCR is specific for the chicken ovalbumin peptide (SIINFEKL), and its derived peptides. Briefly, the mouse spleen was grinded in HBSS buffer with calcium and magnesium in a cell strainer, followed by lysis of erythrocytes using a mouse erythrocyte lysis kit (R&D Systems, Cat: WL2000), and CD8+ T cells were by negative selection using Mouse CD8+ T cell Enrichment kit (StemCell Technologies, Cat:19853). Cells were suspended in R10 medium (RPMI 1640

with 2 mM L-glutamine, 10% fetal bovine serum, 0.01M HEPES buffer, 100ug/ml gentamicin, and 0.2mM 2-beta mercaptoethanol).

4.2.2 Device fabrication

The device consists of a membrane with cell trap microstructure and pores thermally bonded to a 50um chamber at the top with the bottom bonded to a coverslip. The devices were fabricated in PDMS using multilayer soft lithography techniques. Masks were designed using a computer-aid design software (AutoCAD), and printed on high resolution transparency. Master molds for the device were fabricated in SU8. Briefly, for the device layer, multilayer lithography was used to make 2, 10 and 15um features using SU8 2002 and SU8 2015, and a single layer 70um master for the top layer was fabricated with SU8 2050. The PDMS device molding is shown in **Appendix D.** PDMS (10:1) was spun on the device master to make a film of 10um thickness such that the pillar structures were protruding to make the pores in the PDMS membrane. PDMS was poured on the top layer master and partially baked for 25 minutes. Individual devices were cut out from the top layer and aligned to the device layer, followed by baking at 70 degrees overnight. Individual devices were cut out and access holes were punched, and then the device surfaces was treated with oxygen plasma to create hydroxyl groups and bonded to a coverslip.

4.2.3 Stimulating ligands and antibodies

Peptides, OVA (SIINFEKL) and VSV (RGYVYQGL) loaded on biotinylated H2-K^b MHC I were obtained from the NIH Tetramer facility. Costimulatory antibodies, anti-CD28 and anti-CD11a were obtained from eBioscience.

4.2.4 Device preparation

Tubing was connected to the access holes of the devices, and the assembled devices were autoclaved prior to use. As outlined in Appendix D the devices were primed with PBS to remove bubbles, followed by treatment to functionalize the device with specific biotinylated molecules. Biotinylated BSA (1mg/ml) was perfused at a flow rate of ~10μL/hr for one hour, rinsed with PBS, followed by streptavidin (0.5mg/ml) coupling to the biotin surface and finally biotinylated ligands such as pMHC and costimulatory antibodies, anti-CD28 and anti-CD11a (10μg/ml) were coupled to the immobilized streptavidin.

4.2.5 Calcium imaging and analysis

Cells were loaded with Fluo3-AM dye (5ug/mL) in R10 medium for 45 minutes in the cell incubator and washed twice with PBS and then resuspended in RPMI with FBS cell media without phenol red. Surface-functionalized device was mounted on the microscope stage, and a pipette tip containing the cell suspension was placed at the cell inlet. Once the field of view had been established the cell outlet tubing valve was opened and fluorescence images were captured (every 2s) once cells started flowing in the device. Images were captured for 30 minutes for each condition. All calcium imaging experiments were conducted at 37 degrees. Stacks acquired for each condition were

analyzed using a custom-made MATLAB-based software. The intensity of each individual cells was determined in all the images and normalized to the first 5 images after background subtraction. Heatmaps, and individual curves were plotted and characteristics parameters such as area under the curve and maximum peaks were determined.

4.2.6 Immunofluorescence staining on chip

For surface marker staining, cells were incubated with antibody for 45 minutes, washed with PBS then imaged on a epifluorescent microscope. Intracellular cytokine staining was used to determine cytokine production by the cells. Cells were treated with Brefeldin A in the last 4 hours of the stimulation period to prevent the secretion of the cytokines upon stimulation. Cells were fixed in 4% formaldehyde, permeabilized in chilled 100 % methanol, stained with the corresponding antibodies, and then imaged.

4.2.7 smFISH probe design and hybridization

Probes for mRNA quantification using smFISH were designed using an online software (available at: https://www.biosearchtech.com/stellarisdesigner/) by inputting the mRNA coding sequence of the molecule of interest obtained from National Center for Biotechnology Information (NCBI) database http://www.ncbi.nlm.nih.gov/guide/howto/find-transcript-gene/. The probes were 20-nucleotides long with a fluorophore tag. Here, we had IL2 and IFNγ mRNA probes tagged with Quasar 670 and TAMRA fluorophores respectively, and the probe sequences are in Appendix A.4.2. For mRNA quantification, stimulated cells were fixed in 4% formaldehyde, and permeabilized in chilled 100 % methanol. The cells were then washed

in hybridization wash buffer (2X SSC and 10% formamide in nuclease-free water). smFISH probes were pooled in hybridization buffer (0.1g/ml dextran sulfate, 10% formamide, 200 ug/ml BSA in nuclease-free water) to a final concentration of 200 nM for each probe set. Cells were incubated overnight in the probe solution, then washed with prewarmed hybridization wash buffer.

4.2.8 smFISH imaging and analysis

After hybridization, imaging anti-fade buffer (10% glucose, glucose oxidase, catalase, 2X SCC in NF-water) was loaded in the device to prevent photobleaching. Image stacks were acquired at multiple positions of the devices at 63x/1.25 NA, with a 300 nm spacing between slices, and the exposure times ranged from 0.5 – 3s on an epifluorescent microscope with a Hamamatsu Orca-D2 dual CCD camera (15 pixels per micron) To quantify the number of mRNA molecules, the number of spots in the images would correspond to the number of mRNA molecules. We used a spot-quantification algorithm to determine the number of spots for each outlined cell.

4.2.9 Statistical analysis

Unsupervised K-means clustering using a built-in MATLAB functions was performed on the calcium dynamics data for all the cells to group the cells into distinct clusters, with each cluster containing cells exhibiting similar dynamics (Appendix A.4). Principle component analysis using built-in MATLAB functions was used to group data together at a single-cell level using the calcium data (area under the curve and maximum peak) and mRNA transcript count.

4.3 Device system overview

4.3.1 Device functionality overview

We have developed a system for longitudinal single-cell analysis using image-based analytical techniques. In this platform we show the use of a microfluidic device in performing longitudinal analysis of immune cells at a single-cell resolution. We utilize the platform developed in Chapter 3 with modifications to device operation to allow for a simple platform that can be easily setup in any biology lab since minimal auxiliary equipment is required to operate the device. Figure 4-1Figure 4-1 shows an overview of the sequence of data acquisition from the cells upon stimulation. This includes time-lapse imaging to capture cellular response temporal dynamics and endpoint assays on fixed samples.

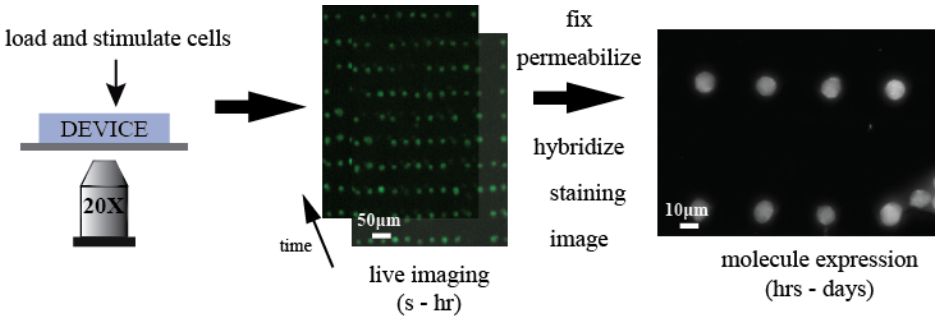

Figure 4-1 Device function overview. Cells are loaded and stimulated while monitoring changes in Ca^{2+} levels, then incubated for a defined duration of time, and can be fixed/permeabilized and stained for specific molecular signatures.

4.3.2 Device modifications and setup

The device is a 2-layer PDMS device with 2 inlets and 2 outlets. There are 2 modules on the device; the cell layer where the cells reside and the fluid layer where all the fluids into the device are introduced (Figure 4-2a,b). The device operation is relatively simple

requiring only gravity to drive the flow (Figure 4-2d, Figure 4-3). Enabled by the high density cell array that keeps the cells in defined spatial positions and robust fluid exchanges from the fluid layer, the cells can be analyzed through multiple assays such as monitoring calcium signaling, mRNA quantification and protein expression (Figure 4-2e)

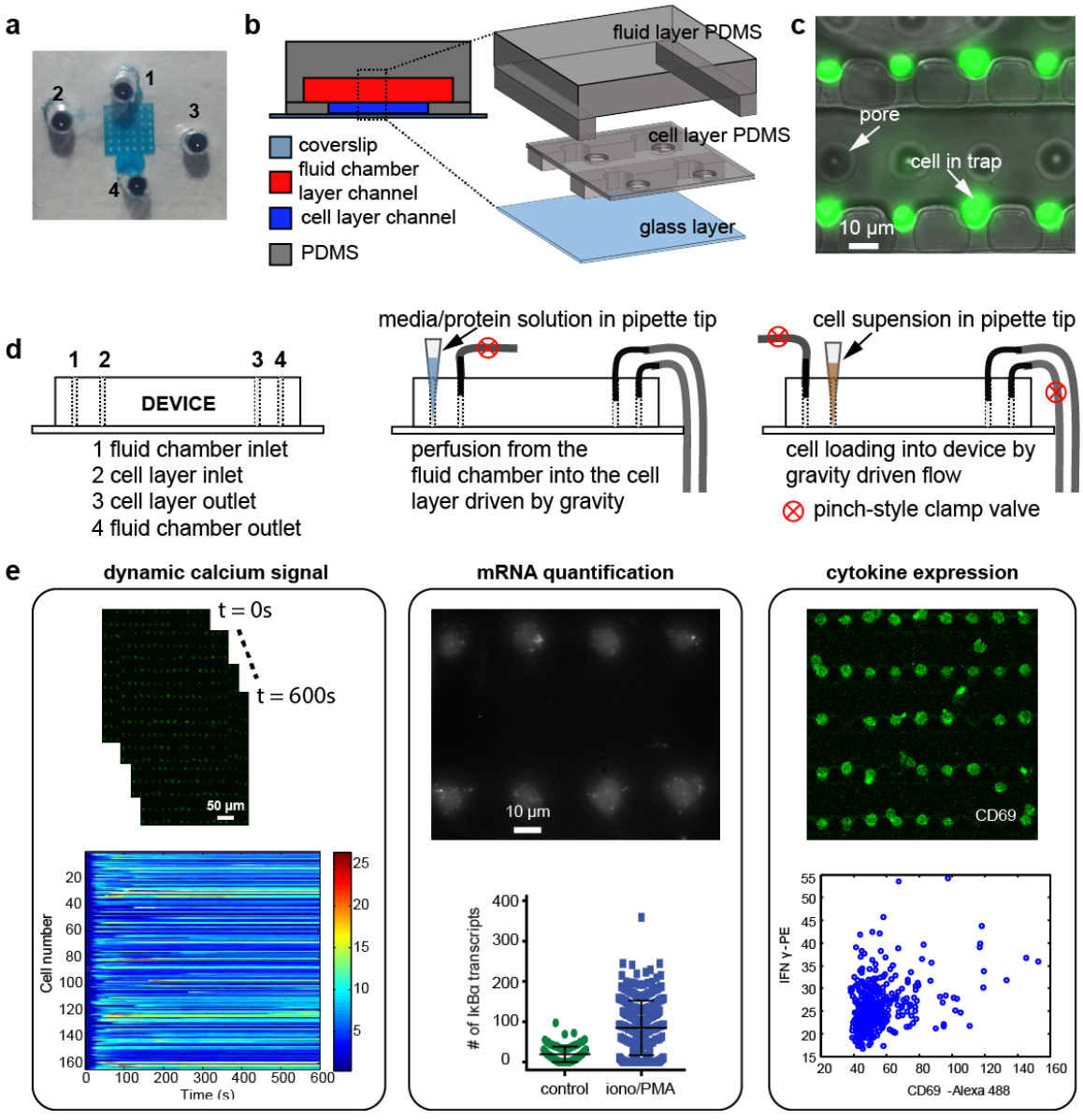

Figure 4-2 Simple microfluidic platform enables high-throughput, multidimensional data acquisition at a single-cell resolution. Schematic overview of the system operation. Microfluidic platform used for analysis of T cell signaling is a 2-layer PDMS device with

a cell trapping module and a fluid exchange chamber that facilitated fluid input using conventional pipette. (a) device filled with dye, b) cross-sectional and 3-D view of the 2-layer device, (c) top-view micrograph with cells loaded, (d) illustration of the device simplicity, solutions and cells are introduced into the device using a pipette tip as a reservoir and gravity-driven flow, and (e) illustration of the assays conducted on the platform starting with tracking of calcium dynamics inside the cell using Ca^{2+}-sensitive dyes and time-lapse fluorescence imaging, with subsequent mRNA quantification with smFISH and high-resolution fluorescence imaging and/or protein expression quantification using immunostaining and fluorescence microscopy.

In addition to enabling acquisition of multiple parameters from the same sample, the simplicity in the setup and operation would make this platform to be easily transferable to other laboratories. To operate the device minimal auxiliary equipment is required. As shown in Figure 4-3a, the chip requires tubing, a syringe and a pipette to be setup, and these are readily available in many laboratories. The flow driving force is gravity that eliminates the use of other complex pressure sources or syringe pumps. All the solutions are introduced in the device are in a pipette tip reservoir place at the inlet.

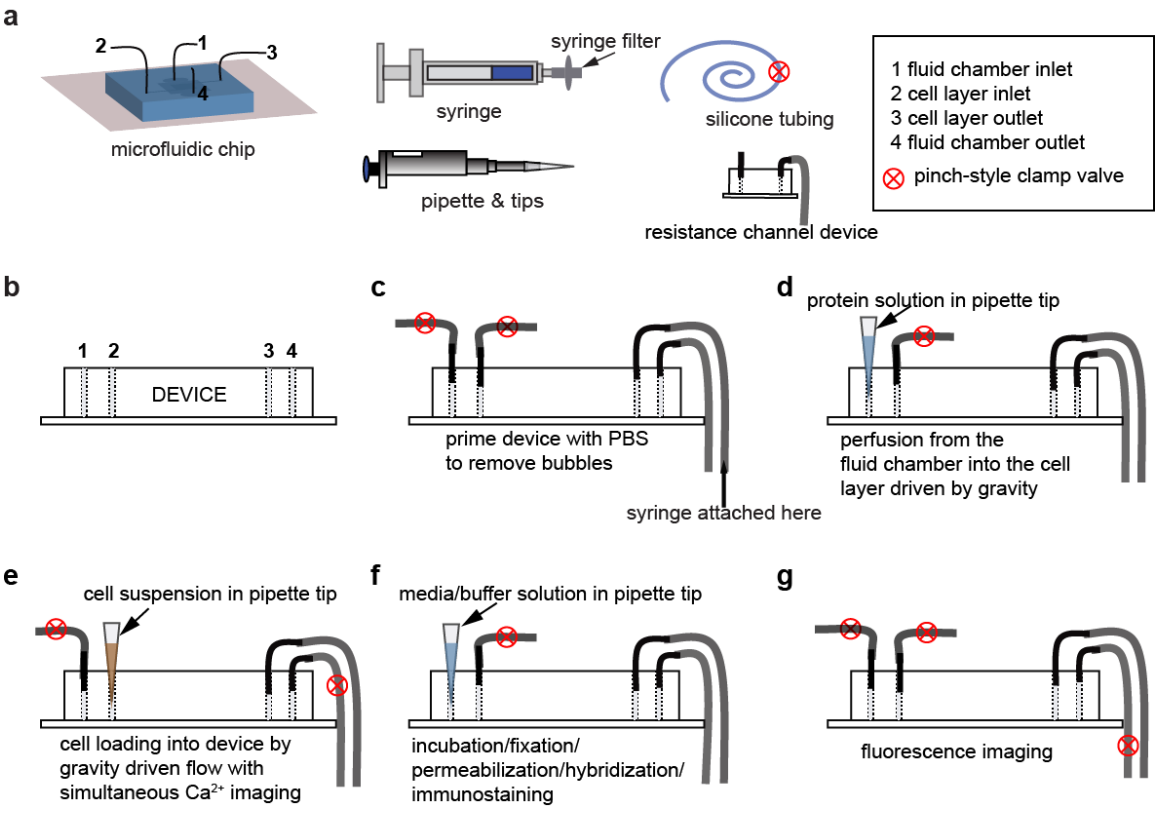

Figure 4-3 Device operation is simple and requires minimum auxiliary equipment. (a) microfluidic chip and all the required materials for running the device, and (b-g) sequence of operation from cell loading to analysis on the same chip. (b) the device cross-section outline showing the inlets and outlets of the cell layer and the fluid layer, (c) a syringe filled with PBS is connected to the outlet of the fluid layer, and thumb pressure is applied to remove bubbles from device, (d) protein coating step where aa pipette tip containing the protein solutions is placed at the fluid layer inlet and the solutions perfuse into the device via gravity-driven flow, (e) once the device is mounted on the microscope stage, a pipette tip containing the cell suspension at the cell layer inlet. Cells are loaded into the device using gravity-driven flow with simultaneous fluorescence imaging to track the Ca^{2+} dynamics, (f) cells are incubated for a defined time by placing the devices in the cell incubator. For long-term incubation (> 4 hours), media is perfused through the fluid layer, and a resistance channel is connected to the outlet to control the flowrate of the media to ~ 10 µL ml^{-1}, (g) device setup for imaging.

The device can be placed in a cell incubator after the Ca^{2+} live imaging for a defined duration of time with media being perfused from the fluid layer for long-term incubation. The average flow rate from the top layer during the protein coating and media perfusion

is ~ 20 μL hr^{-1}. The low flowrate is achieved by having a resistance channel attached to the outlet of the fluid layer since the fluid layer has very low fluid resistance as described in Chapter 3.

4.3.3 Device surface functionalization

In Chapter 3, we developed this 2-layer PDMS platform for soluble cue delivery. Here, we use the same approach demonstrated in Chapter 2 to functionalize the surface with surface molecules of interest. We use physisorption of biotin-BSA and streptavidin and biotin coupling to anchor the stimulatory ligands to the surface. Therefore, we can now use this platform to perturb the cells with both dynamic soluble cues and surface-anchored molecules. The surface-anchored molecules are a mimicry of the cell-cell receptor/ligand interactions in vivo. In Figure 4-4 we show the setup of the device during the protein modification process, where the flow in the device is driven by gravity. We used texas-Red-tagged BSA to demonstrate the physisorption of BSA and biotin-FITC to visualize the coupling of a biotin-tagged molecule to streptavidin as shown in Figure 4-4c.

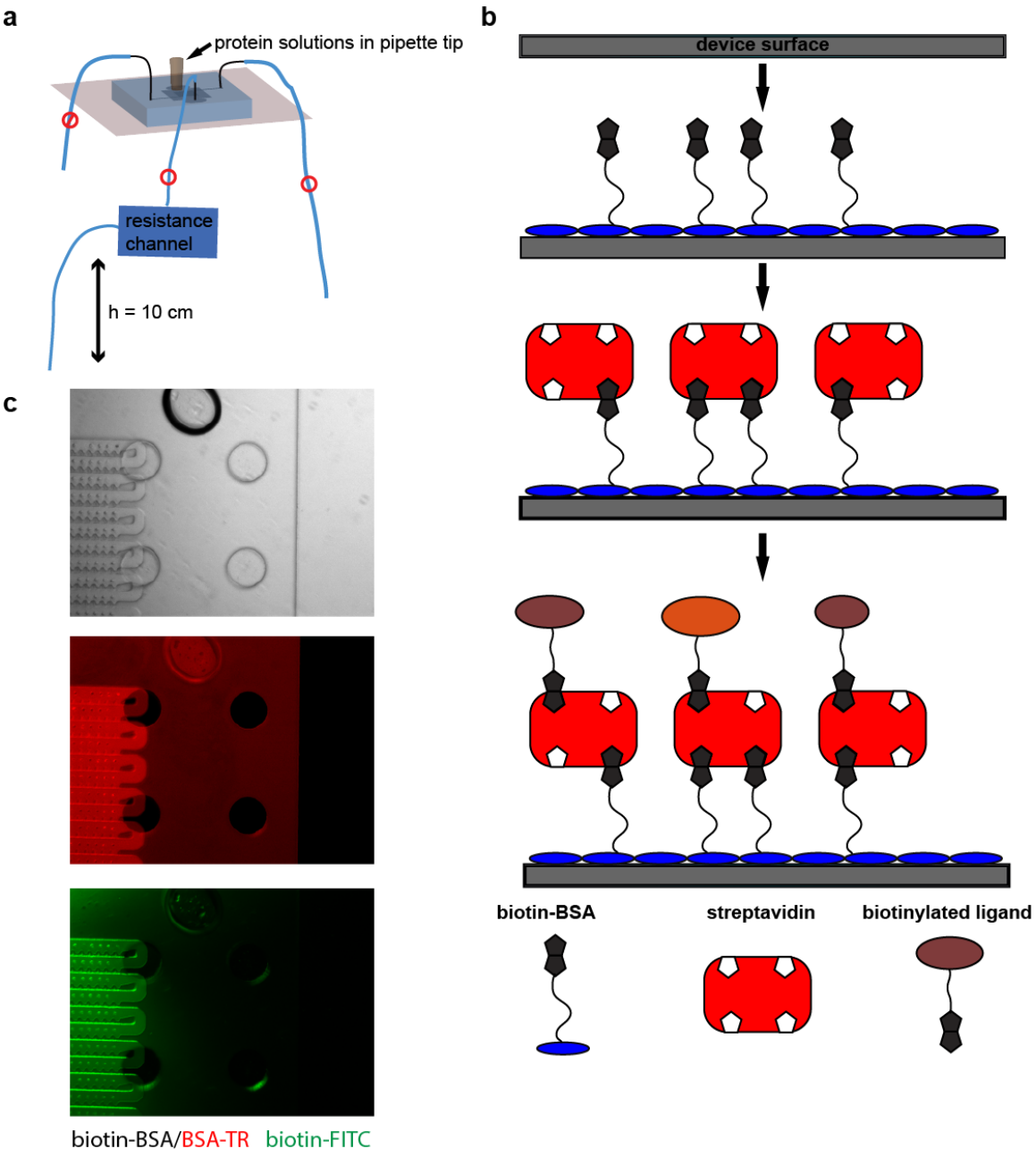

Figure 4-4 Device surface modification using protein physisorption and biotin-streptavidin coupling. (a) illustration of device configuration during the functionalization process, a pipette tip filled with the protein solution is placed at the fluid chamber inlet and the flow is driven by gravity, (b) sequences of the protein functionalization process, and (c) brightfield and fluorescent micrographs showing the device and fluorescence of BSA-Texas Red and biotin-FITC used to verify the protein functionalization sequence.

4.3.4 Cell viability on chip

The cell viability was tested in the device using the Jurkat hybridoma cell line. Because of the interest in performing longer incubation times of 2 – 24 hours, we wanted to ensure that the cells remained viable on chip. Figure 4-5 shows comparable viability of the cells cultured overnight in a multiwell plate and on chip and the viability was maintained above 90 %. This demonstrates that our microfluidic platform is capable of maintaining a healthy cell culture for the duration of our experimental studies.

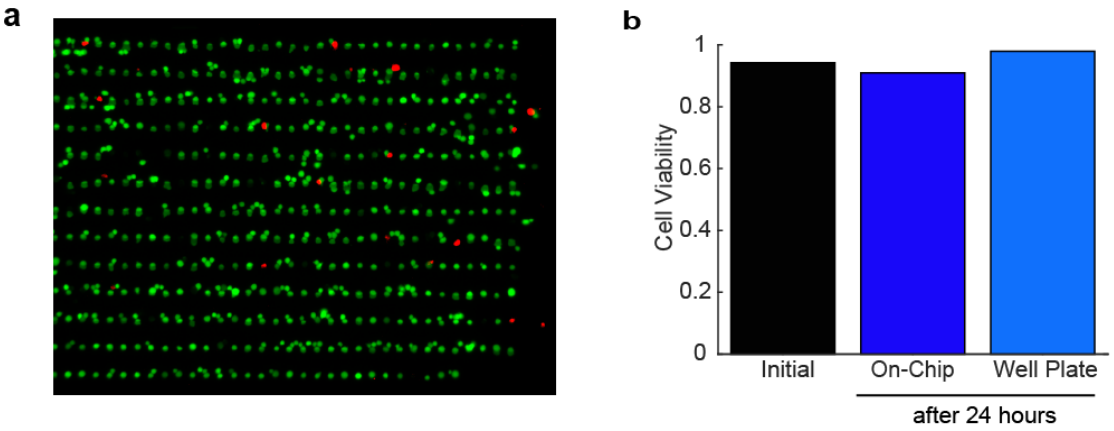

Figure 4-5 Viability in microfluidic platform and multiwell plate. Cells can be incubated in the device with comparable viability to off-chip conventional cell culture methods. (a) micrograph of cells stained with the live (green)/dead (red) fluorescent dye, and (b) cell viability before seeding and after 24 hour incubation on- and off-chip

4.4 Performing single-molecule fluorescence hybridization on chip

4.4.1 mRNA quantification using smFISH

Single-molecule Fluorescence In-Situ Hybridization (smFISH) is used to quantify individual mRNA transcripts in intact cells. The technique utilizes multiple (20-50), fluorescently-labeled 20-bp oligonucleotides to target different regions of the same mRNA (***Figure 4-6***). Each oligonucleotide has a fluorophore attached to its 3' end. The

binding of multiple oligonucleotides to different positions on the same target mRNA appear as individual spots in high magnification fluorescent images (*168-170*). Therefore, the number of mRNAs is determined by counting the number of spots in the image. Images are acquired as 3-dimensional z-stacks to enable the detection of all mRNA spots. Compared to other mRNA determination techniques such as RT-PCR, smFISH allows mRNA to be quantification in intact cells, therefore the spatial information of the mRNA transcripts can be obtained, and the mRNA quantification is at a single-cell level. In addition, smFISH enables mRNA copy number count without any amplification bias. However, because smFISH is a fluorescence imaging-based technique the number of different transcripts that can be analyzed in a single cell is limited to 3-4 on most microscope setups due to spectral overlap. Approaches that uses multiplexing, and spatial, and spectral barcoding have a potential in increasing the number of different molecules. Using super-resolution microscopy and combinatorial labeling, Lubeck and Cai were able to increase the number of mRNA species assayed simultaneously up to 30 species (*165*). Recently, Chen et al introduced multiplexed error-robust FISH (MERFISH), a technique that increases the number of species that can be analyzed using FISH up to thousands of RNA by implementing combinatorial labeling, multiple rounds of hybridization and encoding schemes for editing and error reduction (*164*). This elevates smFISH to a technique that can be utilized in system-wide analysis. In addition, the detection of mRNA in intact cells also enables other molecules such as protein expression to be analyzed in combination with smFISH, thus enriching the data that can be obtained from a biological specimen.

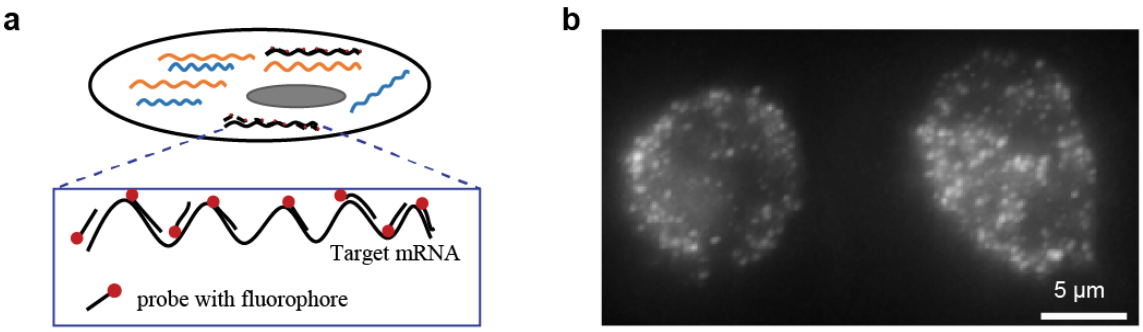

Figure 4-6 smFISH enables the direct quantification of mRNA copy numbers with spatial information. (a) Short (20-base pair) complementary DNA oligonucleotides are hybridized to the target mRNA sequence, and (b) a maximum projection fluorescence image taken at 63x magnification showing the bright, diffraction-limited spots with each spot representing an individual mRNA molecule.

Previous studies have demonstrated how smFISH is a powerful tool in mRNA quantification (*168-170*) and has great potential to be used to quantify up to hundreds of different mRNA molecules (*164*). However, this technique has been largely limited to applications on intact tissue or whole small organisms and adherent mammalian cells placed on coverslips. Applications on suspension-based cells are challenging as significant cell loss can occur during the multiple wash and centrifugation steps involved, and also the difficulty in placing the samples for imaging. Recently, Bushkin et.al. demonstrated the application of smFISH on suspension, immune cells, but used flow cytometry instead of the standard fluorescence microscope imaging used in smFISH (*163*). Here, we have demonstrated the application of smFISH for RNA quantification in T cells after antigenic activation. Being able to confine suspension cells in defined positions combined with robust fluid exchanges allows smFISH to be applied to suspension cells with ease, and for image-based analysis to be conducted. In addition, in

our platform we can also perform live imaging on the same sample allowing direct correlations between Ca^{2+} dynamics and mRNA expression to be elucidated.

Even though smFISH can provide a powerful and quantitative tool for mRNA analysis, it is limited to analyzing cells with low RNA copy numbers, and the number of different mRNA copies analyzed is limited by the spectral overlap. With high copy number mRNA molecules RT-PCR can be used.

4.4.2 mRNA spot quantification

As described the number of mRNA molecules is determined by counting the number of spots in the image for each cell. The spots are easily detectable by eye (***Figure 4-6***b), however manual counting would be tedious as that would involve counting through stacks for each cell. We use the FISH-QUANT Matlab-based software developed by Mueller et al (*171*). The software automatically detects and quantifies the number of spots 3D images, which greatly facilitates the image processing of the large data sets that are obtained in our studies.

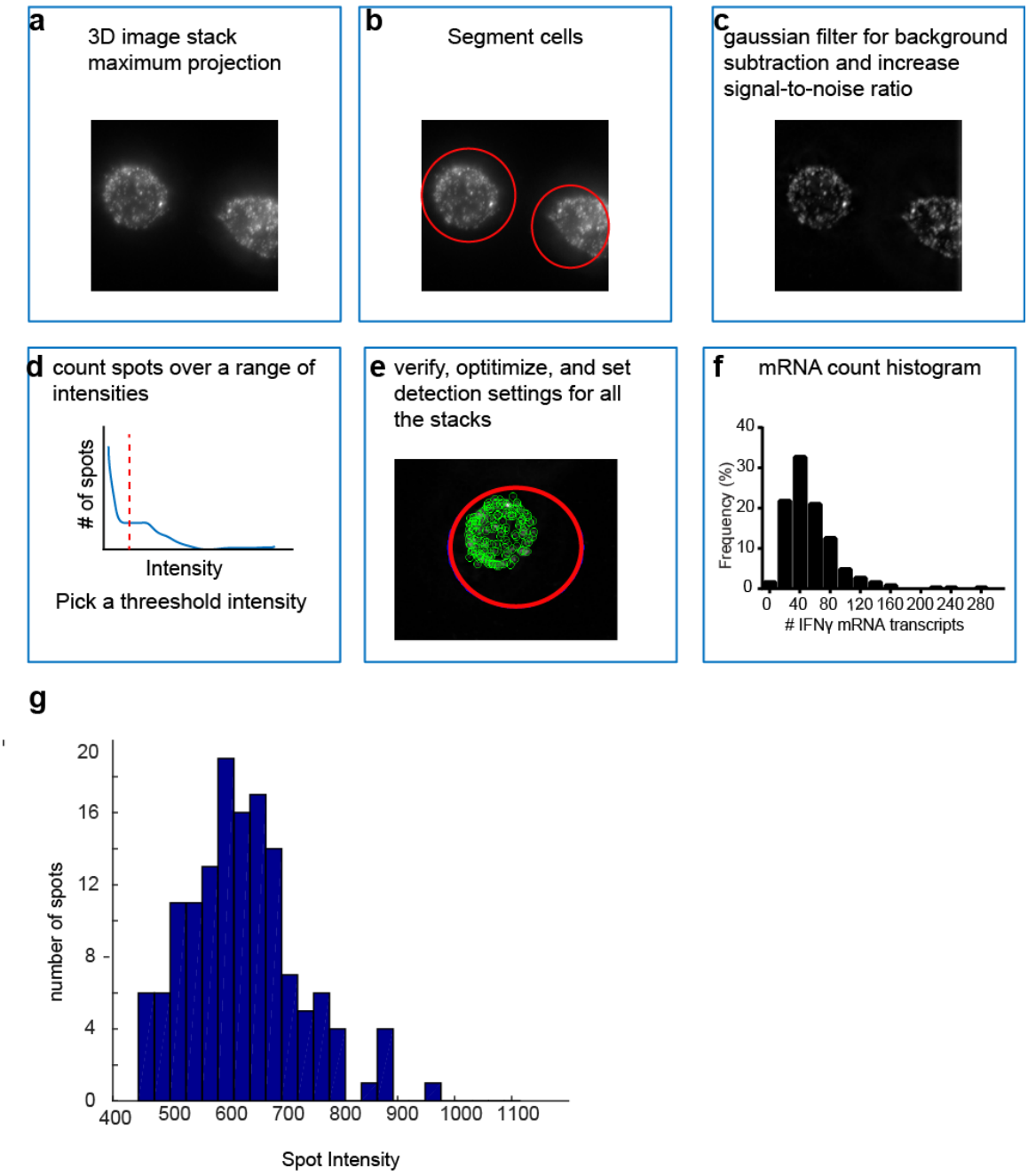

Figure 4-7. Automated spot quantification using FISH-Quant Software. smFISH quantification was performed using a Matlab-based algorithm. (a) example 3D stack, (b) user-defined cell outlines, (c) Gaussian filtering to enhance the signal-to-noise ratio. Background signal is subtracted from the image, and the image signal is smoothed with a small Gaussian kernel, (d) the number of spots in one selected cell is computed over a range of user-defined intensities. Plotting the number of detected spots against intensity, the number of detected spots goes from infinity then plateaus before declining to zero. The intensity threshold is picked to be an intensity when the number of detected spots is invariant with the intensity changes, (e) The threshold intensity is applied to all the cells in the image stack and the number of spots are computed. The spots detected are then

visualized to verify accuracy and the detection setting can be altered to improve the accuracy of spot detection. After the detection settings have been optimized, the detection settings are applied to all the image stacks for the experiment (typically 50 – 100 stacks per experiment), and (f) the mRNA transcript distribution for a population of cells, and (g) observed intensity distribution showing that the intensity of the spots is relatively invariant, and therefore very little impact on the detection of the spots.

In the future, algorithms that enabled automated cell detection in bright field images would reduce the image processing time for large data sets. The current algorithm relies on manual annotation of cell masks that can be time-consuming when handling large data sets as is the case in the analyses performed in this study.

4.4.3 Application of smFISH on Jurkat cell line

In the context of immune cells, smFISH could provide an additional technique for analyzing cell response to stimulation. Antibody staining with flow cytometry detection of expression levels is the one of the main techniques used in analyzing immune cell response. However, the analysis is limited by antibody availability whereas in smFISH only the sequence of the target mRNA is required to design probes for detection, and the probes are synthesized with established protocols commercially. In addition, detection of mRNA is much faster than protein expression changes, therefore allowing for more rapid assays to be developed for the detection of immune cell response to infection.

To test our ability to perform smFISH on individual cells in our device, we analyzed changes in IκBα mRNA expression in Jurkat cells after stimulation with cytokine TNF-α or ionomycin/PMA. In the resting state, IκBα keeps NFκB sequestered in the cytoplasm. Upon cell stimulation, IκBα is phosphorylated and subsequently degraded. The NFκB is

released and translocates into the nucleus where it drives the transcription of a number of genes including IκBα (***Figure 4-8***). NFκB activation results in an increase in IκBα mRNA expression.

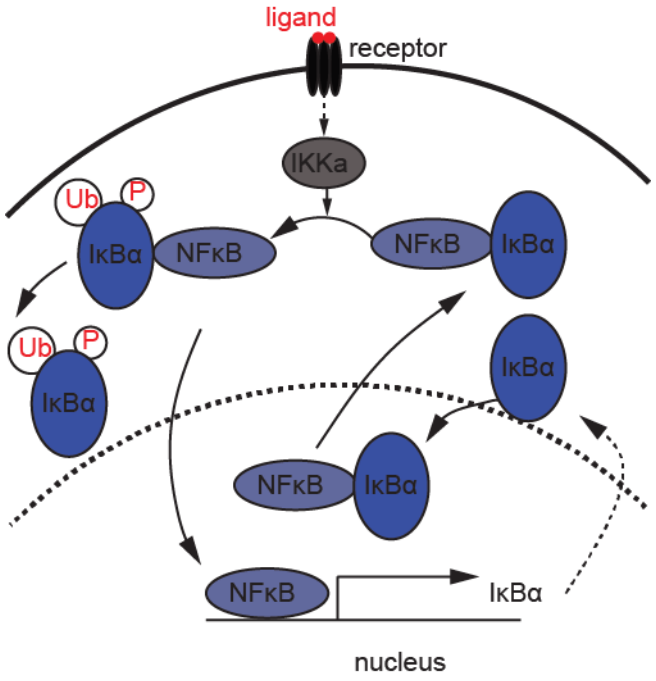

Figure 4-8 Simplified NFκB/IκBα pathway. In the resting state, IκBα keeps NFκB sequestered in the cytoplasm, and when the cell is activated, IκBα undergoes phosphorylation-initiated degradation allowing the NFκB to enter the nucleus where it drives the transcription of many genes including IκBα thus resulting in an increase in IκBα mRNA expression within 30 minutes of activation.

Cells were stimulated on chip then fixed, permeabilized and hybridized on chip. 3D z-stacks were obtained at multiple positions of the device. ***Figure 4-9***a shows a micrograph of the cells in the device with nuclear stain imaged in the green channel, and the transcript in the red channel. The number of spots in each cell was computed, and as expected there was an increase in IkBα expression upon stimulation with either ionomycin/PMA or TNFα (***Figure 4-9***). In addition, the data also shows that the mRNA expression is heterogeneous even though the cells are genetically identical.

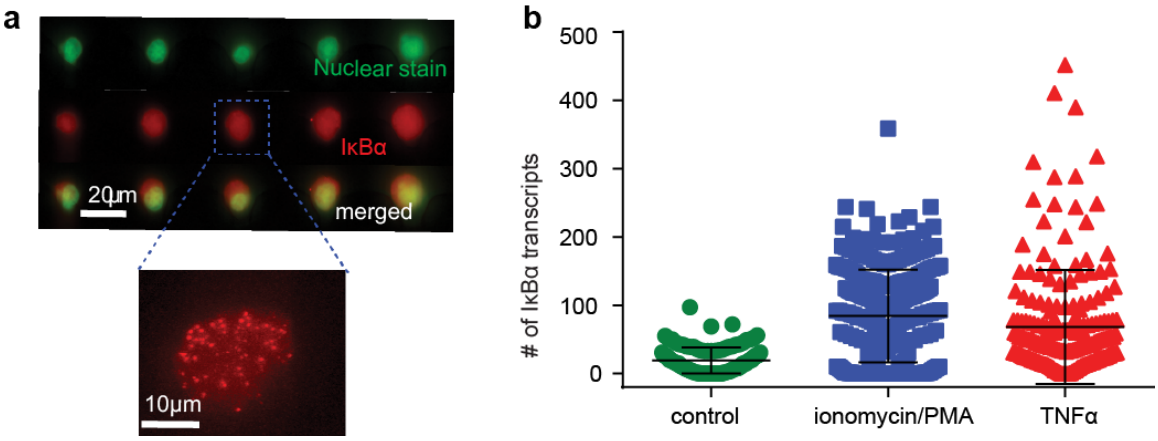

Figure 4-9 Heterogeneity in mRNA expression levels in Jurkat cells. Cells were stimulated on-chip with ionomycin/PMA or TNF-α for one hour, then fixed and permeabilized overnight followed by hybridization with IkBα mRNA probes. (a) micrographs of the cells showing the nuclear stain (green), and probe imaging (red) at 40x magnification and the insert image at 63x during smFISH imaging, (b) distribution of mRNA copy number in each cell for unstimulated cells (control) and cells under stimulation. Overall, there is an increase in IkBα expression after stimulation, and cells show a distribution in their expression levels.

4.4.3.1 Repeatability of assay

We wanted to ensure that our assay was repeatable to allow for comparison of data from different days. We performed smFISH on cells stimulated with TNFα (10 $ngml^{-1}$) where the experiments were done on different days. We show that the cell populations show a similar distribution in mRNA expression levels with the heterogeneity in cell response evident in all the 3 trials that were performed (***Figure 4-10***).

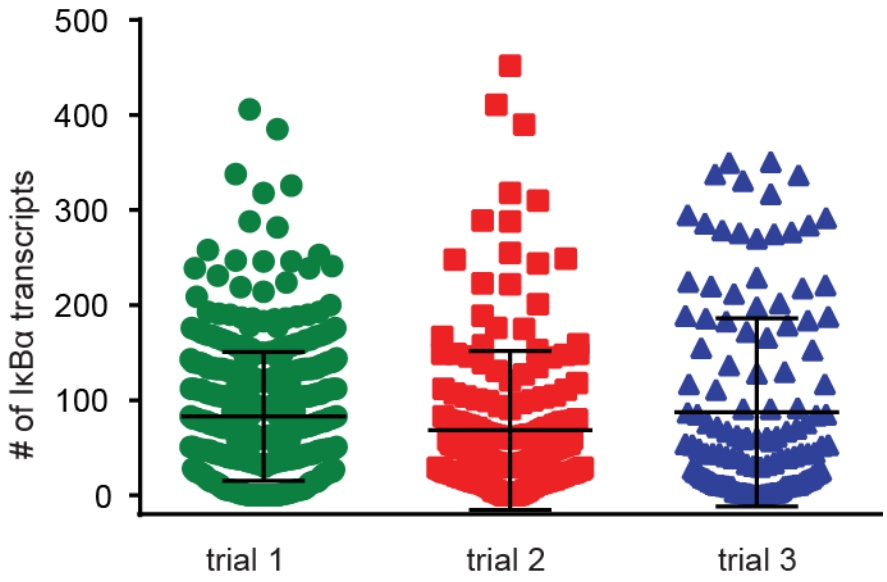

Figure 4-10 The assay is repeatable on chip. Jurkat cells were stimulated with in separate experiments conducted on different days. Quantification of the IκBα mRNA expression who is similar distribution of expression level in 3 trials (n = 400+ for each trial)

4.4.3.2 Combining with CA^{2+} imaging with smFISH imaging for mRNA level characterization

Implementing smFISH on chip allows for easier handling of cells, and minimizes cell loss due to the number of wash steps that are involved in the process. In addition, this approach makes it easier to image the cells, the cells sit directly on the coverslip which is compatible with high resolution imaging. In addition, the cells are in a closed chamber that eliminates the challenges with controlling evaporation of liquids from the sample during mRNA hybridization and imaging. Previous we show how we can perform Ca^{2+} dynamic measurements at a single-cell resolution. Therefore, we sought to combine the Ca^{2+} dynamics measurements with the mRNA quantification. We used the Ca^{2+}-sensitive dye Fluo-3 to monitor Ca^{2+} dynamics. Cells were stimulated with ionomycin/PMA or imaged without any stimulant as a control. As observed previously, the cells flux Ca^{2+} when stimulated with some cells responding more strongly than others (***Figure 4-11***a,b).

We wanted to find out the relationship between the Ca^{2+} response and the mRNA expression level on a single cell level. Therefore, we subsequently hybridized the cells after the imaging determined the IκBα expression level (***Figure 4-11***). With increasing ionomycin/PMA concentration, more cells had a higher mRNA expression level (***Figure 4-11***c). With the spatial position of the cells, we were able to match the Ca^{2+} traces to the corresponding mRNA count. In ***Figure 4-11***d, we show the maximum Ca^{2+} peak reach and the mRNA transcript count. In here we do not observe a correlation between the Ca^{2+} peak and the mRNA expression level, however this study demonstrates the ability of our platform to make direct comparisons of parameters obtained from different assays on a single-cell resolution.

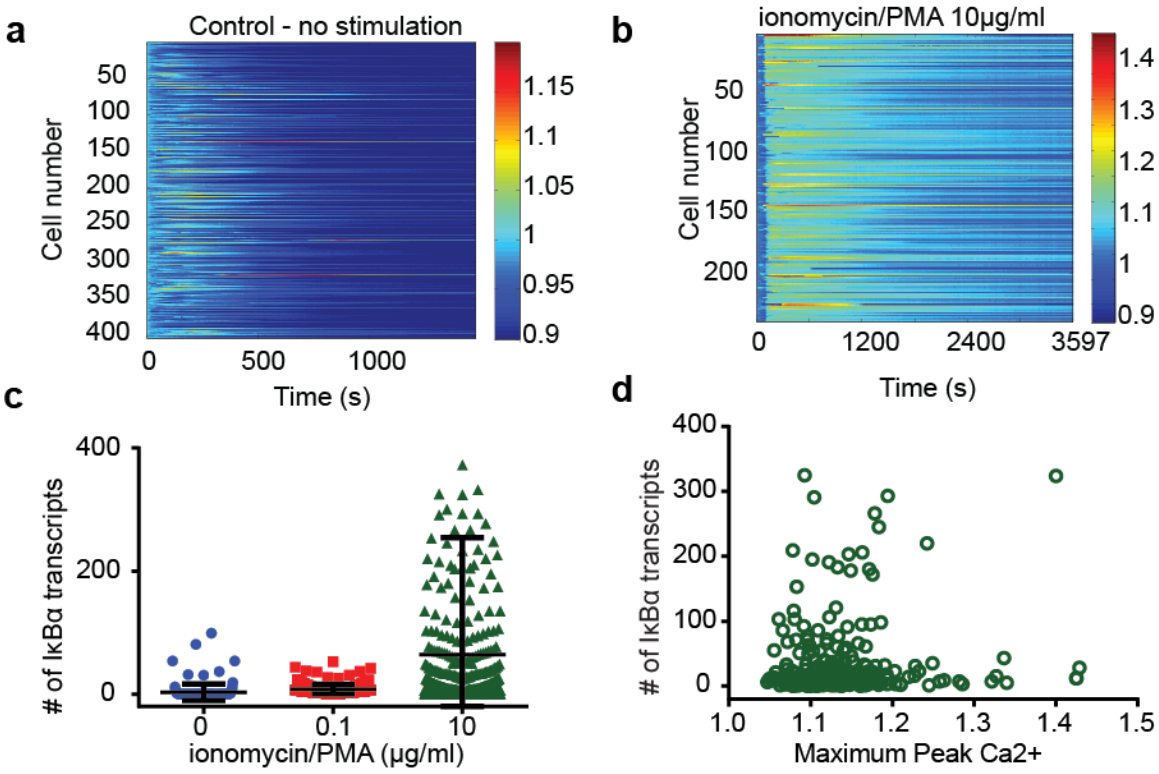

Figure 4-11 Combined Ca^{2+} and IkBα mRNA quantification on chip. Fluo3-loaded Jurkat cells were loaded on the device, and stimulated with ionomycin/PMA or no stimulation in the buffer while monitoring changes in Ca^{2+} by fluorescence imaging for 1 hour. (a) Ca^{2+}

traces for the cell where only buffer was introduced, the cells show no appreciable increase in Ca^{2+} levels, (b) upon introduction of ionomycin/PMA the cells show a rapid increase in Ca^{2+} followed by a plateau (blue is low Ca^{2+} and red is high Ca^{2+}), (c) after Ca^{2+} imaging the cells were subsequently fixed, permeabilized and hybridized with IκBα mRNA. The transcript levels for the cells under different stimulations, the error bars show the standard deviation from the mean indicated by the horizontal line for each condition, and (d) with the spatial information of the positions of the cells in the device, number of transcripts can be directly compared to the Ca^{2+} dynamics.

4.5 OT-1 T cell activation to demonstrate longitudinal cell analysis with multiple assays

Having optimized our system for image-based assays, we wanted to demonstrate the applicability of our platform in evaluating multiple parameters in immune cell response of primary immune cell. This provides an application relevant to the immunology field and mimics some of the physiological environment that the T cells encounter to mount an immune response. In this application we use the OT-1 transgenic mouse T cells harvested from the spleen. These T cells are reactive to ovalbumin peptide, OVA. In chapter 2, we show the Ca^{2+} flux the cells exhibit when they are exposed to a surface bearing the pMHC and costimulatory molecules that interact with CD28 and LFA-1. Here we further characterize more proximal phosphorylation signaling events and downstream signaling signals that include cytokine mRNA expression and protein secretion, and surface marker expression.

4.5.1 Protein phosphorylation events propagate TCR signaling

Protein phosphorylation events are key in T cell activation (*11*). Upon TCR-pMHC engagement, activated Lck on the coreceptor phosphorylates ITAMs on the CD3ζ chains leading to the recruitment of ZAP70 to the plasma membrane. ZAP70 is activated

through phosphorylation of Tyr 315, Tyr 319, and Tyr 493 by Lck. ZAP 70 then phosphorylates LAT and SLP-76. LAT and SLP-76 then signal a number of downstream processes including the production of IP3 from PIP2, and IP3 binds to the IP3 receptor on the ER membrane activating the release of Ca^{2+} from the intracellular stores. In addition LAT is involved in the pathway leading to Erk phosphorylation and Erk drives the transcription of many genes including IL-2 gene.

4.5.2 Coagonism in T cell activation

The role of CD4/8 coreceptor signaling has been of great interest, and has been shown to amplify T cell signaling through the TCR (*6, 172-176*). While the role of CD4 is unclear and has been shown to have very little to no effect on T cell signaling, the absence of CD8 has been shown to alter T cell activation (*177*). The CD8 coreceptor binds to the invariant α3 chain of the MHC molecule, and it is connected to the TCR/CD3 complex via the cytoplasmic domain. The Lck associated with the coreceptor molecule facilitates phosphorylation of the CD3ζ chains that then leads to a cascade of protein phosphorylation events including the recruitment and phosphorylation of ZAP-70. The CD8-MHC interaction kinetics has been shown to vary among different MHC alleles, and also with different T cells for the same MHC allele (*137*). However, the CD8-MHC interaction does have a lower affinity compared to the TCR-pMHC interaction. In addition, during TCR-pMHC interaction with an agonist, the CD8 coreceptor can interact with the MHC of the nonstimulatory/self pMHC that are more abundant on the cell surface leading to an enhanced T cell signaling. This has been termed coagonism where the presence of a nonstimulatory pMHC enhances the activation of a T cell upon

interaction with a cognate (agonist) pMHC. Previous studies have shown that in the presence of both the agonist peptide and a nonstimulatory peptide, T cells show increased CD69 expression and IL-2 secretion compared to having only the agonist peptide (*172*, *178*). These observations shed light on the role of endogenous peptide in amplifying T cell signaling. In addition to coreceptor contribution to T cell signaling, other costimulatory molecules such as LFA-1, CD28, CD45, CD2 and CTLA-4 are important to ensure a productive signal and complete T cell activation. Without costimulation, T cell can undergo deletion, become anergic or develop immune tolerance.

In this study, we analyze the effect of coagonism in TCR-mediated T cell signaling by measuring both proximal (Ca^{2+} flux and phosphorylation) and distal signaling events (cytokine mRNA and secretion) in the same cell sample.

4.6 Combined Ca^{2+} analysis and ZAP-70 and Erk phosphorylation

Our initial analysis involved analyzing the first 10 minutes of activation. Here we draw insights that can be deduced from the proximal signaling events by evaluating Ca^{2+} flux and ZAP-70 and Erk phosphorylation. To evaluate the effect of coagonism, OT-1 spleenocytes were activated on antigenic OVA pMHC- coated surfaces with and without coagonist, VSV, and also with coagonist only. VSV is nonstimulatory to OT-1 T cells. As shown before, we observe a rapid Ca^{2+} flux for T cells on OVA surface (Figure 4-12a,b). In the presence of coagonist peptide, rapid Ca^{2+} flux is observed even though the density of OVA on the surface is reduced 4-fold. The T cells on VSV surface showed no Ca^{2+} flux, supporting the previous findings that the coagonist peptide is nonstimulatory. From Figure 4-12d, the average response show that the presence of coagonist amplifies the

Ca^{2+} signal, an interesting finding given that the number of OVA molecules in the OVA/VSV experiment is reduced compared to the OVA only experiment. In addition, analyzing the individual Ca^{2+} traces, we extracted the area under the Ca^{2+} curve and the maximum Ca^{2+} peak, we observe that the coagonist results in more cells that have a higher Ca^{2+} lebel (***Figure 4-12***e,f).

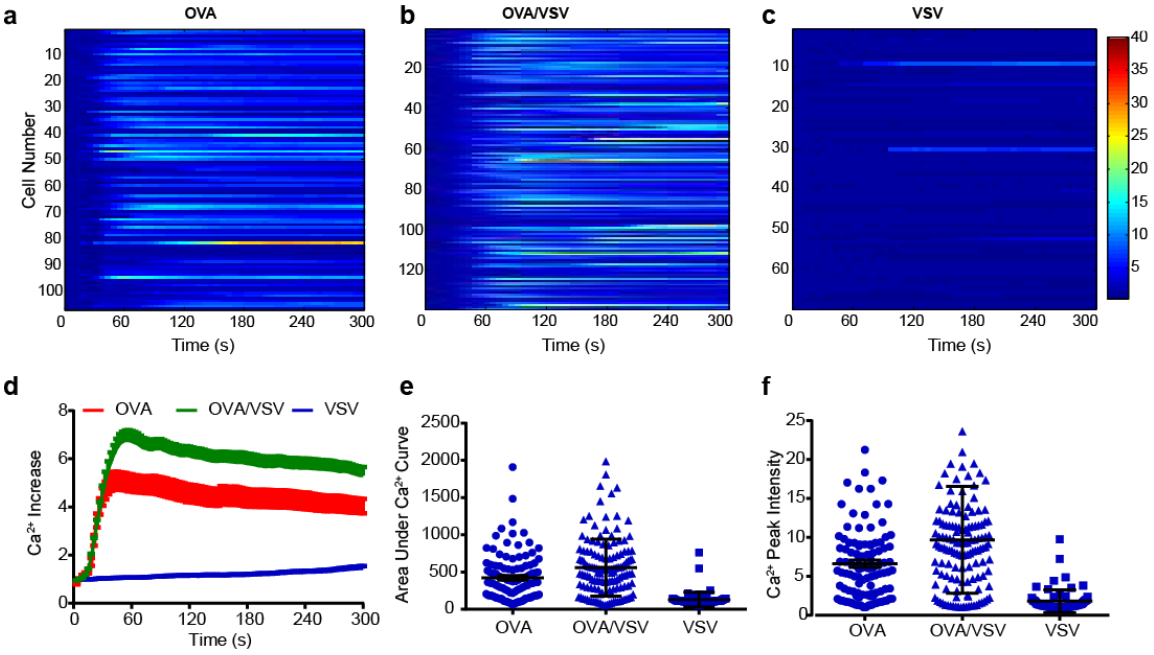

Figure 4-12 Coagonist, VSV amplifies Ca^{2+} signaling OT-1 T cells stimulated with agonist OVA. OT-1 spleenocytes are activated pMHC surfaces while simultaneously measuring Ca^{2+} flux. The cells were activated on surfaces coated with (a) OVA, (b) OVA/VSV, (c) VSV. The cells show no change in calcium on VSV peptide, and rapid Ca^{2+} flux with OVA antigenic peptide. However the presence of OVA/VSV peptides results in some cell that have a much higher Ca^{2+} level compared to the cells on OVA surface only. (d) average Ca^{2+} response show a higher Ca^{2+} level with the coagonist, and (e) and (f) show the area under the curve and the maximum Ca^{2+} peak for the individual cells showing that coagonism increases the number of cell with higher levels of Ca^{2+} responses. The mean for each condition is represented by the horizontal bar and the vertical bar represents the standard deviation.

Next we asked how the coagonism might affect the propagation of TCR signaling by analyzing phosphorylation Erk, which is downstream of Ca^{2+} and also ZAP70 which occurs earlier in the TCR signaling cascade and also activates Erk. After Ca^{2+} measurements, the cells were fixed and permeablized and then stained with antibodies against phosphorylated ZAP70 and Erk on chip. Images were acquired and the intensity levels were measured for each cell. Figure 4-13 shows a representative micrographs of the pErk imaging. As expected, the nonstimulatory ligand, VSV shows lower intensity levels for both ZAP70 and Erk. The OVA-stimulated T cells showed a wider distribution with a fraction of cells having intensity values similar to those of VSV. These cells are likely to not have propagated the TCR-mediated signaling. In addition, the OVA condition show a positive correlation between pZAP70 and pErk. This observation is consistent with one of the proposed models where ZAP70 activates LAT and LAT activates the Erk pathway.

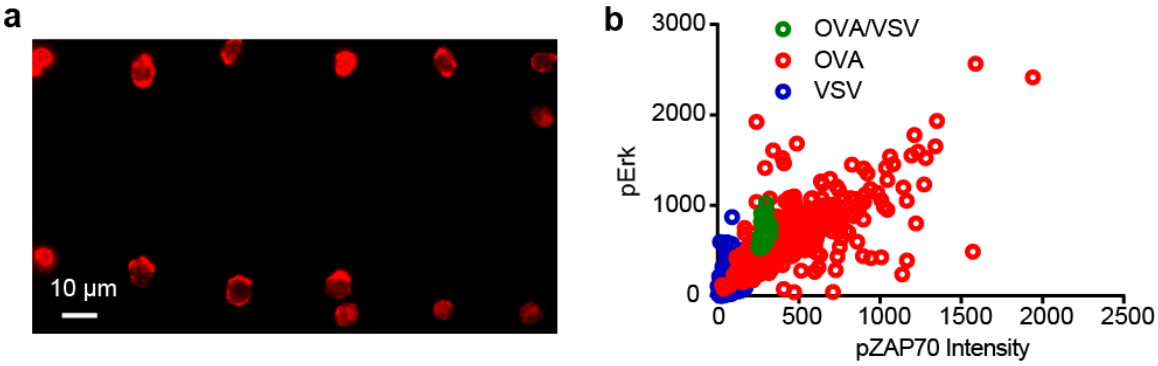

Figure 4-13 Effect of coagonism on pZAP70 and pErk. After Ca^{2+} measurements the cells were fixed, permeabilized and stained against phosphorylated Erk and ZAP-70. (a) fluorescent image of anti-pZAP70, and (b) phosphorylation levels of ZAP-70 and Erk in cells stimulated with antigenic peptide, OVA, antigenic peptide OVA in the presence of coagonist peptide VSV, and only coagonist VSV.

Next, we made single-cell correlations of the Ca^{2+} data with the phosphorylation data. Looking at the OVA-stimulated cells, Figure 4-14a show cells that had high pZAP-70 but low Ca^{2+} levels that may be indicative of lack of signal propagation. This is in contrast to the coagonist condition where pZAP-70 low, and high Ca^{2+} level was observed (Figure 4-14b). The low level of ZAP-70 phosphorylation may be attributed to the fewer number of OVA molecules on the surface. In the setup, the number of MHC molecules is identical in all setups, therefore with the coagonist the OVA density is lower. Coagonist only did not result in appreciable ZAP-70 phosphorylation. Similarly the same trends were obtained for Erk phosphorylation where in OVA-stimulated cells a fraction of cells show cells with low Ca^{2+} and high pZAP70. In the presence of a coagonist the Erk phosphorylation is loosely dependent of Ca^{2+} level. So far, we correlated the static parameters of phosphorylation events to a single parameter (Ca^{2+} peak intensity) of the Ca^{2+} dynamics. However, Ca^{2+} peak does not give a full picture of the Ca^{2+} dynamics. Other parameters such as area under the curve, the time the cell takes to response, and time to reach a percentage of the maximum response can also be used to describe the signaling events. In addition, unsupervised clustering algorithms may be used to group cells that have similar dynamics.

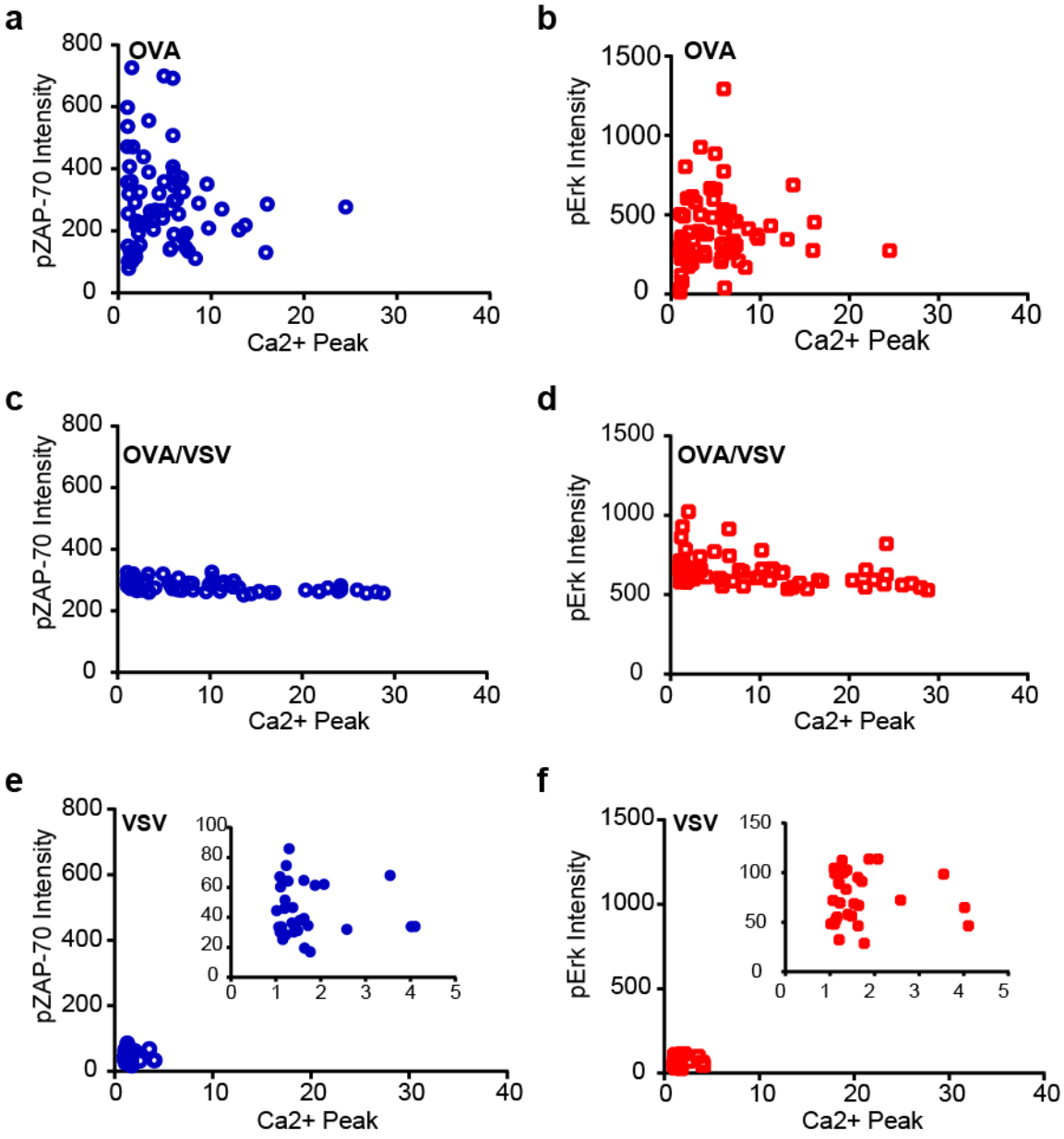

Figure 4-14 Correlation of Ca^{2+} signaling parameters and Erk and ZAP-70 phosphorylation. The maximum peak for each Ca^{2+} trace was deduced from the Ca^{2+} data, and then matched to the corresponding pZAP70 and pErk intensity for the three stimulating conditions; agonist (OVA), agonist/coagonist (OVA/VSV), and coagonist (VSV). (a-c) Ca^{2+} correlations with ZAP70 phosphorylation, and (d-f) Ca^{2+} correlations with Erk phosphorylation.

It is important to note is the dynamic nature of pZAP70 and pErk that might affect the analysis and insights obtained from these studies. Future work would include analyzing these phosphorylation events at different time points.

4.7 Ca^{2+} and cytokine IL-2 and IFNG mRNA expression levels determination

Detection of cytokine mRNA in immune cells could potentially be more insightful and complement cytokine secretion measurements. The short-lived nature of RNA compared to protein ensures that measurements made are a result of the stimulation and not due to prior conditions the cells were exposed to (*163*). In addition, with mRNA detection no pretreatment of the cell with protein transport inhibitors is required as would be needed in intracellular cytokine staining. In addition, RNA detection would be more useful in instances where no antibodies are available for the protein expression analysis to be done. Combined with Ca^{2+} imaging, we analyze IL-2 and IFNγ mRNA expression after stimulation with antigenic peptides.

The time-dependent mRNA expression levels were determined by incubating the cells for 0, 1, 4, and 18 hours before fixation, permeabilization then hybridization. Because smFISH is an endpoint assay, knowledge of the dynamics of mRNA is important in determining the time point for sampling the mRNA expression. ***Figure 4-15*** shows the IFNγ mRNA expression variation in OT-1 T cells stimulated with OVA peptide for different durations. The maximum expression is reached between 1 and 18 hours. From

this, the incubation period of 4 – 6 hours was chosen for evaluating mRNA expression for the rest of the studies.

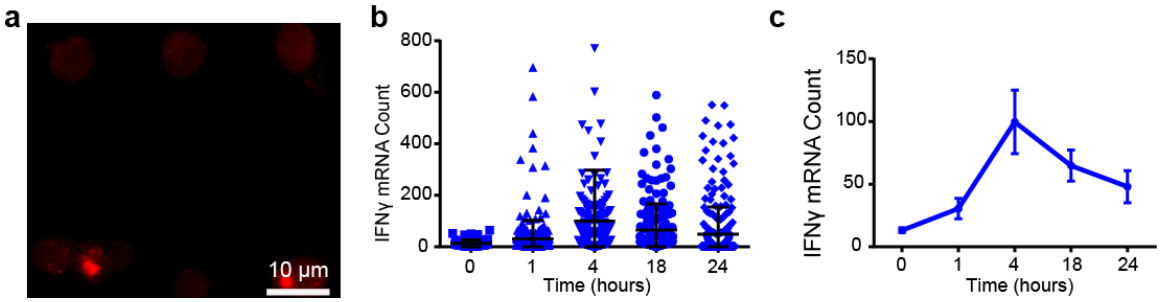

Figure 4-15. IFNγ mRNA expression dynamics in OT1 CD8+ T cells after stimulation with OVA peptide. T cells were stimulated with OVA peptide for different durations before being analyzed for IFNγ mRNA expression. (a) micrograph of maximum projection for imaging IFNγ mRNA fluorescently-labeled probes, (b) number of mRNA transcripts per cell for 0, 1, 4 , 18 and 24 hours of stimulation, the horizontal bar is the mean transcript count and the vertical bars show the standard deviation for the cell population and (c) the population average expression levels. * number of cells = > 600 per condition.

From the mRNA measurements at different time points, a stimulation time of 6 hours was picked for the subsequent studies. OT-1 T cells mRNA expression levels were determined using different stimulations; no stimulation using a BSA-coated surface, non-specific stimulation with ionomycin/PMA, another positive stimulation via crosslinking of the TCR, and stimulation with the antigenic peptide OVA. The mRNA expression level within a cell population shows a range under these different stimulating conditions (***Figure 4-16***). For each condition 400 – 600 cells were analyzed per stimulating condition demonstrating the large number of cells that can be assays in one experiment on the platform. For these studies, the limitation lies in smFISH imaging due to the high exposure times (1 – 3 seconds) required for imaging on a conventional epifluorescent

microscope. However, the long time it takes to image may be overcome with the use of a spinning disk confocal microscope.

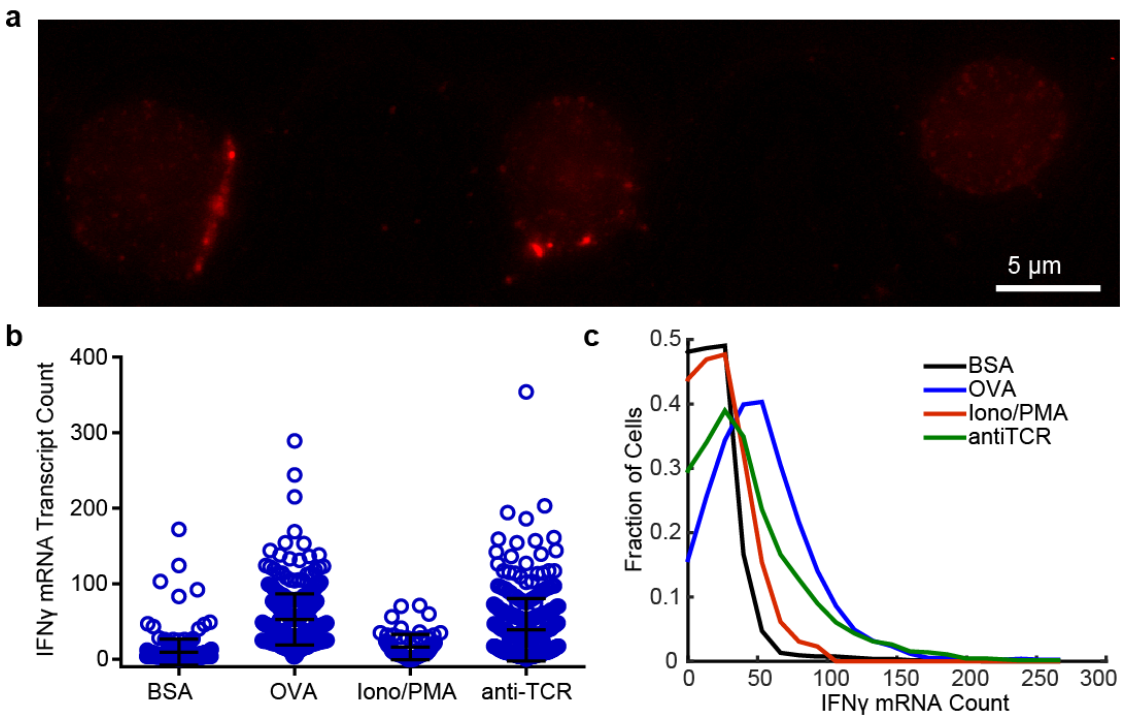

Figure 4-16. IFNγ expression in OT-1 T cells under different stimulating conditions. OT-1 CD8+ T cells were stimulated with OVA, anti-TCR and a negative stimulation control on BSA surface for 4 hours. (a) Representative micrograph of the maximum Z-projection for smFISH probe imaging. The probes are tagged with TAMRA fluorophore, (b) mRNA transcript count for the 4 conditions, each data point represents the total mRNA count for an individual cell, and the mean and standard deviation are shown for each condition, (n = 400 – 600 cells per condition), and (c) histograms showing the distribution of total mRNA count per cell for OT-1 T cells treated under different conditions.

4.8 Effect of coagonist peptide on Ca^{2+} and cytokine mRNA expression

We further showed the effect of coagonists in both Ca^{2+} levels and mRNA expression levels in the same population with single-cell resolution. As previously demonstrated, the presence of coagonist OVA enhances the calcium response (***Figure 4-12***). In addition, the mRNA expression levels are very low in the presence of coagonist alone compared to

the agonist OVA (Figure 8-12). To evaluate the effect of the coagnosist, cells were stimulated on surfaces coated with OVA agonist, OVA/VSV and VSV surface. In all the three conditions the MHC density was kept constant, therefore in the presence of a coagonist the OVA density was reduced by 4-fold. As previously observed, Figure 4-17 show that T cells on OVA and VSV/OVA surfaces show rapid Ca^{2+} flux within the first 120 s of the analysis. On the other hand in the VSV condition, only sporadic Ca^{2+} spikes are observed. Overall, the data shows on average a higher Ca^{2+} rise in the presence of the coagonist VSV, thus supporting the idea that the coagonist enhances T cell signaling (*172, 173, 175, 179*) .

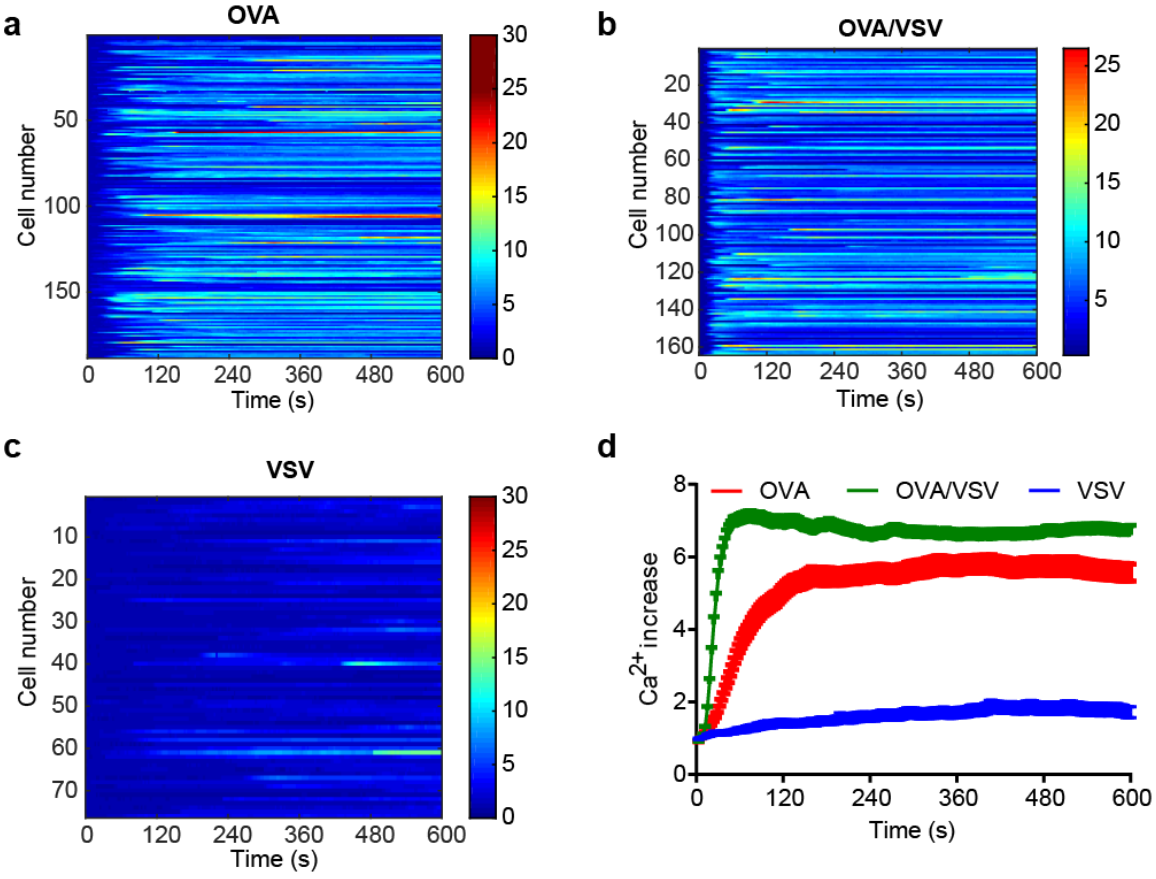

Figure 4-17. OT-1 Ca^{2+} dynamics with and without coagonist VSV. OT-1 T cells were stimulated with the indicated peptide in the presence of anti-CD28 and anti-LFA1.

Heatmaps were plotted for the temporal Ca^{2+} dynamics for the individual cells under stimulation with, (a) OVA agonist, (b) OVA agonist and VSV coagonist, (c) VSV coagonist only, and (d) taking the population average for the three conditions, overall T cells show a higher Ca^{2+} response in the presence of a coagonist compared to having only the agonist.

Furthermore, analyzing the Ca^{2+} response parameters such as the maximum peak reached and the overall Ca^{2+} dose calculated as the area under the calcium curve, we show the amplification of the Ca^{2+} signal by the coagonist. The coagonist amplifies the signal that is initiated by the TCR-pMHC interaction between the TCR and the OVA peptide. Without the agonist the T cells exhibit random Ca^{2+} fluctuations, showing that the interaction with the antigenic peptide is crucial in initiating the signal.

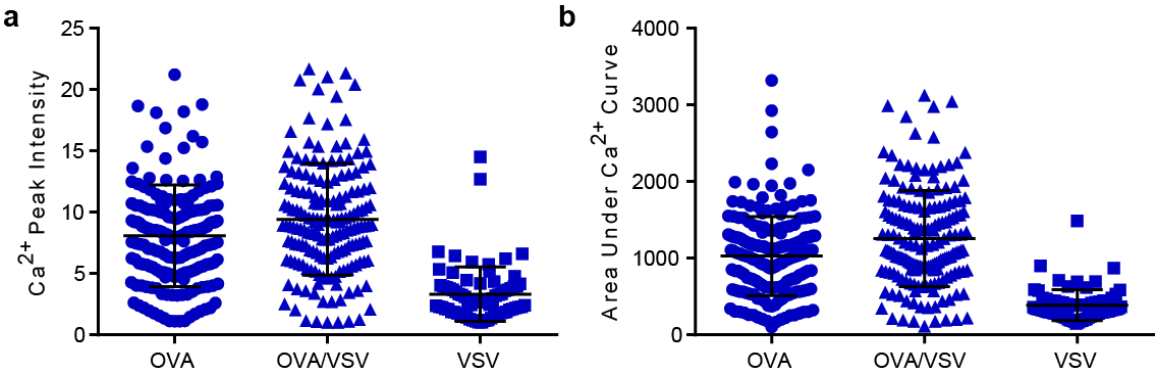

Figure 4-18. Analyzing Ca^{2+} dynamics parameters show an overall higher calcium response in the presence of a coagonist. (a) The maximum Ca^{2+} reached for each cell, the average and standard deviation within each population are shown, and (b) area under the Ca^{2+} curve showing the total calcium dose during the first 10 minutes of stimulation.

With the understanding of how the coagonist amplifies the Ca^{2+} signal, we analyzed how the signal is propagated downstream to cytokine mRNA expression levels. Previous studies have demonstrated increased IL-2 secretion and CD69 surface marker expression in the presence of an agonist (*172, 178*). The cytokine mRNA expression levels will

increase upon stimulation as has been shown in this chapter. The mRNA expression levels for IL-2 and IFNγ cytokines were evaluated. Figure 4-19a shows a higher IFNγ .mRNA expression levels for T cells on OVA surface. In addition, for the OT-1 T cells on OVA surface, the mRNA expression levels spanned a larger range. Surprisingly, the T cells on the OVA/VSV surface showed lower mRNA expression levels almost comparable to cells on VSV surface even though these cells showed an overall high Ca^{2+} level within the first 10 minutes of stimulation. Similar trends were observed with the IL-2 mRNA expression (Figure 4-19b) with no observable mRNA spots on the VSV-stimulated T cells. There are two possible explanations to these observations; the lower OVA density in the presence of the VSV (OVA/VSV condition) may have an overall effect on the different signals involved in T cell activation and thus result in reduced functional or response downstream of calcium. Alternatively, the mRNA peak expression levels for OVA/VSV condition may appear earlier after activation compared to OVA-stimulated cells. Sampling at earlier times could help sheds light on the dynamics of cytokine mRNA levels in the presence of a coagonism.

In addition to evaluating the effect of coagonists in T cell activation by measuring Ca^{2+} changes and mRNA expression levels, we took advantage of our platform to analyze how the Ca^{2+} dynamics are related to the cytokine mRNA levels. The platform enables defined spatial positioning of individual cells on a small footprint, and this high density of cells enables the analysis of hundreds of cells for Ca^{2+} dynamics in a single field of view. The spatial positioning of the individual cells is kept throughout the experiment, and the cells can be incubated in the device for up to 24 hours as has been demonstrated (***Figure 4-5***). The ability to incubate the cells for long time while maintaining their positions, and the

ease of introducing different fluids into the device allows further analysis to be performed including immunostaining and smFISH hybridization after Ca^{2+} live imaging.

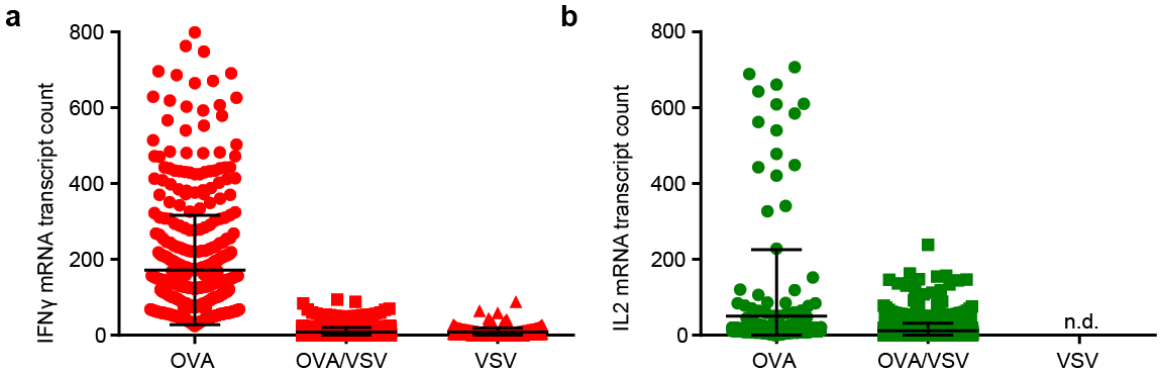

Figure 4-19. mRNA expression levels. After 6 hours of stimulation, cells were fixed, and subsequently hybridized with mRNA probes for IL2 and IFNγ. (a) T cells stimulated on OVA peptide surface show higher mRNA expression level, and a larger dynamic range compared to cells on OVA/VSV and VSV surface, (b) OVA-stimulated surface show a slightly higher IL2 mRNA expression level, and no detectable spots were observed in cells that were on VSV surface. *number of cells = 600 – 800 for each condition.

Therefore, with the information on the identity of each cell in both Ca^{2+} imaging and cytokine mRNA imaging, the Ca^{2+} parameters derived from the Ca^{2+} curves were examined on how they can inform on the cytokine expression levels that can have functional consequences. Overall, no obvious correlations were observed between area under the Ca^{2+} curve and mRNA expression levels (Figure 4-20). These results may indicate that the high Ca^{2+} cells may not necessarily become functionally productive. However, further studies that also probe at the mRNA dynamics would be crucial in determining if there is really a correlation or no correlation between the Ca^{2+} dynamics and cytokine mRNA expression levels. In addition, more conditions will need to be tested

including the presence of a coagonist but with the same agonist density compared to the condition with the agonist only condition.

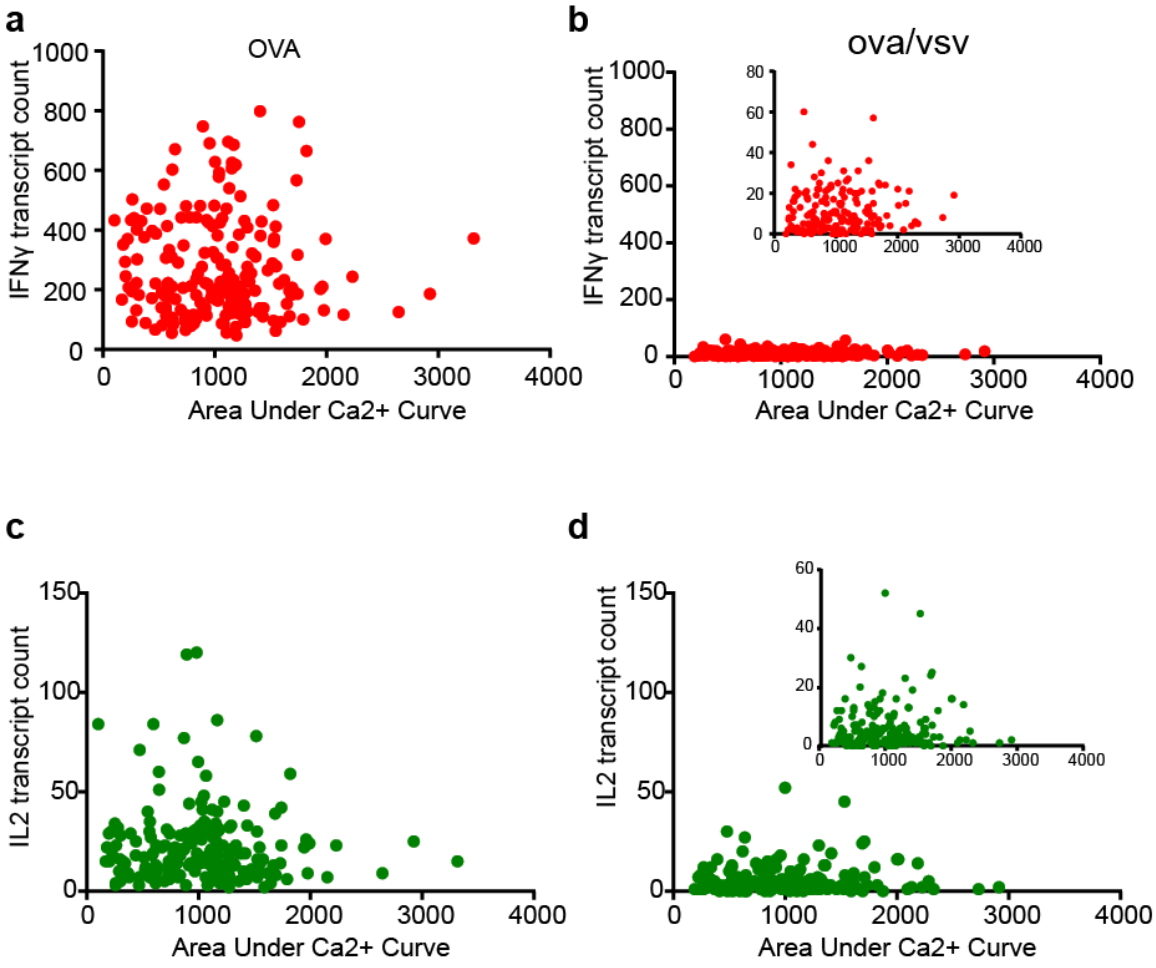

Figure 4-20. Direct correlation of Ca^{2+} response and IL-2 and IFNγ mRNA expression levels. With the identity of each cell conserved throughout the assays, direct correlations between the Ca^{2+} dynamics and mRNA expression were drawn at a single cell level. Overall the data shows no correlation between the Ca^{2+} does and IL2 or IFNγ mRNA, thus demonstrating that the observation of cells exhibiting high Ca^{2+} may not be enough in identifying functionally responsive T cells. Ca^{2+} dose vs IFNγ expression for (a) OVA, and OVA/VSV, and Ca^{2+} dose vs IL-2expression for (c) OVA, and (d) OVA/VSV.

4.8.1 Multiplexed data correlations using clustering algorithms

In addition, more rigorous analysis of the measured calcium and mRNA data is required to better understand any correlations between these parameters. I used k-means clustering algorithm to group together cells that exhibited similar calcium traces. The k-means is an optimization algorithm that minimizes the distance from the center of the cluster for each data set and maximizes the distance between different clusters.

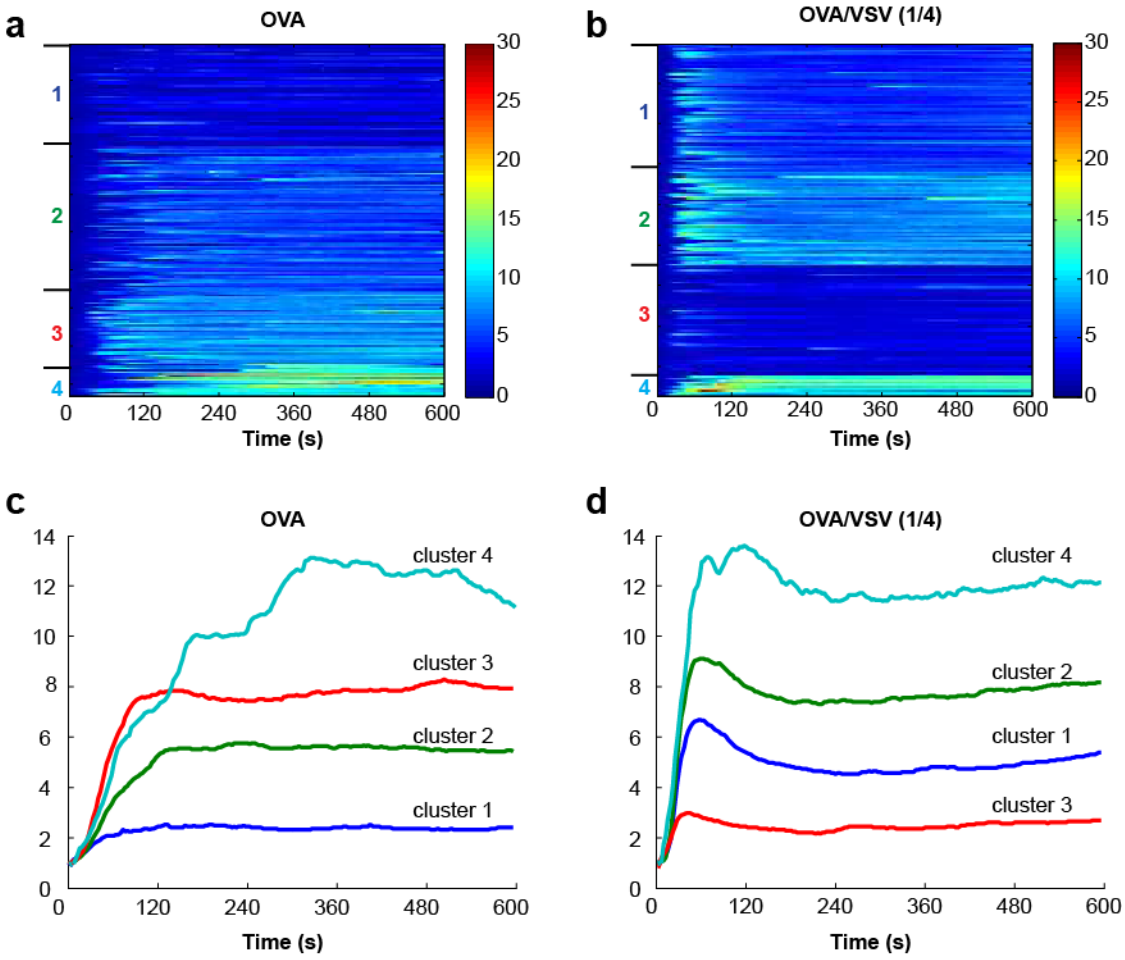

Figure 4-21. Ca^{2+} dynamics clustering using k-means clustering algorithm. The individual calcium traces for OT-1 T cells on either OVA or OVA/VSV surface. For the OVA/VSV surface the OVA density was 0.2 compared to the condition with OVA only. Heatmaps showing individual calcium traces arranged by the clusters, (a) OVA, (b) OVA/VSV. The clusters are indicated on the heatmaps. Average calcium trace for each cluster for (c) OVA and (d) OVA/VSV. Distinct calcium traces are observed for each cluster.

To capture the temporal calcium dynamics and group the cells in similarly behaving groups, k-means to group the cells into 4 distinct clusters for the T cells treated on OVA and OVA/VSV surface. Figure 4-21 shows the clusters that the calcium traces were grouped into. From the heatmap plots (Figure 4-21a,b), the different clusters can be visualized. In addition, by taking the average calcium response for each cluster, the data shows that each cluster is unique (Figure 4-21c,d), with the clusters having different maximum peak values. In particular, for the OVA-treated cells, cluster 4 average calcium

curve show a very distinctive behavior that might indicate that the cells within this cluster had multiple Ca^{2+} bursts during the stimulation (Figure 4-21c). In addition, all the clusters have different peak values and rise time that can also be analyzed to describe the difference in the calcium behaviors. On the other hand for the OVA/VSV treated cells, the 4 clusters show similar peak rise but different peak levels.

Combining the calcium data with the mRNA count analysis, PCA was used to analyze the correlations between the early calcium signaling and late mRNA expression. Figure 4-22 show the calcium clusters (color of each point) after PCA. For the OVA-treated cells the different subsets are described by the first PC (Figure 4-22). However, for the OVA/VSV-treated cells, there was no separation of the calcium clusters in the PCA analysis. This observation may be a result of the lower OVA density on the surface (20% coverage compared to the OVA only condition) that may have an impact on the signal propagation of mRNA expression since higher calcium levels were observed within the OVA/VSV group compared to the OVA group.

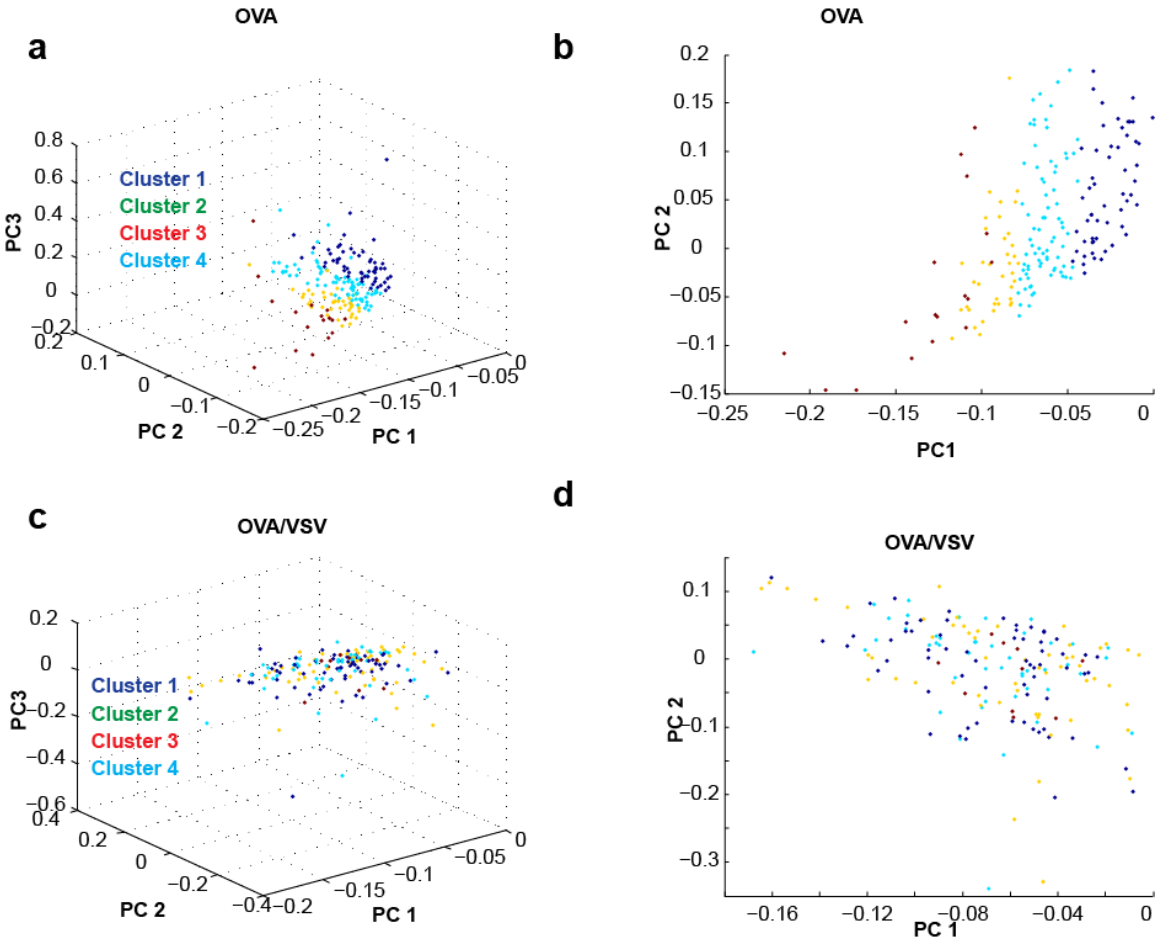

Figure 4-22. Clustering of OT-1 T cells stimulated on OVA surface by PCA of the Ca^{2+} dynamics and mRNA expression. The color for each data point represents the clusters of the cell from the k-means clustering of the calcium dynamics above as indicated in the legend. (a,b) for the OVA-treated cells the 4 clusters from k-means clustering are separated, showing a positive correlation between the calcium dynamics and mRNA expression levels, and (c,d) for the OVA/VSV treated cells, the calcium clusters are diffuse in the PCA analysis showing no direct correlation with the mRNA expression levels.

Additionally, we analyzed the expression profiles for both IL-2 and IFNγ mRNA count. Figure 4-23 shows the PCA for OVA-treated T cells. IFNγ mRNA expression showed some distinct subsets (Figure 4-23a,b) compared to the IL-2 mRNA expression that did not show any obvious correlations (Figure 4-23c,d). From this analysis, it is possible that for the CD8+ T cells, the calcium dynamics and IFNγ mRNA expression may have a correlation that may be used to determine functional response from calcium data.

Similar analysis on the OVA/VSVS-treated cells showed cells with high IFNγ mRNA separated from the main cluster of cells, however no distinct subsets were observed for the IL-2 mRNA count (Figure 4-24).

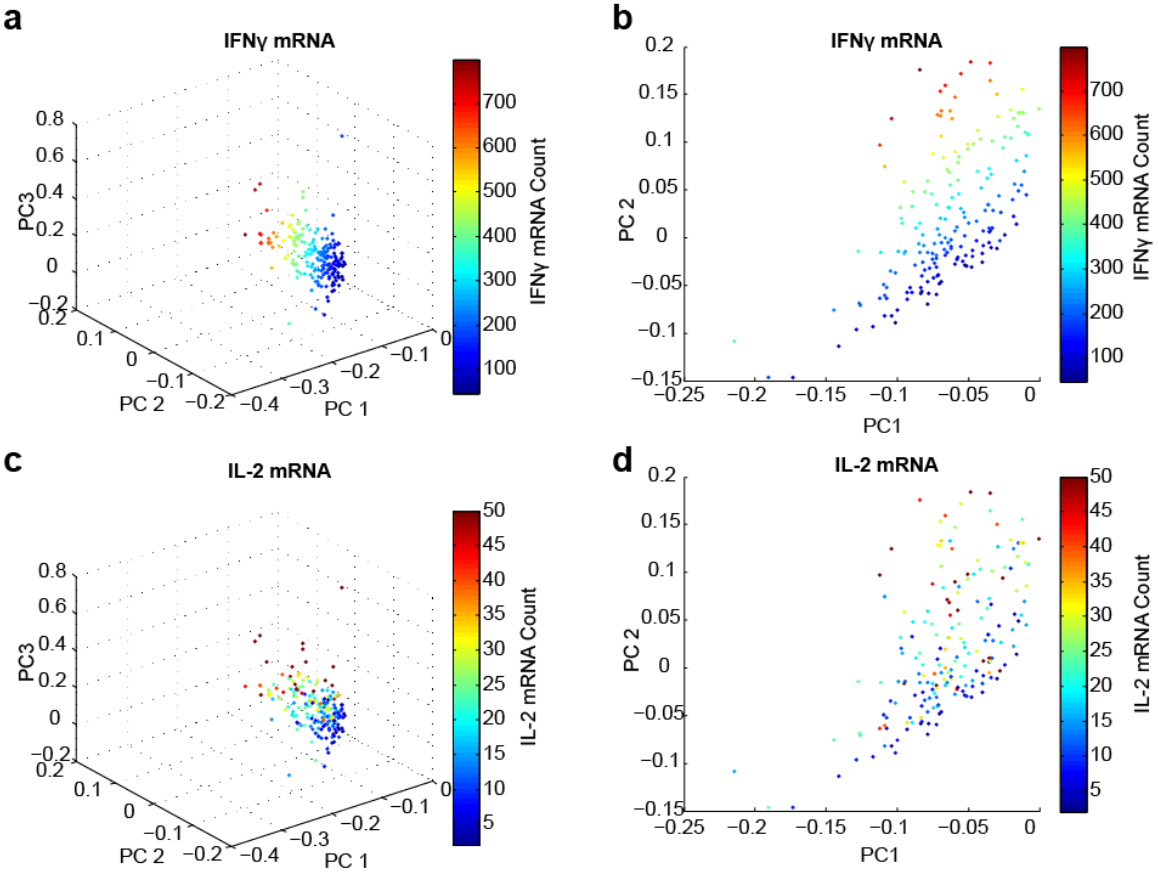

Figure 4-23. Clustering of OT-1 T cells stimulated on OVA surface by PCA of the Ca^{2+} dynamics and mRNA expression. The variance contribution is 83.4 % for PC1 and 14.7 % for PC2. (a) plot of the three principal components , the color of each point represents the IFNγ mRNA count (blue = low, and red = high), (b) PC1 and PC2 plot show that the IFNγ mRNA count is described by the first PC. (c,d) The color of each point represents the IFNγ mRNA count (blue = low, and red = high), (c) a plot for the 3 principal components, and (d) plot of first 2 PCs show no distinct subsets for IL-2 mRNA expression.

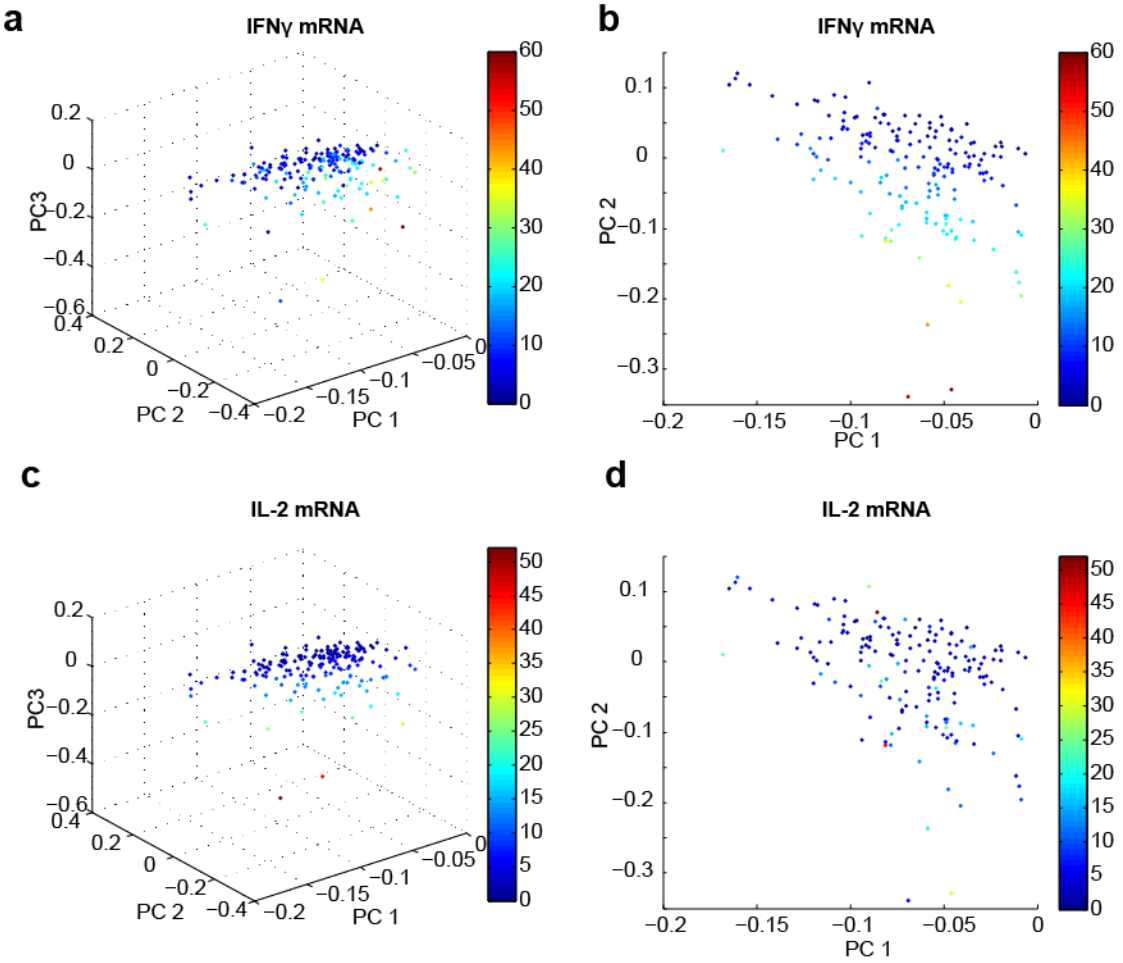

Figure 4-24. Clustering of OT-1 T cells stimulated on OVA/VSV surface by PCA of the Ca^{2+} dynamics and mRNA expression. The variance contribution is 98.6 % for PC1 and ~ 1 % for PC2. (a) plot of the three principal components , the color of each point represents the IFNγ mRNA count (blue = low, and red = high), (b) PC1 and PC2 plot show that the IFNγ mRNA count is described by the first PC. (c,d) The color of each point represents the IFNγ mRNA count (blue = low, and red = high), (c) a plot for the 3 principal components, and (d) plot of first 2 PCs show no distinct subsets for IL-2 mRNA expression.

Finally, we analyzed the ability to identify cells that were under different stimulating conditions using PCA (Figure 4-25). Data from OVA, OVA/VSV, and VSV was pooled together and analyzed. Figure 4-25 show that the cells from the different stimulating conditions group into distinct subsets.

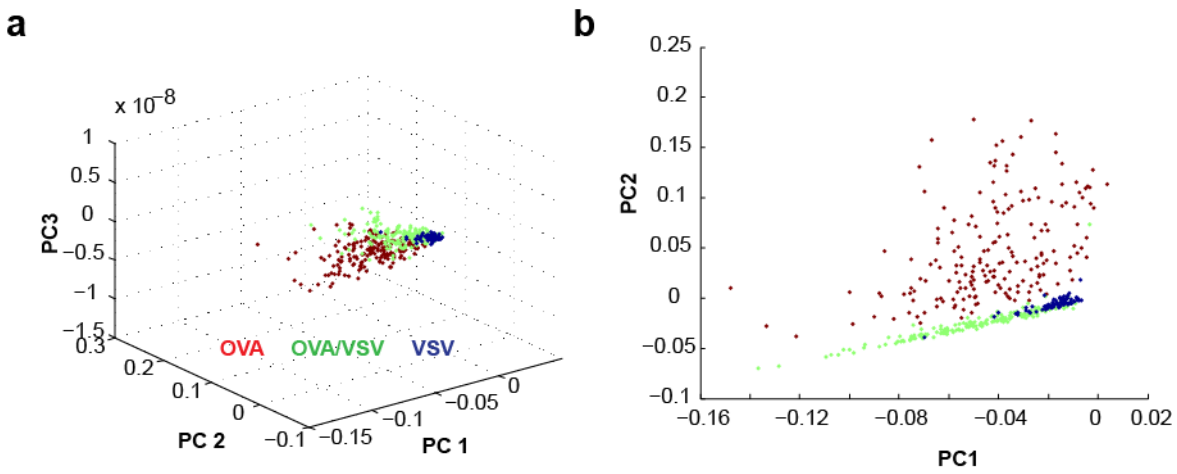

Figure 4-25. PCA clustering of the combined data for OVA, OVA/VSV and VSV conditions for calcium dynamics and IFNγ mRNA expression. The variance contribution is 85.6 % for PC1 and ~ 14.1 % for PC2. All the data for the T cell activation with OVA, OVA/VSV, and VSV was pooled together and PCA was performed. 3 distinct groups are observed that correspond to the cells under the different treatment conditions are observed. The color for each point represents the stimulating condition for that cell.

Overall, the ability to perform longitudinal T cell activation analysis has been demonstrated that allows multiple parameters to be measured employing different analytical techniques.

4.9 Conclusions

Here we have presented a simple, integrated platform combined with image-based approaches for longitudinal analysis of immune cell signaling events. We take advantage of the platform developed in Chapter 3 that enables high-density cell trapping and robust fluid exchanges to allow the analysis of hundreds of cells in a single experiment at a single cell resolution and multiple stain and wash steps for the determination of different molecular signatures on the same sample. The ability to perform multiple assays on the

same sample in a sequential manner while maintaining the identity of each cell allows direct comparisons of different molecular readouts.

The platform requires minimal peripheral equipment, relying only on gravity to drive the flow and no specialized equipment is required to run the device. Therefore, the platform is easily transferable to other laboratories and can be used on a typical microscopy setup without any modifications to the setup.

5 LEUKOCYTE SEPARATION, STIMULATION AND IMMUNOPHENOTYPING FROM LESS THAN A DROP OF WHOLE BLOOD

Ultimately, I would like to take advantage of the small scale offered by microfluidics to reduce the amount of samples required for an assay. Enabling direct preprocessing of cells will allow for smaller volumes to be used in the experiment. This can be important when using patient samples such as blood, where it is necessary to reduce the burden on the patient, or when working with blood from small mammalians such as mice. In this chapter I demonstrate the use of our modified cell trap for the separation of white blood cells from whole blood, thus requiring only 1 – 5 μL of whole blood for an immunophenotyping assay.

5.1 Introduction

5.1.1 Blood for immune analysis

Blood is a more tractable tissue to study as it can be easily acquired through minimally invasive techniques such as the finger prick, and is useful in disease diagnosis and monitoring. Blood is a complex mixture of ~ 55 % plasma and 45 % cells that include platelets (thrombocytes), white blood cells (leukocytes) and red blood cells (erythrocytes), and carries a lot of information about the physiological stage of organs and tissues in the body. Analysis of blood components, both plasma and blood cells provide very important information on the health status of an individual. Changes in the blood cell composition and the different cell subtypes can provide insights on

autoimmunity, chronic illness, acute infection and inflammation. In blood cell analysis, leukocytes are the target cells as they are a critical part of the immune system. Leukocytes total and differential count (**Table *2***) are critical in evaluating inflammation, chronic illness and infection. However, as indicated in ***Table 1*** there are 1,000 red blood cells for each leukocyte cell. As a result, there is need to separate leukocytes for analysis since the overwhelming number of red blood cells that can confound the findings especially in RNA-based assays.

Table 1. Blood Composition

cell type	# of cells per µL
erthyrocytes	$4 - 6 \times 10^6$
Platelets	$150 - 400 \times 10^3$
leukocytes	$4 - 11 \times 10^3$

Leukocytes are crucial in both innate and adaptive immune system response. Changes in the differential composition from the normal (***Table 2***) is used in diagnosis especially in inflammation, burns patients and sepsis. Moreover, the CD4+ T cell count from blood has been used to monitor the immunocompetence of HIV-infected patients (*180-182*).

Conventional techniques for separating blood components include density gradient centrifugation, fluorescence-activated cell sorting (FACS), magnetic-activated cell sorting (MACS) (*183*) and erythrocyte lysis (*184-186*). These approaches generally require at least milliliters of blood that can be challenging when analyzing samples from

patients especially pediatric patients or small experimental organisms such as mice. In addition, these techniques involve complex sample preparation techniques that required experienced individuals, and the sample manipulation can cause cell stimulation thus distorting the immune phenotypes of the cells (*187, 188*). Unintended activation of neutrophils have been observed leading to increased expression of neutrophil activation markers, CD11b/CD18 (*188*). In addition to techniques for separation, subsequent analytical tools are employed for the identification of the different cell types, and stimulation and analysis of immune response, and genomic and proteomic analysis of molecular expression. Flow cytometry is the gold standard technique use to analyze blood cells allowing for the differential enumeration of leukocytes based on morphology and surface marker expression. While flow cytometers are accessible in research laboratories, they are bulky equipment that would not be suitable for point-of-care analysis in low resource setting, or in a doctor's office. The need for point-of-care diagnosis challenges the development of portable and easy-to-use platforms (*189-191*). Therefore, there are opportunities to develop new integrated tools that are portable, easy to use, require minute sample sizes, and enable multiple assays to be performed to allow for both cell enumeration and molecular analysis.

Table 2. Differential Leukocytes count in whole blood (192, 193)

	Cell Type	Number of cells per μL	Size (μm)
Granulocytes	neutrophils	$3 – 7 \times 10^3$	15 – 20
	eosinophils	50 – 400	6 – 8
	basophils	25 – 100	10 – 15
	Monocytes	200 – 800	15 – 20
Lymphocytes	T cells	800 – 3,200	6 – 15
	B cells	100 – 600	8 – 15
	Natural killer Cells	50 – 400	10 -15

5.1.2 Microfluidic-based platforms for cell separation

Microfluidics lends itself to be a technique that utilizes small sample sizes that could enable the use of less than a drop blood in routine testing and the compact size makes microfluidic platforms viable candidates for the development of portable devices. Moreover, the inherent small size and ability to integrate multiple functions on the same chip makes microfluidic platforms amiable to point-of-care diagnostics, and for use in elucidating response to perturbations for analysis of drug response and immune system competence. Microfluidic platforms for blood separation and analysis have been developed to either mimic the separation techniques in conventional assays so as to reduce the required sample size or implement new techniques that would otherwise not be applicable in macroscale techniques. Previous platforms have used differences in cell size and mechanical properties, differential displacement under flow, antibody capture,

and constricted geometry for the separation of plasma (*194-196*), leukocytes (*197*) and circulating tumor cells from whole blood (*198*). These different separation approaches are based on taking advantage of the heterogeneous properties of blood include size, mechanical, electrical, and magnetic properties, and differential expression of surface markers. Sethu *et al* developed a microfluidic chip that enable precisely timed exposure of blood cells to deionized water for red blood cell lysis to isolate leukocytes and perform genomic expression analysis on leukocytes before and after exposure to Staphylococcal enterotoxin B (*199*). This approach relies on the differential duration it takes for cells to undergo lysis, red blood cells rapidly undergo cell lysis compared to leukocytes. The microfluidic systems enables much shorter exposure times to the lysis solution, thus reducing the chances of nonspecific activation of leukocytes during the separation process.

The differential size of blood cells make it an easy characteristic to exploit when separating cells with sizes ranging from 2 μm for platelets, 6 – 8 μm for red blood cells and 6 – 20 μm for leukocytes. Geometric restriction has been utilized to separate blood cells from plasma for analysis of plasma components (*194, 196, 200*). In addition, differences in cell sizes have been applied to separate leukocytes from red blood cells, and also tumor circulating cells from blood cells. However, the filtration approaches can often lead to clogging by the red blood cells and therefore not robust.

Another approach that uses differences in cells sizes and mechanical rigidity is deterministic lateral displacement. Here geometry restriction and flow is used to direct

cells of different sizes to different outlets of the channel; thus similarly size particles are collected together. Surface patterning with specific antibodies (*201*) or receptor-specific ligands enable the separation of specific cellular subtypes (*202, 203*). In addition, the deformability of red blood cells have been used in removing red blood cells using lateral displacement in a microfluidic channel (*204-206*). Combining the lateral displacement under flow and asymmetric patterning of P-Selection, Bose *et al* demonstrated successful separation of neutrophils from whole blood (*207*). Neutrophils exhibit a rolling behavior on p-selectin surfaces (*208-210*), and this interaction on an asymmetric p-selectin pattern displaces the neutrophils to one size of the channel where they exit through a separate channel from all the other cells (*207*). However, this platform does not enable for further on chip analysis of the separated cells relying on off-chip analysis that may require large number of cells, and also may suffer from cell loss. In addition, approaches that rely on capture of cells on coated surfaces may become problematic in diseased samples where the surface interaction properties may be altered.

In this chapter, I use the microscale tools and techniques developed in Chapters 2, 3 and 4 to implement a simple technique for separating leukocytes from whole blood by exploiting the differences in sizes and deformability of blood cells, and passive hydrodynamic trapping to selectively trap only leukocytes in defined microstructures. Erythrocytes, while about 6-8 μm in diameter are highly deformable and tend to flow in the channel or pass through the traps when directed into the traps by the flow, and therefore are not trapped in the device. On the other hand, less flexible leukocytes are directed into the traps by hydrodynamic flow and remain trapped. Our platforms allows

integrated leukocyte separation, stimulation and analysis of response on chip, thus minimizing sample handling and loss, and reagent use, and overall reducing donor burden on drawing large amounts of blood. The ability to separate leukocytes from whole blood utilizing the high-density cell trap-based platforms described in the preceding chapters enables the development of a complete package of analytical techniques from. The platform will integrate cell separation from whole blood, perturbation of target cells, and subsequent analysis of cell behavioral responses using image-based approaches.

5.2 Materials and Methods

5.2.1 Device fabrication

The devices were fabricated as outlined in Appendix A.

5.2.2 Device preparation

Prior to use, the devices were steam autoclaved to sterilize them. Devices were primed with remove bubbles and then the device channels were filled with 2% BSA in PBS and incubated for 30 minutes to passivate the surface so as to prevent nonspecific adhesion of cells on the device surfaces.

5.2.3 Blood preparation

Blood was collected into an EDTA Vacutainer collection tube (BD), and the blood sample was used within an hour after draw. The dilution buffer (RPMI 1640, 2 % BSA) was added to blood to dilute the blood 10-fold so as to prevent clogging of the narrow device channels. The diluted blood was then aspirated in a pipette tip and the tip placed on the device inlet. The blood then flowed into the device by gravity-driven flow, and allowed to run for 15 minutes before the device channels were washed with the dilution

buffer. Once all the excess cells are removed, stimulation or antibody staining was done. Leukocytes were then stimulated with 100 ng/ml lipopolysaccharide (Sigma Aldrich, L3012) for 4 hours. After the stimulation, cells in the device were washed with the buffer, and solution of antibodies against CD11b and CD66b surface markers was added and incubated for 1 hour before washing and them imaging on an epifluorescent microscopes

5.3 Device design and operation principle

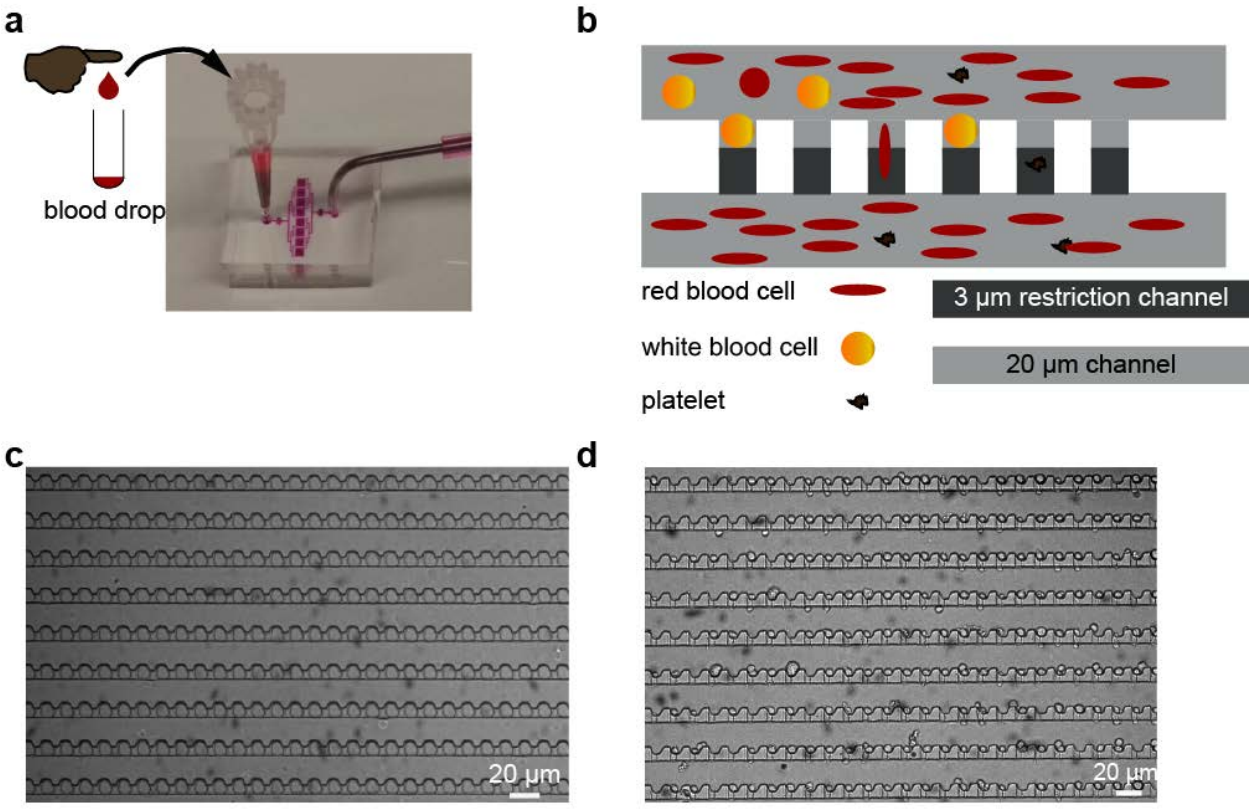

Figure 5-1 Device operation. (a) Single inlet/single outlet device for the separation of leukocytes from whole blood, (b) depiction of the separation of the removal of red blood cells. The red blood cells are very flexible and can pass through very small gaps, therefore in the device the red blood cells can pass through the 2 µm constriction at the cell trap while the more rigid leukocytes are directed to the cell trap and remain in the

cell traps, (c) micrograph of the device showing the array of cell traps in the device, and (d) jurkat cells after being separated from red blood cells and trapped in the device.

The device platform represents a new application of the high density cell trap array to enable processing of whole blood (***Figure 5-1***). As previously described, the platform consists of microstructures for cell trapping with a single inlet and a single outlet, and has been demonstrated to enable cell trapping on mammalian cells in a highly robust manner. The separation of the red blood cells is based on the differential size and mechanical rigidity of the cells. Platelets are very small (1 – 3 μm) and therefore cannot be trapped in the device's microstructures. On the other hand, red blood cells are very flexible and can squeeze through very small channels thus allowing them to pass through the cell traps, and leukocytes that have size ranging 6 – 20 μm are trapped in the device (***Figure 5-1***). The optimal cell trapping microstructures were 10 μm wide and 20 μm tall, and the restriction channel was 2 μm tall. The devices have a capacity of 1,000 – 8,000 cells depending on the number of chambers on the microchip.

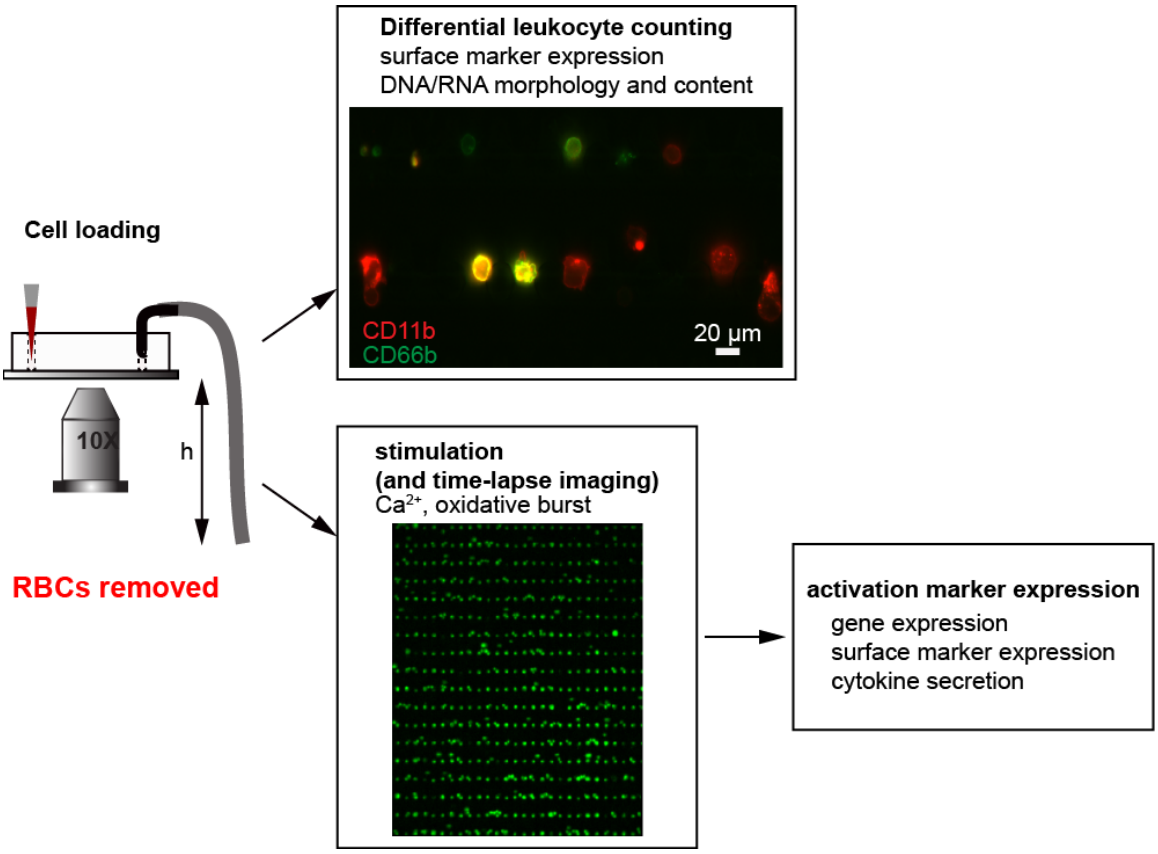

Figure 5-2. Microfluidic platform enables rapid analysis of minute quantities of blood. Multiple analysis can be performed on chip starting with the removal of reds blood cells and trapping of leukocytes for subsequent analysis including differential leukocyte counting, stimulation and time-lapse analysis and measurement of activation marker expression and gene expression of specific cells. The platform is very simple, and the flow is driven by gravity-driven flow implemented by suspending the outlet tubing to a height, h ≈ 15 cm.

With this platform leukocytes are separated and analyzed on the same chip. **Figure 5-2** give an overview of the functional capacity of the microfluidic system. Gravity-driven flow is used to drive the 10-fold diluted blood in the device and the red blood cells and platelets exit through the outlet while the white blood cells are trapped in the device. Once the white blood cells are trapped, differential leukocyte counting is performed using surface marker expression. In addition, further analysis can be performed on the immune response by stimulating the trapped cells, and evaluating activation markers such as

elevation of surface marker expression, cytokine secretion, oxidative burst, calcium dynamics and gene expression as have been shown in chapters 2, 3 and 4 (**Figure 5-2**). Therefore, the platform would offer a simple, high-throughput platform for processing and analysis of leukocytes using a microliter of blood.

5.4 Demonstrating the ability to separate out RBCs

The main goal of this chapter was to enable the removal of RBCs from whole blood to enable immunophenotyping of leukocytes. We characterized the deformability of red blood cells and the ability to remove red blood cells using a mixture of human red blood cells spiked with Jurkat cell to mimic leukocytes. In the mixture, the ratio of RBC to Jurkat cells was 1,000 to 1 to mimic the proportion in blood. Although in this case there is no blood plasma that might affect the flow dynamics, the setup helps us understand the properties of red blood cells and how they move through the device platform without getting trapped.

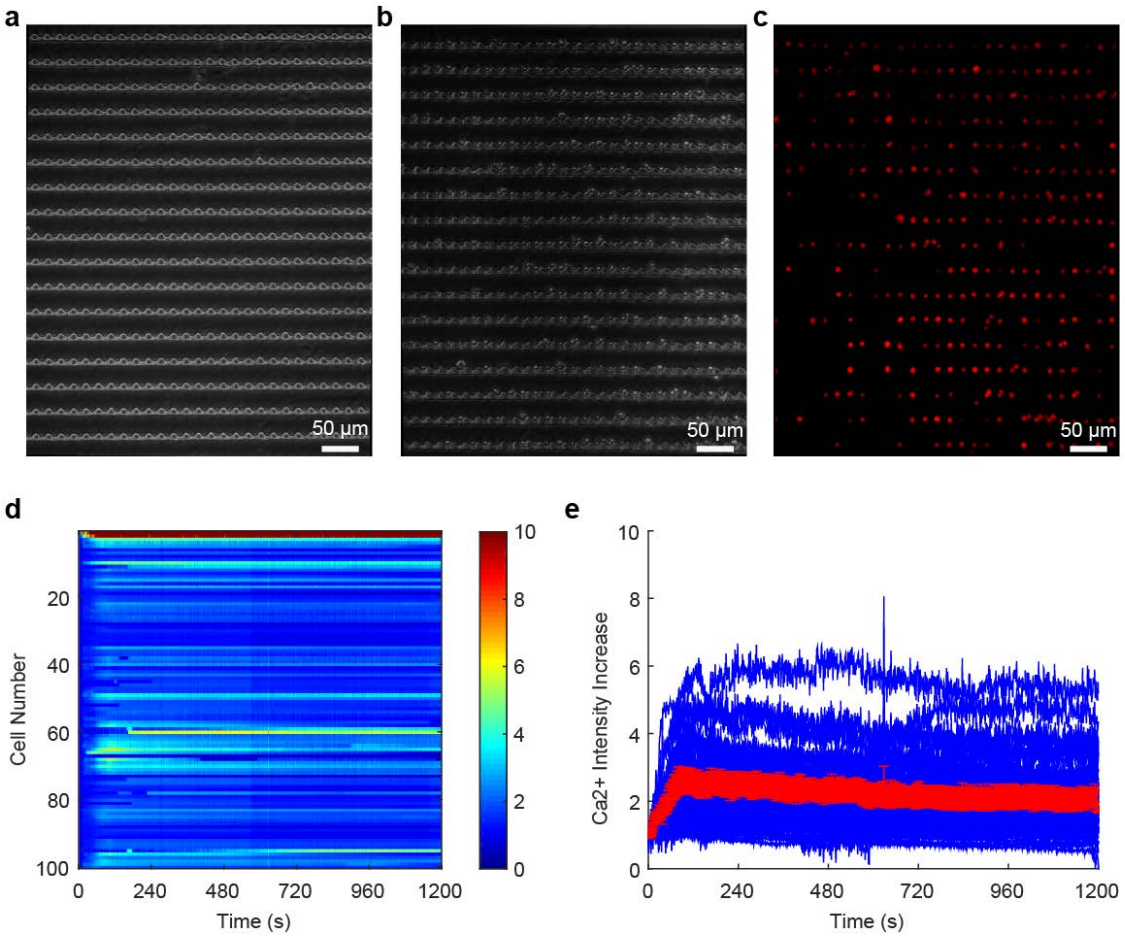

Figure 5-3. Capture of Jurkat cells mixed with red blood cells. Jurkat Jurkat cells mixed with red blood cells (1,000 red blood cells per Jurkat cells), and then introduced into the device. (a) device micrograph, (b) Jurkat cells capture in the device, (c) cell tracker red imaging of Jurkat cells. After trapping the cell were loaded with Fluo3 calcium-sensitive dye and stimulated with ionomycin (1 µg/ml) with simultaneous calcium imaging. (d) heatmap showing the individual cell response upon stimulation with ionomycin, and (e) individual curves and the average (red) calcium response.

The height of the tubing was optimized to 15 cm to enable a flow rate of ~ 12 µL/hr, allowing about 3 µL to be delivered into the device in 15 minutes. The mixture was diluted 10-fold to prevent clogging of the device channels by red blood cells. In 3 µL, there are ~ 600,000 red blood cells and 600 Jurkat cells. Here we used a device with a single chamber and a capacity of 1,000 cells. We were able to capture ~ 450 cells, thus giving a trapping efficiency of at least ~ 75 % of Jurkat cells assuming all the cell went

through the device. In addition, very few red blood cells were trapped in the device and some traps were left unoccupied. Therefore, the platform has a great potential in enriching the concentration of leukocytes, allowing more sensitive analysis such as genomic expression to be performed. Furthermore, once the cells are separated and trapped in the device, additional analyses can be performed as demonstrated in chapters 2, 3, and 4. Here, we show the stimulation of cells with ionomycin/PMA while simultaneously measuring calcium dynamics (Figure 5-3d & e). Cytosolic Ca^{2+} influx was observed after addition of ionomycin/PMA as shown in Figure 5-3d.

5.5 Whole blood separation, stimulation and immunophenotyping

5.5.1 Leukocyte separation from whole blood

After showing the removal of red blood cells from a mixture of Jurkat cells and red blood cells, we moved to separate leukocytes from whole blood. Leukocytes are of interesting in evaluating the immune cell response, and the high abundance of red blood cells (***Figure 5-4***a) makes it necessary to deplete red blood cells in leukocyte immunophenotyping. The red blood cells mostly flow through the main serpentine channel and some go through the traps (***Figure 5-4***b). In ***Figure 5-4***b the trajectory of two red blood cells are tracked as indicated in the figure. The red blood cells flow through the channel and are directed to the cell trap by the passive hydrodynamic flow and the flexibility of the red blood cells allow them to go through the cell traps. Loading of leukocytes starts in the first row of the device, demonstrating again the sequential loading characteristic of the device (***Figure 5-4***c). Once the leukocytes had been separated from red blood cells and trapped in the device, further analysis on the subtype

of the leukocytes can be conducted using differential surface marker expression. In addition, the immune cells can be stimulated on chip and analyzed for their immune response.

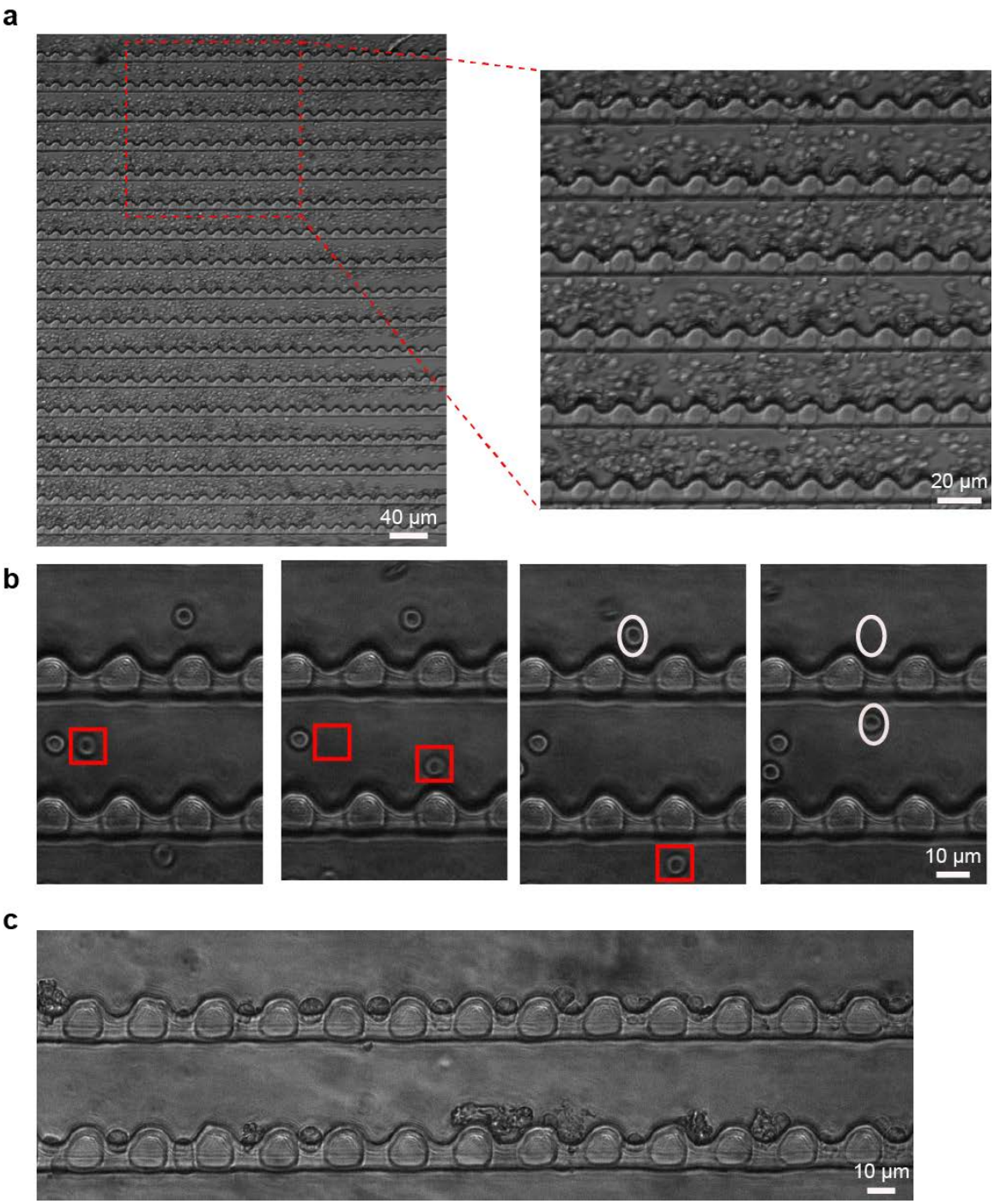

Figure 5-4 Whole blood in the device. (a) Whole blood in device at 10-fold dilution, (b) demonstration of the escape of red blood cells through the cell traps allowing the red blood cells to exit the device channel, and (c) the first 2 rows on the platform showing trapping of leukocytes.

5.5.2 Stimulation and surface marker based immunophenotyping

Whole blood was diluted 10-fold with PBS without $Ca^{2+/}Mg^{2+}$ with 2% BSA and 2mM EDTA, and introduced into the device. Leukocytes were captured in the device, and the excess cells were washed with the buffer. The leukocytes were then stimulated with 10 ng/ml lipopolysaccharides (LPS) for 4 hours. LPS is found on the membrane of gram-negative bacteria, and elicits a strong immune response in immune cells. In addition, LPS endotoxin is common in sepsis condition in patients. After the cell stimulation, the cells were stained for CD11b, and CD66b. Neutrophils constitutively express CD66b, and the expression of CD11b increases when the neutrophils are activated (*211, 212*).

Here, the focus was on the response of neutrophil, however the analysis was done on all leukocytes trapped in the device. Neutrophils were of interest because they are the most abundant leukocytes (30 – 80 % of leukocytes), and are also important in monitoring inflammation and infection. Stimulation with LPS and subsequent immunofluorescence staining showed differential surface marker expression of CD66b and CD11b (***Figure 5-5***). In ***Figure 5-5*** fluorescent images for imaging for both CD66b and CD11b, showing the cells stained on chip.

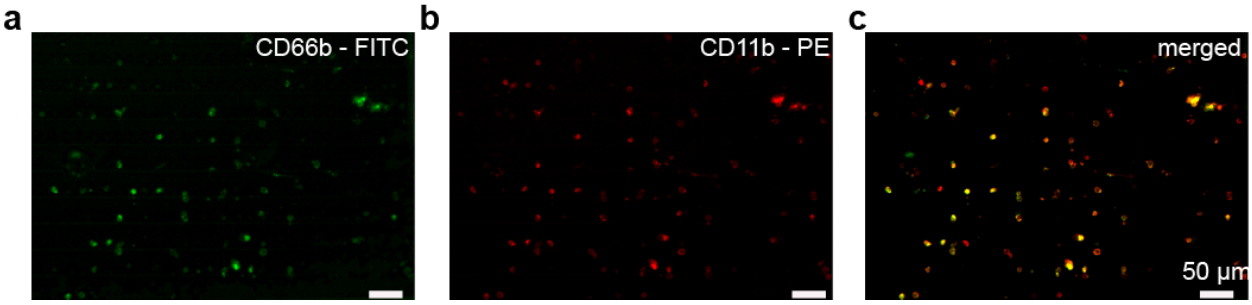

Figure 5-5. Fluorescence imaging to characterize surface marker expression levels. Stimulated cells were stained for CD66b (a), and CD11b (b) expression levels. (c) Merged micrograph image.

The average intensity of each cell were quantified for both CD11b and CD66b (***Figure 5-6***), and cells expressing only CD11b or CD66b or both or none were observed. ***Figure 5-6***a shows an image of a cell expressing only CD11b (center), and cells expressing both CD11b and CD66b but with different intensities. Neutrophils constitutively express CD66a-d and elevated levels of CD11b when activated, and monocytes also express CD11b (*213*). However, other granulocytes and lymphocytes are $CD11b^{-}CD55b^{-}$, and they are represented among the $CD66b^{low}$ and $CD11b^{low}$ cells ***(Figure 5-6)***. ***Figure 5-6***b shows the quantified expression levels of CD11b and CD66b. Leukocytes expressing high levels of both CD11b and CD66b (top right quadrant) are likely activated neutrophils. The bottom right quadrant show cells that are CD66b high and CD11b low, which are likely neutrophils that did not respond to stimulation. The left, bottom quadrant would be a mix of all the leukocytes including neutrophils as well. With the addition of other specific markers such as CD3 for lymphocytes, CD14 for monocytes, differential leukocyte counting can also be performed on the same cells. However, the number of markers that can be probed in ultimately limited by the number of spectrally resolved fluorophores. Overall, the assay demonstrated the ability to separated leukocytes from whole blood, perform stimulation of the leukocytes and analysis of activation markers.

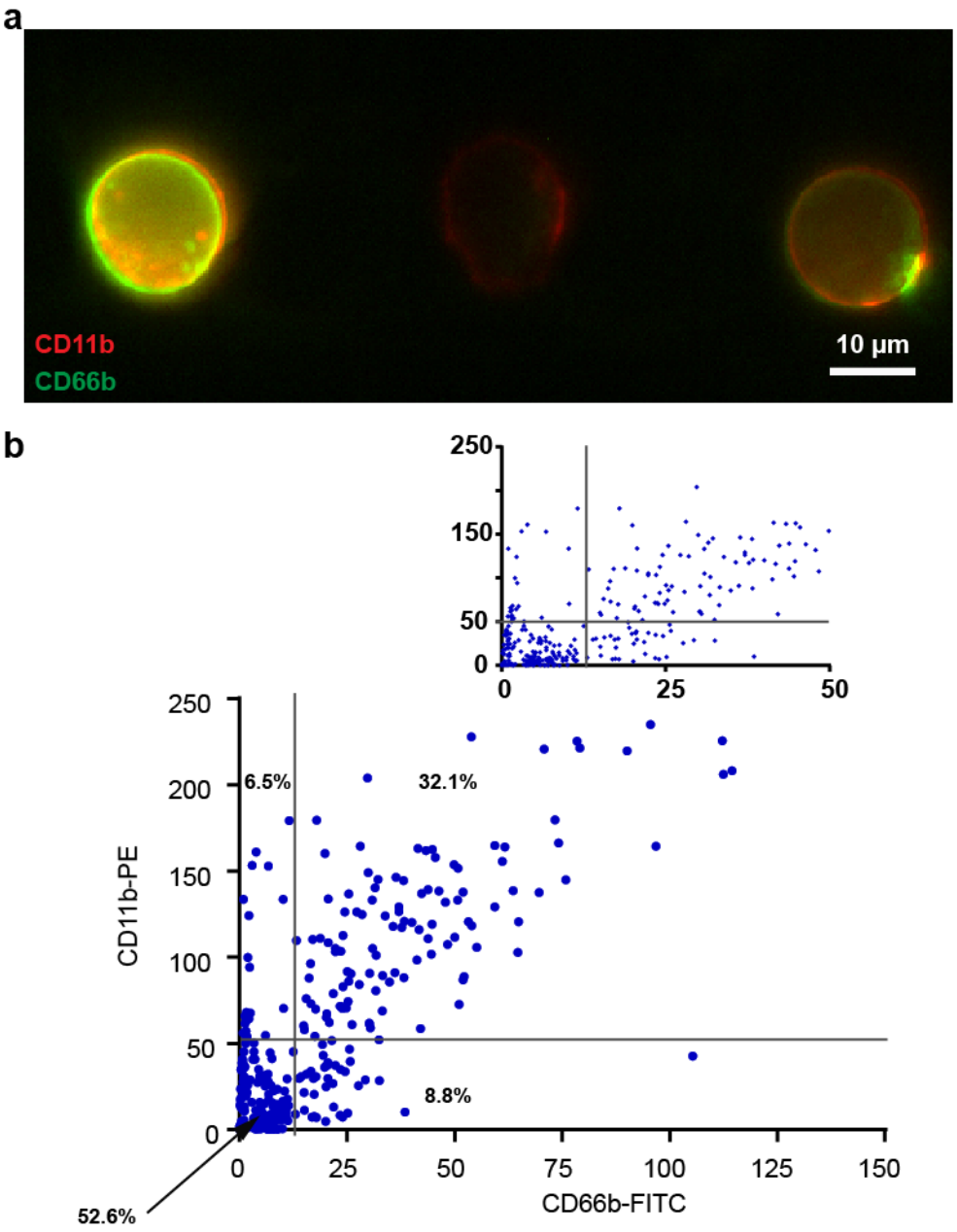

Figure 5-6 Surface marker expression of neutrophils after stimulation with LPS. Leukocytes separated from whole blood and stimulated with LPS were stained for CD66b and CD11b surface marker expression. (a) micrograph for fluorescence imaging in green and red channel (merged) for imaging of expression of CD66b and CD11b showing cells that express both CD11b and CD66b and a cell expressing CD11b only, and (b) Expression levels of CD66b (x-axis) and CD11b (y-axis). The cells were divided into a quadrant representing $CD66b^{low}$ and $CD11b^{low}$, $CD66b^{low}$ and $CD11b^{high}$, $CD66b^{high}$ and $CD11b^{high}$, and $CD66b^{high}$ and $CD11b^{low}$. Neutrophils constitutively express CD66b and CD11b, and higher levels of CD11b when stimulated. (n = 401)

The main challenge in operating the platform is the unavoidable settling of blood due to the cell differential density. Through time the cells settle in the pipette tip and this can result in the clogging on the narrow device channels (30 μm). In performing long-term analysis, the 2-layer PDMS device presented in Chapter 4 can be used. The 2-layer platform allows better fluid exchange capabilities, that may be necessary for long-term incubation times.

5.6 Conclusions

In this chapter we have presented a new application of the high density cell trap array device and image-based approaches in separating and analyzing leukocytes from whole blood. The approach relies on the differences in mechanical rigidity and size differences between red blood cells and leukocytes. Red blood cells are disc-shaped compared to the more spherical while blood cells and are very flexible and are therefore able to squeeze through very small constriction gaps. We use this characteristics to selectively trap leukocytes in the device while allowing red blood cells to exit the device. Therefore, the platform can enable absolute and relative enumeration of leukocytes and subtypes given high trapping efficiency on-chip, and differential leukocyte counting using surface marker expression and differential RNA/DNA expression. In addition, as demonstrated in the previous chapters, further analysis of immune response to stimulation can be implemented. Ultimately, these microfluidic platforms can be coupled with cheap optical imaging technologies (*189, 190, 214*) to allow for the development of complete packages for point-of-care, and point-of-procedure technologies for use in both resource poor settings where technological expertise and infrastructure is scarce and in developed

settings where the time for patient sample analysis is long due to need to send samples to dedicated laboratories that have sophisticated equipment.

6 TOWARDS A HIGH-THROUGHPUT PLATFORM FOR MEASURING ADHESION KINETICS OF MEMBRANE-ANCHORED RECEPTORS AND LIGANDS

So far, we have focused on determining the intracellular signaling signatures after stimulation via receptor-ligand interactions. However, the first step in T cell signaling happens at the cell surface requiring the cells to be in contact, and whether these surface interactions result in a productive signal may depend on the kinetics of the receptor-ligand interactions. Analyzing the first step in the activation involving membrane-bound receptors and ligands can help us understand some of the observed differences in T cell function. Current platforms developed to measure receptor/ligand interaction kinetics are laborious, difficult to implement for non-expert, and low throughput as they only allow a single cell to be analyzed at a time. Here we combine some of the intricate features developed in microfluidic systems to design a platform that could be used to measure interaction kinetics of cell membrane bound receptors and ligands. This assay could also be combined with fluorescence-based calcium imaging demonstrated in the previous chapters to allow for direct observation of both adhesion events and subsequent calcium signaling.

6.1 Introduction

6.1.1 Receptor-ligand interaction kinetics

Receptor-ligand interactions mediate cell adhesion and activation in a wide variety of physiological processes including the initiation of T cell activation through the

interaction of the TCR on the T cell with the pMHC molecule on the antigen presenting cell (APC). Kinetic analysis of receptor-ligand interactions may help better understand how the T cell interacts with a number of different pMHC but only mount an immunological response to a specific antigen. These cross-junctional interactions at the interface between the TCR and pMHC are two-dimensional (2D) because the molecules involved in the interactions are anchored to the membrane surface. This differs from interactions of surface receptors with ligands in three-dimensional (3D) fluid phase. 2D interactions can be analyzed using the adhesion frequency assay, which has been performed using the micropipette adhesion frequency assay (*64, 137, 215*), biomembrane force probe (*58*), atomic force microscopy (AFM), and laser tweezers (*63, 64*). These techniques enable kinetic parameters such as affinity, off rate and on-rate to be deduced. The differences in the kinetic rates of the immune cells can have functional implications. Therefore, these measurements can be insightful in evaluating the immunological potential of T cells. However, these current technologies suffer from being generally expensive, low throughput, laborious, and have been largely challenging to implement in most laboratories. Microfluidic technology enables parallelization of experiments allowing ease of acquisition of large quantities of data. In addition, microfluidic systems allow the integration of multiple functions on the same chip, which enables further downstream analysis to be done simultaneously. Furthermore, automation of the system minimizes handling and ultimately human error.

6.1.2 Conventional techniques for 2D receptor-ligand kinetics measurements

6.1.2.1 Flow chamber platform

Flow-based assays such as the parallel-plate flow chamber allow adhesion events to be determined on both a population and single cell level (*216-222*). Similarly, microfluidic systems have been developed for studying interaction events in platelet adhesion under flow at varying shear stresses and shear rates (*216-218, 223*). However, these adhesion events are random, and factors such as the contact area that determines bond density, duration of contact, collision frequency and densities of the ligands and receptors that determine the adhesion probability are variables in the system rather than constants (*63, 64, 221, 224*). As a result, the kinetic parameters obtained are a function of the aforementioned parameters. In addition, transport may play a significant role in the formation and dissociation of bonds which may have an impact on the measured kinetic constants (*63*). Therefore, there is a need to develop new technologies that would be able to better measure cell adhesion events at a high throughput.

6.1.2.2 Micropipette adhesion frequency assay and biomembrane force probe

The micropipette assay utilizes a human red blood cell (RBC) as picoforce transducer to detect adhesion events in the system owing to its low spring constant that makes it an excellent candidate for sensing small forces (10-100pN) (*63, 64*). As shown in ***Figure 6-1***, the RBC is coated with the ligand of interest via covalent linking as previously described (*63*) and aspirated on a micropipette connected to a piezo-driven micromanipulator. On the other side is a target cell bearing the receptor of interest (Figure 2). The two cells are brought into repeated contact and separation using the micromanipulator at defined contact durations for tens to hundreds of times. Binary

adhesion data is obtained; (1) for adhesion observed as the elongation of the red blood cell when the cells are separated, and (0) for no adhesion. The dependence of adhesion frequency on contact duration enables kinetic rates to be determined from a probabilistic model at constant ligand and receptor densities and constant contact area between the cells (Equation 1) (*64*). The probabilistic model is based on the analysis of kinetics for small systems which assumes a small number of bonds are formed between the receptor and the ligand during the adhesion events(*63*) and that the adhesion events are infrequent and follow a Poisson distribution (*64*, *225*).

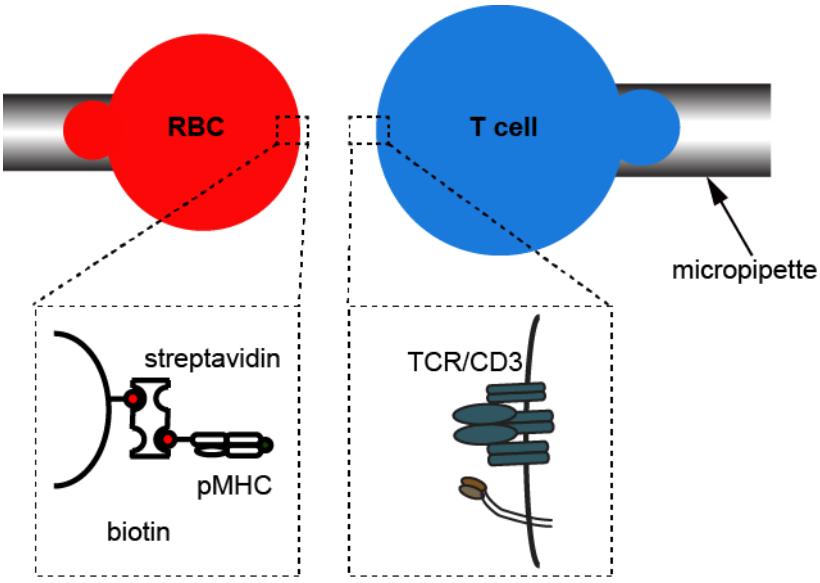

Figure 6-1. Micropipette assay setup. A red blood cell (RBC) bearing the ligand (pMHC) is aspirated on a micropipette and the cell bearing the interacting receptor (TCR) is aspirated on another micropipette. The cells are brought into contact for a defined duration using a piezo-driven micromanipulator. If there is bond formation, the RBC shows detectable elongation upon retraction of the RBC which indicates an adhesion event.

$$P = 1 - \exp(-m_r m_l A_c K_a [1 - \exp(-k_{off} t)]) \quad \text{Equation 6.1}$$

Where P is the adhesion frequency, m_r and m_l are receptor and ligand site densities respectively determined by flow cytometry, A_c is the contact area obtained from imaging, t is the contact time, defined by the user, K_a and k_{off} are the affinity constant and the

dissociation rate respectively. From these parameters the on-rate (k_{on}) can also be determined ($K_a=k_{on}/k_{off}$) (*64*).

A similar but more sensitive platform, the biomembrane force probe, enables the measurement of adhesion events and force (*58, 64*). In this approach a bead bearing the interacting molecules is attached to the red blood cells, and repeated contacts with the receptor-bearing cell are made. These assays enable single-cell analysis of the binding events, and kinetic rates measurements. However, in the micropipette assay only one cell can be interrogated at a time, making this a laborious, low throughput technique. Therefore, this assay would not be suitable for screening a large number of heterogeneous cells such as polyclonal T cell populations where the frequency of antigenic T cells is low. In addition, the complexity in the setup makes it a significant technical barrier in being implemented in a non-expert laboratory.

Therefore, there are opportunities to develop new platforms that would build on the strengths of the existing platforms and address the low throughput challenges in the current systems. Ideally, we want a platform that enable measurement of cell adhesion events and perform force-dependent adhesion measurement at a single-cell resolution. To address this challenge, we developed microfluidic-based designs that would allow for the measurement of adhesion events in multiple cells simultaneously with single –cell resolution. To our knowledge there are no existing platforms for measuring adhesion frequency between receptor and ligand pairs.

The goal of this project was to design and develop a microfluidic-based platform that would enable measurement of adhesion frequency of receptor/ligand interactions of multiple cells simultaneously. **Figure *6-2*** summarizes the main aspects of the assay, and the key parts. The ligand can be on a surface, or another cell, and the receptor is on the cell of interest. These juxtacrine interaction is initiated by bringing the surfaces together for a define time and then retracted at which point the occurrence of bond formation is detected and recorded (*58, 63, 64, 137, 222*). This process will be repeated to get enough data points to extract kinetic parameters using **Equation 6.1**. However, the assays developed so far can only analyze a single cell pair at a time, thus limiting the number of pairs that can be assayed in a single experiment.

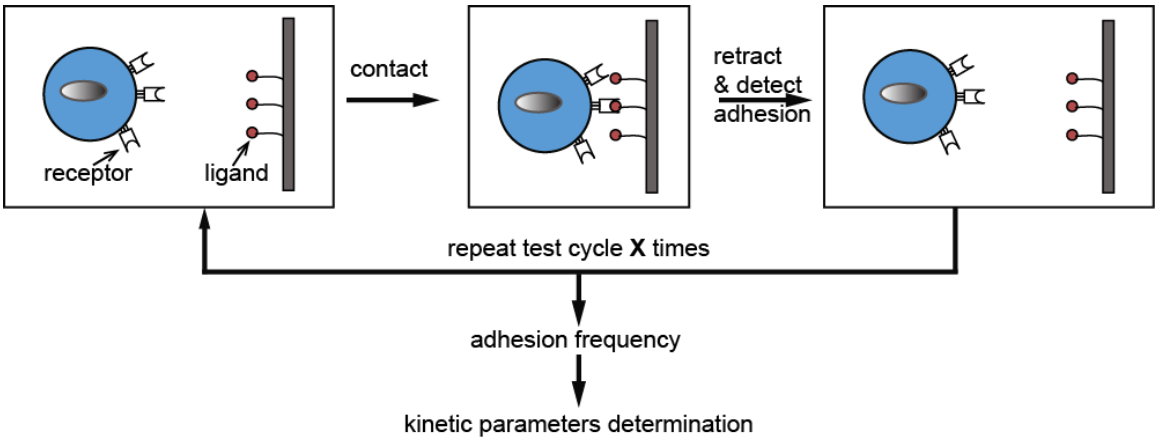

Figure 6-2. Design concept overview. The figure depicts the design concept for developing a platform. A ligand-coated surface or cell and receptor bearing cell needs to come into contact for a defined period of time and then adhesion events are detected and the process is repeated > 50 times to get adhesion probability. From the adhesion probability data kinetic parameters can be computed.

6.1.3 Microfluidic platforms

Through parallelization, automation and integration of multiple functionalities, microfluidic systems may help in closing the technological gaps. Parallelization enables the same experiment to be conducted in individually addressable compartments simultaneously on the same chip, thus increasing the throughput of the experiment. In addition, automated microsystems eliminate the labor-intensive normal laboratory manipulations and reduce the variability in data due to human error and improve the repeatability of the assay (*70, 71, 111*). Another way of improving the throughout is through integration. Integration enables multiple analyses to be conducted on the same chip, which also makes the device more compact. We utilize integration of different components to develop our system including incorporation of cell trapping geometries already discussed in this thesis and elastomeric single-layer (in-plane) microvalves.

Microfluidic platforms developed for cell-cell interactions have focused on measuring the intracellular signaling process downstream of the initial surface receptor-ligand interactions. Dura et al developed a parallelized device with individual trap for pairing antigen presenting cells and T cells and evaluated the Ca^{2+} dynamics induced by the interactions.

6.1.3.1 Single-layer valves

Elastomers such as PDMS allow for the fabrication of active mechanical components such as valves and pumps. PDMS microvalves consists of a very thin membrane that can be deflected to partially or completely close microchannels by application of hydraulic or

pneumatic force. The use of active valves enables the incorporation of movable part in the devices (*76, 226-230*) that are useful in the development of our platform. Membrane valves can either be in plane where both the control and flow channels are in the same plane or top-down valves where the flow channel is below the control channel (***Figure 6-3***). The single-layer valves have reduced complexity in the fabrication process (*226-228*) and we utilize these single-layer microvalves in our microfluidic design.

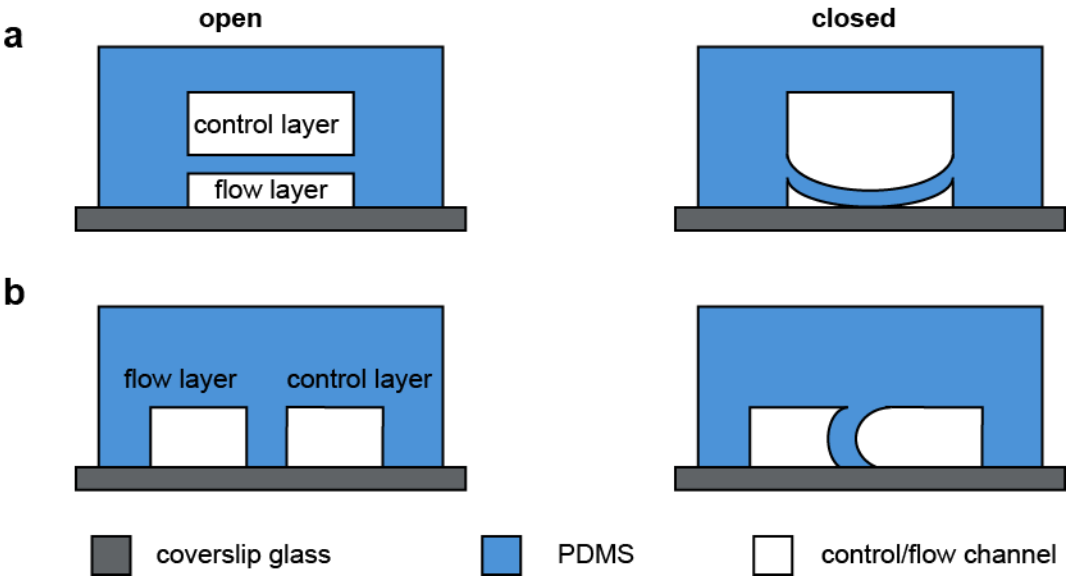

Figure 6-3. PDMS valves. The deformability of the PDMS polymer can be modulated by varying the crosslinking ratio used in the polymer curing. Two main types of valves are used (a) top-down valves that require a 2-layer PDMS device, the top channel is a control layer that is pressurized to deflect the bottom flow channel, and a single-layer (in-plane) valve where both the control and flow layer are on the same plane, and the control channel is deflected into the flow layer. With both valves the control and flow layer are separated by a thin PDMS membrane, and the aspect ratio of this membrane determines that maximum deflection that can be achieved.

In microfluidic platforms single layer valves have been utilized immobilization of the nematode, *C. elegans* for imaging (*75, 231*) by constricting the channels in which the worm is loaded thus restricting the motion of the organism. In addition, the single layer

valves have been used in flow switching for generating dynamic chemical signals (*91*) and particle sorting (*228, 232*). In this chapter we present a new application of these single layer valves in making timed contacts with receptor-bearing cells todevelop an automated, parallelized microfluidic platform that will increase the throughput and ease of performing receptor/ligand adhesion measurements.

6.2 Design concept 1: Membrane-based platform for repeated cell contact

To increase the throughput of the number of cell pairs that can be analyzed simultaneously, we designed a microfluidic platform that integrates a cell/particle trapping module for cell handling and a single-layer control valve module for repeated contact of the cells with ligand-bearing surface (***Figure 6-4***). The cell trapping module has microstructures that fit cells or beads of sizes ranging from 10 – 20 μm with each trap size accommodating an individual particle as shown in ***Figure 6-4***c. Opposite the cell trap module is the control layer than has multiple channels with each channel directly opposite each cell trap structure. The control layer has a single inlet for pressurizing the device to deflect into the cell trapping module resulting in the membrane wall contacting the particles trapped in the cell trap module (***Figure 6-4***). This membrane wall is coated with the ligand of interest prior to the cell/particle loading. With the repeated membrane actuation and retraction, adhesion events may be observed and recorded as outline in **Figure *6-2***.

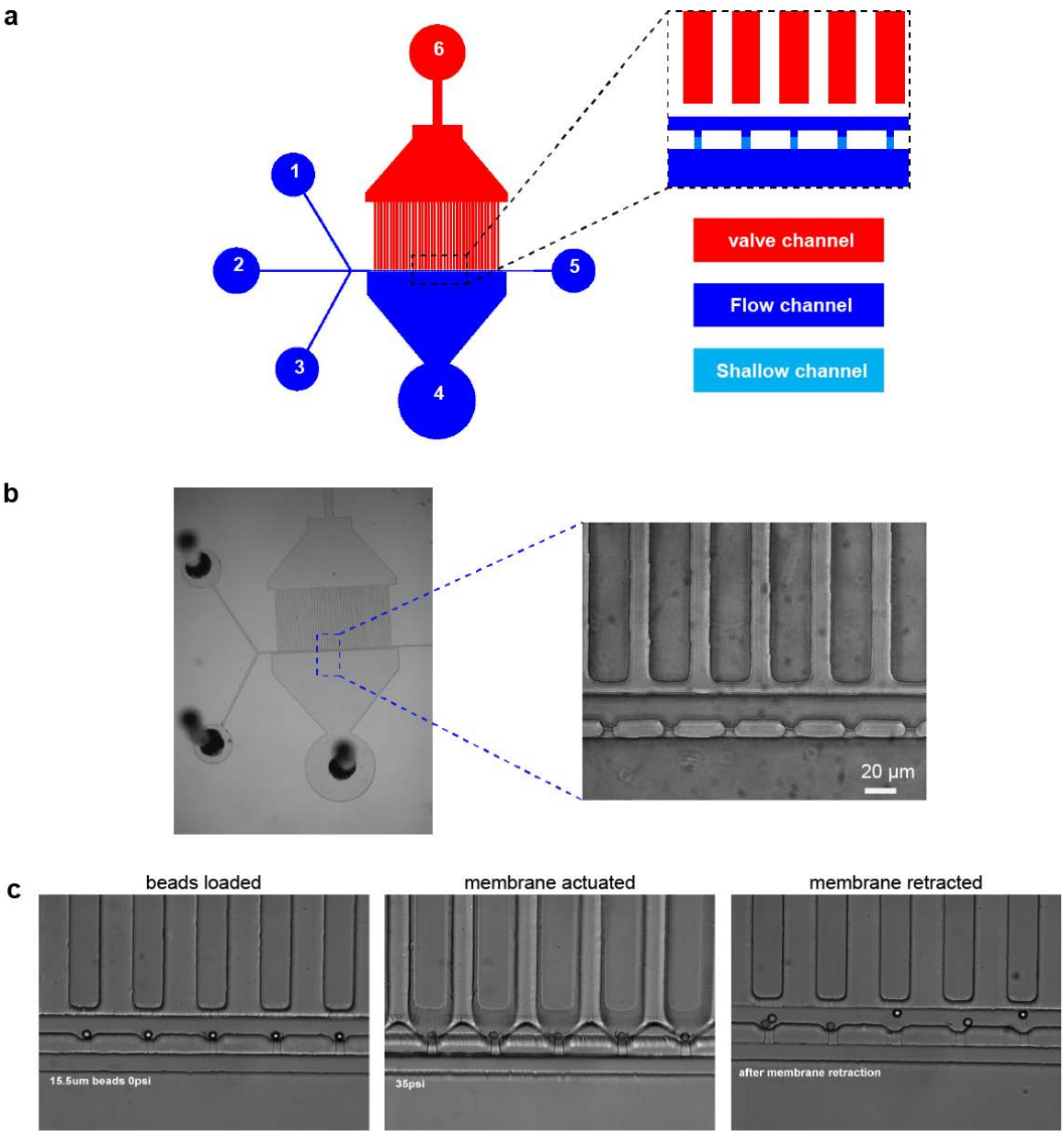

Figure 6-4. Combined single-layer valve control and cell trapping platform. (a) device outline showing the cell trapping module (blue) and the control layer (red), the cell trapping module has 2 or 3 inlets (1-3) and two outlets (4,5). The control layer has a single inlet (6) and no outlet, (b) micrograph of device showing the cell trapping area and the membrane channel. Each cell trap has a corresponding membrane channel on the opposing side, and (c) illustration of how the device works showing beads loaded in the device, membrane actuation to allow the beads to contact the membrane wall bearing the ligand, and after membrane retraction where some beads bind and remain stuck to the wall of the membrane.

The cell trapping module traps are 10 µm wide, and the width of the channel is 30 µm. The cell traps are connected a 2 µm that direct the cells/beads for loading, and the restricted height ensures that the particles are trapped and do no pass through the traps. The overall height of the device is 40 µm (***Figure 6-5***). The overall height of the device is optimize to enable optimal deflection of the membrane to contact the loaded beads/cells.

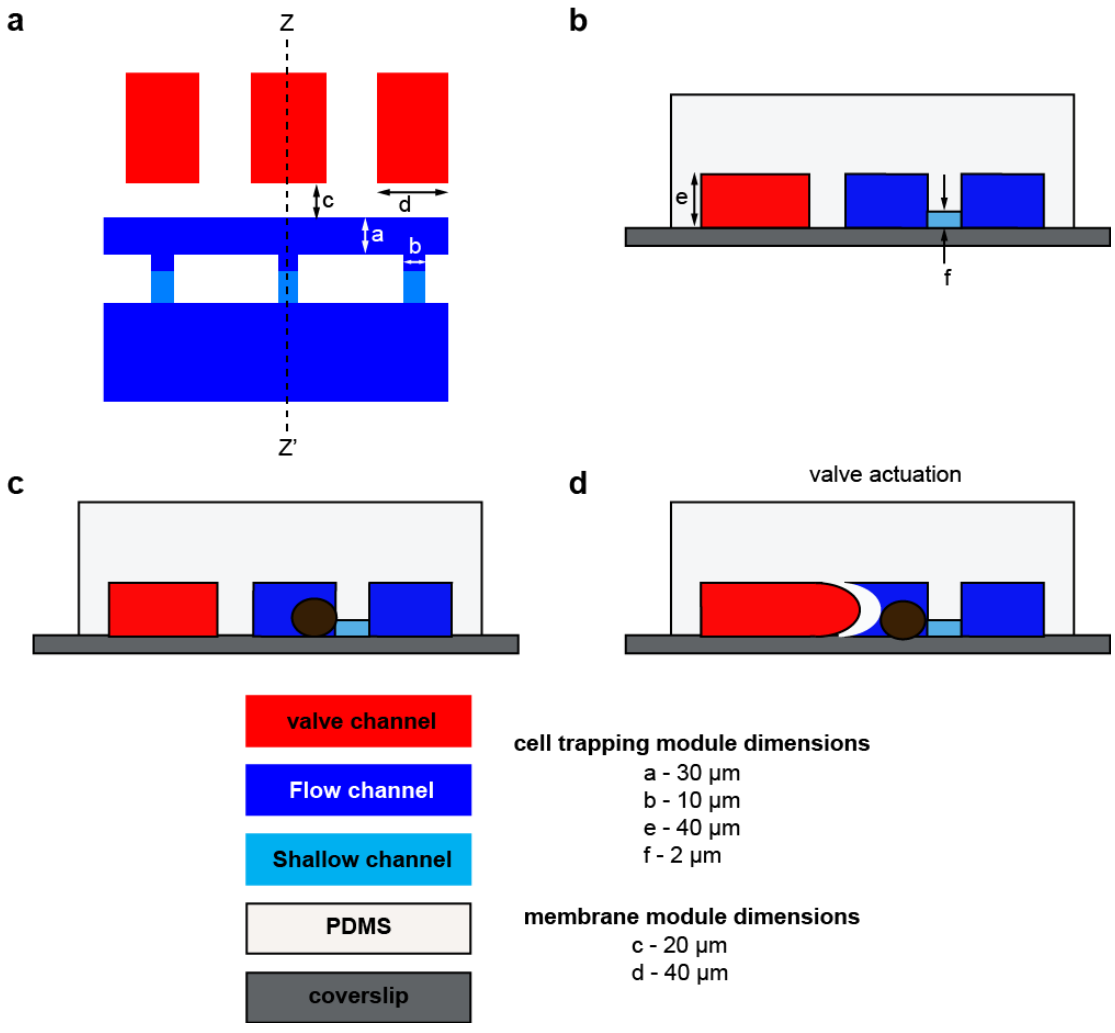

Figure 6-5. Device design layout. (a) top view of device design showing the cell trapping module (blue), and the single-layer membrane valve (red), (b) cross-sectional view (Z → Z') , (c) cross-sectional view showing the position of the cell in the device, and

(membrane actuation that deflects into the cell trapping module channel to contact the loaded cell/bead.

6.2.1 Selective surface functionalization using laminar coflow

The ligand molecules are coated on the membrane wall using biotin-BSA physisorption and biotin-streptavidin coupling as depicted in **Error! Reference source not found.**. In coating the device with the ligand to the device, only the membrane wall should bear the wall to prevent unwanted interaction of the cell receptor with the ligand. We take advantage of the inherent laminar flow (***Figure 6-7***) in microfluidic channels to selectively coat the ligand to one side of the channel by coflowing three different solutions in the device. The membrane to contact the cells will be coated with the protein of interest on the flow channel side using biotin-streptavidin coupling to immobilize a biotinylated ligand on the surface of the channel.

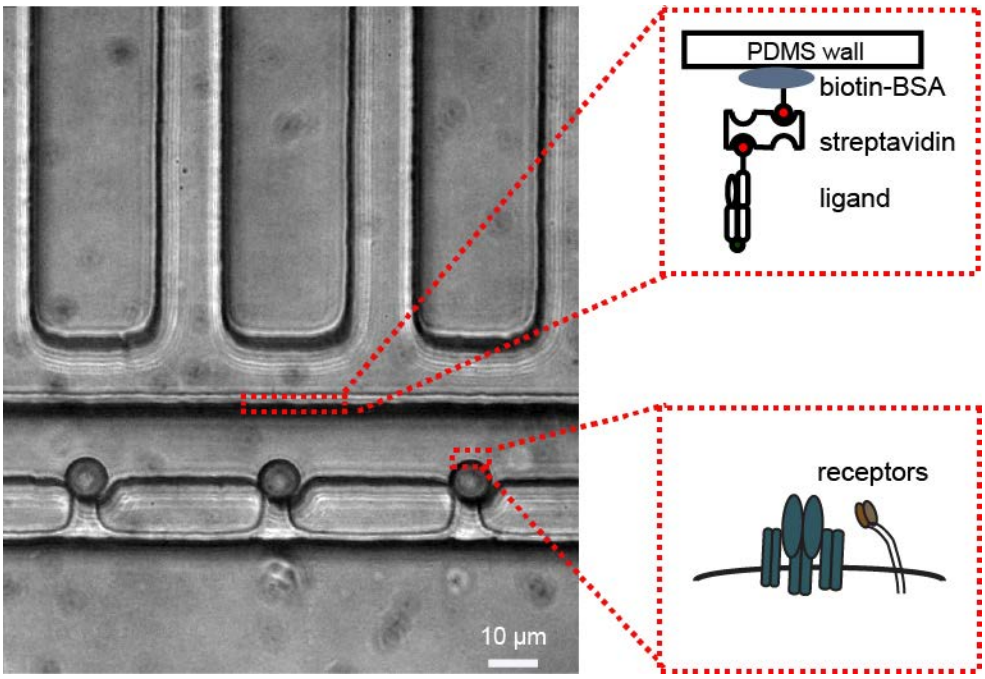

Figure 6-6. Interacting molecules on the device platform. On the platform the receptor is on the cells/beads loaded in the trapping microstructures and the ligands are coated on the side of the membrane using biotin-BSA physisorption and biotin-streptavidin coupling, and laminar coflow for restricted coating of the ligands to the membrane wall only.

The laminar flow allows adjacent stream flow with mixing only by diffusion, and depending on the flowrates the mixing can be negligible (***Figure 6-7***). Laminar coflow (*107*) was used to introduce solutions of biotinylated bovine serum albumin (BSA) and BSA into the device via the three inlets, with the biotinylated bovine serum albumin BSA solution on the side of the membrane to be coated and the subsequent steps are carried out by filling the channels with the appropriate solution (***Figure 6-8***). The formation of the laminar flow streams and effective coating of the device channel was visualized using fluorescently-labels BSA (BSA-FITC). The BSA molecules physisorb on the device channel surface, and the BSA-FITC is visualized during the coating processes and after the device channel is rinsed with PBS buffer (***Figure 6-8***).

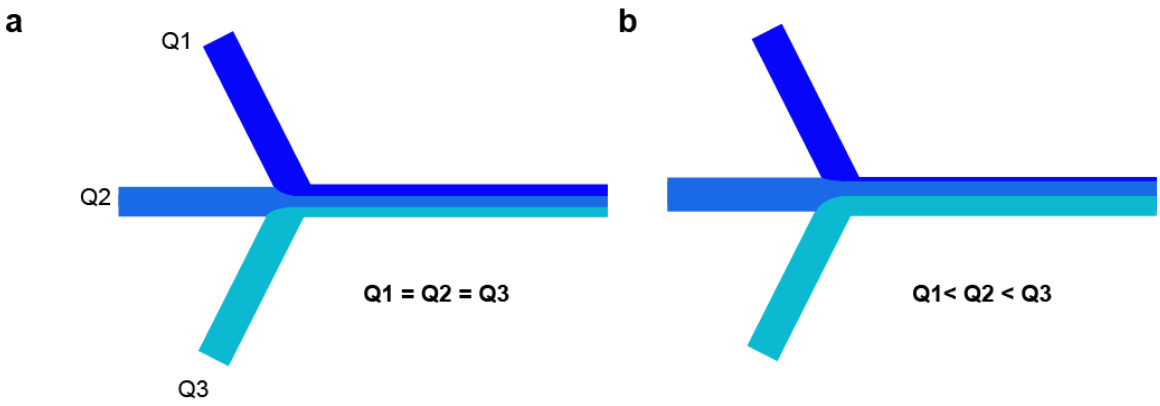

Figure 6-7. Laminar flow in microfluidic channels enable coflow of multiple streams and mixing between adjacent streams is by diffusion. The flow in microfluidic channels is laminar, and convective transport between adjacent streams is minimized. In a 3 inlet channel device, the relative flow rates introduced will determine the width of the individual streams. (a) the streams will have equal widths if the flow rates are the same for all inlets, and (b) changing the relative flow rates will alter the widths of the streams, thus allowing for patterns of different widths to be made in the device, and these can also evolve over time.

The effectiveness of this approach is enabled by the flow characteristics in microchannels. Microchannels have very low Reynolds number and lateral mass transfer is negligibly small and only through diffusion enabling the flow streams to have distinct interfaces (*97*). In our device the Reynolds number is low (Re ~ 6) and the Peclet number is very high (Pe ~ 10^8), therefore mixing between adjacent streams is essentially negligible, thus allowing effective selective coating (*97*). Laminar flow has been used to pattern cells and molecules on PDMS and glass surfaces (*107*, *233-236*). By optimizing the operating parameters we ensured that the diffusion timescale (τ_{diff} ~ 10 s) was much less than the residence time (τ_{res} ~ 0.01 s) of the protein in the microchannel to minimize protein diffusion towards the cell-trapping region. In addition, the flow rate for the stream containing the biotinylated BSA was 10 times lower than that with BSA (or BSA-FITC for visualization purposes) to ensure a very thin portion of the channel (***Figure 6-7***b)

will be coated with the ligand (*237*). The coating of ligand was optimized to ensure homogenous protein surface density by varying the concentration of the ligand, flow rate of the ligand and buffer solution and infusion time.

$$Re = \frac{\rho UW}{\mu} \qquad Pe = \frac{UL}{D} \qquad \tau_{diff} = \frac{L^2}{D} \qquad \tau_{res} = \frac{U}{A_{cs}} \quad \text{Equation 6.2}$$

where U is the flow velocity, W is the channel width, L is the width of the flow stream containing the biotin-BSA, A_{cs} is the cross-sectional area, D is the diffusion coefficient of the protein (~ $10^{-11} m^2/s$, and ρ is density of the solution (~1000kg/m^3)

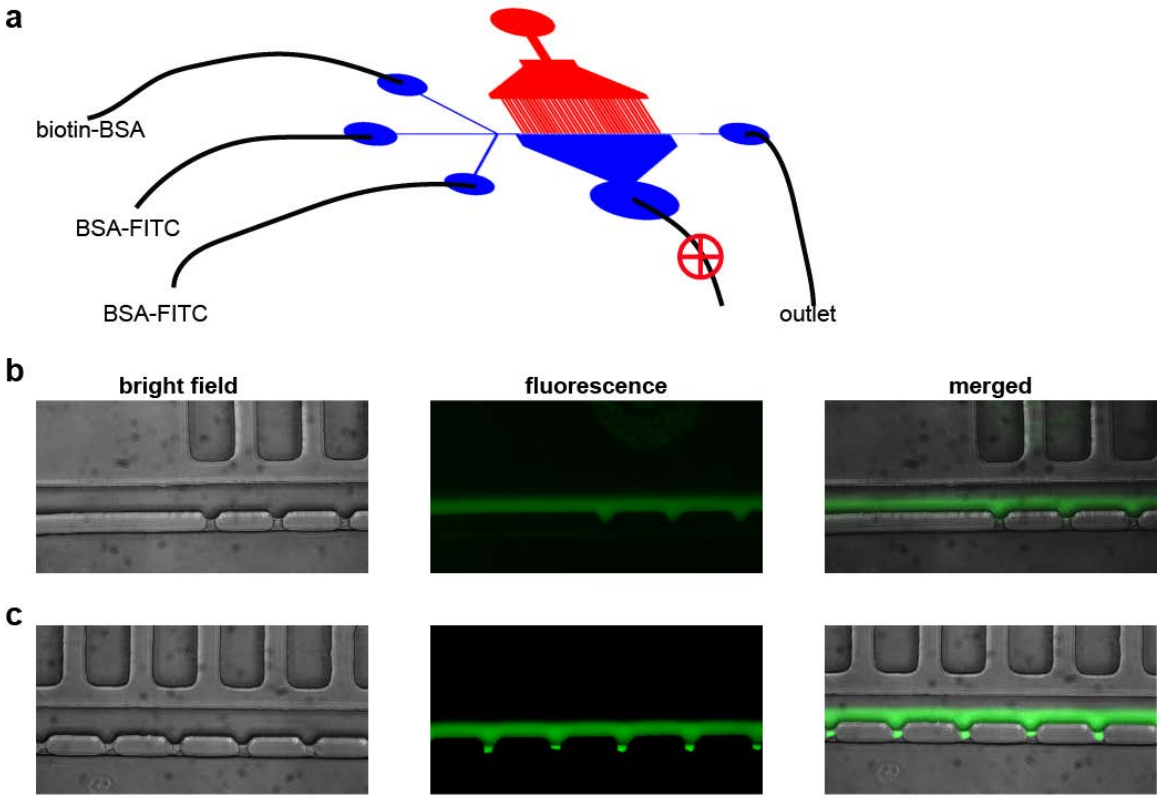

Figure 6-8. Laminar flow-enabled selective device functionalization with stimulating molecules. (a) coflowing of solutions of biotin-BSA and BSA (or BAS-FITC for visualization) with the biotin-BSA stream flowing over the membrane wall enables the membrane well to be biotinylated to coupling of biotinylated ligands using biotin-streptavidin coupling. Micrographs for visualizing the fluorescently tagged stream (BSA-

FITC) to verify the fidelity of the maintenance of the laminar flow stream in the device, (b) upstream, and (c) in the center of the device.

6.2.2 Bead and cell loading

The loading of beads/cells in the device was achieved by passive hydrodynamic flow into cell trapping microstructures. The microstructures are similar in design to those developed in the cell trap array discussed in Chapter 2 – 5. The beads were loaded in the device using pressure-driven flow from a pressurized reservoir. We demonstrate the ability to trap both beads and cells in the device (***Figure 6-9***). The key difference between cells and beads is their mechanical properties, beads are more rigid, and cells are more flexible. These mechanical properties can affect the loading efficiency. However, our platform uses very low flowrates (~ 10 μL/hr), and at this flowrate we can trap either cells or beads of different sizes with high efficiency.

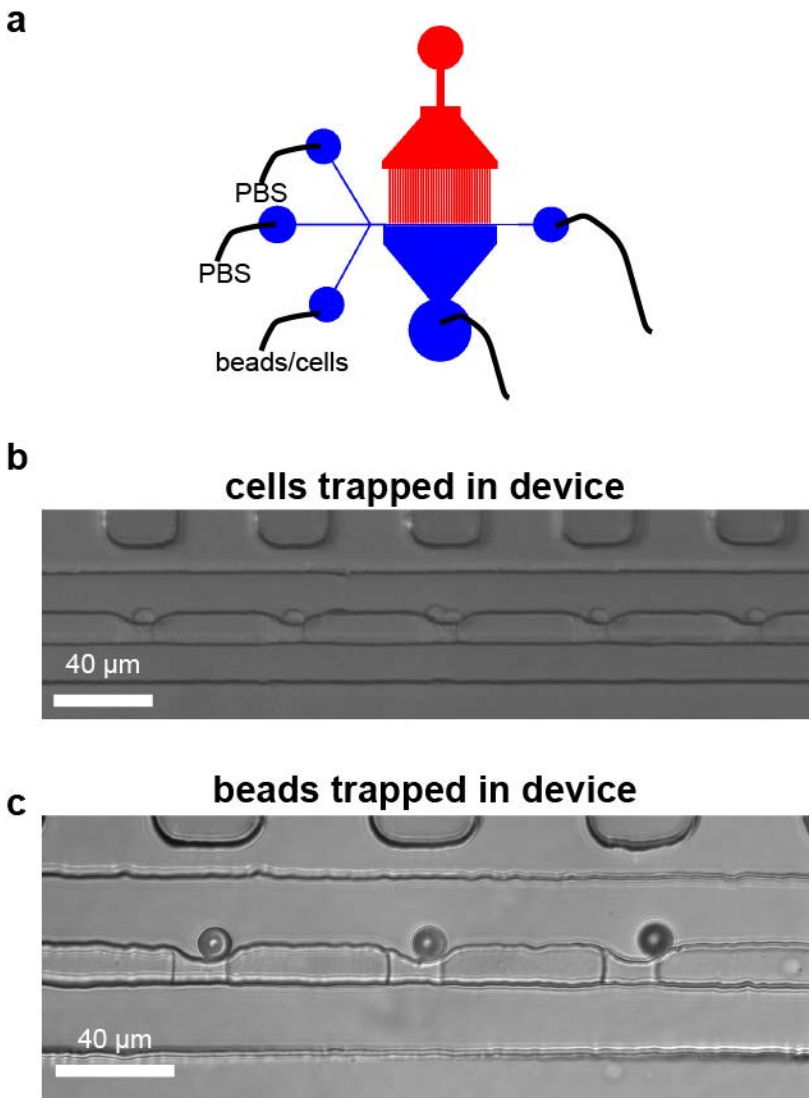

Figure 6-9. Cell and bead loading in the device. (a) Device setup during loading, (b) cells loaded in the device, and (c) beads loaded in the device. Cell and bead loading has an efficiency > 90 % for single cell/bead loading.

The beads are loaded after the device has been coated with the ligand of interest. To ensure that the beads/cells bearing the receptor do not come into premature contact with the ligand-coated membrane wall, the bead suspension is flown in through the third inlet as depicted in ***Figure 6-9***a while simultaneously flowing buffer through the other inlets. Once the cells are loaded then the adhesion frequency measurements can be performed. Each trap on the device accommodates a single cell (Figure 6-9b) or bead (Figure 6-9c).

A single-cell loading of > 90% was achieved in the platform ensuring more than 40 cells were arrayed in parallel for analysis. However, these cells do not fit in one field of view, and the current set up allows up to 10 cells to be viewed simultaneously.

6.2.3 Membrane deformation characterization

The contact between the ligand-coated membrane and receptor-coated bead is enabled by the actuation of the membrane using positive pressure to deflect the cell trapping channel (***Figure 6-4***c & ***Figure 6-5***d). The flexibility of PDMS elastomer is flexible can be modulated by changing the crosslinking ratio added to the polymer for curing. In addition to the stiffness of the PDMS mold, the dimensions of the membrane are critical in determining the extent of deflection of the membrane. The pressure required to obtain enough deflection such that the membrane comes into contact with the cells was determined by varying the pressure applied to the valves using a pressure gauge until the membrane was in contact with cell (30-35psi). An optimal pressure was obtained by varying the crosslinking ratio of the elastomer (22:1 was used) and also by optimizing the thickness of the membrane. The aspect ratio, height-to-thickness of the membrane, will impact the extent of deflection. In general, thinner membranes will have a larger deflection at a given pressure but they have to be able to withstand the pressure without rupturing (*226*).

To pressurize the device, the membrane channels were filled with 50 % glycerol in water w/w, and pressurized at a defined pressure. We characterized the repeatability of the membrane deflection by measuring the deflection against pressure applied to the valve in different devices made in different batches (***Figure 6-10***). As shown in ***Figure 6-10***b, the

deflection at a given pressure is fairly reproducible from device to device at the same elastomer cross-linking ratio. We further verified that the membrane deflection at different channels across the device were the same (***Figure 6-10***c. It is useful to have a uniform deflection across the device to ensure that all the beads loaded come into contact with the membrane. However, we note that with cells due to heterogeneity in particle different deflections might be required to contact the cells to be different to contact. Presorting the cells by size would tighten the size distribution. Overall, we found that using 22:1 PDMS ratio for our device, a pressure input of 30 psi was sufficient for the membrane to contact the beads loaded in the device.

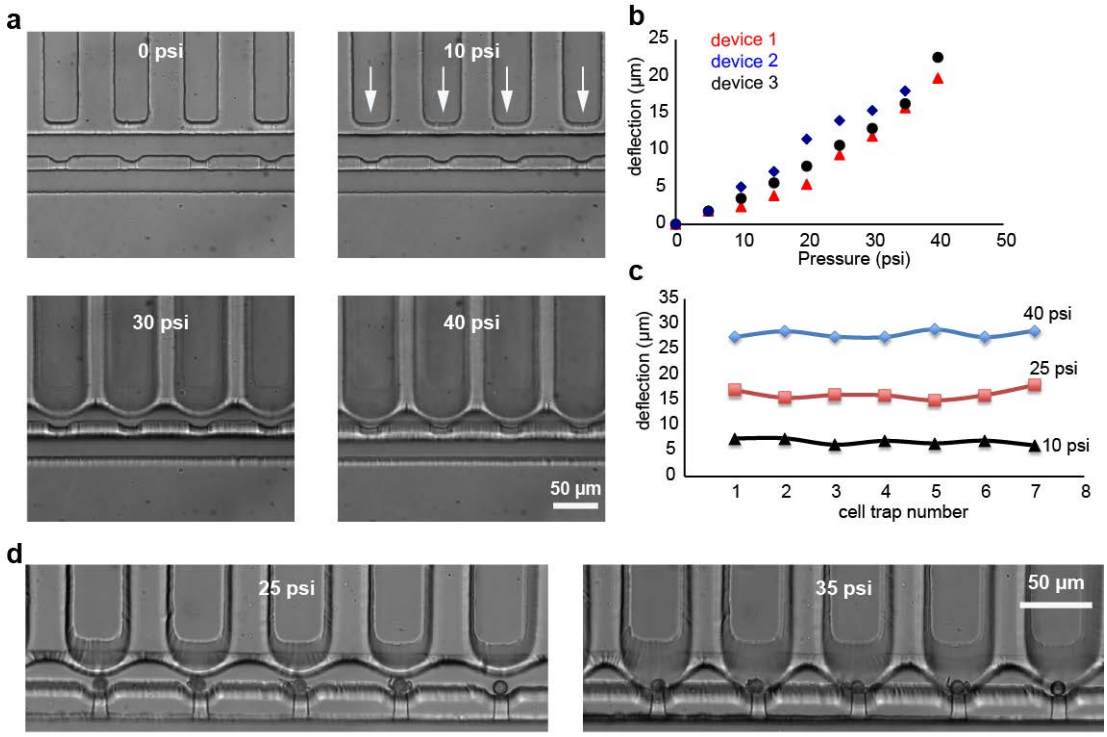

Figure 6-10. Membrane deflection characterization. The membrane channels were filled with 50 % glycol w/w and the inlet of the control module was connected to a pressure source with a electronically-controlled solenoid valve controlling the opening and closing of the valve. (a) micrographs of the device before pressure is applied and at 10, 30, and 40 psi showing the deflection of the membrane into the cell trapping channel, (b) deflection of the membrane as a function of pressure for different devices, (c) deflection

at the indicated pressures on different channels along the device, and (d) membrane deflection with beads loaded in the device at 25 psi and 35 psi.

However, one major drawback with the design was the difficulty in visualizing the point of contact between the bead and the membrane, and this would be more significant when using cells. From ***Figure 6-10***d, it is difficult to ascertain whether the membrane was in contact with the beads at 25 psi. This is mainly because the maximum point of deflection is above the bead position since the channel is twice the diameter of the bead. As a result, the membrane can occlude imaging. To determine the precise pressure and deflection at which the membrane comes into contact with the, we used fluorescently-labeled beads and filled the membrane channels with a fluorescent dye FITC, and visualized the position of the beads and the membrane channels during deflection in 3D using confocal microscopy (**Figure 6-11**a). Once the membrane is actuate, one can easily see the point of contact between the membrane and the beads is 3D with fluorescence imaging. In our analysis, we found that an actuation pressure would ensure that the membrane just contacts the beads. However, understanding that there might be device to device variation, it will be still challenging in using this approach since the samples we would use are not fluorescently labeled and it is impossible to characterize each device used in the experiment.

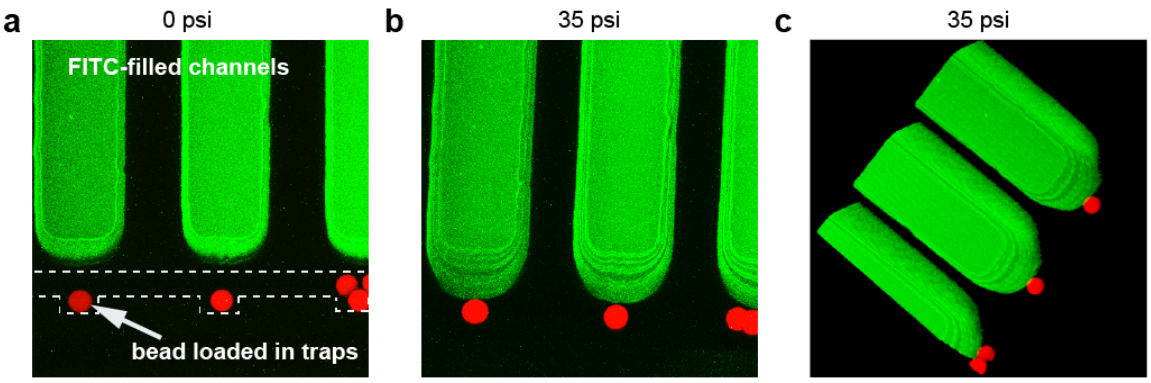

Figure 6-11. Visualizing the contact between membrane wall and beads by confocal microscopy. To get a clear view of the contact point between the membrane and the bead, confocal imaging was performed, the device membrane channels were filled with FITC dye, and red fluorescent beads were loaded in the device. (a) Beads loaded, membrane valve closed, and (b) membrane valve open, the beads are in contact with the membrane.

6.2.4 Adhesion events detection

Finally, once the contact is made for a defined amount of time, the adhesion events are detected through observation of the particle movement when the membrane is retracted. When a bond is formed, the cell/bead becomes attached to the membrane and upon retraction, the bead/cell will be dragged along with the membrane. The bead will either detach if the drag force against the bead movement is stronger than the bond(s) formed or the bead will remain attached to the membrane when pressure returns to 0 psi (***Figure 6-4***c).

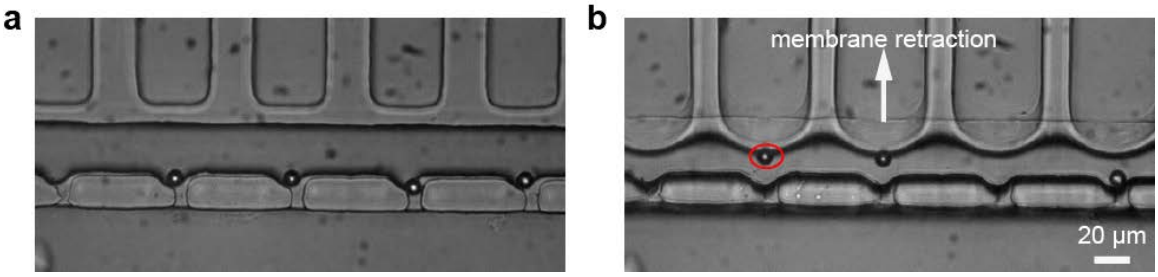

Figure 6-12. Observing adhesion to the ligand-coated membrane wall. Upon contact with the membrane, the receptor-bearing beads can form a bond with the ligand on the

membrane, when the membrane is retracted if the bead forms an attachment with the membrane it will be dragged out of the trap for a distance and may detach if the drag force becomes larger than the bond force. When the bead detaches it may return to the trap or flow along the channel. In the figure the third bead from the left disappeared during membrane retraction as a result of being washed away with the flow induced during membrane movement.

6.2.5 Measuring streptavidin/biotin interactions

Having characterized the bead loading and membrane actuation, we demonstrated the potential of the platform by measuring the interaction of biotin and streptavidin. The device membrane wall was coated with biotin-BSA and then streptavidin-coated beads were loaded. The membrane was actuated and retracted 10 times while taking time-lapse images to then analyze the adhesion off-line. An adhesion event was defined as when the bead was observed to move a distance half the diameter of the bead or when the bead remain attached to the membrane after membrane retraction. We measured the adhesion events at 2 s and 5 s contact time, and observed an increase in adhesion frequency from 2 s to 5 s as shown in Figure 6-13. In addition, we analyzed the effect of site density of the interacting ligands. At the concentration we analyzed, there was no difference in the adhesion probability at 5 s contact time. The reason might be two-fold, saturation of the number of interacting molecules and also saturation of the adhesion probability curve at long contact times. Previous, adhesion frequency data show that the curve plateaus after 2 s contact time (*64*). Overall, this data demonstrates our ability to perform adhesion measurements in the platform. In this study, we are able to observe up to 10 cells simultaneously, thus allowing faster acquisition of the data. With more improvement to the design and also in data acquisition the throughput of the platform can be improved further.

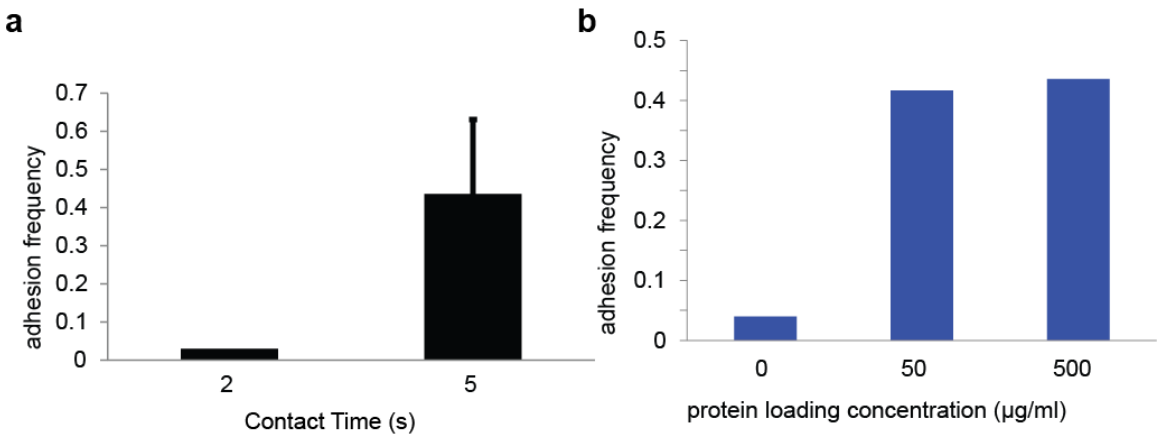

Figure 6-13. Adhesion events between biotin and streptavidin interactions. Repeated contacts between the biotinylated membrane and streptavidin-coated beads loaded in the device, and adhesion events were counted. (a) Contact time dependent adhesion events at 2s and 5 s contact time, and (b) density dependent adhesion frequency showing no change in adhesion frequency at the two concentrations used in the experiments.

6.2.6 Challenges with the setup

While we have demonstrated the ability to perform adhesion measurements on the platform, the platform presented challenges in how to accurately detect when the membrane is in contact with the beads. This is a critical factor in the setup since these adhesion events measurements are time dependent with measurements taken over a range of 0.1 s to 10 s. Therefore, the ability to determine when the membrane contacts the bead is crucial in making these timed contacts. In addition, the platform currently was not amiable to perform similar measurements in mammalian cells. Unlike beads that are rigid, cells are more flexible and susceptible to damage by harsh mechanical forces that they might experience upon contact with the moving membrane. One way to address the harsh contact by the membrane is by using a voltage-controlled pressure valve to ramp up the pressure instead of using the on/off solenoid valves used so far. That way one would

be able to control the rate at which the membrane deforms, and effectively the impact force the cells may feel upon contact with the membrane.

6.2.7 Using a bead attached to the membrane to make the contact

To address the issue of the visualization of the contact point and occlusion of the cells/beads by the membrane, we devised a new format for the device where beads attached to the membrane were used to contact the receptor-bearing beads/cells (***Figure 6-14***). These beads were functionalized with the ligand of interest, and streptavidin. The device is coated with biotin-BSA as described above using laminar coflow. Streptavidin beads are then introduced into the device and loaded in the traps. The membrane is actuated to contact the beads for 10 s to ensure that all the beads have an opportunity to form multiple interactions with the biotin molecules on the membrane surface (***Figure 6-14***a). Finally the membrane is retracted and the beads remain attached to the membrane as shown in ***Figure 6-14***a due to the strong biotin-streptavidin interaction (*144*). With this setup, the ligands are coupled to the streptavidin beads via biotin-streptavidin coupling (***Figure 6-14***b), and these ligands can be coated on the beads in the device once the beads are attached to the membrane or before the beads are loaded using subsaturating concentrations of the ligands to ensure that some of the biotin binding sites are available for the beads to attach to the membrane. Finally, we were able to successfully pair up streptavidin beads attached to the membrane with biotin beads (***Figure 6-14***c).

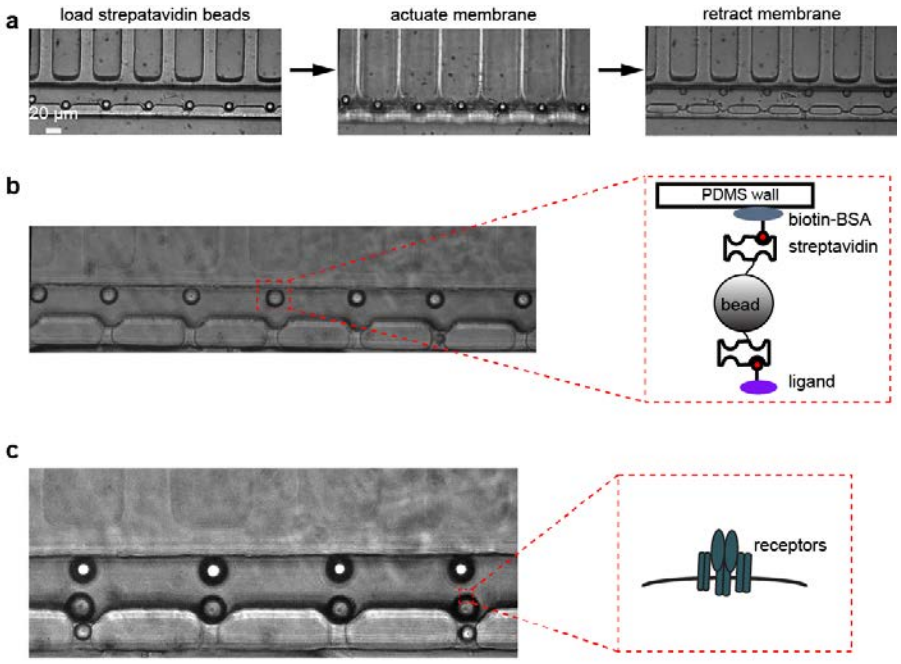

Figure 6-14. Setup using membrane-bead actuation. (a) Streptavidin beads are loaded in the device after the device membrane wall is coated with biotin-BSA. The membrane is then actuation for 10 s to ensure all the beads attach to the membrane via the biotin-streptavidin interaction, and then the membrane is retracted, and we can see that the beads are attached to the membrane. (b) Molecule configuration on the membrane side. The streptavidin beads also have streptavidin molecules coupled to biotinylated beads, and (c) second set of beads bearing the receptor are loaded into the traps

Once the beads are paired repeated and timed contacts were made to measure probability of binding events (***Figure 6-15***). The contact with the beads offers better precision of the contact area that can now be easily visualized on regular microscope setup (***Figure 6-15***). In addition, the site density of both the receptors and ligands can be determined by flow cytometry. In the first setup, it is difficult to determine ligand densities. The ligand and receptor densities have an effect on the binding probability and are parameters in the probability equation used to determine the kinetic parameters (Equation 1). Moreover, the smaller pressure input < 10 psi are required to contact the beads, using lower pressures is beneficial in minimizing chances of the membrane rupture, and reducing the overall deformation of the device.

We observed attachment of the biotin beads to streptavidin beads, and the biotin beads would remain attached to the streptavidin beads. With this platform we anticipate measuring binding events between ligands coated on the bead surface and cells bearing a cognate receptor. In line with the goal of this thesis, we are interesting in making binding measurements between the T cell receptor and pMHC coated on the streptavidin beads. Being able to measure these binding events will close the gap in our ability to measure the initial interacting and then couple with the functional response measurements such as calcium dynamics, and protein expression shown in the preceding chapters.

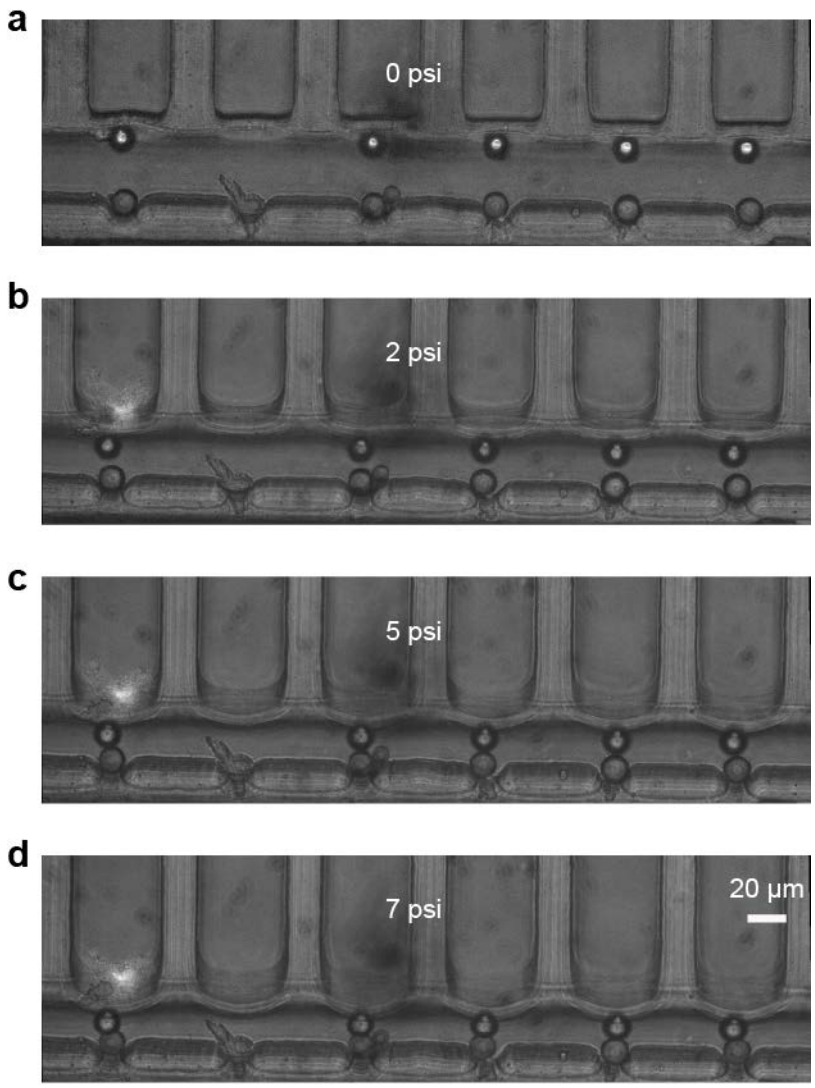

Figure 6-15. Bead-bead contact enables better visualization of contact area. (a) Pairing of streptavidin beads (on the membrane), and biotinylated beads (in the trap), (b – d) membrane actuation at increasing pressures shows that the bead pairs come into contact at 5 psi.

Compared to the micropipette adhesion frequency assay, this platform will allow parallel measurements of individual cells thus increasing the throughput of the assay. The increased throughput is important in expanding the breadth of inquiry that can be done in immune cells. Often with the micropipette adhesion frequency assays monoclonal T cells are used where all the T cells have a common antigenic peptide. However, in the case of

studying interaction T cells from a polyclonal population where only a small percentage of the cells are antigen specific, the current throughput of the micropipette assay makes it impossible to analyze polyclonal populations. Such analysis would require a platform that can assay hundreds to tens of thousands of cells in a single run.

Here we show that we have designed the first generation microfluidic-based adhesion frequency platform that will allow the measurement of receptor/ligand interaction kinetics on the cell surface. More work will need to be done to ensure efficient bead attachment to the membrane > 90% to maximize the number of cell pairs that can be analyzed simultaneously. Through the trapping of tens of cells parallel measurements of cell binding events can be performed simultaneously, and we anticipate the ability to scale up the platform to allow for hundreds of cells to be analyzed simultaneously. Coupling this platform with automated imaging and data processing will enable high-throughput receptor-ligand interaction kinetics. Also, by coupling this system with fluorescence imaging as has been previously demonstrated (*58*), Ca^{2+} dynamics can simultaneously captured to correlate the binding events with the Ca^{2+} data. In our Ca^{2+} measurements we do not know the timing of the bond formation and the subsequent Ca^{2+} signaling, and this setup can give us insights on the timing of these signaling events. In addition, with the addition of other control and flow modules, further downstream analysis can be performed on the same cells after measuring the binding events.

6.3 Design concept 2a: Flow-based adhesion frequency platform

6.3.1 Device design and setup

In parallel to the membrane-based adhesion frequency described above, we developed an adhesion frequency platform based on flow control, which we term flow-based adhesion frequency platform. In the membrane design, we used an actuated PDMS membrane to make a contact between ligand-coated surface and a receptor-bearing cell/bead. One drawback with this approach is that it is difficult to control the membrane impact force that may have an influence on the adhesion measurements. In the flow-based approach, pressure controlled fluid flow is using as a driving force.

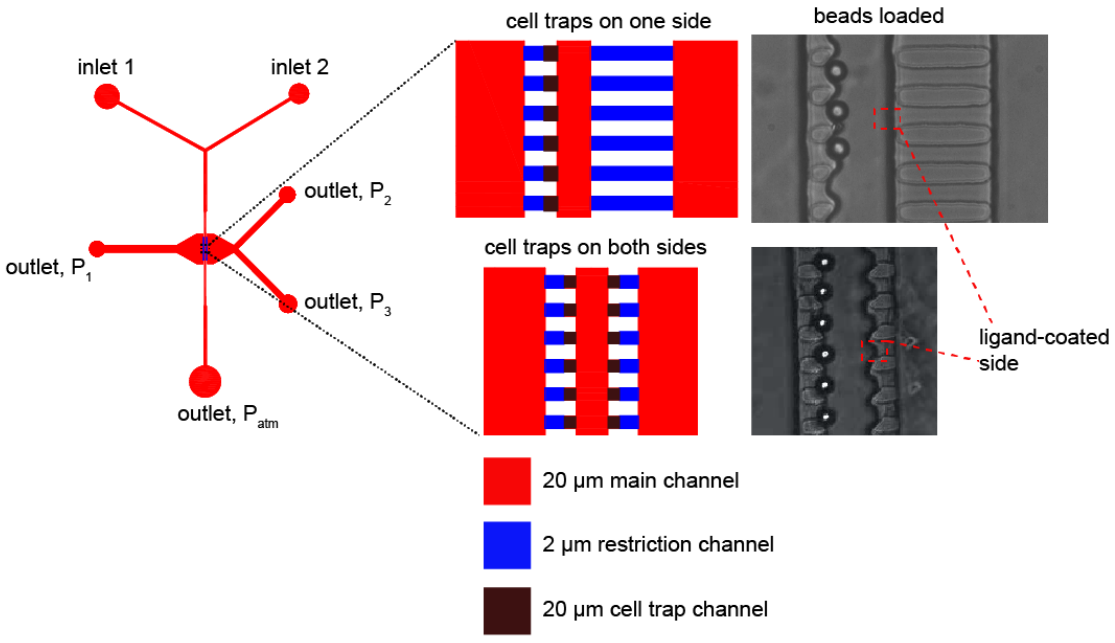

Figure 6-16. Flow-based adhesion frequency platform. The device consists of 2 inlets for use in laminar coflow. The device is a single layer PDMS mold, and is molded from a 2-layer SU8 mold. The main channel is 20 µm and cell traps are 10 µm wide with 2 µm restriction channels. The first configuration had cell traps on one side of a channel and restriction channels 2 µm tall, and the second configuration has cell traps on both sides of the main channel.

6.3.2 Working principle of the flow-based device

The ligands are coated on one side of the channel using laminar coflow, the same approach used in the membrane-based platform described above. During the protein coating, only outlet 4 is open, outlets 1-3 are closed using a clamp-style pinch valve. Once the ligand is coated, in our proof of concept study we used biotin-BSA, with biotin being the ligand of interest, streptavidin beads were loaded in the device on the side without the ligand (Figure 6-17). Modulating the pressure difference in the device then allows the beads to move to the ligand coated surface, and they are in contact with the surface for a defined time. The pressure is switched to move the non-interacting beads from the ligand surface followed by a larger pressure to move all the beads from the ligand coated forces (Figure 6-17). The process is repeated to obtain adhesion frequency data.

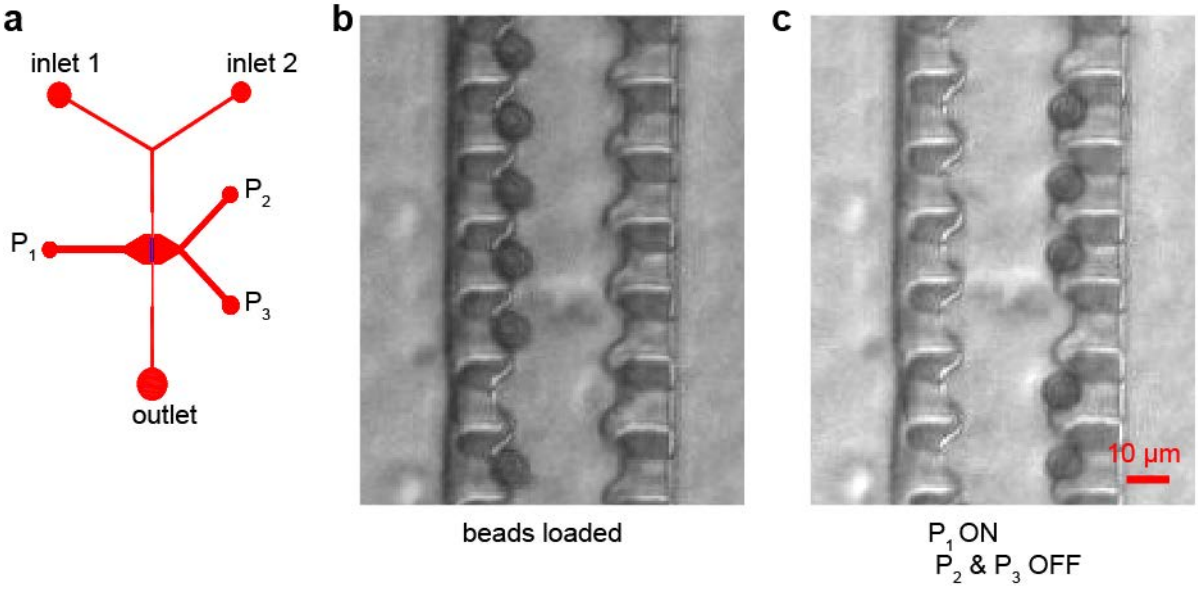

Figure 6-17. Fluid flow setup for device operation. (a) device inlets/outlets, (b) beads are loaded through inlet 1, while P_1 = 1 atm, P_2 & P_3 are off, and the outlet is at

atmospheric pressure, and (c) the beads are moved to the ligand-coated surface by pressure-driven flow, P_1 = 0.5 psi, P_2 and P_3 are off.

The challenge is in modulating the pressure differences, and ensuring that the applied flow is enough to allow the beads to be move back and forth and well-controlled to enable determination of the binding events. The pressure control can be automated, the pressure difference is controlled by on/off solenoid valves. We measured the binding events for streptavidin beads on biotin-BSA-coated beads at 5 s contact time. The measure adhesion probability was lower than expected (< 10 %) likely because the flow force was much larger and resulted in bond breakage before the bond formation was detected. More characterization of the hydrodynamic force will need to be done to ensure all binding events are detected, and account for nonspecific interactions. One of the advantages of this approach over the membrane-based approach is the ability to have the cell traps densely packed enabling up to 40-50 cells to be analyzed simultaneously, with great potential to increase the throughput through arraying of traps to a throughput of 100 – 300.

6.4 Design Concept 2b: Combined microfluidics and magnetic tweezers

Implementing fluid flow is challenging since it is dependent on the flow resistance in the device which may vary from device to device, and may change if some of the device channels become occluded. Moreover, it is difficult to achieve a uniform flow distribution along the device channel, thus resulting in differential force application along the device channel. An alternative approach that can be explored in the future is to utilize magnetic force to drive the bead movement, and use the device with cell traps on both

sides of the channel shown in Figure 6-16. Magnetic tweezers have been used in single-molecule measurements including DNA twisting and stretching (*238-244*). Magnetic tweezers can be easily integrated on conventional microscopes (*245*) or alternatively magnetic electrodes can be integrated on chip. In addition, magnetic tweezers allow for force measurements and force dependent interactions to be analyzed (*239*, *241*, *244*, *246-248*).

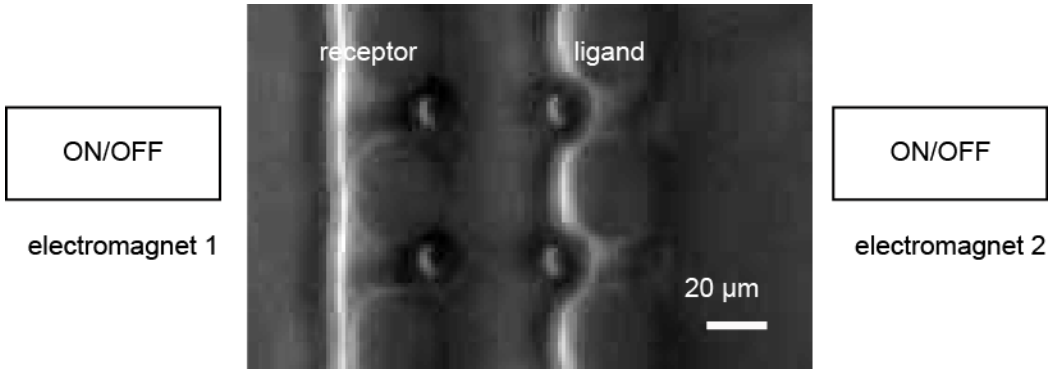

Figure 6-18. Using magnetic force to drive movement of ligand-coated beads. In the proposed setup two electromagnets are setup. Cells or beads are loaded in the device, and then magnetic, ligand-coated beads are loaded on the adjacent traps. Ligand-coated beads come into contact with the receptor-bearing beads/cells by turning on electromagnetic 1 for a defined time and then electromagnet 1 is turned off and electromagnetic 2 is turned on to break the contact. Adhesion is observed by the ability to observe movement of the receptor-bearing bead/cell.

For this setup, two electromagnets are setup on each side of the device as shown in ***Figure 6-18***, and alternating turning on of the magnets allows for the movement of the magnetic, ligand-coated beads to come into repeated contact and no contact with the receptors on the cell surface. The detection of the binding events is based on the observed movement of the cell when the ligand beads are moved from the cells. When a bond is formed between the ligand and the receptor, moving the bead drags the cell with it, and then a small suction is applied at the cell traps to reload the cell in the cell trap. The approach would require force measurements of the force exerted by the magnetic

tweezers, the suction force for retrapping the cells after each contact cycle to allow repeated measurements on each pair. This lays the background on the designs that can be developed further for a platform for high-throughput adhesion frequency assay.

6.5 Conclusions

Here I have demonstrated a proof of concept for the ability to design and develop a microfluidic-based platforms for measuring receptor/ligand interactions on cell membranes and surfaces. Surface molecules are critical in initiating signaling transduction pathways, and understanding these interaction kinetics can be insightful in understanding the mechanisms in these signaling molecules and differentiate between normal and diseased state. Current assays for evaluating surface molecule receptor/ligand interactions are low throughout and require sophisticated equipment and expertise that hampers the dissemination of the assays in more laboratories (*63, 64, 137*). To my best knowledge no platform exists that enables parallel analysis of receptor/ligand interaction kinetics at a single-cell resolution. Taking advantage of the ability to integrate multiple modules and parallelize measurements, microscale based platforms were developed that would enable measurements of cell receptor interactions with a surface-anchored molecule were developed.

The first approach integrates the characteristic single-layer valves and cell trapping microstructures. The trapping microstructures enable deterministic array of cells or beads on the platform and the single-layer valve channels allow for repeated contact between receptors and ligands for determination of adhesion frequency. In the future, with better control of the valve actuation, force measurements can also performed similar to those

performed with the biomembrane force probe with the added advantage of measuring multiple cells in parallel. The second platform design integrates cell trapping and magnetic bead trapping with off-chip magnets to drive the bead bearing the ligands. I envision this platform will be coupled for software for controlling the external magnetic tweezers and image acquisition software, and image analysis software for the detection of adhesion events. Together these two designs presents a new approach in developing simple, high-throughput platforms for receptor/ligand interaction kinetics.

The increased throughput in the assay will enable measurements beyond kinetic parameters including the determination of frequency of interacting cells within a population of cells. In addition to measuring receptor/ligand interactions, this line of work can be expanded to include simultaneous or sequential determination of intracellular signaling events and functional outcome. With the integration of other modules such as the perforated membrane presented in Chapter 3 and 4, more robust fluid exchanges can be performed on chip to enable on-chip staining for immunofluorescence staining and smFISH for mRNA quantification of the cells after the binding events. The next step would be implementation of the platform with mammalian cells. So far we have demonstrated the use of the device in measuring binding events in beads bearing streptavidin on a biotin surface. Biotin/streptavidin form stronger interactions compared to the receptor/ligand interactions in most biological molecules. These platforms will be applicable to many different cell types beyond T cells where juxtacrine interactions are involved.

7 CONCLUSIONS AND FUTURE DIRECTIONS

In this thesis, new microfluidic-based tools for single-cell analysis in immune cells have been introduced with the goal to bridge the gap in the some of the shortcomings encountered in conventional approaches. Evaluating immune cell response specifically in T cells requires tools that allow both dynamic signatures such as $Ca^{2+,}$ mitochondrial polarization, and actin dynamics and static signatures to be evaluated. Thus far, most approaches such as flow cytometry, and western blot have enabled the measurement of one specific readout, and enable the analysis of cells in a bulk population that can mask cell heterogeneity. As an emerging technology, microfluidic systems can address the gaps to advance the type of data that can be obtained.

Utilizing the inherent small size of microfluidic systems, this thesis focused on developing tools that would enable robust handling and positioning of single-cells for stimulation and subsequent analysis of response on a single-cell levels and over a large number of cells for population statistics to be derived. In chapter 2, the versatile application of the high density cell trap array is shown for a simple analysis T cell response to both soluble and surface-molecule stimulation. The assay enable rapid analysis of Ca^{2+} signaling as a functional readout for a large number of cells per condition. This allows screening of Ca^{2+} functional response of T cells to different antigenic peptides, and also analysis of responsiveness of a T cell population. In chapter 2, a monoclonal population was used to demonstrate capability, however this assay would be critical in evaluating immune response in polyclonal T cell population such as for samples obtained from human tissues. The assay has been applied to a number of projects

in the lab including a recent publication in evaluating Ca^{2+} response in cells during the early stages of T cell development (*249*).

In Chapter 3, the development of an integrated high-density cell trap coupled with a perforated membrane for dynamic soluble cue generation was introduced. The platform enables the cellular microenvironment to be experimentally modulated in a precise manner with simultaneous observation of cell response to extracellular space changes. This enabled, the modulation of Ca^{2+} signaling in our studies that would then enable the design of studies that aim to evaluate how the intracellular signaling dynamics affect gene expression and functional response of immune cells (*16, 93, 140*). The platform is currently being used in independent projects in the laboratory that aim to evaluate the effect of oscillatory input signals on the output signal. In addition, the perforated membrane design can be coupled to other existing chip designs beyond the cell trap array including platforms that have been developed for handling small organisms such as the nematode (*1*). To expand on the utility of the device, further optimization of both the cell traps and the pore dimensions will be needed to allow for application with cells of different sizes. The pore dimension is useful in ensuring efficient fluid transport and also efficient cell loading; smaller and more flexible cells can pass through relatively larger pores.

Furthermore, this 2-layer platform has multifaceted applications that are demonstrated in Chapter 4 based on the robust fluid exchanges. The device enables multiple assays to be performed both simultaneously and sequentially, thus allowing different types of readouts

to be obtained. Ca^{2+} signaling dynamic, protein phosphorylation, mRNA expression and cytokine secretion measurements are demonstrated with at least 3 of these different molecular readouts being performed on the same sample, thus enabling direct correlations to be drawn. We envision, that this microchip will be broadly applicable in enabling single-cell analysis to different types of stimulation and functional readouts, and the assays are applicable to other cell types. Furthermore, the dimensions of the cell trap array can be modified to fit different cell sizes; thus allowing the application of the platform in different cell types beyond immune cells. Furthermore, the methodology for operating the platform is relatively easy, making it easy to be used in any biology laboratory with conventional microscopy setups. In this thesis, the ability to keep the cells in the device for up to 24 hours was demonstrated, and this characteristic may be used for long-term monitoring of cell signaling dynamics such as NFκB nuclear localization dynamics on microscopy setups that have a cell incubation chamber.

In addition to the hardware, further improvements in image and data processing will be important in enabling multiparametric analysis. Developing an automated approach that allows cell indexing at both low magnification used in calcium imaging and at high magnification used in smFISH imaging would eliminate manual cell annotation. Moreover, the use of a scanning confocal microscopy for smFISH imaging may provide a faster way to acquire data. Also, with a controlled cell incubator chamber on the microscopy setups, longer duration live imaging may be performed which ensuring that the cells are not under any stress induced by low oxygen or changes in humidity.

In addition to performing stimulation and functional analysis on a single-cell level over a large number of cells, another area of focus is the preprocessing of samples before performing an assay both in conventional assays and microfluidic platforms. Usually, separation techniques are employed to separate the cells from a crude sample that can be either from spleen, thymus, biopsy tissue or whole blood. In Chapter 5, we introduced another new application of the high-density cell trap array in enabling the removal of red blood cells and trapping of leukocytes in the device from less than a drop of blood. Therefore, the platform can be used for multiple functions; (1) separation of leukocytes, (2) stimulation of leukocytes on chip, (3) functional analysis of leukocytes, and (4) leukocytes differential counting that can be informative in disease diagnosis and monitoring. The relative simplicity in device operation lends the platform to being easily disseminated in other labs with little to no expertise in microfluidics. In addition, to use in research lab settings, this presents work towards the development of a platform that can be used for point-of-care diagnosis and routine monitoring assays that use blood. The assay uses 1 μL of blood, therefore only a finger prick would be require. The minimized blood sample requirement is especially critical in pediatric patients, and experimental animals such as mice. We envision that in the future coupling the microfluidic chip and a cheap, simple optical imaging system, a complete package for rapid immunophenotyping of specific immune cells from whole blood can be performed with potential for use in both research and clinical settings.

Finally, understanding that the immune cells response for T cells is initiated by molecular interactions at the cell surface, the ability to probe these interactions can provide insights

on how the interactions occur and identify any loss of function that may occur at the initial interaction. Motivated by the ability of microfluidic systems to enable high-throughput handling of hundreds of cells and the ability to integrate multiple functions, we introduced microfluidic system designs that have a potential to be used to evaluating the interaction of receptor/ligand interactions on the cell surface. Furthermore, in the future the platform can be coupled with additional modules to allow for further functional response of cells after the molecular interactions as demonstrated in Chapters 2 – 4.

Overall, this thesis focused on the development of new tools for the analysis of immune cells at a single-cell level. With the implementation of microfluidic systems, and imaging and analysis software, robust and easy-to-use microfluidics-based systems were developed that will have broad applications in single-cell analysis beyond immune T cells. Moreover some of the impact of the thesis have already been realized with interest and use of the device platforms in other projects in the laboratory and also with external collaborators.

8 APPENDIX

A.1. Device Fabrication

A.1.1. Device design and fabrication process

Microfluidic devices were fabricated using standard lithography techniques (*108, 109*). The fabrication process involves: (1) the design of the device based on application using a computer-aided design software, AutoCAD, (2) master mold fabrication, and (3) replica molding in PDMS. From the AutoCAD design, negative masks are printed on a transparency at a resolution of 20 000 dpi. For the master mold fabrication, SU8 negative photoresist (Microchem, Woburn MA) of varying viscosities were used depending on the desired heights, and fabrication is performed in a cleanroom, facility. SU8 was poured on a silicon wafer and spun at a specific speed to achieve the desired thickness based on manufacture's protocol (**Error! Reference source not found.**). For example, to achieve a 10 μm thickness, SU8 2010 was poured on the wafer, and the wafer was spun at 3 000 rpm for 30 s. After spinning the SU8, the wafer is baked on a hot plate following instructions manual (Microchem), then the wafer was placed in a mask aligner with the mask on top of the wafer, and exposed to 365 nm UV light through the photomask. The exposed portions of the SU8 photoresist crosslink and become resistant to developer. The wafer is then baked again to complete the crosslinking process. After baking the wafer is developed in propylene glycol monomethyl ether acetate (PGMEA, Doe & Ingalls K447200402) for a single-layer master. For multilayer masters, after baking the second layer is spun and process repeated until all the layers have been made, and finally the master is developed (Figure 8-1). Heights of the structures can be measured with a

profilomter. The master molds are then treated with trodecafluoro-1,1,2,2-tetrahydrooctyl-1-trichlorosilane (United Chemicals Technology) to enable ease of release of PDMS during replica molding.

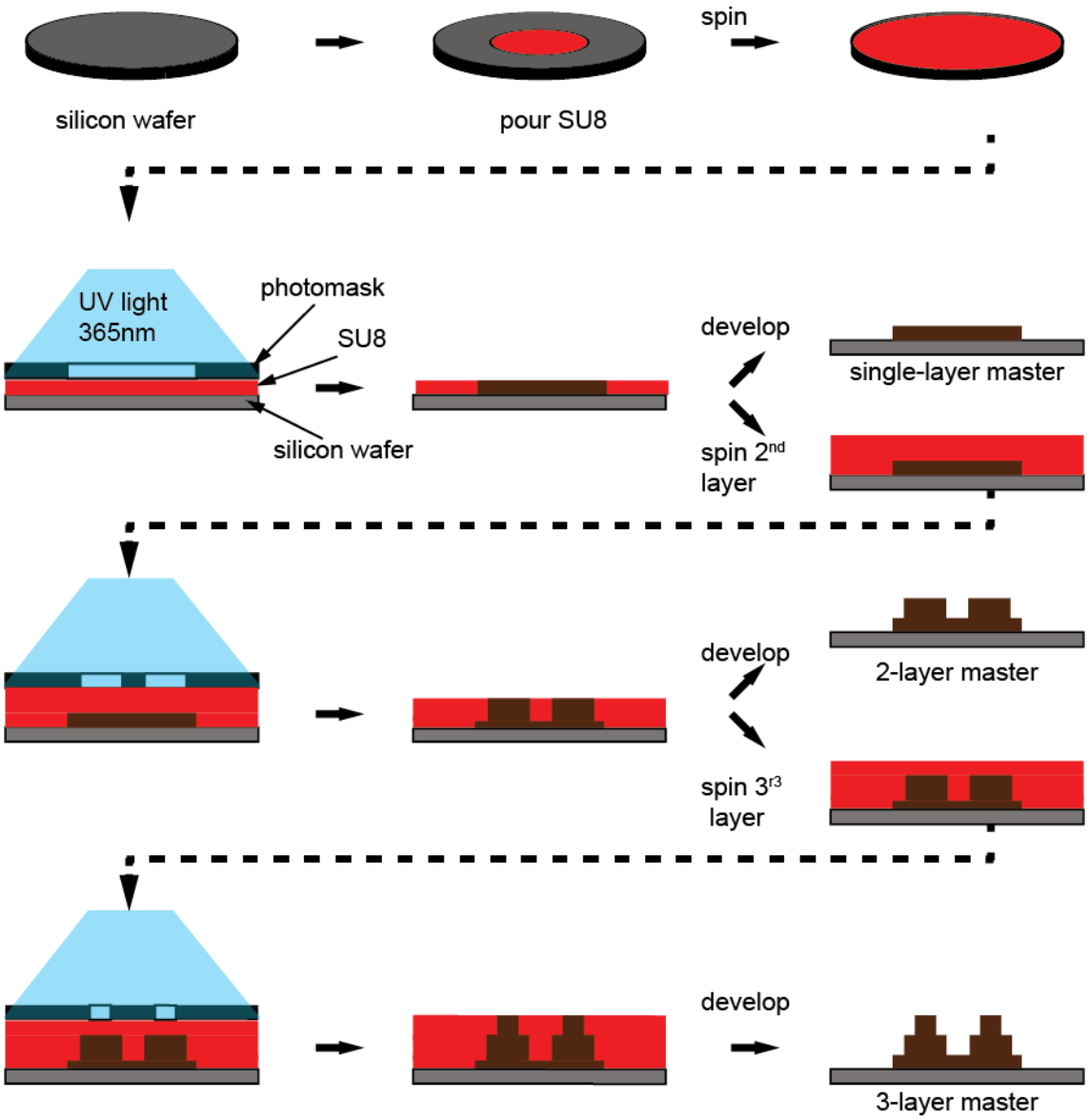

Figure 8-1. SU-8 master mold fabrication.

A.1.2. PDMS replica molding

Once the master molds are fabricated, device in PDMS mold (**Figure 8-2**). For a single layer PDMS device, PDMS prepolymer is mixed with crosslinker at a ratio of 10:1 (other ratios can be used depending on the desired stiffness of the PDMS). The PDMS is poured on the wafer, and then baked at 70 degrees to cure PDMS, then peeled off and individual devices are cut out and access holes punched. The devices are then cleaned with tap to remove any dust, treated with oxygen plasma for 20 s and bonded to a coverslip.

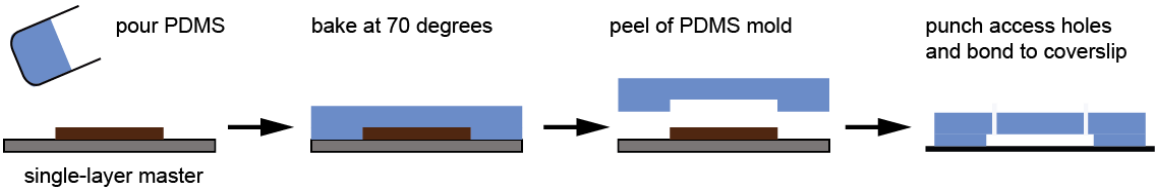

Figure 8-2 Device PDMS molding for a single-layer PDMS device. PDMS prepolymer is mixed with the curing agent at a ratio of 10:1 w/w prepolymer to crosslinker. The PDMS is degassed is a vacuum desiccator, then poured on the silicon master mold. The PDMS is baked at 70 degrees Celsius for at least 2 hours. The cured PDMS mold is then peeled off the mold, individual devices are cut out, and access holes are punched at the device inlets and outlets with a blunt 19-gauge needle. The devices are treated with oxygen plasma and bonded to a coverslip.

A.2. Calcium Response Analysis

A.2.1. Calcium assay protocol

A.2.1.1. Materials

Imaging buffer of choice (may vary depending on cells, but usually used cell culture media (RPMI in our case) without phenol red with 10% fetal bovine serum)

Fluo-3 AM calcium indicator dye (Life Technologies # F-1242)

PBS 1X pH 7.4 (Life Technologies # AM9625)

Biotin-BSA (Sigma Aldrich # A8549)

Streptavidin (Sigma Aldrich # S0677)

Biotinylated pMHC (NIH Tetramer Facility)

Cell trap devices

10 ml syringe (VWR # 309604)

0.45 μm syringe filter (VWR)

Tygon tubing (McMaster Carr # 8349T11)

24 gauge plastic dispensing luer lock tips (McMaster Carr # 6699A6)

19 gauge stainless steel tubing (McMaster Carr # 8987K51)

A.2.1.2. Device preparation

*ensure that all the solutions used are filtered to remove dust and particles that might clog the devices.

1. Fill the syringe with PBS, attach the syringe filter and tubing to syringe, and connect the tubing to the device

2. Prime the device with PBS to remove bubbles by applying pressure to the syringe plunger using your thumb.
3. Check under the tissue culture microscope to ensure the device channels are free of any bubbles.
4. Allow a puddle of liquid to form at the inlet of the device. Pipette 10 µL of biotin-BSA (500ug/ml) and place the pipette tip at the inlet. The puddle of liquid at the inlet prevents trapping of bubbles when placing the pipette at the inlet.
5. Suspend the outlet tubing to a height of ~10cm to allowing the solution in the pipette to flow through the device. This gives a flowrate of ~10 µL/hr. Let the fluid perfuse through the device for 1hr for the biotin-BSA coating. Check regularly to ensure that the solution does not completely drain out of the pipette tip, thus introducing bubbles in the device. If bubbles get in the device, prime the device with PBS to remove the bubbles.
6. After 1 hour, wash the device with PBS by placing a pipette filled with PBS at the inlet and letting the outlet tubing at a height of ~ 90 cm.
7. Repeat steps 4-6 to coat the device with streptavidin (0.5 mg/ml).
8. Repeat steps 4-6 to coat the device with biotinylated pMHC (10 µg/ml) or any of the biotinylated proteins of interest.

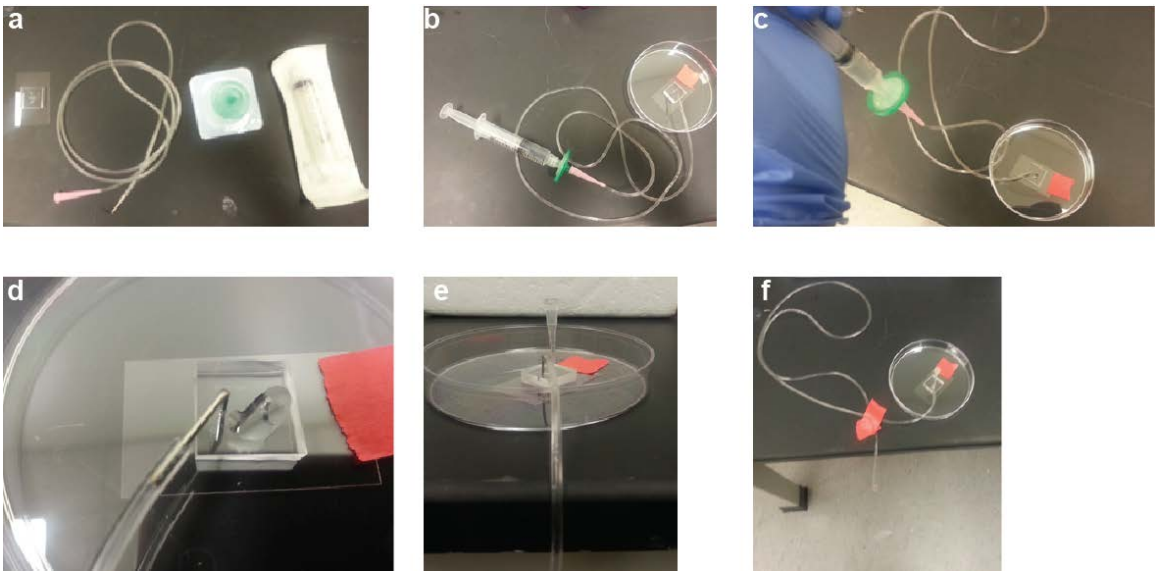

Figure 8-3 Device preparation for the Calcium assay. (a) This a simple assay that requires the microfluidic chip, tubing with a 19-gauge pin, syringe filter and a syringe, (b & c) the syringe is filled with PBS used to prime the device to remove bubbles, (d) can see a puddle of fluid at the inlet of the device, (e) insert a pipette tip filled with solutions for coating the device at the inlet, and (f) allow the solution to perfuse for a defined time with flow driven by gravity.

A.2.1.3. Cell preparation

1. Resuspend cells in either PBS, HBSS or cell media. Add Fluo-3 dye (500µg/ml) to final concentration of 5µg/ml (5µL to 500uL cell suspension).
2. Incubate at 37 degrees for 30mins
3. Wash twice with PBS and resuspend cells in imaging buffer at final concentration of 10^6 cells/ml

A.2.1.4. Calcium assay

1. Pipette the cell suspension on a coverslip mounted in the stage insert and view under fluorescent microscope. Establish the exposure time and all the camera settings for the image acquisition. **Imaging is done at 10x**.
2. Mount the device on the stage insert. Ensure the device is primed with either PBS or imaging buffer and that there are no bubbles.
3. Pipette 5-10 μL of cell suspension (5 x 10^6 cells/ml), and place the pipette tip at the cell inlet, mount on the scope.
4. Start imaging once you see cells start loading.
5. Acquire images every 3s for 20 minutes

A.2.1.5. Automated image analysis code

```
function IntensityAnalysis()
%%
% this algorithm is used for the automated segmentation and intensity
% determination in a time series stack. The code is used for analyzing
% changes in calcium intensity levels visualized by Fluo3 calcium sensitive
% dye. The cells are automatically segmented using one of the slices with
% the highest intensities for better contrast, and the mask is applied to
% all the stacks.
clear all;
close all;
clc
%% load image stack
[FileName,PathName] = uigetfile('*.tif','Select the tif file');
Stack = tiffread(FileName);
NbImages = length(Stack)
%% image segmentation to identify the individual cells in the image
prompt = 'enter slice number for segmentation';
ImSlice = input(prompt);
Im = Stack(ImSlice).data;
ImAdjust = imadjust(Im);
imshow(ImAdjust), title('ImAjust')
```

```
[~, bw1] = thresh_tool(ImAdjust);
figure
imshow(bw1), title('bw1')
bw2 = imfill(bw1, 'holes');
bw3 = imopen(bw2, ones(5,5));
figure
imshow(bw3), title('bw3')
bw4 = bwareaopen(bw3,20); % remove objects too small to be cells
bw4_perim = bwperim(bw4);
overlay1 = imoverlay(ImAdjust, bw4_perim, [.3 1 .3]);
figure, imshow(bw4), title('bw4');
%% opening-closing by reconstruction
se = strel('disk', 4);
ImErode = imerode(Im, se);
Iobr = imreconstruct(ImErode, Im);
figure, imshow(Iobr, []), title('Iobr')
Iobrd = imdilate(Iobr, se);
Iobrcbr = imreconstruct(imcomplement(Iobrd), imcomplement(Iobr));
Iobrcbr = imcomplement(Iobrcbr);
figure, imshow(Iobrcbr, []), title('Iobrcbr')
%% locate regional maxima
fgm = imregionalmax(Iobrcbr);
se2 = strel(ones(3,3));
fgm2 = imclose(fgm, se2);
figure, imshow(fgm, []), title('fgm')
fgm3 = imerode(fgm2, se2);
fgm4 = bwareaopen(fgm3, 10);
%% watershed-based segmentation
I_c = imcomplement(Im);
I_mod = imimposemin(I_c, ~bw4 | fgm4);
L = watershed(I_mod);
figure, imshow(fgm4, []), title('fgm4')
overlay2 = imoverlay(fgm4, bw4_perim, [0.3 1 0.3]);
figure, imshow(overlay2), title('overlay2')
%% object labeling
[L2, NUM] = bwlabel(L);
stats = regionprops(L, 'PixelIdxList');
figure, imshow(label2rgb(L,'jet','w'))
figure, vislabels(L)
%% meassuring intensity for easch object in all image slices
CellIntensityC = zeros(length(Stack), NUM);
CellIntensityCorrBack= zeros(length(Stack), NUM);
CellIntensityCorr = zeros(length(Stack), NUM);
% CellIntensitySync = zeros(length(Stack), NUM);
% CellIntensityInitial = zeros(10, NUM);
% CellIntensityFinal = zeros(length(Stack), NUM);
```

```
% CellIntensityInitialAvg = zeros (1,NUM);
for i=1:NUM % for all the selected objects
   for j=1:length(Stack) % for all the images
   CellIntensity(j,i)= mean(Stack(j).data(stats(i).PixelIdxList)); %mean intensity for each
cell on each image
   CellIntensityCorr (j,i) = CellIntensity(j,i) - CellIntensity(j,1); % subtract the
background intensity for every image
   end
end

Background = CellIntensity(:,1);
BackgroundAvg = mean(Background);
BackgroundStdev = std(Background);
IntensityThreshold = 3;
CellIntensityCorr(:,1) = []; % remove the first column that represents background
CellIntensity(:,1) =[];
nCols = size(CellIntensityCorr,2);
nRows = size(CellIntensityCorr,1);
CellIntensityC = zeros(nRows,nCols);
% CellIntensityNorm = zeros(length(Data), nCols);

for i=1:nCols % all columns
   for j=1:nRows
      CellIntensityC(j,i) = CellIntensityCorr(j,i);
      if CellIntensityC(j,i) <= IntensityThreshold% remove values at the time the cell trap
was unoccupied
         CellIntensityC (j,i) = NaN;
      else
      CellIntensityC (j,i) = CellIntensityC (j,i);
      end
      CellIntensitySync{i}time = CellIntensityC(~isnan(CellIntensityC(:,i)),i); %
synchronize the cells' time zero
      CellLength = cellfun('length',CellIntensitySync);
      CellIntensityFinal(1:CellLength(i),i) = CellIntensitySync{i};
  end
end

% CellIntensityFinal = zeros(length(Data), nCols);

%       CellLength = cellfun('length',CellIntensitySync);
% %       CellIntensityInitial = zeros(10,CellLength);
nCols = size(CellIntensityFinal,2);
nRows = size(CellIntensityFinal,1);
CellIntensityInitial = zeros(10,nCols);
CellIntensityNorm = zeros(10,nCols);
```

```
for k = 1:nCols
   for m = 1:10
      for n = 1:nRows
      CellIntensityInitial(m,k) = CellIntensityFinal(m,k);
      CellIntensityInitialAvg(:,k) = mean(CellIntensityInitial(:,k));
      CellIntensityNorm(n,k) = CellIntensityFinal(n,k)/CellIntensityInitialAvg(:,k);
      %CellIntensityNorm(1:CellLength(k),k) =
CellIntensityFinal(1:CellLength(k),k)/CellIntensityInitialAvg(:,k);
   end
   end
end
%% parameter calculation
% prompt = 'time between frames';
% FrameRate = input(prompt);
% Time = 0:FrameRate:FrameRate*(length(Data)-1);
% CellIntensityTrunc = zeros(1200, length(CellIntensityNorm));
% MaxIntensityNorm = zeros(1, length(CellIntensityNorm));
% AreaUnderCurve = zeros(1, length(CellIntensityNorm));
for i = 1:size(CellIntensityNorm,2)
   for j = 1:nRows
      CellIntensityTrunc(j,i) = CellIntensityNorm(j,i);
      MaxIntensityNorm(:,i) = max(CellIntensityTrunc(:,i));
      AreaUnderCurve(:,i) = trapz(CellIntensityTrunc(:,i));
   end
end

FrameRate = 3;
% measures mean fluorescence intensity for all objects
CellIntensityAvg =(mean(CellIntensityTrunc'))';
CellIntensityStd =(std(CellIntensityTrunc'))';
CellIntensitySde =CellIntensityStd/sqrt(nCols-1);
AveData = [CellIntensityAvg CellIntensityStd CellIntensitySde];

% exports individual traces in excel
xlswrite('FileName.xlsx',CellIntensity,'RawIntensity');
xlswrite('FileName.xlsx',CellIntensityCorr,'CellIntensityCorr');
xlswrite('FileName.xlsx',CellIntensityNorm,'CellIntensityNorm');
xlswrite('FileName.xlsx',Background,'Background');
xlswrite('FileName.xlsx',MaxIntensityNorm','MaxIntensityNorm');
xlswrite('FileName.xlsx',AreaUnderCurve','AUC');
xlswrite('FileName.xlsx',AveData','AveData');

Time =1:3:3*nRows;
%individual curves and the mean curve
figure,
hold on
```

```
plot(Time, CellIntensityTrunc, 'b')
errorbar(Time, CellIntensityAvg, CellIntensitySde,'r');
set(gca,'Fontsize',[16],'Xlim',[0 900])
xlabel('Time (s)');
ylabel('FI (a.u)');
title('20140825P14CalciumSpleenCircPMA')
hold off

% % Time = 1:1:nRows;
% figure,
% hold on
% plot(Time,CellIntensityTrunc)
% set(gca,'Fontsize',[16],'Xlim',[0 900])
% xlabel('Time (s)');
% ylabel('FI (a.u)');
% title('20140825P14CalciumSpleenCircPMA')
hold off

%heatmap
figure
y = 1:1:nCols-1;
imagesc(Time, y, CellIntensityTrunc')
set(gca,'Fontsize',[14],'Xlim',[0 600])
xlabel('Time (s)')
ylabel('Cell number')
title('20140825P14CalciumSpleenCircPMA')
```

A.2.2. Calcium Assay Supplemental results

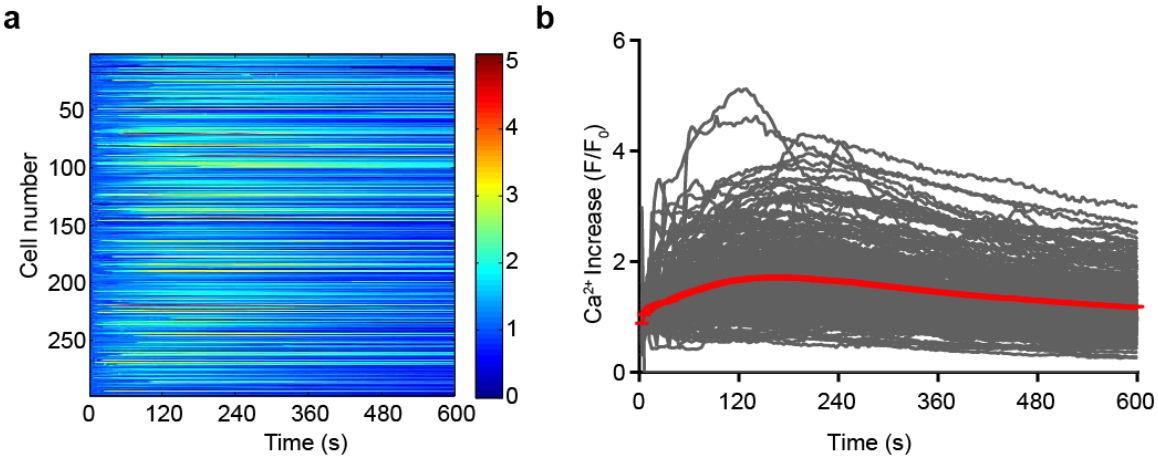

Figure 8-4. Heterogeneous calcium response of Jurkat E6.1 on anti-CD3-coated surfaces

A.3. Multilayer design fabrication and characterization

A.3.1. Device 2-layer PDMS mold fabrication

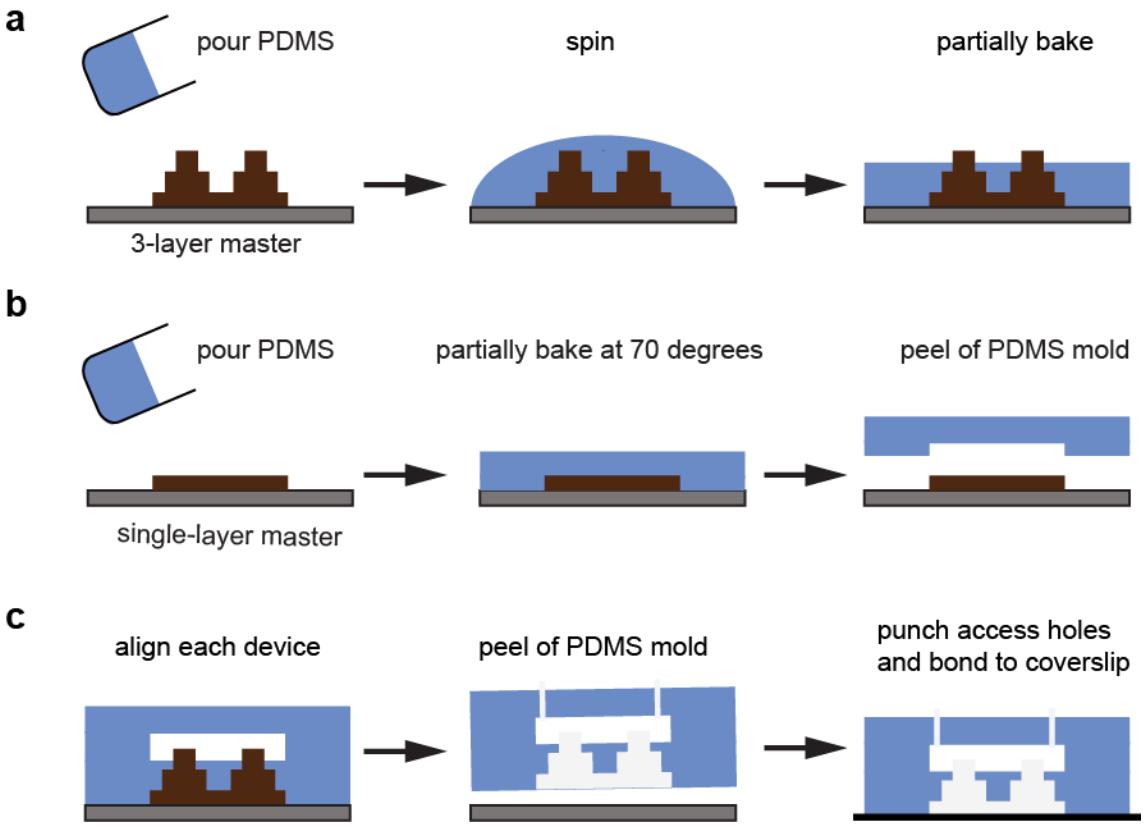

Figure 8-5. Fabrication of the 2-layer PDMS device**.** The device mold fabrication utilizes multilayer lithography and thermal bonding between the PDMS layers. (a) The cell trap layer is molded by spinning PDMS prepolymer:crosslinker (10:1) at 1500rpm for 5 minutes to make a ~10-15 um layer of PDMS such that the features of the posts used to make pores in the PDMS are protruding and then partially baked for 15 minutes. This layer is then partially baked and then aligned to the partially baked top layer, and then fully baked, (b) for the top layer, PDMS (10:1) is poured on the wafer and partially baked for 20 -25 minutes, and (c) individual devices from the top layer mold are cut out and aligned to the cell trap layer mold. PDMS is poured on the master mold and then baked at 70 degrees for at least 2 hours, the PDMS is peeled off, access holes are punched and devices are bonded to a coverslip.

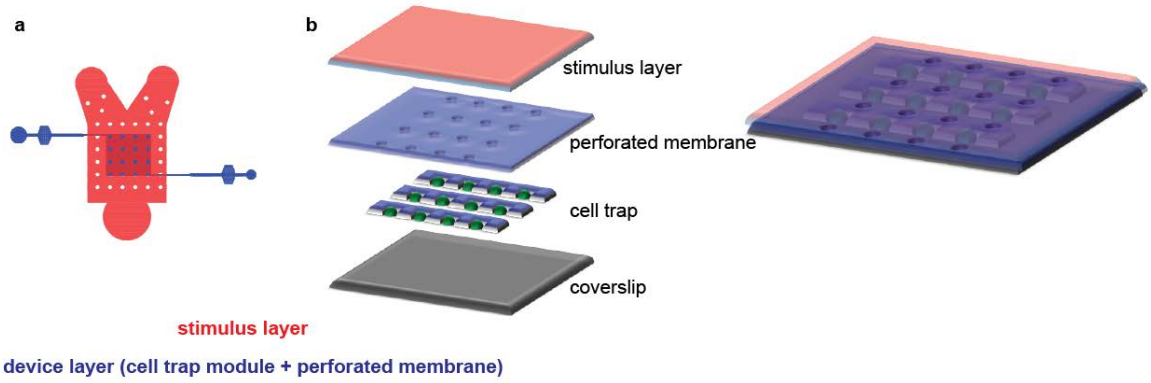

Figure 8-6 Microfluidic device components. (a) overall depiction of the device showing the top view of the stimulus and device layer which consists of the cell trapping module, and (b) an illustration of the different layers of the device module, the cell trap and perforated membrane make up one module and the access holes on the membrane connect fluid exchange between the stimulus layer and the cell trap layer.

A.3.2. Flow characterization

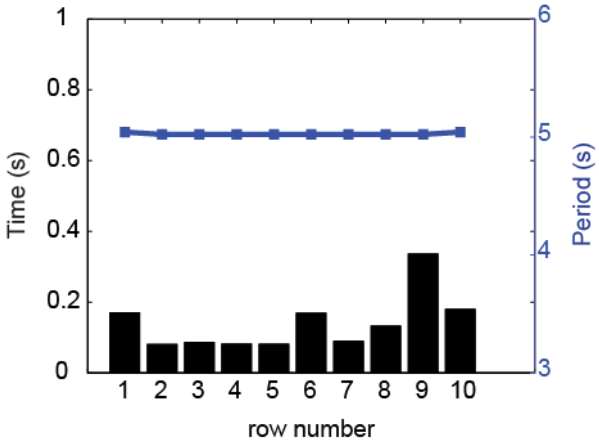

Figure 8-7 Characterization of the pulse signal showing the periodicity in each row (5 s) and the risetime. The period is approximately the same regardless of the position in the device and the rise time is on average 150 ms.

A.3.3. Additional Calcium Oscillation data

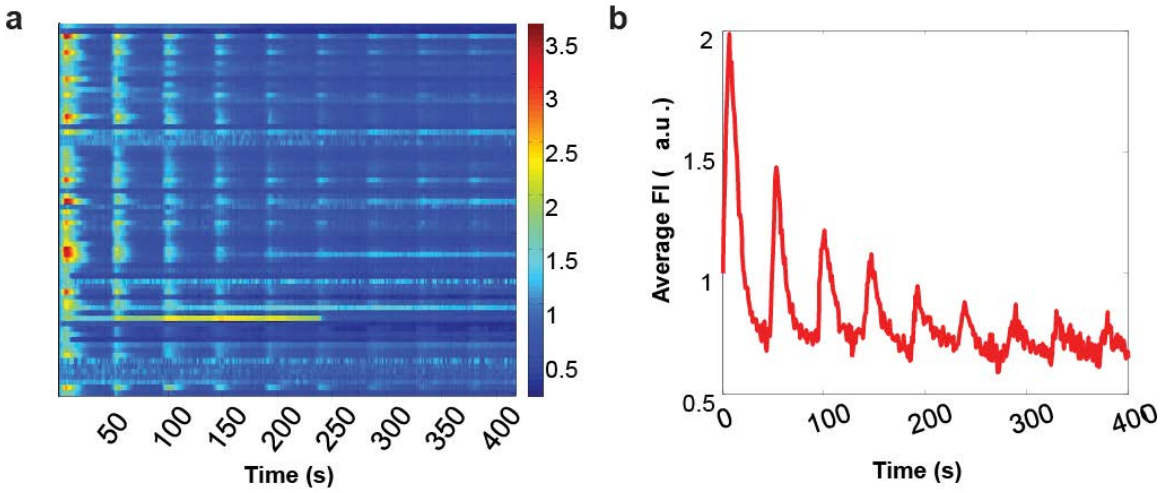

Figure 8-8 Calcium response of cells exposed to 20 s pulses of calcium and 100 s of buffer, and (b) the average cell response.

A.4. Muitiplexed single-cell analysis on chip

A.4.1. Statistical analysis algorithms for correlating different readouts

Unsupervised clustering using k-means is performed to group cells with similar calcium dynamic behavior together using the following MATLAB-based script.

```
clear all;
close all;
clc
%load calcium data
[FileName,PathName] = uigetfile('*.xlsx','Select the xlsx file');
C = xlsread(FileName,3);
% number of clusters for analysis defined by user
N_clusters = 4;
idx = kmeans(C',4);
xlswrite('ClustersOVA.xlsx',idx);
```

To obtain correlations between the calcium data and the mRNA transcript quantification, PCA analysis was performed using the area under the calcium curve, maximum calcium peak, and the mRNA transcript as variables using the script shown below.

```
function CalciumClusters()
clear all;
close all;
clc
%load file with the parameters for each cell
% parameters: area under curve, calcium peak, IFNG mRNA count, IL2 mRNA
% count
[FileName,PathName] = uigetfile('*.xlsx','Select the xlsx file');
data = xlsread(FileName,1);
%load data for the cluster each cell belongs to determined by k-means
%clustering
cluster1=xlsread(FileName,2);
%perform PCA analysis
[pc] = pca(data);
pc=pc'; %principle components

% data plots
c1 = cluster1(:,1);
figure
scatter(pc(1,:),pc(2,:),[],c1,'.');
title('Ca2+ clusters'); xlabel('PC 1'); ylabel('PC 2')
 figure
 scatter(pc(1,:),pc(3,:),[],c1,'.');
 title('Ca2+ clusters'); xlabel('PC 1'); ylabel('PC 3')
  figure
```

```
    scatter(pc(2,:),pc(3,:),[],c1,'.');
    title('Ca2+ clusters'); xlabel('PC 2'); ylabel('PC 3')
    figure
     scatter3(pc(1,:),pc(2,:),pc(3,:),[],c1,'.')
    title('Ca2+ clusters'); xlabel('PC 1'); ylabel('PC 2');
zlabel('PC3');
 figure
scatter3(data(:,1),data(:,3),data(:,4))
title('Ca2+ AUC/mRNA Count')
    xlabel('Ca2+ AUC'); ylabel('IFNG'); zlabel('IL2')
     figure
scatter3(data(:,2),data(:,3),data(:,4))
title('Ca2+ peak/mRNA Count')
    xlabel('Ca2+ peak'); ylabel('IFNG'); zlabel('IL2')

% vs mRNA count
c1 = data(:,3);
figure
scatter(pc(1,:),pc(2,:),[],c1,'.');
title('IFNG'); xlabel('PC 1'); ylabel('PC 2')
 figure
 scatter(pc(1,:),pc(3,:),[],c1,'.');
 title('IFNG'); xlabel('PC 1'); ylabel('PC 3')
  figure
    scatter(pc(2,:),pc(3,:),[],c1,'.');
    title('IFNG'); xlabel('PC 2'); ylabel('PC 3')
    figure
     scatter3(pc(1,:),pc(2,:),pc(3,:),[],c1,'.')
    title('IFNG'); xlabel('PC 1'); ylabel('PC 2'); zlabel('PC3');


     [COEFF,latent,explained] = pcacov(data);
     %variance contribution for each principle component
      PC_percentage = explained;
    %IL2

   c1 = data(:,4);
figure
scatter(pc(1,:),pc(2,:),[],c1,'.');
title('IL2'); xlabel('PC 1'); ylabel('PC 2')
 figure
 scatter(pc(1,:),pc(3,:),[],c1,'.');
 title('IL2'); xlabel('PC 1'); ylabel('PC 3')
  figure
    scatter(pc(2,:),pc(3,:),[],c1,'.');
    title('IL2'); xlabel('PC 2'); ylabel('PC 3')
    figure
     scatter3(pc(1,:),pc(2,:),pc(3,:),[],c1,'.')
    title('IL2'); xlabel('PC 1'); ylabel('PC 2'); zlabel('PC3');
figure
scatter(cluster1(:,1),data(:,4))
xlabel('cluster'); ylabel('IL2')
```

```
    figure
    plot(data(:,1),data(:,3),'.')
    title('total RNA count'); xlabel('Ca2+ AUC'); ylabel('IFNG count')
    figure
    plot(data(:,1),data(:,4),'.')
    title('total RNA count'); xlabel('Ca2+ AUC'); ylabel('IL2 count')
    figure
    plot3(cluster1,data(:,3),data(:,4),'.')
    title('Ca2+ Peak/mRNA Count'); xlabel('Ca2+ Peak'); ylabel('IFNG
count'); zlabel('IL2 count')
    figure
    scatter3(pc(1,:),pc(2,:),pc(3,:),[],c1,'.')
    title('Principle Components'); xlabel('PC 1'); ylabel('PC 2');
zlabel('PC3');
    figure
    plot3(data(:,1),data(:,3),data(:,4),'.')
    title('Ca2+ AUC/mRNA Count')
    xlabel('Ca2+ AUC'); ylabel('IFNG'); zlabel('IL2')
    figure
    c1 = data(:,3);
    scatter3(pc(1,:),pc(2,:),pc(3,:),[],c1,'.')
     title('PC/IFNG')
      xlabel('PC 1'); ylabel('PC 2'); zlabel('PC3');
    figure
    c1 = data(:,4);
    scatter3(pc(1,:),pc(2,:),pc(3,:),[],c1,'.')
     title('PC/IL2')
      xlabel('PC 1'); ylabel('PC 2'); zlabel('PC3');
```

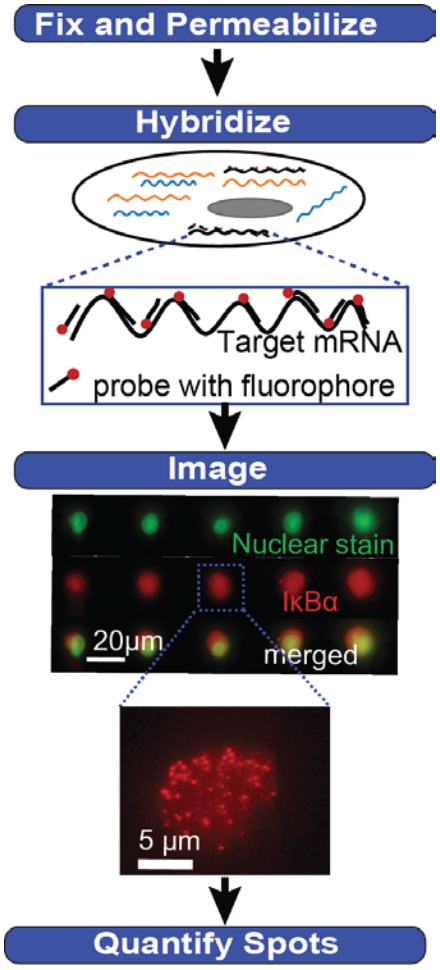

Figure 8-9 Overview of mRNA quantification using smFISH. T

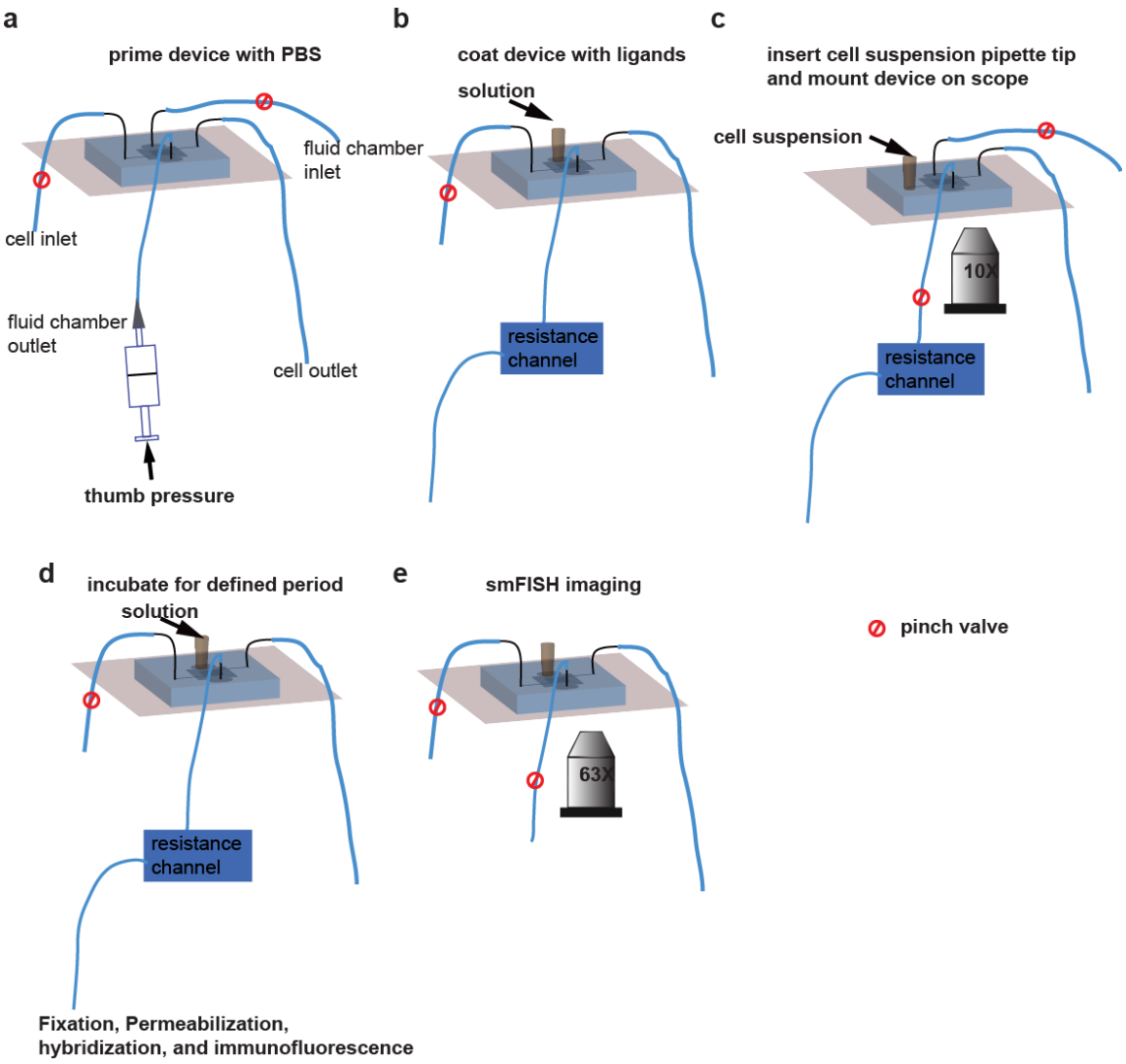

Figure 8-10. Device setup and operation setup demonstrate ease of use. The platforms requires very few simple peripheral supporting systems for operation. (a) The autoclaved device is primed with sterile PBS through the fluid layer outlet/inlet using the thumb finger pressure to remove bubbles and fill the device with PBS, (b) the device setup during protein coating. Protein solutions are introduced through the fluid inlet by gravity-driven flow, (c) cell loading by gravity-driven flow and simultaneous image acquisitions, (d) device configuration during incubation, fixation, hybridization and immunostaining steps, and (e) imaging.

A.4.2. mRNA probe sequence design

Probes for mRNA quantification using smFISH were designed using an online software (available at: https://www.biosearchtech.com/stellarisdesigner/) by inputting the mRNA

coding sequence of the molecule of interest. The probes were 20-nucleotides long with a fluorophore tag. Here we had IL2 and IFNγ mRNA probes tagged with Quasar 670 and TAMRA fluorophores respectively. For mRNA quantification, stimulated cells were fixed in 4% formaldehyde, and permeabilized in chilled 100 % methanol. The cells were then washed in hybridization wash buffer (2X SSC and 10% formamide in nuclease-free water). smFISH probes were pooled in hybridization buffer (0.1g/ml dextran sulfate, 10% formamide, 200 ug/ml BSA in nuclease-free water) to a final concentration of 200 nM for each probe set. Cells were incubated overnight in the probe solution, then washed with prewarmed hybridization wash buffer.

IFNγ mRNA sequence (http://www.ncbi.nlm.nih.gov/guide/howto/find-transcript-gene/)

1 atagctgcca tcggctgacc tagagaagac acatcagctg atcctttgga ccctctgact
61 tgagacagaa gttctgggct tctcctcctg cggcctagct ctgagacaat gaacgctaca
121 cactgcatct tggctttgca gctcttcctc atggctgttt ctggctgtta ctgccacggc
181 acagtcattg aaagcctaga aagtctgaat aactatttta actcaagtgg catagatgtg
241 gaagaaaaga gtctcttctt ggatatctgg aggaactggc aaaaggatgg tgacatgaaa
301 atcctgcaga gccagattat ctctttctac ctcagactct ttgaagtctt gaaagacaat
361 caggccatca gcaacaacat aagcgtcatt gaatcacacc tgattactac cttcttcagc
421 aacagcaagg cgaaaaagga tgcattcatg agtattgcca agtttgaggt caacaaccca
481 caggtccagc gccaagcatt caatgagctc atccgagtgg tccaccagct gttgccggaa
541 tccagcctca ggaagcggaa aaggagtcgc tgctgattcg gggtggggaa gagattgtcc
601 caataagaat aattctgcca gcactatttg aatttttaaa tctaaaccta tttattaata
661 tttaaaacta tttatatgga gaatctattt tagatgcatc aaccaaagaa gtatttatag
721 taacaactta tatgtgataa gagtgaattc ctattaatat atgtgttatt tataatttct
781 gtctcctcaa ctatttctct ttgaccaatt aattattctt tctgactaat tagccaagac
841 tgtgattgcg gggttgtatc tgggggtggg ggacagccaa gcggctgact gaactcagat
901 tgtagcttgt acctttactt cactgaccaa taagaaacat tcagagctgc agtgaccccg
961 ggaggtgctg ctgatgggag gagatgtcta cactccgggc cagcgcttta acagcaggcc
1021 agacagcact cgaatgtgtc aggtagtaac aggctgtccc tgaaagaaag cagtgtctca
1081 agagacttga cacctggtgc ttccctatac agctgaaaac tgtgactaca cccgaatgac
1141 aaataactcg ctcatttata gtttatcact gtctaattgc atatgaataa agtatacctt
1201 tgcaacc

Table 3. IFNγ mRNA probe sequences labeled with TAMRA.

Probe	Probe sequence (5' → 3')
1	agctgatgtgtcttctctag
2	aagtcagagggtccaaagga
3	gaggagaagcccagaacttc
4	tcattgtctcagagctaggc
5	gccaagatgcagtgtgtagc
6	agccatgaggaagagctgca
7	cgtggcagtaacagccagaa
8	tcagactttctaggctttca
9	gccacttgagttaaaatagt
10	gactcttttcttccacatct
11	ttcctccagatatccaagaa
12	attttcatgtcaccatcctt
13	agagataatctggctctgca
14	gacttcaaagagtctgaggt
15	tgatggcctgattgtctttc
16	aggtgtgattcaatgacgct
17	tgctgttgctgaagaaggta
18	atgaatgcatccttttcgc
19	gttgacctcaaacttggcaa
20	attgaatgcttggcgctgga
21	tggtggaccactcggatgag
22	aatcagcagcgactcctttt
23	ttattgggacaatctcttcc
24	attcaaatagtgctggcaga
25	acttctttggttgatgcatc
26	aggaattcactcttatcaca
27	gtcttggctaattagtcaga
28	cagatacaaccccgcaatca
29	acaatctgagttcagtcagc
30	ttggtcagtgaagtaaaggt
31	actgcagctctgaatgtttc
32	cggagtgtagacatctcctc
33	gtctggcctgctgttaaag
34	actacctgacacattcgagt
35	ctgctttctttcagggacag
36	aggtgtcaagtctcttgaga
37	cagttttcagctgtataggg
38	gagttatttgtcattcgggt

IL2 mRNA sequence http://www.ncbi.nlm.nih.gov/nuccore/BX519775,%20K02292

1 tatcaccctt gctaatcact cctcacagtg acctcaagtc ctgcaggcat gtacagcatg
61 cagctcgcat cctgtgtcac attgacactt gtgctccttg tcaacagcgc acccacttca
121 agctccactt caagctctac agcggaagca cagcagcagc agcagcagca gcagcagcag
181 cagcagcacc tggagcagct gttgatggac ctacaggagc tcctgagcag gatggagaat
241 tacaggaacc tgaaactccc caggatgctc accttcaaat tttacttgcc caagcaggcc
301 acagaattga aagatcttca gtgcctagaa gatgaacttg gacctctgcg gcatgttctg
361 gatttgactc aaagcaaaag ctttcaattg gaagatgctg agaatttcat cagcaatatc
421 agagtaactg ttgtaaaact aaagggctct gacaacacat ttgagtgcca attcgatgat
481 gagtcagcaa ctgtggtgga ctttctgagg agatggatag ccttctgtca aagcatcatc
541 tcaacaagcc ctcaataact atgtacctcc tgcttacaac acataaggct ctctatttat
601 ttaaatattt aactttaatt tatttttgga tgtattgttt actatctttt gtaactacta
661 gtcttcagat gataaatatg gatctttaaa gattcttttt gtaagcccca agggctcaaa
721 aatgttttaa actatttatc tgaaattatt tattatattg aattgttaaa tatcatgtgt
781 aggtagactc attaataaaa gtatttagat gattcaaata taaaa

Table 4. IL2 mRNA probe sequences labeled with Quasar 670 fluorophore

Probe	**Probe sequence (5' → 3')**
1	ggagtgattagcaagggt
2	aggacttgaggtcactgt
3	tgcatgctgtacatgcct
4	atgtgacacaggatgcga
5	gctgttgacaaggagcac
6	gtggagcttgaagtgggt
7	atcaacagctgctccagg
8	ctcaggagctcctgtagg
9	tcctgtaattctccatcc
10	catcctggggagtttcag
11	ttcaattctgtggcctgc
12	gttcatcttctaggcact
13	agaacatgccgcagaggt
14	agcttttgctttgagtca
15	attctcagcatcttccaa
16	gagccctttagttttaca
17	ggcactcaaatgtgttgt
18	gttgctgactcatcatcg
19	tcctcagaaagtccacca
20	ttgacagaaggctatcca
21	gagggcttgttgagatga
22	gcaggaggtacatagtta
23	gagagccttatgtgttgt
24	catttttgagcccttggg

25	gagtctacctacacatga

Table 5. IκBα mRNA probe sequences with TAMRA fluorophore

Probe	Probe sequence (5' → 3')
1	tgttctggagtttctgttct
2	tttctgggagctatttccaa
3	gtgaaagggacagaacctgc
4	cttttctggagggagatgtg
5	atcatgctttctgtgctcat
6	agaggctgagacataggcac
7	cctgccacaagcaggaatga
8	agtagacagaagagcgtggt
9	ccatttgggaacttctcatc
10	tgggccatagaactgatgag
11	agatgatctgagtgtgaggg
12	tacaggcttgtcactcgaat
13	acttggtggtttgctacgac
14	cactagttggttgtctttga
15	agtagacaaggtacaaccca
16	tgtcccttgaagagaacctg
17	caaatcggctgacggtgtgg
18	actttctcctggtatgagat
19	ctcttgacggcagagaggag
20	ataccagggtttgagctcag
21	aagactcctcccaggtatat
22	agattgacctcagcgctgag
23	ctccgcaaagtctaagtact
24	ttcacagagcaatgactcca
25	gctgggtagagaatggatga
26	gagtaaaggggtcagagtgg
27	ggagtagacaataaaggggt
28	aaggatacagactgggggct
29	cataatccccttctaagtt
30	gaaagctctgagcacagagt
31	cagcatcttgtgtttctgag
32	atggacattcgaggctccag
33	tctccctttgcagaactcag
34	tgagacagaggcaacctgac
35	gagatcttatccagcctcat
36	aggtctgaaggtaggaaggc
37	cacctcagggaagaatctgg
38	ctgtgaggaaggctgtgcat
39	tataaatagagggggctgg
40	atgtctgtctgaagacagct
41	cagctccgttttcacagaaa
42	caacaaggtagagaggccag
43	gtcaccaaatcagcgttatt

44	gttcagtgatgtagcgacag
45	ttatttctctcaatgacccg
46	cacatttcttttccaagcga

A.4.3. Additional smFISH data

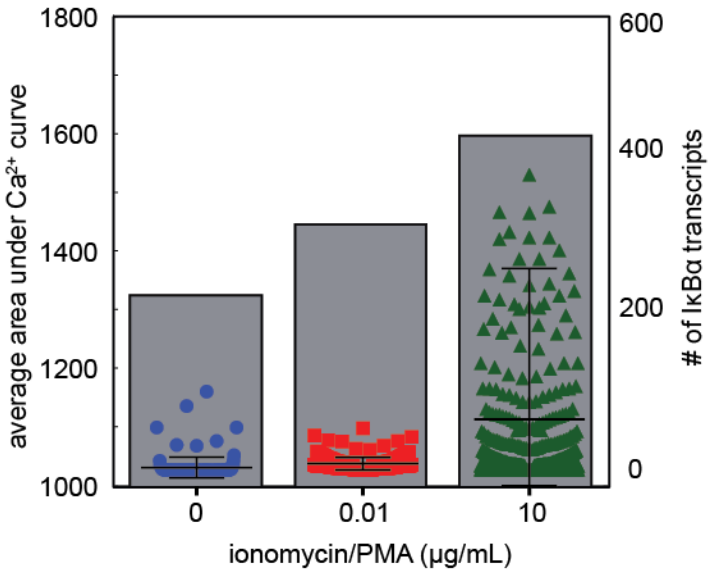

Figure 8-11 Ca^{2+} dynamics and subsequent mRNA quantification. Jurkat cells were stimulated while simultaneously measuring the calcium dynamics and subsequently mRNA transcripts were hybridized. On a population average, the higher average calcium level measured by the area under the calcium curve corresponded with higher average mRNA level expression.

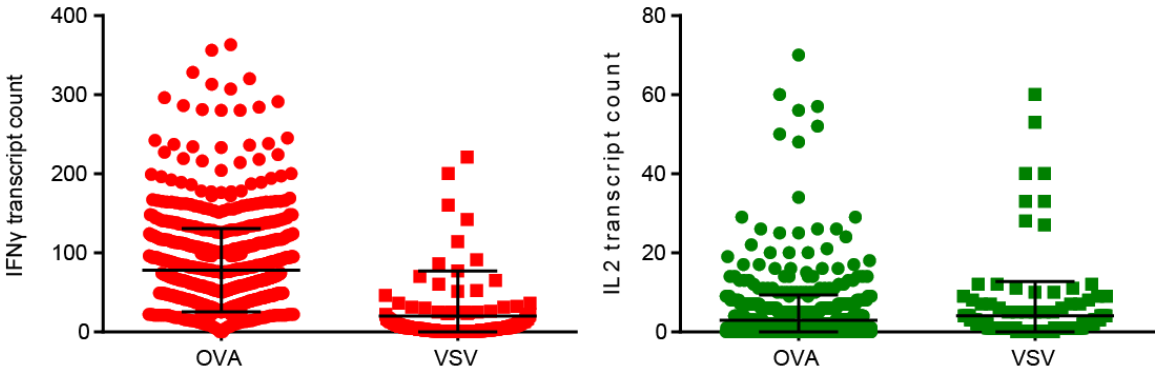

Figure 8-12 IFNγ and IL-2 mRNA expression of OT-1 T cells. OT-1 CD8+ spleenocytes were stimulated with either OVA or VSV peptides in the presence of anti-CD28 and anti-LFA1 for 6 hours. As expected T cells stimulated on OVA surface showed significantly higher IFNγ mRNA expression levels compared to those on VSV, nonstimulatory surface but the IL-2 mRNA expression was comparable.

A.5. Single-layer valve device fabrication in PDMS

The device master molds are fabricated in SU8 as outlined in Appendix A. For the molding of the membrane-based adhesion device, PDMS prepolymer-to-crosslinking ratio of 22:1 was used for the device, and a layer of 10:1 ratio PDMS was poured on top as a support layer for the device as shown in Figure 8-13.The 22:1 PDMS is more flexible to enable the deflection of the membrane upon pressurization.

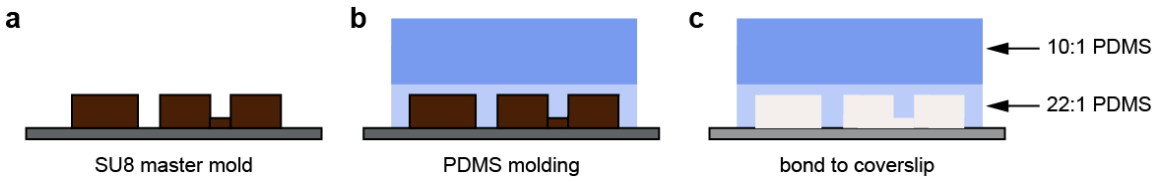

Figure 8-13 Membrane-based adhesion device replica molding. (a) Device 2-layer master mold, (b) 22:1 PDMS prepolymer-to-crosslinker ratio was poured and partially baked for 30 minutes then a 10:1 PDMS PDMS prepolymer-to-crosslinker ratio was poured on top then the mold was fully baked, and (c) the mold was peeled off and bonded to a coverslip.

REFERENCES

1. K. Chung, M. Zhan, J. Srinivasan, P. W. Sternberg, E. Gong, F. C. Schroeder, H. Lu, Microfluidic chamber arrays for whole-organism behavior-based chemical screening. *Lab on a Chip* **11**, 3689-3697 (2011)10.1039/C1LC20400A).
2. D. Bumann, *T cell receptor-transgenic mouse models for studying cellular immune responses to Salmonella in vivo*. (2003), vol. 37, pp. 105-109.
3. B. Dura, J. Voldman, Spatially and temporally controlled immune cell interactions using microscale tools. *Current Opinion in Immunology* **35**, 23-29 (2015); published online Epub8// (http://dx.doi.org/10.1016/j.coi.2015.05.006).
4. J. E. Smith-Garvin, G. A. Koretzky, M. S. Jordan, T Cell Activation. *Annual Review of Immunology* **27**, 591-619 (2009)doi:10.1146/annurev.immunol.021908.132706).
5. E. M. Gallo, K. Cante-Barrett, G. R. Crabtree, Lymphocyte calcium signaling from membrane to nucleus. *Nat Immunol* **7**, 25-32 (2006); published online EpubJan (Doi 10.1038/Ni1295).
6. M. M. Davis, M. Krogsgaard, M. Huse, J. Huppa, B. F. Lillemeier, Q.-j. Li, T Cells as a Self-Referential, Sensory Organ. *Annual Review of Immunology* **25**, 681-695 (2007)doi:10.1146/annurev.immunol.24.021605.090600).
7. A. J. T. George, J. Stark, C. Chan, Understanding specificity and sensitivity of T-cell recognition. *Trends in Immunology* **26**, 653-659 10.1016/j.it.2005.09.011).
8. D. J. Irvine, M. A. Purbhoo, M. Krogsgaard, M. M. Davis, Direct observation of ligand recognition by T cells. *Nature* **419**, 845-849 (2002); published online EpubOct 24 (Doi 10.1038/Nature01076).
9. J. Huang, M. Brameshuber, X. Zeng, J. M. Xie, Q. J. Li, Y. H. Chien, S. Valitutti, M. M. Davis, A Single Peptide-Major Histocompatibility Complex Ligand Triggers Digital Cytokine Secretion in CD4(+) T Cells. *Immunity* **39**, 846-857 (2013); published online EpubNov 14 (DOI 10.1016/j.immuni.2013.08.036).
10. M. Huse, L. O. Klein, A. T. Girvin, J. M. Faraj, Q.-J. Li, M. S. Kuhns, M. M. Davis, Spatial and Temporal Dynamics of T Cell Receptor Signaling with a Photoactivatable Agonist. *Immunity* **27**, 76-88 10.1016/j.immuni.2007.05.017).
11. M. L. Dustin, T-cell activation through immunological synapses and kinapses. *Immunological Reviews* **221**, 77-89 (2008)10.1111/j.1600-065X.2008.00589.x).
12. E. Donnadieu, D. Cefai, Y. P. Tan, G. Paresys, G. Bismuth, A. Trautmann, Imaging Early Steps of Human T-Cell Activation by Antigen-Presenting Cells. *J Immunol* **148**, 2643-2653 (1992); published online EpubMay 1 (
13. N. Joseph, B. Reicher, M. Barda-Saad, The calcium feedback loop and T cell activation: How cytoskeleton networks control intracellular calcium flux. *Bba-Biomembranes* **1838**, 557-568 (2014); published online EpubFeb (DOI 10.1016/j.bbamem.2013.07.009).
14. R. S. Lewis, Calcium signaling mechanisms in T lymphocytes. *Annual Review of Immunology* **19**, 497-521 (2001)DOI 10.1146/annurev.immunol.19.1.497).
15. S. Feske, Calcium signalling in lymphocyte activation and disease. *Nature Reviews Immunology* **7**, 690-702 (2007); published online EpubSep (Doi 10.1038/Nri2152).

16. R. E. Dolmetsch, R. S. Lewis, C. C. Goodnow, J. I. Healy, Differential activation of transcription factors induced by Ca^{2+} response amplitude and duration. *Nature* **386**, 855-858 (1997); published online Epub04/24/print (
17. C. Utzny, M. Faroudi, S. Valitutti, Frequency encoding of T-cell receptor engagement dynamics in calcium time series. *Biophys J* **88**, 1-14 (2005); published online EpubJan (DOI 10.1529/biophysj.103.038216).
18. H. P. Arrol, L. D. Church, P. A. Bacon, S. P. Young, Intracellular calcium signalling patterns reflect the differentiation status of human T cells. *Clinical & Experimental Immunology* **153**, 86-95 (2008)10.1111/j.1365-2249.2008.03677.x).
19. C. Wulfing, J. D. Rabinowitz, C. Beeson, M. D. Sjaastad, H. M. McConnell, M. M. Davis, Kinetics and extent of T cell activation as measured with the calcium signal. *J Exp Med* **185**, 1815-1825 (1997); published online EpubMay 19 (DOI 10.1084/jem.185.10.1815).
20. S. N. Christo, K. R. Diener, R. E. Nordon, M. P. Brown, H. J. Griesser, K. Vasilev, F. C. Christo, J. D. Hayball, Scrutinizing calcium flux oscillations in T lymphocytes to deduce the strength of stimulus. *Sci Rep-Uk* **5**, (2015); published online EpubJan 14 (Artn 7760
Doi 10.1038/Srep07760).
21. O. Eerbeek, E. G. Mik, C. J. Zuurbier, M. v. ë. Loo, C. Donkersloot, C. Ince, Ratiometric intracellular calcium imaging in the isolated beating rat heart using indo-1 fluorescence. *Journal of Applied Physiology* **97**, 2042-2050 (2004); published online EpubDecember 1, 2004 (10.1152/japplphysiol.01125.2003).
22. O. L. Barreto-Chang, R. E. Dolmetsch, Calcium Imaging of Cortical Neurons using Fura-2 AM. *J Vis Exp*, e1067 (2009).
23. J. Deguine, B. Breart, F. Lemaître, J. P. Di Santo, P. Bousso, Intravital Imaging Reveals Distinct Dynamics for Natural Killer and CD8+ T Cells during Tumor Regression. *Immunity* **33**, 632-644 (2010); published online Epub10/29/ (http://dx.doi.org/10.1016/j.immuni.2010.09.016).
24. B. Réthi, C. Detre, P. Gogolák, A. Kolonics, M. Magócsi, É. Rajnavölgyi, Flow cytometry used for the analysis of calcium signaling induced by antigen-specific T-cell activation. *Cytometry* **47**, 207-216 (2002)10.1002/cyto.10086).
25. M. E. Lidstrom, M. C. Konopka, The role of physiological heterogeneity in microbial population behavior. *Nat Chem Biol* **6**, 705-712 (2010); published online Epub10//print (
26. H. H. Chang, M. Hemberg, M. Barahona, D. E. Ingber, S. Huang, Transcriptome-wide noise controls lineage choice in mammalian progenitor cells. *Nature* **453**, 544-547 (2008); published online Epub05/22/print (http://www.nature.com/nature/journal/v453/n7194/suppinfo/nature06965_S1.html).
27. S. Tay, J. J. Hughey, T. K. Lee, T. Lipniacki, S. R. Quake, M. W. Covert, Single-cell NF-[kgr]B dynamics reveal digital activation and analogue information processing. *Nature* **466**, 267-271 (2010); published online Epub07/08/print (http://www.nature.com/nature/journal/v466/n7303/abs/nature09145.html#supplementary-information).

28. E. W. Newell, M. M. Davis, Beyond model antigens: high-dimensional methods for the analysis of antigen-specific T cells. *Nat Biotech* **32**, 149-157 (2014); published online Epub02//print (10.1038/nbt.2783).
29. M. Wu, A. K. Singh, Single-cell protein analysis. *Current Opinion in Biotechnology* **23**, 83-88 (2012); published online Epub2// (http://dx.doi.org/10.1016/j.copbio.2011.11.023).
30. D. Di Carlo, L. P. Lee, Dynamic single-cell analysis for quantitative biology. *Analytical Chemistry* **78**, 7918-7925 (2006); published online EpubDec 1 (
31. P. K. Chattopadhyay, M. Roederer, Good Cell, Bad Cell: Flow Cytometry Reveals T-cell Subsets Important in HIV Disease. *Cytom Part A* **77A**, 614-622 (2010); published online EpubJul (Doi 10.1002/Cyto.A.20905).
32. N. Varadarajan, B. Julg, Y. J. Yamanaka, H. B. Chen, A. O. Ogunniyi, E. McAndrew, L. C. Porter, A. Piechocka-Trocha, B. J. Hill, D. C. Douek, F. Pereyra, B. D. Walker, J. C. Love, A high-throughput single-cell analysis of human CD8(+) T cell functions reveals discordance for cytokine secretion and cytolysis. *J Clin Invest* **121**, 4322-4331 (2011); published online EpubNov (Doi 10.1172/Jci58653).
33. D. J. Wang, S. Bodovitz, Single cell analysis: the new frontier in 'omics'. *Trends in Biotechnology* **28**, 281-290 (2010); published online EpubJun (DOI 10.1016/j.tibtech.2010.03.002).
34. J. L. Wilson, S. Suri, A. Singh, C. A. Rivet, H. Lu, T. C. McDevitt, Single-cell analysis of embryoid body heterogeneity using microfluidic trapping array. *Biomed Microdevices* **16**, 79-90 (2014); published online EpubFeb (DOI 10.1007/s10544-013-9807-3).
35. A. K. Shalek, R. Satija, X. Adiconis, R. S. Gertner, J. T. Gaublomme, R. Raychowdhury, S. Schwartz, N. Yosef, C. Malboeuf, D. N. Lu, J. J. Trombetta, D. Gennert, A. Gnirke, A. Goren, N. Hacohen, J. Z. Levin, H. Park, A. Regev, Single-cell transcriptomics reveals bimodality in expression and splicing in immune cells. *Nature* **498**, 236-240 (2013); published online EpubJun 13 (Doi 10.1038/Nature12172).
36. R. Losick, C. Desplan, Stochasticity and Cell Fate. *Science* **320**, 65-68 (2008); published online EpubApril 4, 2008 (10.1126/science.1147888).
37. S. J. Altschuler, L. F. Wu, Cellular Heterogeneity: Do Differences Make a Difference? *Cell* **141**, 559-563 10.1016/j.cell.2010.04.033).
38. H. Rubin, The significance of biological heterogeneity. *Cancer metastasis reviews* **9**, 1-20 (1990); published online EpubJul (
39. W. M. Elsasser, Outline of a theory of cellular heterogeneity. *Proc Natl Acad Sci U S A* **81**, 5126-5129 (1984); published online EpubAug (
40. S. V. Sharma, D. Y. Lee, B. Li, M. P. Quinlan, F. Takahashi, S. Maheswaran, U. McDermott, N. Azizian, L. Zou, M. A. Fischbach, K. K. Wong, K. Brandstetter, B. Wittner, S. Ramaswamy, M. Classon, J. Settleman, A chromatin-mediated reversible drug-tolerant state in cancer cell subpopulations. *Cell* **141**, 69-80 (2010); published online EpubApr 2 (10.1016/j.cell.2010.02.027).
41. K. E. Gascoigne, S. S. Taylor, Cancer cells display profound intra- and interline variation following prolonged exposure to antimitotic drugs. *Cancer cell* **14**, 111-122 (2008); published online EpubAug 12 (10.1016/j.ccr.2008.07.002).

42. A. A. Cohen, N. Geva-Zatorsky, E. Eden, M. Frenkel-Morgenstern, I. Issaeva, A. Sigal, R. Milo, C. Cohen-Saidon, Y. Liron, Z. Kam, L. Cohen, T. Danon, N. Perzov, U. Alon, Dynamic proteomics of individual cancer cells in response to a drug. *Science* **322**, 1511-1516 (2008); published online EpubDec 5 (10.1126/science.1160165).
43. N. Q. Balaban, J. Merrin, R. Chait, L. Kowalik, S. Leibler, Bacterial persistence as a phenotypic switch. *Science* **305**, 1622-1625 (2004); published online EpubSep 10 (10.1126/science.1099390).
44. D. K. Singh, C. J. Ku, C. Wichaidit, R. J. Steininger, 3rd, L. F. Wu, S. J. Altschuler, Patterns of basal signaling heterogeneity can distinguish cellular populations with different drug sensitivities. *Mol Syst Biol* **6**, 369 (2010); published online EpubMay 11 (10.1038/msb.2010.22).
45. L. H. Loo, H. J. Lin, D. K. Singh, K. M. Lyons, S. J. Altschuler, L. F. Wu, Heterogeneity in the physiological states and pharmacological responses of differentiating 3T3-L1 preadipocytes. *J Cell Biol* **187**, 375-384 (2009); published online EpubNov 2 (10.1083/jcb.200904140).
46. D. Verhoeven, J. R. Teijaro, D. L. Farber, Heterogeneous Memory T Cells in Antiviral Immunity and Immunopathology. *Viral Immunology* **21**, 99-114 (2008); published online Epub2008/06/01 (10.1089/vim.2008.0002).
47. R. Satija, A. K. Shalek, Heterogeneity in immune responses: from populations to single cells. *Trends in Immunology* **35**, 219-229 10.1016/j.it.2014.03.004).
48. C. Ma, R. Fan, H. Ahmad, Q. H. Shi, B. Comin-Anduix, T. Chodon, R. C. Koya, C. C. Liu, G. A. Kwong, C. G. Radu, A. Ribas, J. R. Heath, A clinical microchip for evaluation of single immune cells reveals high functional heterogeneity in phenotypically similar T cells. *Nature Medicine* **17**, 738-U133 (2011); published online EpubJun (Doi 10.1038/Nm.2375).
49. K. Klepárník, F. Foret, Recent advances in the development of single cell analysis—A review. *Analytica Chimica Acta* **800**, 12-21 (2013); published online Epub10/24/ (http://dx.doi.org/10.1016/j.aca.2013.09.004).
50. C. A. Smurthwaite, B. J. Hilton, R. O'Hanlon, Z. D. Stolp, B. M. Hancock, D. Abbadessa, A. Stotland, L. A. Sklar, R. Wolkowicz, Fluorescent Genetic Barcoding in Mammalian Cells for Enhanced Multiplexing Capabilities in Flow Cytometry. *Cytom Part A* **85A**, 105-113 (2014); published online EpubJan (Doi 10.1002/Cyto.A.22406).
51. P. O. Krutzik, G. P. Nolan, Fluorescent cell barcoding in flow cytometry allows high-throughput drug screening and signaling profiling. *Nat Methods* **3**, 361-368 (2006); published online EpubMay (Doi 10.1038/Nmeth872).
52. E. W. Newell, N. Sigel, S. C. Bendall, G. P. Nolan, M. M. Davis, Cytometry by Time-of-Flight Shows Combinatorial Cytokine Expression and Virus-Specific Cell Niches within a Continuum of CD8(+) T Cell Phenotypes (vol 36, pg 142, 2012). *Immunity* **38**, 198-199 (2013); published online EpubJan 24 (DOI 10.1016/j.immuni.2012.12.002).
53. N. Zivanovic, A. Jacobs, B. Bodenmiller, A Practical Guide to Multiplexed Mass Cytometry. *Curr Top Microbiol* **377**, 95-109 (2014)Doi 10.1007/82_2013_335).
54. B. Bodenmiller, E. R. Zunder, R. Finck, T. J. Chen, E. S. Savig, R. V. Bruggner, E. F. Simonds, S. C. Bendall, K. Sachs, P. O. Krutzik, G. P. Nolan, Multiplexed

mass cytometry profiling of cellular states perturbed by small-molecule regulators. *Nat Biotechnol* **30**, 858-U889 (2012); published online EpubSep (Doi 10.1038/Nbt.2317).

55. K. R. Atkuri, J. C. Stevens, H. Neubert, Mass Cytometry: A Highly Multiplexed Single-Cell Technology for Advancing Drug Development. *Drug Metab Dispos* **43**, 227-233 (2015); published online EpubFeb (DOI 10.1124/dmd.114.060798).
56. C. Giesen, H. A. O. Wang, D. Schapiro, N. Zivanovic, A. Jacobs, B. Hattendorf, P. J. Schuffler, D. Grolimund, J. M. Buhmann, S. Brandt, Z. Varga, P. J. Wild, D. Gunther, B. Bodenmillerthat, Highly multiplexed imaging of tumor tissues with subcellular resolution by mass cytometry. *Nat Methods* **11**, 417-+ (2014); published online EpubApr (Doi 10.1038/Nmeth.2869).
57. H. E. Mei, M. D. Leipold, A. R. Schulz, C. Chester, H. T. Maecker, Barcoding of Live Human Peripheral Blood Mononuclear Cells for Multiplexed Mass Cytometry. *J Immunol* **194**, 2022-2031 (2015); published online EpubFeb 15 (DOI 10.4049/jimmunol.1402661).
58. B. Y. Liu, W. Chen, B. D. Evavold, C. Zhu, Accumulation of Dynamic Catch Bonds between TCR and Agonist Peptide-MHC Triggers T Cell Signaling. *Cell* **157**, 357-368 (2014); published online EpubApr 10 (DOI 10.1016/j.cell.2014.02.053).
59. B. Dura, S. K. Dougan, M. Barisa, M. M. Hoehl, C. T. Lo, H. L. Ploegh, J. Voldman, Profiling lymphocyte interactions at the single-cell level by microfluidic cell pairing. *Nat Commun* **6**, (2015); published online EpubJan (Artn 5940

Doi 10.1038/Ncomms6940).

60. N. S. P.A. Negulescu, and M.D. Cahalan, Intracellualr calcium dependence of gene expression in single T lymphocytes. *Proceedings of the National Academy of Sciences* **91**, 2873-2877 (1994).
61. M. J. Miller, O. Safrina, I. Parker, M. D. Cahalan, Imaging the Single Cell Dynamics of CD4+ T Cell Activation by Dendritic Cells in Lymph Nodes. *The Journal of Experimental Medicine* **200**, 847-856 (2004); published online EpubOctober 4, 2004 (10.1084/jem.20041236).
62. N. Jiang, J. Huang, L. J. Edwards, B. Liu, Y. Zhang, C. D. Beal, B. D. Evavold, C. Zhu, Two-Stage Cooperative T Cell Receptor-Peptide Major Histocompatibility Complex-CD8 Trimolecular Interactions Amplify Antigen Discrimination. *Immunity* **34**, 13-23 (2011); published online Epub1/28/ (http://dx.doi.org/10.1016/j.immuni.2010.12.017).
63. S. E. Chesla, P. Selvaraj, C. Zhu, Measuring Two-Dimensional Receptor-Ligand Binding Kinetics by Micropipette. *Biophysical journal* **75**, 1553-1572 (1998).
64. W. Chen, V. Zarnitsyna, K. Sarangapani, J. Huang, C. Zhu, Measuring Receptor–Ligand Binding Kinetics on Cell Surfaces: From Adhesion Frequency to Thermal Fluctuation Methods. *Cellular and Molecular Bioengineering* **1**, 276-288 (2008)10.1007/s12195-008-0024-8).
65. K. S. Weber, Q. J. Li, S. P. Persaud, J. D. Campbell, M. M. Davis, P. M. Allen, Distinct CD4(+) helper T cells involved in primary and secondary responses to infection. *Proceedings of the National Academy of Sciences of the United States*

of America **109**, 9511-9516 (2012); published online EpubJun 12 (DOI 10.1073/pnas.1202408109).
66. G. P. O'Donoghue, R. M. Pielak, A. A. Smoligovets, J. J. Lin, J. T. Groves, Direct single molecule measurement of TCR triggering by agonist pMHC in living primary T cells. *Elife* **2**, (2013); published online EpubJul 3 (UNSP e00778 DOI 10.7554/eLife.00778.001).
67. L. Flatz, R. Roychoudhuri, M. Honda, A. Filali-Mouhim, J. P. Goulet, N. Kettaf, M. Lin, M. Roederer, E. K. Haddad, R. P. Sekaly, G. J. Nabel, Single-cell gene-expression profiling reveals qualitatively distinct CD8 T cells elicited by different gene-based vaccines. *Proceedings of the National Academy of Sciences of the United States of America* **108**, 5724-5729 (2011); published online EpubApr 5 (DOI 10.1073/pnas.1013084108).
68. E. K. Sackmann, A. L. Fulton, D. J. Beebe, The present and future role of microfluidics in biomedical research. *Nature* **507**, 181-189 (2014); published online Epub03/13/print (10.1038/nature13118).
69. M. Zhan, L. Chingozha, H. Lu, Enabling Systems Biology Approaches Through Microfabricated Systems. *Analytical Chemistry* **85**, 8882-8894 (2013); published online EpubOct 1 (Doi 10.1021/Ac401472y).
70. G. M. Whitesides, The origins and the future of microfluidics. *Nature* **442**, 368-373 (2006).
71. J. El-Ali, P. K. Sorger, K. F. Jensen, Cells on chips. *Nature* **442**, 403-411 (2006).
72. D. B. Weibel, W. R. DiLuzio, G. M. Whitesides, Microfabrication meets microbiology. *Nat Rev Micro* **5**, 209-218 (2007).
73. J. Voldman, M. L. Gray, M. A. Schmidt, Microfabrication in Biology and Medicine. *Annual Review of Biomedical Engineering* **1**, 401-425 (1999)doi:10.1146/annurev.bioeng.1.1.401).
74. G. Velve-Casquillas, M. Le Berre, M. Piel, P. T. Tran, Microfluidic tools for cell biological research. *Nano Today* **5**, 28-47 (2010); published online EpubFeb (DOI 10.1016/j.nantod.2009.12.001).
75. K. H. Chung, M. M. Crane, H. Lu, Automated on-chip rapid microscopy, phenotyping and sorting of C. elegans. *Nat Methods* **5**, 637-643 (2008); published online EpubJul (Doi 10.1038/Nmeth.1227).
76. S. R. Quake, A. Scherer, From Micro- to Nanofabrication with Soft Materials. *Science* **290**, 1536-1540 (2000); published online EpubNovember 24, 2000 (10.1126/science.290.5496.1536).
77. J. K. Osiri, H. Shadpour, M. A. Witek, S. A. Soper, Integrated multifunctional microfluidics for automated proteome analyses. *Topics in current chemistry* **304**, 261-294 (2011)10.1007/128_2011_152).
78. T. Thorsen, S. J. Maerkl, S. R. Quake, Microfluidic large-scale integration. *Science* **298**, 580-584 (2002); published online EpubOct 18 (DOI 10.1126/science.1076996).
79. J. Melin, S. R. Quake, Microfluidic large-scale integration: The evolution of design rules for biological automation. *Annu Rev Bioph Biom* **36**, 213-231 (2007)DOI 10.1146/annurev.biophys.36.040306.132646).

80. I. E. Araci, P. Brisk, Recent developments in microfluidic large scale integration. *Curr Opin Biotech* **25**, 60-68 (2014); published online EpubFeb (DOI 10.1016/j.copbio.2013.08.014).
81. K. Chung, C. A. Rivet, M. L. Kemp, H. Lu, Imaging Single-Cell Signaling Dynamics with a Deterministic High-Density Single-Cell Trap Array. *Analytical Chemistry* **83**, 7044-7052 (2011); published online Epub2011/09/15 (10.1021/ac2011153).
82. H. Zhang, K.-K. Liu, Optical tweezers for single cells. *Journal of The Royal Society Interface* **5**, 671-690 (2008); published online EpubJuly 6, 2008 (10.1098/rsif.2008.0052).
83. R. D. Sochol, M. E. Dueck, S. Li, L. P. Lee, L. Lin, Hydrodynamic resettability for a microfluidic particulate-based arraying system. *Lab on a Chip* **12**, 5051-5056 (2012).
84. J. R. Rettig, A. Folch, Large-Scale Single-Cell Trapping And Imaging Using Microwell Arrays. *Analytical Chemistry* **77**, 5628-5634 (2005)10.1021/ac0505977).
85. X. Ding, S.-C. S. Lin, B. Kiraly, H. Yue, S. Li, I.-K. Chiang, J. Shi, S. J. Benkovic, T. J. Huang, On-chip manipulation of single microparticles, cells, and organisms using surface acoustic waves. *Proceedings of the National Academy of Sciences*, (2012); published online EpubJune 25, 2012 (10.1073/pnas.1209288109).
86. S. Takayama, E. Ostuni, P. LeDuc, K. Naruse, D. E. Ingber, G. M. Whitesides, Laminar flows - Subcellular positioning of small molecules. *Nature* **411**, 1016-1016 (2001); published online EpubJun 28 (Doi 10.1038/35082637).
87. B. Mosadegh, C. Huang, J. W. Park, H. S. Shin, B. G. Chung, S. K. Hwang, K. H. Lee, H. J. Kim, J. Brody, N. L. Jeon, Generation of stable complex gradients across two-dimensional surfaces and three-dimensional gels. *Langmuir* **23**, 10910-10912 (2007); published online EpubOct 23 (Doi 10.1021/La7026835).
88. D. Kim, M. A. Lokuta, A. Huttenlocher, D. J. Beebe, Selective and tunable gradient device for cell culture and chemotaxis study. *Lab Chip* **9**, 1797-1800 (2009); published online EpubJun 21 (10.1039/b901613a).
89. A. Jovic, S. M. Wade, A. Miyawaki, R. R. Neubig, J. J. Linderman, S. Takayama, Hi-Fi transmission of periodic signals amid cell-to-cell variability. *Molecular BioSystems* **7**, 2238-2244 (2011).
90. N. L. Jeon, S. K. W. Dertinger, D. T. Chiu, I. S. Choi, A. D. Stroock, G. M. Whitesides, Generation of Solution and Surface Gradients Using Microfluidic Systems. *Langmuir* **16**, 8311-8316 (2000); published online Epub2000/10/01 (10.1021/la000600b).
91. L. He, A. Kniss, A. San-Miguel, T. Rouse, M. L. Kemp, H. Lu, An automated programmable platform enabling multiplex dynamic stimuli delivery and cellular response monitoring for high-throughput suspension single-cell signaling studies. *Lab on a Chip* **15**, 1497-1507 (2015)10.1039/C4LC01070A).
92. B. G. Chung, F. Lin, N. L. Jeon, A microfluidic multi-injector for gradient generation. *Lab on a Chip* **6**, 764-768 (2006); published online EpubJun (Doi 10.1039/B512667c).

93. L. Chingozha, M. Zhan, C. Zhu, H. Lu, A Generalizable, Tunable Microfluidic Platform for Delivering Fast Temporally Varying Chemical Signals to Probe Single-Cell Response Dynamics. *Analytical Chemistry* **86**, 10138-10147 (2014); published online EpubOct 21 (Doi 10.1021/Ac5019843).
94. Y.-A. Chen, A. D. King, H.-C. Shih, C.-C. Peng, C.-Y. Wu, W.-H. Liao, Y.-C. Tung, Generation of oxygen gradients in microfluidic devices for cell culture using spatially confined chemical reactions. *Lab on a Chip* **11**, 3626-3633 (2011).
95. K. Campbell, A. Groisman, Generation of complex concentration profiles in microchannels in a logarithmically small number of steps. *Lab Chip* **7**, 264-272 (2007); published online EpubFeb (10.1039/b610011b).
96. J. Atencia, J. Morrow, L. E. Locascio, The microfluidic palette: A diffusive gradient generator with spatio-temporal control. *Lab on a Chip* **9**, 2707-2714 (2009).
97. J. Atencia, D. J. Beebe, Controlled microfluidic interfaces. *Nature* **437**, 648-655 (2005).
98. D. Amarie, J. A. Glazier, S. C. Jacobson, Compact Microfluidic Structures for Generating Spatial and Temporal Gradients. *Analytical Chemistry* **79**, 9471-9477 (2007); published online Epub2007/12/01 (10.1021/ac0714967).
99. D. Ahmed, C. Y. Chan, S.-C. S. Lin, H. S. Muddana, N. Nama, S. J. Benkovic, T. Jun Huang, Tunable, pulsatile chemical gradient generation via acoustically driven oscillating bubbles. *Lab on a Chip* **13**, 328-331 (2013).
100. Y. Ben-Ari, Y. Glick, S. Kipper, N. Schwartz, D. Avrahami, E. Barbiro-Michaely, D. Gerber, Microfluidic large scale integration of viral-host interaction analysis. *Lab on a Chip* **13**, 2202-2209 (2013)Doi 10.1039/C3lc00034f).
101. W. H. Grover, A. M. Skelley, C. N. Liu, E. T. Lagally, R. A. Mathies, Monolithic membrane valves and diaphragm pumps for practical large-scale integration into glass microfluidic devices. *Sensor Actuat B-Chem* **89**, 315-323 (2003); published online EpubApr 1 (Doi 10.1016/S0925-4005(02)00468-9).
102. S. Quake, The chips are down - microfluidic large-scale integration. *Trac-Trend Anal Chem* **21**, Xii-Xiii (2002); published online EpubNov (
103. P. N. Nge, C. I. Rogers, A. T. Woolley, Advances in Microfluidic Materials, Functions, Integration, and Applications. *Chemical Reviews* **113**, 2550-2583 (2013); published online Epub2013/04/10 (10.1021/cr300337x).
104. J. C. McDonald, D. C. Duffy, J. R. Anderson, D. T. Chiu, H. Wu, O. J. A. Schueller, G. M. Whitesides, Fabrication of microfluidic systems in poly(dimethylsiloxane). *ELECTROPHORESIS* **21**, 27-40 (2000)10.1002/(sici)1522-2683(20000101)21:1<27::aid-elps27>3.0.co;2-c).
105. R. Jackman, J. Wilbur, G. Whitesides, Fabrication of submicrometer features on curved substrates by microcontact printing. *Science* **269**, 664-666 (1995); published online EpubAugust 4, 1995 (10.1126/science.7624795).
106. D. R. Reyes, D. Iossifidis, P.-A. Auroux, A. Manz, Micro Total Analysis Systems. 1. Introduction, Theory, and Technology. *Analytical Chemistry* **74**, 2623-2636 (2002); published online Epub2002/06/01 (10.1021/ac0202435).
107. P. J. A. Kenis, R. F. Ismagilov, G. M. Whitesides, Microfabrication Inside Capillaries Using Multiphase Laminar Flow Patterning. *Science* **285**, 83-85 (1999); published online EpubJuly 2, 1999 (10.1126/science.285.5424.83).

108. X.-M. Zhao, Y. Xia, G. M. Whitesides, Soft lithographic methods for nano-fabrication. *Journal of Materials Chemistry* **7**, 1069-1074 (1997).
109. Y. Xia, G. M. Whitesides, SOFT LITHOGRAPHY. *Annual Review of Materials Science* **28**, 153-184 (1998)doi:10.1146/annurev.matsci.28.1.153).
110. G. M. Whitesides, E. Ostuni, S. Takayama, X. Jiang, D. E. Ingber, SOFT LITHOGRAPHY IN BIOLOGY AND BIOCHEMISTRY. *Annual Review of Biomedical Engineering* **3**, 335-373 (2001)doi:10.1146/annurev.bioeng.3.1.335).
111. H. Craighead, Future lab-on-a-chip technologies for interrogating individual molecules. *Nature* **442**, 387-393 (2006).
112. S. K. Sia, G. M. Whitesides, Microfluidic devices fabricated in Poly(dimethylsiloxane) for biological studies. *ELECTROPHORESIS* **24**, 3563-3576 (2003)10.1002/elps.200305584).
113. W.-H. Tan, S. Takeuchi, A trap-and-release integrated microfluidic system for dynamic microarray applications. *Proceedings of the National Academy of Sciences* **104**, 1146-1151 (2007); published online EpubJanuary 23, 2007 (10.1073/pnas.0606625104).
114. S. Kobel, A. Valero, J. Latt, P. Renaud, M. Lutolf, Optimization of microfluidic single cell trapping for long-term on-chip culture. *Lab on a Chip* **10**, 857-863 (2010).
115. R. D. Sochol, S. Li, L. P. Lee, L. Lin, Continuous flow multi-stage microfluidic reactors via hydrodynamic microparticle railing. *Lab on a Chip* **12**, 4168-4177 (2012).
116. P. J. Lee, P. J. Hung, R. Shaw, L. Jan, L. P. Lee, Microfluidic application-specific integrated device for monitoring direct cell-cell communication via gap junctions between individual cell pairs. *Applied Physics Letters* **86**, 223902 (2005).
117. T. P. Hunt, D. Issadore, R. M. Westervelt, Integrated circuit/microfluidic chip to programmably trap and move cells and droplets with dielectrophoresis. *Lab on a Chip* **8**, 81-87 (2008)10.1039/B710928H).
118. X. Y. Hu, P. H. Bessette, J. R. Qian, C. D. Meinhart, P. S. Daugherty, H. T. Soh, Marker-specific sorting of rare cells using dielectrophoresis. *Proceedings of the National Academy of Sciences of the United States of America* **102**, 15757-15761 (2005); published online EpubNov 1 (DOI 10.1073/pnas.0507719102).
119. T. Arakawa, M. Noguchi, K. Sumitomo, Y. Yamaguchi, S. Shoji, High-throughput single-cell manipulation system for a large number of target cells. *Biomicrofluidics* **5**, 014114-014111 (2011).
120. D. Di Carlo, N. Aghdam, L. P. Lee, Single-Cell Enzyme Concentrations, Kinetics, and Inhibition Analysis Using High-Density Hydrodynamic Cell Isolation Arrays. *Analytical Chemistry* **78**, 4925-4930 (2006)10.1021/ac060541s).
121. J.-P. Frimat, M. Becker, Y.-Y. Chiang, U. Marggraf, D. Janasek, J. G. Hengstler, J. Franzke, J. West, A microfluidic array with cellular valving for single cell co-culture. *Lab on a Chip* **11**, 231-237 (2011).
122. R. Johann, Cell trapping in microfluidic chips. *Analytical and Bioanalytical Chemistry* **385**, 408-412 (2006)10.1007/s00216-006-0369-6).
123. C. Liu, J. Liu, D. Gao, M. Ding, J.-M. Lin, Fabrication of Microwell Arrays Based on Two-Dimensional Ordered Polystyrene Microspheres for High-

Throughput Single-Cell Analysis. *Analytical Chemistry* **82**, 9418-9424 (2010)10.1021/ac102094r).

124. J. Nilsson, M. Evander, B. Hammarstrˆm, T. Laurell, Review of cell and particle trapping in microfluidic systems. *Analytica Chimica Acta* **649**, 141-157 (2009).
125. T. Teshima, H. Ishihara, K. Iwai, A. Adachi, S. Takeuchi, A dynamic microarray device for paired bead-based analysis. *Lab on a Chip* **10**, 2443-2448 (2010).
126. A. R. Wheeler, W. R. Throndset, R. J. Whelan, A. M. Leach, R. N. Zare, Y. H. Liao, K. Farrell, I. D. Manger, A. Daridon, Microfluidic Device for Single-Cell Analysis. *Analytical Chemistry* **75**, 3581-3586 (2003)10.1021/ac0340758).
127. Y. Yamaguchi, T. Arakawa, N. Takeda, Y. Edagawa, S. Shoji, Development of a poly-dimethylsiloxane microfluidic device for single cell isolation and incubation. *Sensors and Actuators B: Chemical* **136**, 555-561 (2009).
128. W. H. Henley, P. J. Dennis, J. M. Ramsey, Fabrication of Microfluidic Devices Containing Patterned Microwell Arrays. *Analytical Chemistry* **84**, 1776-1780 (2012); published online Epub2012/02/07 (10.1021/ac202445g).
129. J. Clausell-Tormos, D. Lieber, J.-C. Baret, A. El-Harrak, O. J. Miller, L. Frenz, J. Blouwolff, K. J. Humphry, S. Köster, H. Duan, C. Holtze, D. A. Weitz, A. D. Griffiths, C. A. Merten, Droplet-Based Microfluidic Platforms for the Encapsulation and Screening of Mammalian Cells and Multicellular Organisms. *Chemistry & Biology* **15**, 427-437 (2008); published online Epub5/19/ (http://dx.doi.org/10.1016/j.chembiol.2008.04.004).
130. E. Brouzes, M. Medkova, N. Savenelli, D. Marran, M. Twardowski, J. B. Hutchison, J. M. Rothberg, D. R. Link, N. Perrimon, M. L. Samuels, Droplet microfluidic technology for single-cell high-throughput screening. *Proc Natl Acad Sci U S A* **106**, 14195-14200 (2009); published online EpubAug 25 (10.1073/pnas.0903542106).
131. J. Clausell-Tormos, D. Lieber, J. C. Baret, A. El-Harrak, O. J. Miller, L. Frenz, J. Blouwolff, K. J. Humphry, S. Koster, H. Duan, C. Holtze, D. A. Weitz, A. D. Griffiths, C. A. Merten, Droplet-based microfluidic platforms for the encapsulation and screening of Mammalian cells and multicellular organisms. *Chem Biol* **15**, 427-437 (2008); published online EpubMay (10.1016/j.chembiol.2008.04.004).
132. T. Konry, A. Golberg, M. Yarmush, Live single cell functional phenotyping in droplet nano-liter reactors. *Sci Rep-Uk* **3**, (2013); published online EpubNov 11 (Artn 3179

Doi 10.1038/Srep03179).

133. P. K. Chattopadhyay, T. M. Gierahn, M. Roederer, J. C. Love, Single-cell technologies for monitoring immune systems. *Nat Immunol* **15**, 128-135 (2014); published online EpubFeb (Doi 10.1038/Ni.2796).
134. N. Varadarajan, B. Julg, Y. J. Yamanaka, H. Chen, A. O. Ogunniyi, E. McAndrew, L. C. Porter, A. Piechocka-Trocha, B. J. Hill, D. C. Douek, F. Pereyra, B. D. Walker, J. C. Love, A high-throughput single-cell analysis of human CD8+ T cell functions reveals discordance for cytokine secretion and cytolysis. *The Journal of Clinical Investigation* **121**, 4322-4331 (2011)10.1172/JCI58653).

135. E. M. Bradshaw, S. C. Kent, V. Tripuraneni, T. Orban, H. L. Ploegh, D. A. Hafler, J. C. Love, Concurrent detection of secreted products from human lymphocytes by microengraving: Cytokines and antigen-reactive antibodies. *Clin Immunol* **129**, 10-18 (2008); published online EpubOct (DOI 10.1016/j.clim.2008.06.009).
136. A. M. Skelley, O. Kirak, H. Suh, R. Jaenisch, J. Voldman, Microfluidic control of cell pairing and fusion. *Nat Meth* **6**, 147-152 (2009)http://www.nature.com/nmeth/journal/v6/n2/suppinfo/nmeth.1290_S1.html).
137. J. Huang, L. J. Edwards, B. D. Evavold, C. Zhu, Kinetics of MHC-CD8 Interaction at the T Cell Membrane. *The Journal of Immunology* **179**, 7653-7662 (2007); published online EpubDecember 1, 2007 (10.4049/jimmunol.179.11.7653).
138. V. I. Zarnitsyna, C. Zhu, Adhesion Frequency Assay for In Situ Kinetics Analysis of Cross-Junctional Molecular Interactions at the Cell-Cell Interface. e3519 (2011); published online Epub2011/11/02/ (doi:10.3791/3519).
139. V. Pérez Koldenkova, T. Nagai, Genetically encoded Ca2 + indicators: Properties and evaluation. *Biochimica et Biophysica Acta (BBA) - Molecular Cell Research* **1833**, 1787-1797 (2013); published online Epub7// (http://dx.doi.org/10.1016/j.bbamcr.2013.01.011).
140. R. E. Dolmetsch, K. Xu, R. S. Lewis, Calcium oscillations increase the efficiency and specificity of gene expression. *Nature* **392**, 933-936 (1998); published online Epub04/30/print (
141. J. Herz, V. Siffrin, A. E. Hauser, A. U. Brandt, T. Leuenberger, H. Radbruch, F. Zipp, R. A. Niesner, Expanding Two-Photon Intravital Microscopy to the Infrared by Means of Optical Parametric Oscillator. *Biophys J* **98**, 715-723 (2010); published online Epub2/17/ (http://dx.doi.org/10.1016/j.bpj.2009.10.035).
142. D. Kim, A. E. Herr, Protein immobilization techniques for microfluidic assays. *Biomicrofluidics* **7**, (2013); published online EpubJul (Artn 041501
Doi 10.1063/1.4816934).
143. F. Rusmini, Z. Zhong, J. Feijen, Protein Immobilization Strategies for Protein Biochips. *Biomacromolecules* **8**, 1775-1789 (2007); published online Epub2007/06/01 (10.1021/bm061197b).
144. N. M. Green, The use of [14C] biotin for kinetic studies and for assay. *Biochemical Journal* **89**, 585-591.
145. L. Baitsch, P. Baumgaertner, Dev, xEa, E. vre, S. K. Raghav, A. Legat, L. Barba, S. Wieckowski, xE, bastien, H. Bouzourene, B. Deplancke, P. Romero, N. Rufer, D. E. Speiser, Exhaustion of tumor-specific CD8+ T cells in metastases from melanoma patients. *The Journal of Clinical Investigation* **121**, 2350-2360 (2011)10.1172/JCI46102).
146. D. H. Munn, A. L. Mellor, The tumor-draining lymph node as an immune-privileged site. *Immunological Reviews* **213**, 146-158 (2006)10.1111/j.1600-065X.2006.00444.x).
147. A. Zippelius, P. Batard, V. Rubio-Godoy, G. Bioley, D. Liénard, F. Lejeune, D. Rimoldi, P. Guillaume, N. Meidenbauer, A. Mackensen, N. Rufer, N. Lubenow, D. Speiser, J.-C. Cerottini, P. Romero, M. J. Pittet, Effector Function of Human

Tumor-Specific CD8 T Cells in Melanoma Lesions: A State of Local Functional Tolerance. *Cancer Research* **64**, 2865-2873 (2004); published online EpubApril 15, 2004 (10.1158/0008-5472.can-03-3066).

148. Y. Zhang, C. Ge, C. Zhu, K. Salaita, DNA-based digital tension probes reveal integrin forces during early cell adhesion. *Nat Commun* **5**, (2014); published online Epub10/24/online (10.1038/ncomms6167).
149. P. Hersen, M. N. McClean, L. Mahadevan, S. Ramanathan, Signal processing by the HOG MAP kinase pathway. *Proceedings of the National Academy of Sciences of the United States of America* **105**, 7165-7170 (2008); published online EpubMay 20 (DOI 10.1073/pnas.0710770105).
150. Y. Kim, S. D. Joshi, W. C. Messner, P. R. LeDuc, L. A. Davidson, Detection of Dynamic Spatiotemporal Response to Periodic Chemical Stimulation in a Xenopus Embryonic Tissue. *Plos One* **6**, (2011); published online EpubJan 31 (ARTN e14624
DOI 10.1371/journal.pone.0014624).
151. T. Tomida, S. Oda, M. Takekawa, Y. Iino, H. Saito, The Temporal Pattern of Stimulation Determines the Extent and Duration of MAPK Activation in a Caenorhabditis elegans Sensory Neuron. *Sci Signal* **5**, (2012); published online EpubOct 16 (ARTN ra76
DOI 10.1126/scisignal.2002983).
152. J. Kawada, H. Kimura, H. Akutsu, Y. Sakai, T. Fujii, Spatiotemporally controlled delivery of soluble factors for stem cell differentiation. *Lab Chip* **12**, 4508-4515 (2012); published online EpubNov 7 (10.1039/c2lc40268h).
153. J. S. Garanich, R. A. Mathura, Z. D. Shi, J. M. Tarbell, Effects of fluid shear stress on adventitial fibroblast migration: implications for flow-mediated mechanisms of arterialization and intimal hyperplasia. *Am J Physiol-Heart C* **292**, H3128-H3135 (2007); published online EpubJun (DOI 10.1152/ajpheart.00578.2006).
154. J. Dalous, E. Burghardt, A. Muller-Taubenberger, F. Bruckert, G. Gerisch, T. Bretschneider, Reversal of cell polarity and actin-myosin cytoskeleton reorganization under mechanical and chemical stimulation. *Biophys J* **94**, 1063-1074 (2008); published online EpubFeb 1 (DOI 10.1529/biophysj.107.114702).
155. C. J. Wang, A. Bergmann, B. Lin, K. Kim, A. Levchenko, Diverse sensitivity thresholds in dynamic signaling responses by social amoebae. *Sci Signal* **5**, ra17 (2012); published online EpubFeb 28 (10.1126/scisignal.2002449).
156. J. T. Mettetal, D. Muzzey, C. Gómez-Uribe, A. van Oudenaarden, The Frequency Dependence of Osmo-Adaptation in Saccharomyces cerevisiae. *Science* **319**, 482-484 (2008); published online EpubJanuary 25, 2008 (10.1126/science.1151582).
157. Y. Awwad, T. Geng, A. S. Baldwin, C. Lu, Observing Single Cell NF-κB Dynamics under Stimulant Concentration Gradient. *Analytical Chemistry* **84**, 1224-1228 (2012); published online Epub2012/02/07 (10.1021/ac203209t).
158. O. Thastrup, P. J. Cullen, B. K. Drøbak, M. R. Hanley, A. P. Dawson, Thapsigargin, a tumor promoter, discharges intracellular Ca^{2+} stores by specific inhibition of the endoplasmic reticulum Ca2(+)-ATPase. *Proceedings of the National Academy of Sciences* **87**, 2466-2470 (1990); published online EpubApril 1, 1990 (

159. A. Edelstein, N. Amodaj, K. Hoover, R. Vale, N. Stuurman, *Computer Control of Microscopes Using μManager*. Current Protocols in Molecular Biology (John Wiley & Sons, Inc., 2010).
160. Y. Q. Luo, R. N. Zare, Perforated membrane method for fabricating three-dimensional polydimethylsiloxane microfluidic devices. *Lab on a Chip* **8**, 1688-1694 (2008); published online EpubOct (Doi 10.1039/B807751g).
161. H. B. Wei, B. H. Chueh, H. L. Wu, E. W. Hall, C. W. Li, R. Schirhagl, J. M. Lin, R. N. Zare, Particle sorting using a porous membrane in a microfluidic device. *Lab on a Chip* **11**, 238-245 (2011)Doi 10.1039/C0lc00121j).
162. M. Treiman, C. Caspersen, S. B. Christensen, A tool coming of age: thapsigargin as an inhibitor of sarco-endoplasmic reticulum Ca^{2+}-ATPases. *Trends in Pharmacological Sciences* **19**, 131-135 (1998); published online Epub4/1/ (http://dx.doi.org/10.1016/S0165-6147(98)01184-5).
163. Y. Bushkin, F. Radford, R. Pine, A. Lardizabal, B. T. Mangura, M. L. Gennaro, S. Tyagi, Profiling T Cell Activation Using Single-Molecule Fluorescence In Situ Hybridization and Flow Cytometry. *J Immunol* **194**, 836-841 (2015); published online EpubJan 15 (DOI 10.4049/jimmunol.1401515).
164. K. H. Chen, A. N. Boettiger, J. R. Moffitt, S. Wang, X. Zhuang, Spatially resolved, highly multiplexed RNA profiling in single cells. *Science* **348**, (2015); published online EpubApril 24, 2015 (10.1126/science.aaa6090).
165. E. Lubeck, L. Cai, Single-cell systems biology by super-resolution imaging and combinatorial labeling. *Nat Methods* **9**, 743-U159 (2012); published online EpubJul (Doi 10.1038/Nmeth.2069).
166. Proteomics research accelerated by new lab-on-a-chip device. *Expert Rev Proteomic* **4**, 338-338 (2007); published online EpubJun (
167. W. Pan, W. Chen, X. Jiang, Microfluidic Western Blot. *Analytical Chemistry* **82**, 3974-3976 (2010); published online EpubMay 15 (10.1021/ac1000493).
168. A. M. Femino, F. S. Fay, K. Fogarty, R. H. Singer, Visualization of Single RNA Transcripts in Situ. *Science* **280**, 585-590 (1998); published online EpubApril 24, 1998 (10.1126/science.280.5363.585).
169. A. Raj, P. van den Bogaard, S. A. Rifkin, A. van Oudenaarden, S. Tyagi, Imaging individual mRNA molecules using multiple singly labeled probes. *Nat Methods* **5**, 877-879 (2008); published online EpubOct (Doi 10.1038/Nmeth.1253).
170. A. Raj, A. van Oudenaarden, Single-Molecule Approaches to Stochastic Gene Expression. *Annu Rev Biophys* **38**, 255-270 (2009)DOI 10.1146/annurev.biophys.37.032807.125928).
171. F. Mueller, A. Senecal, K. Tantale, H. Marie-Nelly, N. Ly, O. Collin, E. Basyuk, E. Bertrand, X. Darzacq, C. Zimmer, FISH-quant: automatic counting of transcripts in 3D FISH images. *Nat Methods* **10**, 277-278 (2013); published online EpubApr (Doi 10.1038/Nmeth.2406).
172. J. A. H. Hoerter, J. Brzostek, M. N. Artyomov, S. M. Abel, J. Casas, V. Rybakin, J. Ampudia, C. Lotz, J. M. Connolly, A. K. Chakraborty, K. G. Gould, N. R. J. Gascoigne, Coreceptor affinity for MHC defines peptide specificity requirements for TCR interaction with coagonist peptide-MHC. *J Exp Med* **210**, 1807-1821 (2013); published online EpubAug 26 (Doi 10.1084/Jem.20122528).

173. M. Krogsgaard, Q.-j. Li, C. Sumen, J. B. Huppa, M. Huse, M. M. Davis, Agonist/endogenous peptide-MHC heterodimers drive T cell activation and sensitivity. *Nature* **434**, 238-243 (2005); published online Epub03/10/print (http://www.nature.com/nature/journal/v434/n7030/suppinfo/nature03391_S1.html).
174. Q.-J. Li, A. R. Dinner, S. Qi, D. J. Irvine, J. B. Huppa, M. M. Davis, A. K. Chakraborty, CD4 enhances T cell sensitivity to antigen by coordinating Lck accumulation at the immunological synapse. *Nat Immunol* **5**, 791-799 (2004); published online Epub08//print (http://www.nature.com/ni/journal/v5/n8/suppinfo/ni1095_S1.html).
175. P. P. Yachi, J. Ampudia, N. R. J. Gascoigne, T. Zal, Nonstimulatory peptides contribute to antigen-induced CD8-T cell receptor interaction at the immunological synapse. *Nat Immunol* **6**, 785-792 (2005); published online Epub08//print (http://www.nature.com/ni/journal/v6/n8/suppinfo/ni1220_S1.html).
176. P. P. Yachi, C. Lotz, J. Ampudia, N. R. J. Gascoigne, T cell activation enhancement by endogenous pMHC acts for both weak and strong agonists but varies with differentiation state. *The Journal of Experimental Medicine* **204**, 2747-2757 (2007); published online EpubOctober 29, 2007 (10.1084/jem.20062610).
177. J. D. Stone, D. H. Aggen, A. S. Chervin, S. Narayanan, T. M. Schmitt, P. D. Greenberg, D. M. Kranz, Opposite Effects of Endogenous Peptide–MHC Class I on T Cell Activity in the Presence and Absence of CD8. *The Journal of Immunology* **186**, 5193-5200 (2011); published online EpubMay 1, 2011 (10.4049/jimmunol.1003755).
178. N. R. J. Gascoigne, Do T cells need endogenous peptides for activation? *Nat Rev Immunol* **8**, 895-900 (2008); published online Epub11//print (
179. D. K. Cole, B. Laugel, M. Clement, D. A. Price, L. Wooldridge, A. K. Sewell, The molecular determinants of CD8 co-receptor function. *Immunology* **137**, 139-148 (2012)10.1111/j.1365-2567.2012.03625.x).
180. X. Cheng, D. Irimia, M. Dixon, K. Sekine, U. Demirci, L. Zamir, R. G. Tompkins, W. Rodriguez, M. Toner, A microfluidic device for practical label-free CD4+ T cell counting of HIV-infected subjects. *Lab on a Chip* **7**, 170-178 (2007)10.1039/B612966H).
181. M. A. Alyassin, S. Moon, H. O. Keles, F. Manzur, R. L. Lin, E. Haeggstrom, D. R. Kuritzkes, U. Demirci, Rapid automated cell quantification on HIV microfluidic devices. *Lab on a Chip* **9**, 3364-3369 (2009)Doi 10.1039/B911882a).
182. X. Cheng, A. Gupta, C. Chen, R. G. Tompkins, W. Rodriguez, M. Toner, Enhancing the performance of a point-of-care CD4+ T-cell counting microchip through monocyte depletion for HIV/AIDS diagnostics. *Lab on a Chip* **9**, 1357-1364 (2009)10.1039/B818813K).
183. M. J. Cotter, K. E. Norman, P. G. Hellewell, V. C. Ridger, A Novel Method for Isolation of Neutrophils from Murine Blood Using Negative Immunomagnetic Separation. *The American Journal of Pathology* **159**, 473-481 10.1016/S0002-9440(10)61719-1).

184. A. Boyum, Isolation of Mononuclear Cells and Granulocytes from Human Blood - Isolation of Mononuclear Cells by One Centrifugation and of Granulocytes by Combining Centrifugation and Sedimentation at L G. *Scand J Clin Lab Inv* **S 21**, 77-& (1968).
185. A. Boyum, Isolation of Lymphocytes, Granulocytes and Macrophages. *Scandinavian Journal of Immunology*, 9-15 (1976).
186. A. Bøyum, Separation of Blood Leucocytes, Granulocytes and Lymphocytes. *Tissue Antigens* **4**, 269-274 (1974)10.1111/j.1399-0039.1974.tb00252.x).
187. D. T. Fearon, L. A. Collins, Increased expression of C3b receptors on polymorphonuclear leukocytes induced by chemotactic factors and by purification procedures. *The Journal of Immunology* **130**, 370-375 (1983); published online EpubJanuary 1, 1983 (
188. J. Lundahl, G. Halldén, M. Hallgren, C. M. Sköld, J. Hed, Altered expression of CD11b/CD18 and CD62L on human monocytes after cell preparation procedures. *Journal of Immunological Methods* **180**, 93-100 (1995); published online Epub3/13/ (http://dx.doi.org/10.1016/0022-1759(94)00303-E).
189. S. A. Boppart, R. Richards-Kortum, *Point-of-care and point-of-procedure optical imaging technologies for primary care and global health*. (2014), vol. 6, pp. 253rv252-253rv252.
190. S. Seo, S. O. Isikman, I. Sencan, O. Mudanyali, T.-W. Su, W. Bishara, A. Erlinger, A. Ozcan, High-Throughput Lens-Free Blood Analysis on a Chip. *Analytical Chemistry* **82**, 4621-4627 (2010); published online Epub2010/06/01 (10.1021/ac1007915).
191. M. Toner, D. Irimia, BLOOD-ON-A-CHIP. *Annual Review of Biomedical Engineering* **7**, 77-103 (2005); published online Epub2005/08/15 (10.1146/annurev.bioeng.7.011205.135108).
192. H. M. Shapiro, E. R. Schildkraut, R. Curbelo, C. W. Laird, B. Turner, T. Hirschfeld, Combined blood cell counting and classification with fluorochrome stains and flow instrumentation. *Journal of Histochemistry & Cytochemistry* **24**, 396-401 (1976); published online EpubJanuary 1, 1976 (10.1177/24.1.56391).
193. B. George-Gay, K. Parker, Understanding the complete blood count with differential. *Journal of PeriAnesthesia Nursing* **18**, 96-117 (2003); published online Epub4// (http://dx.doi.org/10.1053/jpan.2003.50013).
194. R. Fan, O. Vermesh, A. Srivastava, B. K. H. Yen, L. D. Qin, H. Ahmad, G. A. Kwong, C. C. Liu, J. Gould, L. Hood, J. R. Heath, Integrated barcode chips for rapid, multiplexed analysis of proteins in microliter quantities of blood. *Nat Biotechnol* **26**, 1373-1378 (2008); published online EpubDec (Doi 10.1038/Nbt.1507).
195. T. Tachi, N. Kaji, M. Tokeshi, Y. Baba, Simultaneous Separation, Metering, and Dilution of Plasma from Human Whole Blood in a Microfluidic System. *Analytical Chemistry* **81**, 3194-3198 (2009); published online EpubApr 15 (Doi 10.1021/Ac802434z).
196. V. VanDelinder, A. Groisman, Separation of plasma from whole human blood in a continuous cross-flow in a molded microfluidic device. *Analytical Chemistry* **78**, 3765-3771 (2006); published online EpubJun 1 (Doi 10.1021/Ac060042r).

197. S. S. Shevkoplyas, T. Yoshida, L. L. Munn, M. W. Bitensky, Biomimetic autoseparation of leukocytes from whole blood in a microfluidic device. *Analytical Chemistry* **77**, 933-937 (2005); published online EpubFeb 1 (Doi 10.1021/Ac049037i).
198. Y. Tang, J. Shi, S. Li, L. Wang, Y. E. Cayre, Y. Chen, Microfluidic device with integrated microfilter of conical-shaped holes for high efficiency and high purity capture of circulating tumor cells. *Sci. Rep.* **4**, (2014); published online Epub08/13/online (10.1038/srep06052
http://www.nature.com/srep/2014/140813/srep06052/abs/srep06052.html#supplementary-information).
199. P. Sethu, L. L. Moldawer, M. N. Mindrinos, P. O. Scumpia, C. L. Tannahill, J. Wilhelmy, P. A. Efron, B. H. Brownstein, R. G. Tompkins, M. Toner, Microfluidic isolation of leukocytes from whole blood for phenotype and gene expression analysis. *Analytical Chemistry* **78**, 5453-5461 (2006); published online EpubAug 1 (Doi 10.1021/Ac060140c).
200. S. Yang, A. Undar, J. D. Zahn, A microfluidic device for continuous, real time blood plasma separation. *Lab on a Chip* **6**, 871-880 (2006)10.1039/B516401J).
201. S. Mittal, I. Y. Wong, W. M. Deen, M. Toner, Antibody-Functionalized Fluid-Permeable Surfaces for Rolling Cell Capture at High Flow Rates. *Biophys J* **102**, 721-730 (2012); published online EpubFeb 22 (DOI 10.1016/j.bpj.2011.12.044).
202. E. A. Warner, K. T. Kotz, R. F. Ungaro, A. S. Abouhamze, M. C. Lopez, A. G. Cuenca, K. M. Kelly-Scumpia, C. Moreno, K. A. O'Malley, J. D. Lanz, H. V. Baker, L. C. Martin, M. Toner, R. G. Tompkins, P. A. Efron, L. L. Moldawer, Microfluidics-based capture of human neutrophils for expression analysis in blood and bronchoalveolar lavage. *Lab Invest* **91**, 1787-1795 (2011); published online EpubDec (DOI 10.1038/labinvest.2011.94).
203. A. W. Greenberg, D. A. Hammer, Cell separation mediated by differential rolling adhesion. *Biotechnol Bioeng* **73**, 111-124 (2001); published online EpubApr 20 (Doi 10.1002/Bit.1043).
204. T. Krüger, D. Holmes, P. V. Coveney, Deformability-based red blood cell separation in deterministic lateral displacement devices—A simulation study. *Biomicrofluidics* **8**, 054114 (2014)doi:http://dx.doi.org/10.1063/1.4897913).
205. S. Choi, J. M. Karp, R. Karnik, Cell sorting by deterministic cell rolling. *Lab on a Chip* **12**, 1427-1430 (2012).
206. L. R. Huang, E. C. Cox, R. H. Austin, J. C. Sturm, Continuous Particle Separation Through Deterministic Lateral Displacement. *Science* **304**, 987-990 (2004); published online EpubMay 14, 2004 (10.1126/science.1094567).
207. S. Bose, R. Singh, M. Hanewich-Hollatz, C. Shen, C. H. Lee, D. M. Dorfman, J. M. Karp, R. Karnik, Affinity flow fractionation of cells via transient interactions with asymmetric molecular patterns. *Sci Rep-Uk* **3**, (2013); published online EpubJul 31 (Artn 2329
Doi 10.1038/Srep02329).
208. C. H. Lee, S. Bose, K. J. Van Vliet, J. M. Karp, R. Karnik, Examining the Lateral Displacement of HL60 Cells Rolling on Asymmetric P-Selectin Patterns. *Langmuir* **27**, 240-249 (2011); published online EpubJan 4 (Doi 10.1021/La102871m).

209. S. Hong, D. Lee, H. Zhang, J. Q. Zhang, J. N. Resvick, A. Khademhosseini, M. R. King, R. Langer, J. M. Karp, Covalent immobilization of P-selectin enhances cell rolling. *Langmuir* **23**, 12261-12268 (2007); published online EpubNov 20 (Doi 10.1021/La7014397).
210. C. Edington, H. Murata, R. Koepsel, J. Andersen, S. Eom, T. Kanade, A. Balazs, G. Kolmakov, Z. Liron, A. Russell, Tailoring the trajectory of cell rolling with cytotactic surfaces. *J Tissue Eng Regen M* **6**, 230-231 (2012); published online EpubSep (
211. T. Kuijpers, A. Tool, C. van der Schoot, L. Ginsel, J. Onderwater, D. Roos, A. Verhoeven, *Membrane surface antigen expression on neutrophils: a reappraisal of the use of surface markers for neutrophil activation*. (1991), vol. 78, pp. 1105-1111.
212. M. T. Elghetany, F. Lacombe, Physiologic variations in granulocytic surface antigen expression: impact of age, gender, pregnancy, race, and stress. *Journal of Leukocyte Biology* **75**, 157-162 (2004); published online EpubFebruary 1, 2004 (10.1189/jlb.0503245).
213. D. Strauss-Ayali, S. M. Conrad, D. M. Mosser, Monocyte subpopulations and their differentiation patterns during infection. *Journal of Leukocyte Biology* **82**, 244-252 (2007); published online EpubAugust 1, 2007 (10.1189/jlb.0307191).
214. H. Y. Zhu, I. Sencan, J. Wong, S. Dimitrov, D. Tseng, K. Nagashima, A. Ozcan, Cost-effective and rapid blood analysis on a cell-phone. *Lab on a Chip* **13**, 1282-1288 (2013)Doi 10.1039/C3lc41408f).
215. N. Jiang, J. Huang, L. J. Edwards, B. Y. Liu, Y. Zhang, C. D. Beal, B. D. Evavold, C. Zhu, Two-Stage Cooperative T Cell Receptor-Peptide Major Histocompatibility Complex-CD8 Trimolecular Interactions Amplify Antigen Discrimination. *Immunity* **34**, 13-23 (2011); published online EpubJan 28 (DOI 10.1016/j.immuni.2010.12.017).
216. N. Kent, L. Basabe-Desmonts, G. Meade, B. MacCraith, B. Corcoran, D. Kenny, A. Ricco, Microfluidic device to study arterial shear-mediated platelet-surface interactions in whole blood: reduced sample volumes and well-characterised protein surfaces. *Biomedical Microdevices* **12**, 987-1000 (2010)10.1007/s10544-010-9453-y).
217. E. Gutierrez, B. G. Petrich, S. J. Shattil, M. H. Ginsberg, A. Groisman, A. Kasirer-Friede, Microfluidic devices for studies of shear-dependent platelet adhesion. *Lab on a Chip* **8**, 1486-1495 (2008).
218. F. J. Tovar-Lopez, G. Rosengarten, E. Westein, K. Khoshmanesh, S. P. Jackson, A. Mitchell, W. S. Nesbitt, A microfluidics device to monitor platelet aggregation dynamics in response to strain rate micro-gradients in flowing blood. *Lab on a Chip* **10**, 291-302 (2010).
219. J. J. NORMAN, V. MUKUNDAN, D. BERNSTEIN, B. L. PRUITT, Microsystems for Biomechanical Measurements. *Pediatric Research* **63**, 576-583 510.1203/PDR.1200b1013e31816b31812ec31814 (2008).
220. K. Christ, K. Williamson, K. Masters, K. Turner, Measurement of single-cell adhesion strength using a microfluidic assay. *Biomedical Microdevices* **12**, 443-455 (2010)10.1007/s10544-010-9401-x).

221. T. Yago, V. I. Zarnitsyna, A. G. Klopocki, R. P. McEver, C. Zhu, Transport Governs Flow-Enhanced Cell Tethering through L-Selectin at Threshold Shear. *Biophysical journal* **92**, 330-342 (2007).
222. C. Zhu, T. Yago, J. Lou, V. Zarnitsyna, R. McEver, Mechanisms for Flow-Enhanced Cell Adhesion. *Annals of Biomedical Engineering* **36**, 604-621 (2008)10.1007/s10439-008-9464-5).
223. B. Lincoln, A. J. Ricco, N. J. Kent, L. Basabe-Desmonts, L. P. Lee, B. D. MacCraith, D. Kenny, G. Meade, Integrated system investigating shear-mediated platelet interactions with von Willebrand factor using microliters of whole blood. *Analytical Biochemistry* **405**, 174-183 (2010).
224. C. E. Orsello, D. A. Lauffenburger, D. A. Hammer, Molecular properties in cell adhesion: a physical and engineering perspective. *Trends in Biotechnology* **19**, 310-316 (2001)10.1016/s0167-7799(01)01692-4).
225. C. Cozens-Roberts, D. A. Lauffenburger, J. A. Quinn, Receptor-mediated cell attachment and detachment kinetics. I. Probabilistic model and analysis. *Biophysical journal* **58**, 841-856 (1990).
226. Characterization of laterally deformable elastomer membranes for microfluidics. *Journal of Micromechanics and Microengineering* **17**, 843-851 (2007).
227. A. R. Abate, et al., Microfluidic sorting with high-speed single-layer membrane valves. *Applied Physics Letters* **96**, 203509 (2010).
228. A. R. Abate, D. A. Weitz, Single-layer membrane valves for elastomeric microfluidic devices. *Applied Physics Letters* **92**, 243509 (2008).
229. N. Sundararajan, D. Kim, A. A. Berlin, Microfluidic operations using deformable polymer membranes fabricated by single layer soft lithography. *Lab on a Chip* **5**, 350-354 (2005).
230. M. A. Unger, H.-P. Chou, T. Thorsen, A. Scherer, S. R. Quake, Monolithic Microfabricated Valves and Pumps by Multilayer Soft Lithography. *Science* **288**, 113-116 (2000); published online EpubApril 7, 2000 (10.1126/science.288.5463.113).
231. I. d. C. Cáceres, N. Valmas, M. A. Hilliard, H. Lu, Laterally Orienting <italic>C. elegans</italic> Using Geometry at Microscale for High-Throughput Visual Screens in Neurodegeneration and Neuronal Development Studies. *Plos One* **7**, e35037 (2012)10.1371/journal.pone.0035037).
232. A. R. Abate, J. J. Agresti, D. A. Weitz, Microfluidic sorting with high-speed single-layer membrane valves. *Applied Physics Letters* **96**, (2010); published online EpubMay (10.1063/1.3431281).
233. A. Hatch, A. E. Kamholz, K. R. Hawkins, M. S. Munson, E. A. Schilling, B. H. Weigl, P. Yager, A rapid diffusion immunoassay in a T-sensor. *Nat Biotech* **19**, 461-465 (2001).
234. A. Lionello, J. Josserand, H. Jensen, H. H. Girault, Dynamic protein adsorption in microchannels by "stop-flow" and continuous flow. *Lab on a Chip* **5**, 1096-1103 (2005).
235. S. Takayama, J. C. McDonald, E. Ostuni, M. N. Liang, P. J. A. Kenis, R. F. Ismagilov, G. M. Whitesides, Patterning cells and their environments using multiple laminar fluid flows in capillary networks. *Proceedings of the National*

Academy of Sciences **96**, 5545-5548 (1999); published online EpubMay 11, 1999 (10.1073/pnas.96.10.5545).
236. B. H. Weigl, P. Yager, Microfluidic Diffusion-Based Separation and Detection. *Science* **283**, 346-347 (1999); published online EpubJanuary 15, 1999 (10.1126/science.283.5400.346).
237. R. Chein, S. H. Tsai, Microfluidic Flow Switching Design Using Volume of Fluid Model. *Biomedical Microdevices* **6**, 81-90 (2004)10.1023/b:bmmd.0000013370.86639.61).
238. A. R. Bausch, W. Moller, E. Sackmann, Measurement of local viscoelasticity and forces in living cells by magnetic tweezers. *Biophys J* **76**, 573-579 (1999); published online EpubJan (
239. C. Danilowicz, D. Greenfield, M. Prentiss, Dissociation of ligand-receptor complexes using magnetic tweezers. *Analytical Chemistry* **77**, 3023-3028 (2005); published online EpubMay 15 (Doi 10.1021/Ac050057+).
240. W. Liu, N. Dechev, I. G. Foulds, R. Burke, A. Parameswaran, E. J. Park, A novel permalloy based magnetic single cell micro array. *Lab on a Chip* **9**, 2381-2390 (2009)Doi 10.1039/B821044f).
241. K. C. Neuman, A. Nagy, Single-molecule force spectroscopy: optical tweezers, magnetic tweezers and atomic force microscopy. *Nat Methods* **5**, 491-505 (2008); published online EpubJun (Doi 10.1038/Nmeth.1218).
242. N. D. Shapiro, K. A. Mirica, S. Soh, S. T. Phillips, O. Taran, C. R. Mace, S. S. Shevkoplyas, G. M. Whitesides, Measuring Binding of Protein to Gel-Bound Ligands Using Magnetic Levitation. *Journal of the American Chemical Society* **134**, 5637-5646 (2012); published online EpubMar 28 (Doi 10.1021/Ja211788e).
243. N. D. Shapiro, S. Soh, K. A. Mirica, G. M. Whitesides, Magnetic Levitation as a Platform for Competitive Protein–Ligand Binding Assays. *Analytical Chemistry* **84**, 6166-6172 (2012); published online Epub2012/07/17 (10.1021/ac301121z).
244. A. J. W. te Velthuis, J. W. J. Kerssemakers, J. Lipfert, N. H. Dekker, Quantitative Guidelines for Force Calibration Through Spectral Analysis of Magnetic Tweezers Data. *Biophys J* **100**, 481-481 (2011); published online EpubFeb 2 (
245. C. Claudet, J. Bednar, Magneto-optical tweezers built around an inverted microscope. *Appl Optics* **44**, 3454-3457 (2005); published online EpubJun 10 (Doi 10.1364/Ao.44.003454).
246. C. M. Fu, C. M. Han, C. W. Cheng, C. S. Chou, Bio-mechanical Properties of Human Renal Cancer Cells probed by Magneto-Optical Tweezers. *Ieee Sensor*, 111-114 (2012).
247. C. Haber, D. Wirtz, Magnetic tweezers for DNA micromanipulation. *Rev Sci Instrum* **71**, 4561-4570 (2000); published online EpubDec (Pii [S0034-6748(00)05212-6]
Doi 10.1063/1.1326056).
248. N. D. Shapiro, S. Soh, K. A. Mirica, G. M. Whitesides, Magnetic Levitation as a Platform for Competitive Protein-Ligand Binding Assays. *Analytical Chemistry* **84**, 6166-6172 (2012); published online EpubJul 17 (Doi 10.1021/Ac301121z).
249. R. J. Mallis, K. Bai, H. Arthanari, R. E. Hussey, M. Handley, Z. Li, L. Chingozha, J. S. Duke-Cohan, H. Lu, J.-H. Wang, C. Zhu, G. Wagner, E. L. Reinherz, Pre-TCR ligand binding impacts thymocyte development before αβTCR expression.

Proceedings of the National Academy of Sciences, (2015); published online EpubJune 8, 2015 (10.1073/pnas.1504971112).